

Use Authorization

In presenting this dissertation in partial fulfillment of the requirements for an advanced degree at Idaho State University, I agree that the Library shall make it freely available for inspection. I further state that permission to download and/or print my dissertation for scholarly purposes may be granted by the Dean of the Graduate School, Dean of my academic division, or by the University Librarian. It is understood that any copying or publication of this dissertation for financial gain shall not be allowed without my written permission.

Signature_____

Date_____

Neutron Skin Measurement of ^{208}Pb Using
Parity-Violating Electron Scattering

by

Devi Lal Adhikari

A dissertation
submitted in partial fulfillment
of the requirements for the degree of
Doctor of Philosophy in the Department of Physics
Idaho State University
Summer 2021

Copyright (2021) Devi Lal Adhikari
All rights reserved.

Committee Approval

To the Graduate Faculty:

The members of the committee appointed to examine the dissertation of DEVI LAL ADHIKARI find it satisfactory and recommend that it be accepted.

Dr. Dustin McNulty,
Major Advisor

Dr. Daniel Dale,
Committee Member

Dr. Tony Forest,
Committee Member

Dr. Steven Shropshire,
Committee Member

Dr. Chikashi Sato,
Graduate Faculty Representative

Acknowledgements

This dissertation is an outcome of many years of continuous effort, devotion, and studies, not only by the author but also by many people who have supported the author by providing their time, advice, and expertise. During my graduate study and in providing today's shape to this document, I received generous support, guidance, and thoughtful advice from my advisor, Dr. Dustin McNulty. I would like to extend my deepest gratitude to him for the motivation, enthusiasm, great effort and immense knowledge he put into training me in this field. This work is supported by NSF award 1615146 and DOE office of science award DE-SC0021244.

I am profoundly grateful to the faculties of the Physics Department, at Idaho State University (ISU), especially to Dr. Daniel Dale, Dr. Steven Shropshire, and Dr. Tony Forest for their intellectual suggestions and encouragements throughout this journey. My sincere appreciation goes to Dr. Chikashi Sato for introducing me to the ISU family and for your continuous support and guidance during my M.Sc. degree back in Nepal and Ph.D. degree here in the USA.

I would like to thank Dr. Krishna Kumar (UMass), Dr. Robert Michaels (JLab), Dr. Kent Paschke (UVa), Dr. Paul King (Ohio U.), and all other spokespersons and PIs of PREX-2/CREX collaboration. Thanks to an army of postdocs for all of their sleepless nights, especially Dr. Chandan Ghosh for teaching me a lot of Physics and instrument handling skills. I would also like to thank and congratulate all the graduate

students for their hard work that led to the success of these experiments.

Last but not least, I would like to acknowledge my parents (Bal Ram Adhikari and Dhanu Maya Adhikari) and relatives for their support in making this journey fruitful. Durga Tiwari Adhikari, my wife, your trust, devotion, and everything you could do encouraged me to undertake this venture. Thank you very much for taking care of three babies, Dibya, Dewan, and myself.

Contents

List of Figures	xi
List of Tables	xvi
Abstract	xx
1 Introduction and Background	1
1.1 Concept of Neutron Skin	1
1.2 Connection to Isovector Parameters	4
1.3 PREX-2/CREX and Author's Contribution	6
2 Physics Motivation and Pertinent Theory	9
2.1 Basic Concepts Behind Weak Interactions	9
2.1.1 The Fundamental Forces of Nature	9
2.1.2 Electromagnetic and Weak Interactions	10
2.1.3 Helicity	11
2.1.4 Symmetry and Conservation Law	12
2.1.5 Parity	12
2.2 Parity-Violation in Weak Interaction	14
2.3 Electroweak Theory and Higgs Mechanism	15
2.4 Electromagnetic Scattering and Form Factor	17
2.5 Weak Neutral Current	20

CONTENTS

2.6	Electron Scattering From a Weak Potential	21
2.7	Parity-Violating Asymmetry (A_{PV})	22
2.8	Importance of Q^2	24
2.9	History of PVeS Experiments	26
2.10	Motivations	28
2.10.1	Choice of Targets	28
2.10.2	PVeS versus Other Approaches	29
2.10.3	Choice of Kinematics	30
2.10.4	Neutron Skin (R_{skin}) Calculation	30
2.10.5	Importance of PREX-2/CREX measurements	32
3	Experimental Setups	35
3.1	Jefferson Lab	35
3.2	Injector	37
3.2.1	Intensity Attenuator (IA) System	38
3.2.2	RTP Pockels cell	39
3.2.3	Insertable Halfwave Plate (IHWP)	41
3.2.4	Rotatable Halfwave Plate (RHWP)	41
3.2.5	Gallium Arsenide (GaAs) Photocathode	42
3.2.6	Double Wien	43
3.3	The Accelerator	44
3.4	Hall A Beamline	44
3.4.1	Beam Modulation (or Dithering)	45
3.4.2	Harp Scan and Beam Raster	46
3.4.3	Beam Position Monitors (BPMs)	49
3.4.4	Beam Current Monitors (BCMs)	52
3.4.5	Polarimetry	53
3.4.6	Scattering Chamber and Targets	57

CONTENTS

3.4.7	Collimator and Septum Magnet	64
3.4.8	Radiation shielding	66
3.5	High Resolution Spectrometers (HRSs)	68
3.6	PREX-2/CREX Detector System	69
3.6.1	Vertical Drift Chamber (VDC)	70
3.6.2	Scintillators	71
3.6.3	Focal Plane Detector Package	74
3.6.4	Detector Non-linearity	90
3.7	Small Angle Monitors (SAMs)	96
3.7.1	SAM Installation	98
3.7.2	SAM Performance	101
3.8	Data Acquisition Systems (DAQs)	102
3.9	Counting DAQ	102
3.10	Integrating DAQ	104
4	Data Analysis	107
4.1	Focal-Plane Detector Alignment	108
4.1.1	HRS Dispersion and Quartz Acceptance	111
4.1.2	Rejecting Inelastic Flux from the Acceptance	113
4.2	Asymmetry Analysis	115
4.2.1	Cuts	116
4.2.2	Pedestal Calibration	117
4.2.3	Raw Asymmetry and Charge Normalization	118
4.2.4	Helicity-correlated Position Differences (HCPD)	119
4.2.5	Beam Fluctuation-corrected Asymmetry (A_{cor})	122
4.2.6	Helicity-correlated Pedestal Asymmetry (HCPA)	128
4.3	Backgrounds and Possible Corrections	130
4.3.1	Coulomb Distortion	131

CONTENTS

4.3.2	Beam Polarization	131
4.3.3	Detector Non-linearity	132
4.3.4	Target Backing and Impurity Correction	133
4.3.5	Inelastic Contributions	136
4.3.6	Rescattering during HRS Transport	140
4.4	Blinded Tube/Stubby Quartz Test	144
4.5	Auxiliary Detectors (Background Monitors)	149
4.5.1	Position Scan	151
4.5.2	Blinded Tube Test	152
4.5.3	HCPA for Auxiliary Detectors	152
4.5.4	HCPD and Correction Slopes for Auxiliary Detectors	154
4.5.5	Non-linearity	155
4.5.6	Summary of Auxiliary Detectors	157
4.6	Q^2 Measurement	158
4.6.1	Energy Measurement	158
4.6.2	Scattering Angle Measurement	159
4.6.3	Average Q^2	160
4.6.4	Other Systematic Uncertainties on Q^2 Measurement	162
4.7	Finite Acceptance	163
4.8	Transverse Asymmetry Measurements	165
4.8.1	Beam Corrections	167
4.8.2	Target Impurity Corrections	168
4.8.3	Correction for Imperfect Beam Polarization	169
4.8.4	Summary of A_T Measurements	170
4.9	Summary of Corrections to A_{PV}	170
4.10	Parity-Violating Asymmetry (A_{PV})	170
4.11	Weak Charge Radius (R_W) of ^{208}Pb	172

CONTENTS

4.12 Neutron Skin (R_{skin}) of ^{208}Pb	175
5 Result and Conclusion	176
5.1 Parity-Violating Asymmetry A_{PV}	176
5.2 Neutron Skin (R_{skin}) of ^{208}Pb	177
5.3 Implications of PREX results	178
5.4 Conclusions	179
A Detector Non-linearity	182
B Possible Background Corrections	196
B.1 Strangeness and Neutron Electric Form Factor	196
B.2 Parity Admixtures and Meson Exchange Currents	198
B.3 Dispersion Corrections	199
B.4 Shape Dependence and Surface Thickness	199
C CREX Inelastic Contamination	201
D PREX-2 Transverse Asymmetries	205

List of Figures

1.1	The nuclear landscape.	2
1.2	Density distributions in ^{208}Pb a nucleus.	3
1.3	Slope of the symmetry energy as a function of R_{skin} for ^{208}Pb	6
2.1	Feynman diagram for an electromagnetic interaction.	11
2.2	Feynman diagrams for weak interactions.	11
2.3	Depiction of helicity reversal under parity operation.	14
2.4	The first experimental proof of parity-violation.	16
2.5	Running coupling strengths of fundamental forces.	18
2.6	Schematic of a typical electromagnetic scattering process.	18
2.7	Correlation coefficients between R_n and F_W	25
2.8	Experimental blueprint of the E122 experiment at SLAC.	27
2.9	An example energy level diagram of single-particle spherical shell model.	29
3.1	Sketch of JLab accelerator site and experimental halls.	36
3.2	Simple cartoon of the JLab injector setup.	37
3.3	Detailed schematic of the JLab polarized electron source.	38
3.4	Illustration of various sources of helicity-correlated false asymmetries.	40
3.5	Photo-emission process in a strained GaAs photocathode.	43
3.6	JLab injector Wien filter setup.	44

LIST OF FIGURES

3.7	Schematic view of Hall A, JLab.	45
3.8	Schematic view of dithering coils.	47
3.9	Typical spot++ run on a ^{208}Pb target during PREX-2.	49
3.10	Typical spot++ run on a ^{48}Ca target during CREX.	49
3.11	Schematic diagram of the four wire-antennae of a stripline BPM. . .	51
3.12	Schematic of the Hall A beam current monitoring system.	52
3.13	Schematic of Hall A Møller polarimeter.	55
3.14	Simple schematic of the Compton polarimeter in Hall A at JLab. . .	57
3.15	Compton photon detector table.	58
3.16	PREX-2/CREX scattering chamber.	59
3.17	PREX-2/CREX production target ladder sketch.	59
3.18	PREX-2/CREX optics target ladder sketch.	60
3.19	Evidence of target degradation during production running.	63
3.20	Evidence of target degradation from counting mode raster checks. .	63
3.21	Photograph of accidental damage to ^{48}Ca target.	64
3.22	PREX-2/CREX beamline collimator.	65
3.23	Photograph of PREX-2/CREX HRS acceptance collimators.	66
3.24	PREX-2/CREX septum drawing.	67
3.25	Side-view drawing of a Hall A HRS.	69
3.26	CAD view of the PREX-2/CREX detectors in the HRS hut.	70
3.27	Schematic views of the Hall A VDCs.	72
3.28	Schematic drawing of the S0 scintillator.	73
3.29	An indication of S0 damage.	73
3.30	Photograph of S3 scintillator used in CREX.	74
3.31	CAD render of the PREX-2/CREX focal plane main detector package.	75
3.32	Photograph of the left-HRS focal plane detector package.	78
3.33	Main detector quartz design change from PREX-1 to PREX2. . . .	79

LIST OF FIGURES

3.34	Schematic representation of a Čerenkov cone.	80
3.35	PREX-2 detector yields over time.	85
3.36	CAD drawing of a PREX-2 GEM chamber.	87
3.37	Timing diagram for PMT non-linearity bench tests.	93
3.38	Experimental setup for PMT non-linearity bench-tests.	95
3.39	Sample non-linearity data for PMT ZK5407.	96
3.40	Summary non-linearity results for PREX-2 PMTs.	97
3.41	Collage of drawings and photos for the SAM system.	99
3.42	Wiring configuration of a SAM detector.	100
3.43	DAQ flowchart of counting mode triggers in use during CREX. . . .	104
3.44	Helicity pattern train combinations.	106
4.1	Electron hit distributions on the three small GEMs in right-HRS. . .	108
4.2	Comparison of the reconstructed track variables distributions using GEMs and VDCs.	109
4.3	Pulse-height distribution for left-HRS upstream main detector. . . .	110
4.4	Estimating the dispersion constant in the left-HRS.	112
4.5	Dispersion constant in the left-HRS via dp scan.	112
4.6	Schematic of the transport and detector coordinate systems.	113
4.7	Left-HRS main detector alignment plots during PREX-2.	114
4.8	Left-HRS main detector alignment plots during CREX.	115
4.9	Pedestal calibration for upstream main detectors.	118
4.10	Demonstration of the power of beam corrections.	123
4.11	Correlation between raw asymmetry and beam position difference. . .	124
4.12	An example of beam modulation for a typical modulation cycle. . .	126
4.13	PREX-2 Lagrange-corrected (blinded) asymmetry as a function of slug number.	128

LIST OF FIGURES

4.14	Helicity-correlated pedestal asymmetry for a typical beam-off run during PREX-2.	129
4.15	Grand aggregated helicity-correlated pedestal asymmetry.	130
4.16	Electroweak interaction and Coulomb distortion effect.	132
4.17	Energy or momentum distribution for ^{208}Pb	137
4.18	Rescattering probability plotted against HRS dipole setting.	142
4.19	Relative rate for ^{208}Pb as a function of relative momentum.	143
4.20	Radiative effects before, after, and at the scattering vertex.	144
4.21	Photograph of left-HRS detectors installed with stubby quartz and blinded PMT.	145
4.22	Normal vs blinded/stubby detector ADC distributions in the left-HRS.	147
4.23	Helicity-correlated false asymmetry due to blinded fraction in right-HRS.	148
4.24	Relative positions of auxiliary detectors in the HRSs.	150
4.25	Pedestal asymmetry distribution for a typical beam-off run.	153
4.26	Non-linearity plotted against anode current for PMT ZK5363.	156
4.27	PREX-2 Q^2 distributions in left and right HRS.	161
4.28	PREX-2 Q^2 measurement results as a function of time.	162
4.29	PREX-2 acceptance function versus scattering angle (θ).	164
4.30	Scattering plane relative to the hall coordinate system.	166
4.31	Weak charge radius (R_W) and neutron skin ($R_{skin} = R_n - R_p$) of ^{208}Pb as a function of A_{PV} for various theoretical models.	174
5.1	Electric dipole polarizability times symmetry energy plotted against R_{skin} of ^{208}Pb	180
B.1	Electroweak interaction and dispersion corrections.	199
C.1	The momentum (or energy) spectrum of ^{208}Ca	202

LIST OF FIGURES

C.2	Quartz acceptance function for CREX.	203
D.1	Dither corrected transverse asymmetries for ^{208}Pb	206
D.2	Dither corrected transverse asymmetries for ^{40}Ca	206
D.3	Dither corrected transverse asymmetries for ^{12}C	207

List of Tables

2.1	The fundamental forces of nature.	10
2.2	Neutral vector and axial vector couplings for electron and light quarks.	20
2.3	Past PVeS experiments at JLab.	28
3.1	A complete list of PREX-2/CREX targets.	61
3.2	Details about the three foils used in new ^{48}Ca target.	64
3.3	Factory specifications for the quartz used in PREX-2/CREX detectors.	82
3.4	Anode current comparison of PMTs used in PREX-2 detectors.	86
3.5	PMT and HV settings for PREX-2/CREX main detectors.	97
3.6	SAM system PMT gain and pre-amplifier settings for PREX-2 and CREX.	101
4.1	Average raw asymmetry (blinded) and charge asymmetry.	119
4.2	Helicity-correlated position and energy differences.	121
4.3	Helicity-correlated beam position and angle differences at the target.	122
4.4	Helicity-correlated beam-off asymmetries and pedestal noise.	130
4.5	Acceptance probability of the elastic peak and first four excited states of ^{208}Pb	138
4.6	Relative cross-section of the first excited state of ^{208}Pb	139
4.7	Corrections and systematic errors on A_{PV} due to the inelastic back- ground for PREX-2.	140

LIST OF TABLES

4.8	Corrections and systematic errors on A_{PV} due to the rescattering background.	143
4.9	Helicity-correlated asymmetries due to blinded/stubby fraction. . .	146
4.10	Helicity-correlated false asymmetries due to the blinded fraction. . .	148
4.11	Asymmetries measured by auxiliary detectors during PREX-2. . . .	151
4.12	Blinded tube test results for auxiliary detectors.	152
4.13	Helicity-correlated pedestal asymmetries measured by auxiliary detectors during PREX-2.	153
4.14	Helicity-correlated position differences relevant for the auxiliary detectors.	154
4.15	Position and energy slopes for auxiliary detectors.	155
4.16	Residual position and energy slopes for auxiliary detectors.	155
4.17	Spectrometer central scattering angles measured for PREX-2.	160
4.18	Asymmetries and corresponding Q^2 measurements for transverse running.	168
4.19	Beam normal single spin asymmetry (A_T) results for various targets.	170
4.20	Summary of PREX-2 corrections and systematic uncertainties. . . .	171
5.1	Summary of experimental uncertainties from various sources.	177
A.1	Non-linearities for PMT ZK5407 at 10 nA light level.	182
A.2	Non-linearities for PMT ZK5407 at 7 nA light level.	183
A.3	Non-linearities for PMT ZK5407 at 3.5 nA light level.	183
A.4	Non-linearities for PMT ZK5407 at 0.3 nA light level.	183
A.5	Non-linearities for PMT ZK5401 at 10 nA light level.	184
A.6	Non-linearities for PMT ZK5401 at 3.5 nA light level.	184
A.7	Non-linearities for PMT ZK5401 at 0.3 nA light level.	184
A.8	Non-linearities for PMT ZK5401 at 0.18 nA light level.	185

LIST OF TABLES

A.9	Non-linearities for PMT ZK5401 at 0.15 nA light level.	185
A.10	Non-linearities for PMT ZK4033 at 10 nA light level.	185
A.11	Non-linearities for PMT ZK4033 at 7 nA light level.	186
A.12	Non-linearities for PMT ZK4033 at 3.5 nA light level.	186
A.13	Non-linearities for PMT ZK4033 at 0.3 nA light level.	186
A.14	Non-linearities for PMT ZK4033 at 0.18 nA light level.	187
A.15	Non-linearities for PMT ZK4033 at 0.15 nA light level.	187
A.16	Non-linearities for PMT ZK5370 at 10 nA light level.	187
A.17	Non-linearities for PMT ZK5370 at 7 nA light level.	187
A.18	Non-linearities for PMT ZK5370 at 3.5 nA light level.	188
A.19	Non-linearities for PMT ZK5370 at 0.3 nA light level.	188
A.20	Non-linearities for PMT ZK5370 at 0.18 nA light level.	188
A.21	Non-linearities for PMT ZK5365 at 10 nA light level.	189
A.22	Non-linearities for PMT ZK5365 at 7 nA light level.	189
A.23	Non-linearities for PMT ZK5365 at 3.5 nA light level.	189
A.24	Non-linearities for PMT ZK5365 at 0.3 nA light level.	190
A.25	Non-linearities for PMT ZK5365 at 0.18 nA light level.	190
A.26	Non-linearities for PMT ZK5365 at 0.15 nA light level.	190
A.27	Non-linearities for PMT ZK5555 at 7 nA light level.	191
A.28	Non-linearities for PMT ZK5555 at 3.5 nA light level.	191
A.29	Non-linearities for PMT ZK5555 at 0.3 nA light level.	191
A.30	Non-linearities for PMT ZK5555 at 0.18 nA light level.	192
A.31	Non-linearities for PMT ZK5555 at 0.15 nA light level.	192
A.32	Non-linearities for PMT ZK5553 at 7 nA light level.	192
A.33	Non-linearities for PMT ZK5553 at 3.5 nA light level.	193
A.34	Non-linearities for PMT ZK5553 at 0.3 nA light level.	193
A.35	Non-linearities for PMT ZK5553 at 0.18 nA light level.	193

LIST OF TABLES

A.36	Non-linearities for PMT ZK5363 at 10 nA light level.	193
A.37	Non-linearities for PMT ZK5363 at 7 nA light level.	194
A.38	Non-linearities for PMT ZK5363 at 3.5 nA light level.	194
A.39	Non-linearities for PMT ZK5363 at 0.3 nA light level.	194
A.40	Non-linearities for PMT ZK5363 at 0.18 nA light level.	195
A.41	Non-linearities for PMT ZK5363 at 0.15 nA light level.	195
C.1	Inelastic background fractions for CREX.	204

ABSTRACT

Neutron Skin Measurement of ^{208}Pb Using
Parity-Violating Electron Scattering
Dissertation Abstract–Idaho State University (2021)

Nuclear stability requires large nuclei to have more neutrons than protons. While the central core of the nucleus is composed of symmetric nuclear matter, the extra neutrons in heavy nuclei are pushed out to the surface of the nucleus, forming a pure outer neutron skin layer. While the proton distribution inside a nucleus has been accurately measured using electromagnetic probes, previous measurements of neutron distributions in complex nuclei have suffered a lack of systematic precision. PREX-2 and CREX use Parity-Violating electron Scattering (PVeS), as an electroweak interaction probe, to measure the neutron distributions in ^{208}Pb and ^{48}Ca , respectively. Making use of elastic scattering of longitudinally polarized electrons from unpolarized (isotopically pure) targets, PREX-2 and CREX measure the asymmetry in scattering rates between opposite beam polarization states. Since both experiments share the same exact measurement concept and apparatus, much of this dissertation applies to both PREX-2 and CREX. However, the presented asymmetry analysis and neutron skin extraction are only for PREX-2. PREX-2 measures the parity-violating asymmetry, A_{PV} , for 953 MeV electrons scattered elastically from ^{208}Pb at $\sim 5^\circ$ in the lab. The final result is $A_{PV} = 550.00 \pm 16.09(\text{stat.}) \pm 8.16(\text{syst.})$ ppb. From this measurement, we report the neutron skin thickness in ^{208}Pb nuclei to be, $R_{skin} = 0.278 \pm 0.078(\text{exp.}) \pm 0.012(\text{model})$ fm. This measurement has broad implications throughout the physics community, increasing our knowledge in neutron star structure, the equation of state of nuclear matter, nuclear baryon density, nuclear electric dipole polarizability, and more.

Key Words: Neutron skin, electroweak interaction, PREX-2, CREX, parity-violating asymmetry, neutron star, quartz detector, weak charge radius, symmetry energy, Hall A, Jefferson Lab

Chapter 1

Introduction and Background

Let's start by asking a couple of questions: How big is an atomic nucleus? What about a neutron star? A question immediately follows: What does "the size of an atomic nucleus" mean, exactly? It should be worth noting a few common facts here. There is no rigid boundary of a nucleus and thus no simple definition of its size. Rather its size is determined in terms of a probabilistic approach and is expressed as the root-mean-square (RMS) radius, $R = \sqrt{\langle r^2 \rangle}$. Another point is that the nucleus is a composite structure made of protons and neutrons. Protons and neutrons are non-identical fermions and fill up their energy levels independently. For lighter nuclei, the number of protons (Z) and the number of neutrons (N) are roughly equal or symmetric (i.e. $\frac{N}{Z} \approx 1$), but the story is quite different ($\frac{N}{Z} > 1$) in the case of heavier nuclei. Figure 1.1 shows how the nuclear composite symmetry fades away as the nuclear size increases.

1.1 Concept of Neutron Skin

If one ignores the minute differences between the proton and neutron energy levels, arising from them having or not having electromagnetic charge, their distributions

1.1. CONCEPT OF NEUTRON SKIN

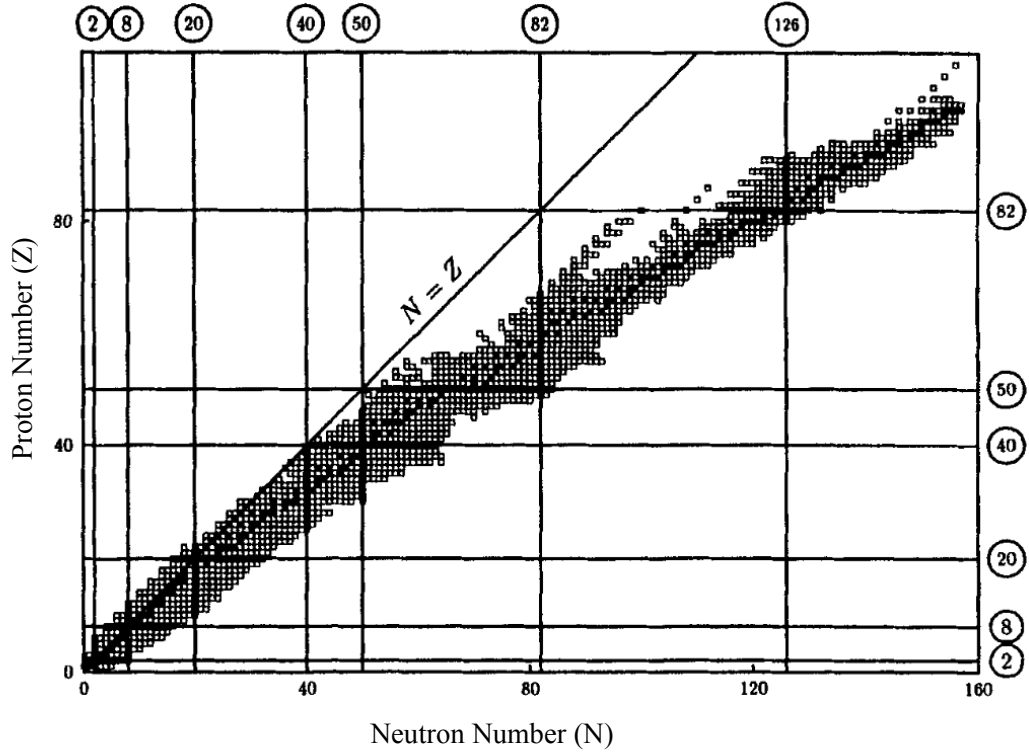


Figure 1.1: The nuclear landscape: distribution of nuclei as a function of proton and neutron numbers [1]. The proton-neutron symmetry ends after $Z = N \approx 20$ (calcium).

within a nucleus extend up to the same boundary as long as the nucleus is small enough to maintain or have proton-neutron symmetry. As we go higher in Z , the nucleus tends to have a larger $\frac{N}{Z} (> 1)$ fraction to maintain stability—compensating for increased electromagnetic repulsion between the larger number of protons. Therefore, when one refers to the nuclear radius of large or complex nuclei, one should clarify whether it is the neutron or proton distribution. Figure 1.2 shows the neutron and proton density distributions in a ^{208}Pb nucleus.

It is commonly understood, but has never been measured with precision, that while the central region of a complex nucleus is composed of a more symmetrical mixture of protons and neutrons, there is an outer-most region composed purely of neutrons. This layer of pure neutrons is referred to as the “neutron skin.” ^{208}Pb has 82 protons and 126 neutrons giving $\frac{N}{Z} \approx 1.54$ while ^{48}Ca has 20 protons and

1.1. CONCEPT OF NEUTRON SKIN

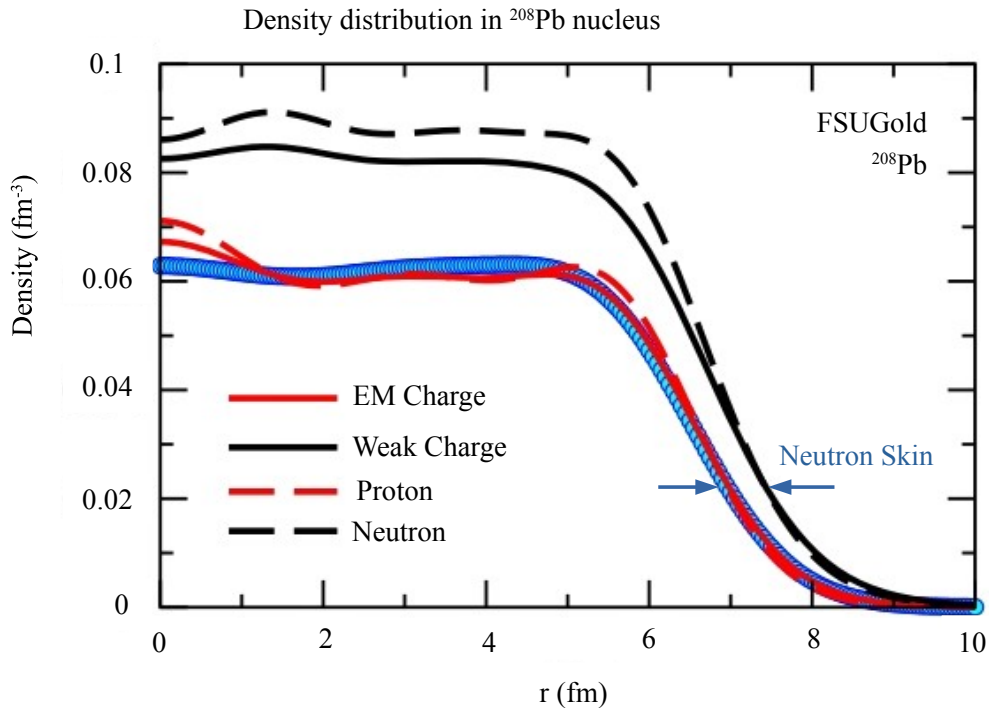


Figure 1.2: Density distributions of proton and neutron in a ^{208}Pb nucleus as predicted by FSUGold [2]. The blue circles represent the experimental charge distribution [3].

28 neutrons giving $\frac{N}{Z} = 1.4$. Therefore, these nuclei are expected to have a layer of pure neutron matter on their outer surface. The thickness of the neutron skin can be thought of as simply the difference between the RMS neutron radius, $R_n = \sqrt{\langle r_n^2 \rangle}$, and the RMS proton radius, $R_p = \sqrt{\langle r_p^2 \rangle}$ (i.e. $R_{skin} = R_n - R_p$). Larger, more asymmetric nuclei typically have thicker neutron skins. For instance, the neutron distribution in ^{208}Pb is reported to be $\sim 20\%$ more diffuse than its charge distribution according to the analyses of coherent π^0 photo-production data from a ^{208}Pb target at the MAMI (Mainzer Mikrotron) facility in Mainz, Germany [4]. The theoretically “clean” PREX-2 measurement of R_{skin} helps probe the formation and structure of neutron stars – objects which are ~ 18 orders of magnitude larger than atomic nuclei. Here, what we mean by clean measurement is that a detailed study has been done on the various possible corrections, and it has been shown over time that the systematic uncertainties corresponding to such corrections are negligible. It turns out that the

1.2. CONNECTION TO ISOVECTOR PARAMETERS

size of a neutron star is directly related to the neutron skin thickness of a heavy nucleus [5].

Being electrically charged, it is not that difficult to probe the distribution of protons, even in complex nuclei. Conversely, there is no (simple) analogous way to probe the distribution of neutrons in nuclei. However, in 1989 it was proposed by Donnelly, Dubach, and Sick [6] to use a *weak-force* probe to get a theoretically clean measurement of neutron distributions in nuclei. The realization of this idea is the underlying theme of this document. The idea is to utilize the fact that parity conservation is not a fundamental symmetry in the realm of weak interactions, as it is in all other known types of interactions. Scrutinizing neutron distributions in neutron-rich nuclei has recently become a highly active area of nuclear particle physics research. This activity is motivated in part by the approval for the construction of the Facility for Rare Isotope Beams (FRIB), and our desire to better understand the fundamental structure of nuclei and neutron stars.

1.2 Connection to Isovector Parameters

It turns out that knowledge of neutron skins (from measurements) provides critical input parameters to the Equation of State (EOS) of neutron-rich matter. The EOS governs the structure of nuclear matter, and better knowledge of it increases the predictive power of the theory. The EOS is a function of nucleon density (ρ) that relates the energy per nucleon, inside neutron-rich matter, to appropriate thermodynamic quantities such as temperature and pressure. And while the EOS has well-known isoscalar terms, that depend on the sum of the number of neutrons and protons, it also has relatively unknown isovector terms, which depend only on the difference in these numbers, and these are (at present) barely constrained by experimental data.

1.2. CONNECTION TO ISOVECTOR PARAMETERS

These parameters are the symmetry energy¹, $S(\rho)$, and its density dependence or slope, $L(\rho) = \frac{dS}{d\rho}|_{\rho_0}$ ($\rho = \rho_n + \rho_p$ being the baryon density, ρ_n and ρ_p are the neutron and proton densities, respectively, and ρ_0 is the saturation density of nuclear matter— which is 0.15 fm^{-3}). To first order, the EOS can be written as a sum of pure isoscalar terms $\xi(\rho, \alpha = 0)$ and $S(\rho)$ as [7]

$$\xi(\rho, \alpha) = \xi(\rho, \alpha = 0) + S(\rho)\alpha^2, \quad (1.1)$$

where $\alpha = \frac{\rho_n - \rho_p}{\rho}$. Figure 1.3 shows $L(\rho)$ as a function of R_{skin} for ^{208}Pb , using predictions from sixteen covariant energy density functionals, at nuclear saturation density ρ_0 and $\frac{2}{3}\rho_0$. At saturation, the pressure of pure neutron matter, $P_{PNM}(\rho_0)$, is closely related to $L(\rho = \rho_0)$ through the expression [7]

$$P_{PNM}(\rho_0) \approx \frac{1}{3}L\rho_0. \quad (1.2)$$

It should also be mentioned that the other important isovector quantity that researchers are focused on measuring is the nuclear electric dipole polarizability, α_D . This is an isovector deformation parameter, which can be used to constrain the neutron skin thickness (of its associated nuclear species); this is done using nuclear energy density functional theory (DFT) in a covariant analysis framework [8]. α_D is essentially an oscillation of the neutron skin against its nuclear core with the restoring force coming from the symmetry energy. α_D in ^{208}Pb was recently determined at the RCNP (Research Center for Nuclear Physics), Osaka University, Japan [9], while the Darmstadt-Osaka collaboration at Oak Ridge National Laboratory (ORNL) recently calculated α_D for ^{48}Ca [10] using an *ab initio* framework and the Titan supercomputer at ORNL. These recent measurements and calculations have built-up even more

¹The symmetry energy can be thought of as a “correction” to the nuclear binding energy due to having asymmetric numbers of protons and neutrons. In a sense, the symmetry energy, which lowers the binding energy, is the energy cost per nucleon for having asymmetric matter.

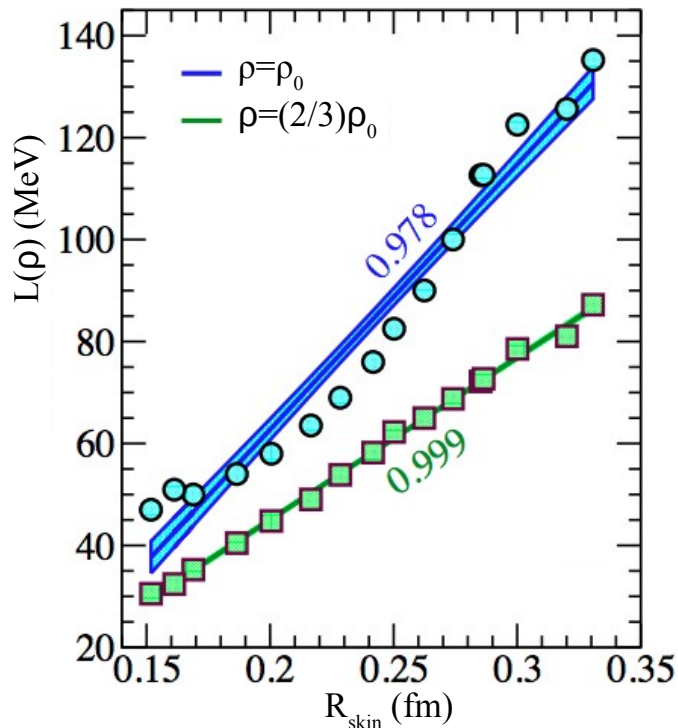


Figure 1.3: Slope of the symmetry energy ($L(\rho)$) as a function of R_{skin} for ^{208}Pb at nuclear saturation density ρ_0 and $\frac{2}{3}\rho_0$ [7].

anticipation for the neutron radii measurements, PREX-2 and CREX, at Jefferson Laboratory (JLab).

1.3 PREX-2/CREX and Author's Contribution

This dissertation presents two experimental endeavors that measure the neutron skin of ^{208}Pb and ^{48}Ca using Parity-Violating Electron Scattering (PVES). The two experiments ran consecutively from June 2019 to September 2020 at JLab. The Continuous Electron Beam Accelerator Facility (CEBAF) and its polarized electron source (Injector) at JLab are capable of providing up to $\approx 90\%$ longitudinally polarized electron beam. PREX-2 and CREX use isotopically pure ^{208}Pb (10 % radiation length) and ^{48}Ca (6 % radiation length) targets, respectively, for physics production. Their measurements are statistics-limited and with a theoretically “clean” interpretation. They

1.3. PREX-2/CREX AND AUTHOR'S CONTRIBUTION

significantly improve the experimental input parameters and confidence in the predictive power of the EOS of neutron-rich matter.

PREX-2 and CREX measure tiny parity-violating asymmetries (A_{PV}), at the part-per-million (ppm) level, to access neutral current weak interaction amplitudes with high precision and uncertainty dominated by statistical error. In order to achieve the high precision in a relatively short time, the experiment's main integrating detectors integrate (count continuously) elastically scattered electron flux at very high rates (≈ 2.2 GHz for PREX-2 and ≈ 28 MHz for CREX). R&D design preparation and operation of such high flux detectors, combined with stringent control of overall systematic errors, are crucial for high precision measurements of tiny quantities such as those from PREX-2 and CREX. Since the work performed by the ISU (Idaho State University) parity group is centered around achieving several of the systematic error goals, they will each be addressed at some point in this document. It is also important to point out that both PREX-2 and CREX use the same measurement concept and apparatus, thus the two experiments have similar systematic error contributions. The only differences between the two experiments are the target material, beam energy, and beam current.

Besides extensive participation in taking shifts, coordinating weekly data analysis, and planning, the author is heavily involved in the design, characterization, installation, and operation of the PREX-2/CREX detectors that include the main detectors, auxiliary detectors (A-T background monitors), small-angle monitors (SAMs), and Gas Electron Multipliers (GEMs). The author is also involved in establishing and maintaining the counting-mode DAQ (data acquisition) electronics setup that includes NIM, Fastbus, and VME (Versa Module European) electronic modules, trigger systems, and tracking detectors. Furthermore, the author also works in maintaining and calibrating the Hall A Vertical Drift Chambers (VDCs) and trigger scintillators. The author plays a major role in systematic and background studies, which include de-

1.3. PREX-2/CREX AND AUTHOR'S CONTRIBUTION

tector pedestal calibrations, electronic (pedestal) noise studies (both integrating and counting mode), detector non-linearity, transverse asymmetry background (from both horizontal- and vertical-transverse beam polarization components), helicity-correlated false beam asymmetries, inelastic contribution, background from rescattering, Q^2 measurements, target impurity correction, and acceptance function calculation.

Chapter 2

Physics Motivation and Pertinent Theory

2.1 Basic Concepts Behind Weak Interactions

2.1.1 The Fundamental Forces of Nature

There are four fundamental forces in nature—gravitational force, electromagnetic force, strong force, and weak force. The first two forces have infinite range and are common to everyone’s experience. The other two are extremely short-range, make up the nuclear force, and are not noticeable in everyday life. In the Standard Model of Particle Physics, when a force exists between any two objects, there is always an associated particle mediating that force. Table 2.1 lists the various forces of nature, their mediators, relative strengths, and ranges. The gravitational force is experienced by every particle that has mass; an electromagnetic force acts on an electromagnetically charged particle; weak force involves quarks and leptons, while only quarks and gluons experience the strong force.

2.1. BASIC CONCEPTS BEHIND WEAK INTERACTIONS

Force	Mediator	Strength	Range
Gravitational	Graviton (hypothetical)	10^{-40}	∞
Weak	W^\pm and Z^0	10^{-11}	10^{-18} m
Electromagnetic	Photon (γ)	1	∞
Strong	Gluon (g)	10^3	10^{-15} m

Table 2.1: The fundamental forces of nature.

2.1.2 Electromagnetic and Weak Interactions

The electromagnetic interaction between any two electrically charged particles (objects) is mediated by a massless photon. A tree-level¹ Feynman diagram for a typical electromagnetic interaction is shown in Fig. 2.1. In contrast, the weak interaction is mediated by massive (and rather heavy) intermediate vector bosons, W^\pm , and Z^0 . A tree-level diagram of a weak interaction involving the W^\pm (charged weak interaction) is shown in Fig. 2.2(a), and a similar diagram for a neutral weak interaction involving the Z^0 is shown in Fig. 2.2(b). While the electromagnetic coupling constant is given by the fine structure constant (α_{em}) as $g_{em} = \sqrt{4\pi\alpha_{em}} \approx 0.303$, the weak coupling constant can also be obtained in a similar way: $g_W = \sqrt{4\pi\alpha_W} \approx 0.653$, where α_W is the weak-force analog of the fine structure constant. This implies that the intrinsic coupling of the weak interaction is stronger than that of the electromagnetic interaction. However, the general form of the amplitude (\mathcal{M}_x) for an interaction can be expressed in terms of the four-momentum transfer squared (q^2) and the mass (M_x) of the propagator as

$$\mathcal{M}_x(q^2) \propto \frac{g_x^2}{q^2 - M_x^2}, \quad (2.1)$$

where g_x is the general coupling constant. For electromagnetic interaction, $M_x = M_\gamma = 0$ while for weak interaction, $M_x \approx 80$ GeV for W^\pm and $M_x \approx 91$ GeV for Z^0 . Normally, $q^2 \ll M_x^2$ for the weak interaction, which makes the amplitude very small.

¹A leading-order Feynman diagram with no closed loops.

2.1. BASIC CONCEPTS BEHIND WEAK INTERACTIONS

Therefore, weak interactions are feeble not because the intrinsic coupling is small, but because the mediators are so massive [11]. However, at much higher energies the q^2 term dominates making the electromagnetic and weak interactions behave the same way. This leads to the electromagnetic and weak force unification and hence the birth of “Electroweak Theory.” A brief introduction to the theory is presented in Sec. 2.3.

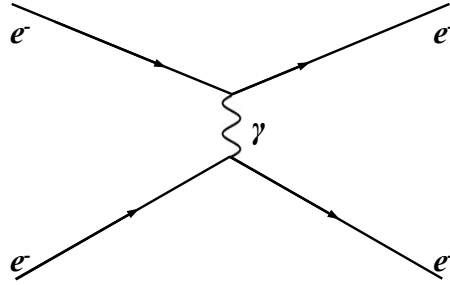


Figure 2.1: Feynman diagram for an electromagnetic interaction at tree-level.

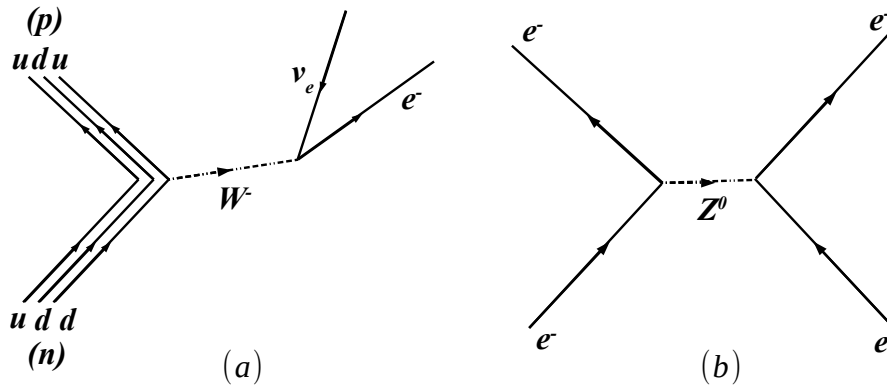


Figure 2.2: Tree-level Feynman diagram (a) for the flavor changing, charged current weak interaction of β^- decay, and (b) for a flavor conserving, neutral current weak interaction, such as those in PVeS.

2.1.3 Helicity

Mathematically, the helicity (h) of a particle is the projection of its spin vector (\vec{s}) into the direction of its momentum (\vec{p}). It can have a positive or negative sign depending on the sign of the projection

2.1. BASIC CONCEPTS BEHIND WEAK INTERACTIONS

$$h = \vec{s} \cdot \hat{p}, \quad (2.2)$$

where $\hat{p} = \frac{\vec{p}}{|\vec{p}|}$ is the unit vector defining the direction of the particle's momentum. If h is positive, the particle is called right-handed (if you curl the four fingers of your right hand while keeping your thumb pointed in a constant direction, then the thumb represents the direction of momentum while the curled fingers represent the spin of the particle). If h is negative then the particle is said to be left-handed (apply the same above rule, but using your left hand). While helicity is Lorentz invariant for a massless particle, its sign completely depends on the speed of the observer in the case of particles with mass. Therefore, helicity, in general, is not an intrinsic property of a particle but rather is frame-dependent.

2.1.4 Symmetry and Conservation Law

If a physical system remains unchanged under a certain transformation, it is said to be symmetric under the transformation. The transformation can be continuous (for example rotation) or discrete (for example mirror reflection). In 1915, Emmy Noether showed that there is always a conserved quantity associated with a given continuous symmetry. For example, if a system is symmetric under translation in time, the energy of the system is conserved. If the system is symmetric under translation in space, the linear momentum of the system is conserved.

2.1.5 Parity

Parity is a discrete transformation under which a physical system flips the sign of its spatial coordinates. The parity operator, \mathbf{P} , acts on the spatial wave function of a system, $\psi(\vec{r})$, and alters the sign of its coordinates as

2.1. BASIC CONCEPTS BEHIND WEAK INTERACTIONS

$$\mathbf{P}\psi(\vec{r}) = \psi(-\vec{r}). \quad (2.3)$$

When the parity operator is applied to Eq. 2.3 a second time, it returns the original wave function $\psi(\vec{r})$, i.e.

$$\mathbf{P}^2\psi(\vec{r}) = \mathbf{P}\psi(-\vec{r}) = \psi(\vec{r}). \quad (2.4)$$

If p is an eigenvalue of \mathbf{P} then $\mathbf{P}^2\psi(\vec{r}) = p^2\psi(\vec{r})$, which requires that $p^2 = 1$. Therefore, $p = \pm 1$ are the eigenvalues of \mathbf{P} . When there is symmetry under the parity operation (i.e. when $\mathbf{P}\psi(\vec{r}) = p\psi(\vec{r})$), parity is said to be conserved. Note that when operating on a polar vector, parity reverses the sign or the direction of the vector (taking $p = -1$ eigenvalue) while it leaves an axial-vector (pseudovector²) unchanged (taking $p = +1$ eigenvalue). In general, if a system reverses its sign after parity operation, its parity is odd and if a system is unaffected by the parity transformation, its parity is even. Therefore, under parity operation, the helicity of a particle gets flipped because it (\mathbf{P}) alters the direction of the particle's momentum (\vec{p}) and leaves its spin (\vec{s}) unaffected as shown in Fig. 2.3 (note that \vec{s} is a pseudovector).

In PREX-2 and CREX we change the helicity of the electron beam at a given frequency, which effectively performs a parity operation on our apparatus during the experiment (at the given frequency). Historically, parity was assumed to be a universal symmetry for all forces, but in the 1950s it was discovered to be violated in nuclear beta decay.

²A pseudovector is a vector, which is obtained from a cross (vector) product of two polar vectors. For example, the angular momentum \vec{L} of a particle is given by the cross product of the particle's position vector \vec{r} and its momentum vector \vec{p} . That is $\vec{L} = \vec{r} \times \vec{p}$. Under parity operation, $\mathbf{P}(\vec{L}) = \mathbf{P}(\vec{r} \times \vec{p}) = \mathbf{P}(\vec{r}) \times \mathbf{P}(\vec{p}) = (-\vec{r}) \times (-\vec{p}) = \vec{r} \times \vec{p}$. Hence, pseudovectors remain unchanged under parity operation.

2.2. PARITY-VIOLATION IN WEAK INTERACTION

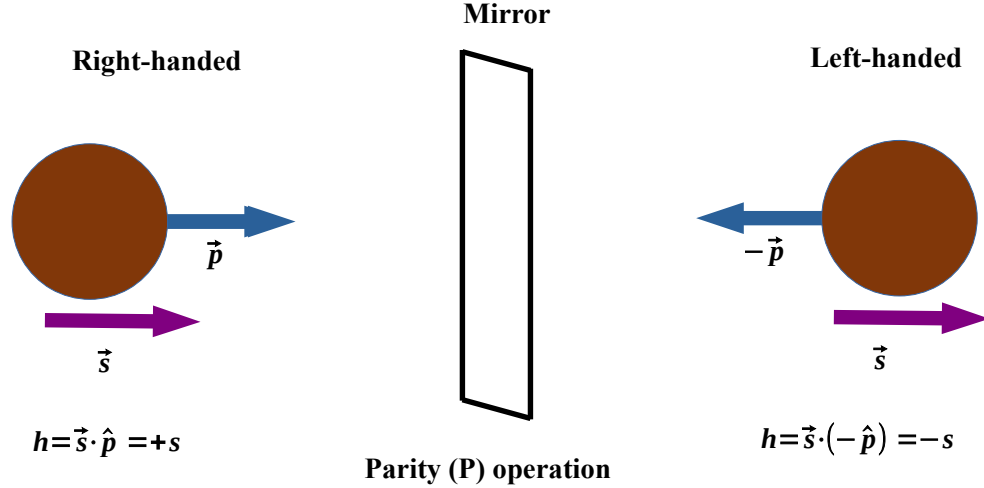


Figure 2.3: Depiction of helicity reversal under parity operation (mirror symmetry violation). The helicity of a particle changes its sign under parity operation. It is because the parity operator (\mathbf{P}) changes the direction of the particle’s motion while leaving the spin direction unchanged.

2.2 Parity-Violation in Weak Interaction

Before the 1950s parity was assumed to be a universal symmetry, although it had never been tested in weak interactions. In the early 50s, there was a puzzling problem that physicists were trying to solve. The puzzle was famously dubbed the “ $\tau - \theta$ ” puzzle. τ and θ were identified as two particles, which were identical in every respect but had completely separate decay modes: the τ was observed to decay into three pions ($\pi^+\pi^0\pi^0$ or $\pi^+\pi^+\pi^-$), while the θ was found to decay into two pions ($\pi^+\pi^0$). This implies that the τ decays into a final state with odd parity, while the θ decays into a parity even state. How come the particles with the same initial parity decay into the final states with different parity? This was the question physicists were trying to answer. In the mid-50s Tsung-Dao Lee and Chen-Ning Yang questioned parity conservation in the weak interaction [12] and suggested an experimental test. In 1956, Chien-Shiung Wu and her team observed beta decay in cobalt-60 nuclei and demonstrated that parity symmetry was maximally violated [13]. For this pioneering achievement, Lee and Yang were awarded the 1957 Nobel Prize for Physics. With this

2.3. ELECTROWEAK THEORY AND HIGGS MECHANISM

groundbreaking discovery, it was suggested that τ and θ are not different particles but a single particle now known as a K^+ (kaon).

The Wu experiment was carried out at the “National Bureau of Standards’ low-temperature laboratory,” now known as the “National Institute of Standards and Technology (NIST).” The idea was to observe if nuclear beta decay, which happens via weak interaction, were to violate or conserve parity symmetry. The experiment was carried out on ^{60}Co nuclei at extremely low temperature (≈ 0.003 K) inside a magnetic solenoid. Low temperature was required to avoid thermal agitation; at higher temperatures, the ^{60}Co nuclei lose polarization due to thermal effects. The ^{60}Co nuclei were polarized using a magnetic field \mathbf{H} produced by the solenoid. The spin of ^{60}Co nuclei orient in the same direction as \mathbf{H} , and the ^{60}Co nuclei undergo β decay via the weak interaction as



The emitted β particles were counted in the direction parallel and antiparallel to \mathbf{H} . It was discovered that the β particles were emitted predominantly in the direction opposite to the direction of \mathbf{H} , as shown in Fig. 2.4, suggesting parity-violation in the weak interactions. Many other experiments followed and confirmed that parity is violated maximally in the weak interaction.

2.3 Electroweak Theory and Higgs Mechanism

At very high energies, ~ 100 GeV and above, the weak and electromagnetic forces become completely equivalent. The pure electroweak force would be mediated by four massless spin-1 particles (vector bosons): two charged (W^+ and W^-) and two uncharged (W^0 and B^0). The four particles would be massless, and the electromag-

2.3. ELECTROWEAK THEORY AND HIGGS MECHANISM

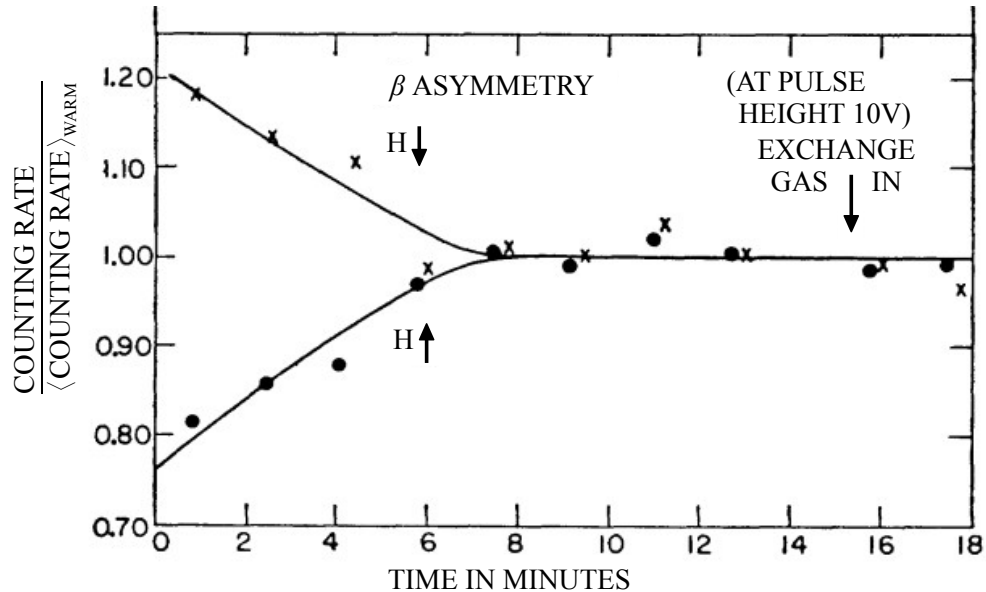


Figure 2.4: The first experimental proof of parity-violation. The Beta asymmetry for polarizing field pointing up and pointing down [13]. The β emission is preferentially in a direction opposite to the applied magnetic field \mathbf{H} . After about 8 minutes the β asymmetry goes away because the ^{60}Co nuclei lose polarization due to thermal agitation.

netic and weak forces would unify to a single electroweak force (and hence share the same coupling strength) at those higher energies. At low energies, the symmetry between the weak and electromagnetic forces gets broken spontaneously, and the two charged particles lose their massless character and become the massive charged weak bosons (W^\pm). In the process of spontaneous symmetry breaking³, the two uncharged vector bosons (W^0 and B^0) mix through the “weak mixing angle, θ_W (also called the Weinberg angle),” to produce γ and Z^0 bosons as given by

$$\begin{pmatrix} \gamma \\ Z^0 \end{pmatrix} = \begin{pmatrix} \cos \theta_W & \sin \theta_W \\ -\sin \theta_W & \cos \theta_W \end{pmatrix} \begin{pmatrix} B^0 \\ W^0 \end{pmatrix}. \quad (2.6)$$

³In electroweak theory, the spontaneous symmetry breaking can be understood as a manifestation of non-zero vacuum expectation value of the Higgs field [14]. The weak force interacts with the Higgs field, and hence the mediating particles acquire mass, whereas the electromagnetic force does not interact with the Higgs field leaving the photon massless [15].

2.4. ELECTROMAGNETIC SCATTERING AND FORM FACTOR

During the mixing, the weak Z^0 boson acquires mass while the γ boson remains massless and is the ordinary photon of electromagnetism.

The mechanism by which the three weak bosons acquire mass, through spontaneous electroweak symmetry breaking, is the Higgs mechanism. The mechanism was proposed in a series of papers [16, 17, 18] in the 1960s, by different groups of physicists, and was experimentally verified with the discovery of the Higgs boson at the LHC (Large Hadron Collider) at CERN (The European Organization for Nuclear Research) in 2012 [19].

The electroweak unification is possible at energies near ~ 100 GeV, where the electromagnetic and weak forces can be explained by a single “Electroweak Theory.” At even higher energies the electroweak force combines with the strong force, and at much higher energies all four forces get unified and can be explained by a single coupling constant. Figure 2.5 shows how the coupling strengths for the four fundamental forces “run” or change as a function of energy. It also shows an approximate location for “Electroweak Unification,” “Grand Unification (where the electroweak and strong forces become equivalent),” and “Theory of Everything (where gravity combines with the other three forces).”

2.4 Electromagnetic Scattering and Form Factor

A schematic of a typical electromagnetic scattering process is shown in Fig. 2.6, which depicts an incident electron with momentum, \vec{p}_i , scattering off a target nucleus at rest in the lab. During the process of scattering, the electron transfers part of its momentum to the target, so its final momentum (\vec{p}_f) is different than \vec{p}_i . The momentum transfer during the interaction is given by $\vec{q} = \vec{p}_i - \vec{p}_f$.

The differential scattering cross-section is directly related to the scattering ampli-

2.4. ELECTROMAGNETIC SCATTERING AND FORM FACTOR

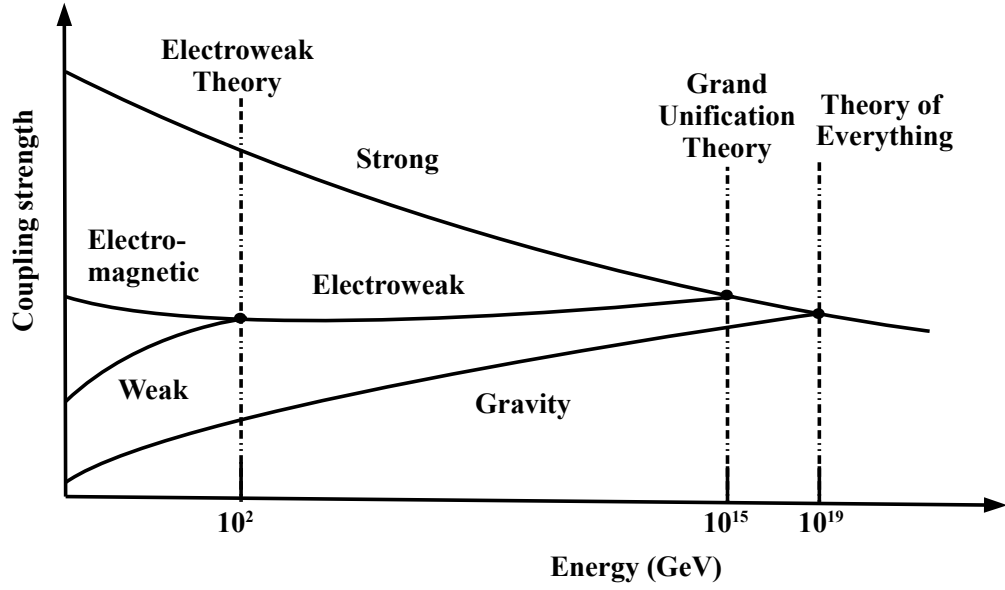


Figure 2.5: Running coupling strengths of the four fundamental forces as functions of energy (reproduced from [20], not to scale). The approximate energy scale of force unifications are given.

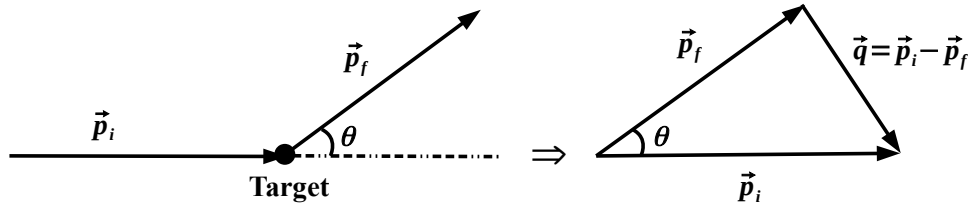


Figure 2.6: Schematic of a typical electromagnetic scattering process.

tude:

$$\frac{d\sigma}{d\Omega} \propto |\mathcal{M}_{fi}|^2. \quad (2.7)$$

If $\Phi_i(\vec{r})$ and $\Phi_f(\vec{r})$ are the wave functions for the incoming and outgoing electrons, respectively, then \mathcal{M}_{fi} can be expressed in terms of the matrix element

$$\mathcal{M}_{fi} = \langle \Phi_f | V(\vec{r}) | \Phi_i \rangle, \quad (2.8)$$

where $V(\vec{r})$ is the potential of the target associated with a particular interaction. In

2.4. ELECTROMAGNETIC SCATTERING AND FORM FACTOR

the first order Born approximation, the incoming and outgoing waves can be approximated by plane waves, $\Phi_i(\vec{r}) = e^{i\frac{\vec{p}_i \cdot \vec{r}}{\hbar}}$ and $\Phi_f(\vec{r}) = e^{i\frac{\vec{p}_f \cdot \vec{r}}{\hbar}}$, respectively. Therefore

$$\mathcal{M}_{fi} = \int e^{i\frac{\vec{q} \cdot \vec{r}}{\hbar}} V(\vec{r}) d^3\vec{r}. \quad (2.9)$$

If the target is an atomic nucleus with electromagnetic charge distribution $Ze\rho(\vec{r})$, such that $\int \rho(\vec{r}) d^3\vec{r} = 1$, then the potential experienced by an electron located at position \vec{r} is given by

$$V(\vec{r}) = \frac{-Ze^2}{4\pi\epsilon_0} \int \frac{\rho(\vec{r}')}{|\vec{r} - \vec{r}'|} d^3\vec{r}'. \quad (2.10)$$

Substituting this into Eq. 2.9, we obtain

$$\mathcal{M}_{fi} = \frac{-Ze^2}{4\pi\epsilon_0} \int e^{i\frac{\vec{q} \cdot \vec{r}}{\hbar}} \int \frac{\rho(\vec{r}')}{|\vec{r} - \vec{r}'|} d^3\vec{r}' d^3\vec{r}. \quad (2.11)$$

With $\vec{R} = \vec{r} - \vec{r}'$, the above equation becomes

$$\mathcal{M}_{fi} = \frac{-Ze^2}{4\pi\epsilon_0} \int \frac{e^{i\frac{\vec{q} \cdot \vec{R}}{\hbar}}}{|\vec{R}|} d^3\vec{R} \left[\int e^{i\frac{\vec{q} \cdot \vec{r}'}{\hbar}} \rho(\vec{r}') d^3\vec{r}' \right]. \quad (2.12)$$

The quantity within the brackets is the Fourier transform of the charge distribution and is referred to as a form factor:

$$F(q) = \int e^{i\frac{\vec{q} \cdot \vec{r}'}{\hbar}} \rho(\vec{r}') d^3\vec{r}'. \quad (2.13)$$

For spin-zero target nuclei, such as ^{208}Pb and ^{48}Ca , the form factor $F(q)$ is purely electric. At extremely small momentum transfer, $F(q) \approx 1$ and Eq. 2.12 reduces to the famous Mott scattering amplitude. Therefore, for a finite sized target nucleus, Eq. 2.7 can be written as

$$\frac{d\sigma}{d\Omega} = \left(\frac{d\sigma}{d\Omega} \right)_{Mott} |F(q)|^2. \quad (2.14)$$

2.5 Weak Neutral Current

The weak neutral interaction is a flavor conserving process, which takes place through the exchange of a Z^0 vector boson. The vertex factor⁴ for a weak neutral interaction is of the form $\mathcal{V} = \frac{-ig_Z}{2}\gamma^\mu(c_V^f - c_A^f\gamma^5)$, where $g_Z = \frac{g_{em}}{\sin\theta_W \cos\theta_W}$ ($g_{em} = \sqrt{4\pi\alpha_{em}}$ is the electromagnetic coupling constant and θ_W is the weak mixing angle as defined in Sec. 2.3) is the weak neutral coupling constant, γ^μ ($\mu = 0, 1, 2, 3$) are the Dirac matrices, $\gamma^5 = i\gamma^0\gamma^1\gamma^2\gamma^3$, and c_V^f and c_A^f are the weak neutral current vector and axial-vector couplings that depend on the type of quark or lepton (f) involved [21]. Table 2.2 gives the values of c_V and c_A for the electron and light quarks in the Glashow-Weinberg-Salam (GWS) model.

f	c_V	c_A
e^-	$-\frac{1}{2} + 2\sin^2\theta_W$	$-\frac{1}{2}$
u	$\frac{1}{2} - \frac{4}{3}\sin^2\theta_W$	$\frac{1}{2}$
d, s	$-\frac{1}{2} + \frac{2}{3}\sin^2\theta_W$	$-\frac{1}{2}$

Table 2.2: Neutral vector and axial vector couplings for the electron and light quarks.

The weak neutral current for a given electron (e) is given by

$$J^\mu(e) = \bar{u}(e)\mathcal{V}u(e) = \bar{u}(e) \left[\frac{-ig_Z}{2}\gamma^\mu(c_V^f - c_A^f\gamma^5) \right] u(e), \quad (2.15)$$

where $u(e)$ and $\bar{u}(e)$ are the electron initial and final spinors, respectively. The term containing γ^μ is odd under parity, while the term containing $\gamma^\mu\gamma^5$ is even. Therefore,

⁴Vertex factor is one of two building blocks of the interaction amplitude (matrix element) in the Feynman diagrams. The other one is the propagator, which in general is of order $\frac{g_x^2}{q^2 - M_x^2}$, as given in Eq. 2.1.

2.6. ELECTRON SCATTERING FROM A WEAK POTENTIAL

it is the sum of these two terms (with opposite parity) that leads to the “so-called” maximal violation of parity in weak interactions.

2.6 Electron Scattering From a Weak Potential

As we discussed in Sec. 2.5, the weak interaction occurs via $V - A$ (vector and axial-vector) coupling. When an electron scatters from a spinless nucleus, the potential involved in the interaction is of the form [22]

$$\hat{V}(r) = V(r) + \gamma^5 A(r), \quad (2.16)$$

where $V(r)$ is the vector potential responsible for Coulomb interaction and $A(r)$ is the axial-vector potential coming from the weak neutral current. $A(r)$ can be expressed as a function of the weak charge density $\rho_W(r)$ by

$$A(r) = \frac{G_F}{2^{\frac{3}{2}}} \rho_W(r), \quad (2.17)$$

where G_F is the Fermi constant. For a general target nucleus, with neutron number N and proton number Z , the weak charge density is given by

$$\int d^3r \rho_W(r) = -N + (1 - 4 \sin^2 \theta_W) Z. \quad (2.18)$$

Since, $\sin^2 \theta_W = 0.23$, the term containing N dominates. Therefore, $\rho_W(r)$ approximates the neutron density $\rho_n(r)$ normalized to neutron number N .

One can express the electron wave function ψ for right-handed (+) and left-handed (-) electrons as

2.7. PARITY-VIOLATING ASYMMETRY (A_{PV})

$$\psi_{\pm} = \frac{1}{2}(1 \pm \gamma^5)\psi, \quad (2.19)$$

and the corresponding potentials as

$$V_{\pm}(r) = V(r) \pm A(r). \quad (2.20)$$

From this, we see that right-handed electrons scatter from a potential $V(r) + A(r)$, while left-handed electrons scatter from a potential $V(r) - A(r)$ [22]. Therefore, the parity-violating asymmetry arises from the scattering of opposite helicity states, of longitudinally polarized electrons, from the two different potentials.

2.7 Parity-Violating Asymmetry (A_{PV})

When a polarized beam of electrons is scattered from an unpolarized nuclear target, such as ^{208}Pb or ^{48}Ca , both electromagnetic and weak interactions are observed. The electromagnetic interaction, between the electric charge of the electrons (of the beam) and the protons (of the target nucleus), is mediated through the exchange of the γ -boson. The weak interaction, between the weak charge of the beam electrons and that of the target nucleus, is mediated through the Z^0 -boson exchange. The normalized difference or asymmetry between the scattering cross sections for incident electrons with left- and right-handed helicity states gives rise to the parity-violating asymmetry, A_{PV} , which can be written as

$$A_{PV} = \frac{\sigma_R - \sigma_L}{\sigma_R + \sigma_L}, \quad (2.21)$$

where $\sigma_{L(R)}$ is the differential scattering cross-section for left(right)-handed incident electrons, and is given by

2.7. PARITY-VIOLATING ASYMMETRY (A_{PV})

$$\sigma_{L(R)} = \frac{d\sigma_{L(R)}}{d\Omega} \propto (\mathcal{M}_\gamma + \mathcal{M}_Z^{L(R)})^2, \quad (2.22)$$

where \mathcal{M}_γ and $\mathcal{M}_Z^{L(R)}$ (note that $\mathcal{M}_Z^L = -\mathcal{M}_Z^R = -\mathcal{M}_Z$) are the electromagnetic and weak amplitudes, respectively. In practice, A_{PV} arises from the quantum interference between the electromagnetic and weak interaction amplitudes. Substituting Eq. 2.22 in Eq. 2.21, one gets

$$A_{PV} \approx \frac{(\mathcal{M}_\gamma + \mathcal{M}_Z)^2 - (\mathcal{M}_\gamma - \mathcal{M}_Z)^2}{(\mathcal{M}_\gamma + \mathcal{M}_Z)^2 + (\mathcal{M}_\gamma - \mathcal{M}_Z)^2}, \quad (2.23)$$

Note that $\mathcal{M}_Z \ll \mathcal{M}_\gamma$. So Eq. 2.23 reduces to

$$A_{PV} \approx \frac{2\mathcal{M}_\gamma\mathcal{M}_Z}{\mathcal{M}_\gamma^2}. \quad (2.24)$$

In the limit $Q^2 \ll M_Z^2$, $\mathcal{M}_Z \sim [1/M_Z]^2$, where $M_Z \approx 91$ GeV while $\mathcal{M}_\gamma \sim 1/Q^2$, so the Born approximation can be used to write:

$$A_{PV} = \frac{G_F Q^2}{4\pi\alpha\sqrt{2}} \left[1 - 4\sin^2\theta_W - \frac{F_n(Q^2)}{F_p(Q^2)} \right], \quad (2.25)$$

where $G_F = 1.166 \times 10^{-5}$ (GeV) $^{-2}$ is the Fermi coupling constant, α is the fine structure constant (equal to 1/137), θ_W is the weak mixing angle, Q^2 represents the square of the four-momentum transferred to the target nucleus, and $F_{n(p)}(Q^2)$ represents the nuclear form factors for the neutron(proton). The form factors act as a convenient bridge between theoretical analysis and experimental observations in particle physics. By definition, the form factor is the Fourier transform of the associated density distribution, $\rho_{n(p)}$, and is given by [23]

2.8. IMPORTANCE OF Q^2

$$F_{n(p)}(Q^2) = \frac{1}{4\pi} \int j_0(qr) \rho_{n(p)}(r) d^3r, \quad (2.26)$$

where $j_0(qr) = \sin(qr)/(qr)$ is the zeroth-order spherical Bessel function, q is the spatial momentum. The Born approximation is approximately valid for lighter nuclei, however, Coulomb distortion effects (which are of order $Z\alpha/\pi$ [23], where Z is the nuclear electromagnetic charge number) significantly modify the A_{PV} [22], and thus corrections are needed for heavy nuclei like ^{208}Pb . For example, for PREX, Coulomb distortions decrease A_{PV} by $\approx 20\%$. The mean square radius of the neutron(proton) distribution is related to the form factor by

$$\langle R_{n(p)}^2 \rangle \propto \left. \frac{dF_{n(p)}(Q^2)}{dQ^2} \right|_{Q^2=0}. \quad (2.27)$$

From electroweak theory, it is understood that the magnitude of the weak charge of a neutron (Q_W^n) is much greater than that of a proton (Q_W^p). As per the Standard Model (SM), $Q_W^p \propto 1 - 4\sin^2\theta_W \approx 0.07$, while $Q_W^n \approx -1$. This indicates that the Z^0 -boson interaction couples primarily to neutrons [24]. This makes PVeS a natural tool to probe neutron distributions in complex nuclei.

2.8 Importance of Q^2

As the electron beam scatters from the target, part of its momentum transfers to the target nucleus. The average 4-momentum transfer squared, $\langle Q^2 \rangle$, is an important calibration in our analysis and must be carefully measured during the experiment. A key point of the measurement concept is that R_n can be determined from a measurement of $F_n(Q^2)$ at effectively a single Q^2 point. This is made possible by a very high correlation between R_n and F_n (or F_W) at sufficiently low Q^2 . Knowledge of this cor-

2.8. IMPORTANCE OF Q^2

relation, as well as how one translates a measurement of $F_W(Q^2)$ to R_n , comes from the covariant analysis framework for energy density functionals. These correlation coefficients and F_W calculations for PREX-2 and CREX are shown in Fig. 2.7 using an example relativistic mean field model called FSUGold [2].

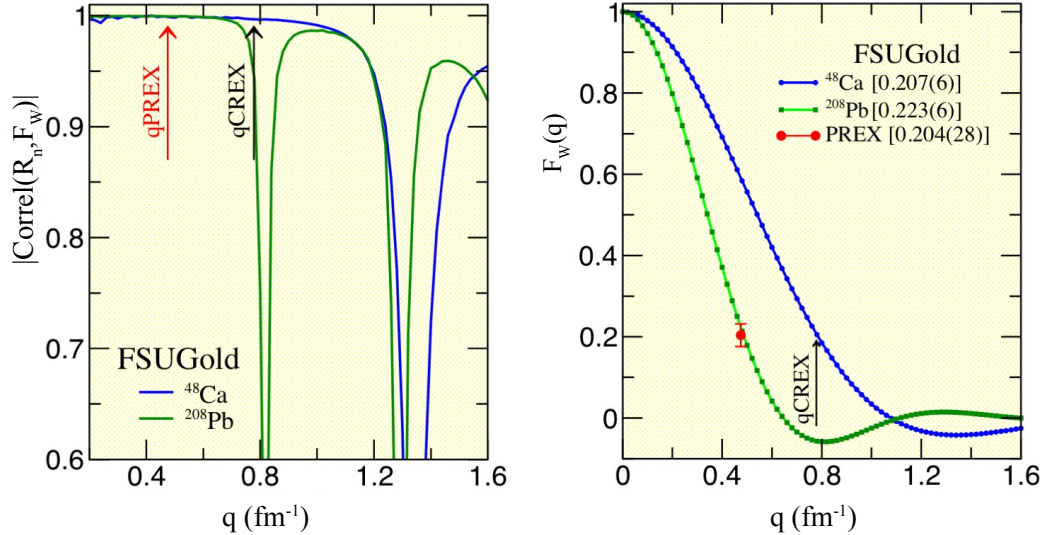


Figure 2.7: Left-hand side plot shows the correlation coefficient between R_n and F_W . Right-hand side plot shows $F_W(q)$ for ^{48}Ca and ^{208}Pb . Shown on each plot are the q (four-momentum transfer) values for PREX-2 and CREX. Note that, as long as q is small and far from a diffractive minimum, the correlation is near 100 %.

During the experiments, a spread or distribution of Q^2 values is accepted by the spectrometer, and it is the uncertainty in this distribution that leads to the “Effective Q^2 ” systematic error contribution. To determine the Q^2 distribution during PREX-2, we also use a Gas Electron Multiplier (GEM) tracking chamber system along with the Hall A standard Vertical Drift Chamber (VDC) system. As the ISU parity group is responsible for the GEM system, a detailed explanation of its design, including the working principle of GEMs, is given in Sec. 3.6.3. The value of Q^2 can be estimated by

$$Q^2 = -(q_i - q_f)^2 = 2EE'(1 - \cos \Theta), \quad (2.28)$$

2.9. HISTORY OF PVES EXPERIMENTS

where $q_i(q_f)$ and $E(E')$ are, respectively, the momentum and energy of the incident(scattered) electron beam, and Θ is the scattering angle. The quantities E' and Θ can be evaluated using the following equation:

$$E' = \frac{E}{1 + \frac{E}{M_t}(1 - \cos \Theta)}, \quad (2.29)$$

where M_t is the mass of the target, and

$$\Theta = \arccos \left(\frac{\cos \Theta_0 - \phi_{tg} \sin \Theta_0}{\sqrt{1 + \theta_{tg}^2 + \phi_{tg}^2}} \right), \quad (2.30)$$

where Θ_0 is the central scattering angle (i.e. the spectrometer’s central polar angle acceptance) in the xz-plane of the “Hall A” coordinate system. θ_{tg} and ϕ_{tg} are the angles subtended by the reconstructed trajectories of the electrons to the z-axis along the xz- and yz-planes of the “transport” coordinate system [25] (see Fig. 4.6). The uncertainty in the measurement of Q^2 is related to the uncertainties in the measurement of these angles and energies. Indeed, the main source of error in Q^2 comes from the uncertainty in the “pointing” measurement of the spectrometer’s central scattering angle [26], which is accomplished in Hall A using the standard waterfall target approach (see Sec. 4.6.2 for details).

2.9 History of PVeS Experiments

The experimental technique for parity-violating electron scattering was pioneered by the E122 experiment at SLAC in the late 1970s. E122 utilized a new polarization source and new spectrometer design to observe the weak neutral current predicted by the Winberg-Salam model. The measurement technique, and relatively small size of the predicted asymmetry, imposed the need for stringent control over systematic

2.9. HISTORY OF PVE S EXPERIMENTS

corrections related to the beam quality. For example, a feedback system was employed that could help stabilize the beam's position, angle, and energy on the target [27]. An experimental blueprint for the E122 experiment is shown in Fig. 2.8. The same essential technique is still in use for all PVE S experiments.

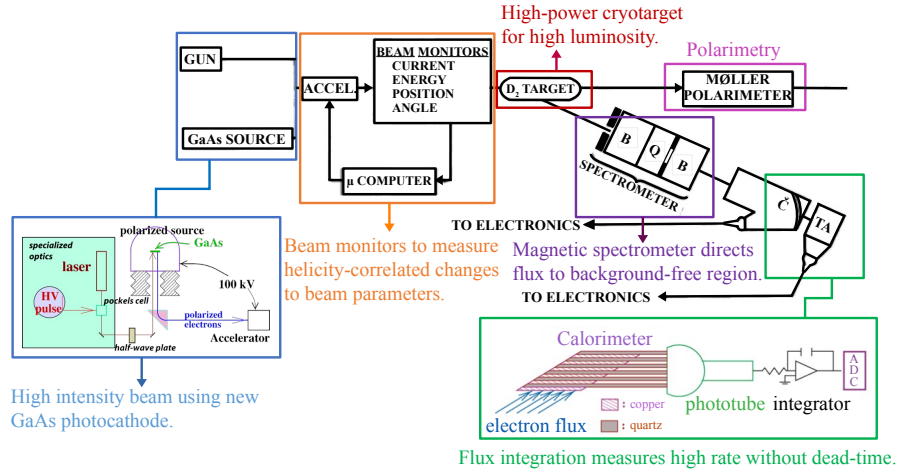


Figure 2.8: Experimental blueprint of the E122 experiment at SLAC (reproduced from [28]). The same technique of polarized electron beam source feedback system is still in use in modern PVE S experiments.

Several other experiments followed E122 and measured A_{PV} with better precision over time. E158 measured A_{PV} for the first time in Møller scattering in 2002-2003 at SLAC. A series of PVE S experiments have run at JLab since the mid-90s. The high-quality CEBAF beam makes PVE S measurements especially possible at JLab. Past PVE S experiments completed at JLab, along with their observations, are listed in Table 2.3.

2.10. MOTIVATIONS

Experiment	Measurement
HALL A:	
HAPPEX(-I, -II, -He, -III)	measured “strange” quark contributions to electromagnetic structure of proton and neutron
PVDIS	measured “weak” quark coupling parameters (c_1 's and c_2 's)
PREX-1	application of parity-violation to measure Neutron Radius of ^{208}Pb
HALL C:	
G0	determined contribution of strange quarks to charge and magnetization distributions of the nucleon and many more
Q_{weak}	measured weak charge of proton through PVeS at very low Q^2

Table 2.3: Past PVeS experiments at JLab, not including PREX-2 and CREX.

2.10 Motivations

2.10.1 Choice of Targets

Why PREX and CREX? Both calcium (^{48}Ca) and lead (^{208}Pb) are the only readily available, stable, spin-less, doubly magic, and neutron-rich nuclei. ^{208}Pb is an abundant isotope of Pb that can be found naturally enriched up to 90 % in thorium ores [29], and it has 44 excess neutrons. Here, what we mean by doubly magic is that both neutron and proton form closed shell structures. Since the energy gap between the last filled shell and the excited states is higher than their neighbours these nuclei are comparatively stable. A schematic of the single-particle spherical shell model is shown in Fig. 2.9. Because it is doubly magic, the first excited state of ^{208}Pb has relatively high excitation energy (2.615 MeV) compared to a typical heavy nucleus, and it has been thought to have a relatively large value of R_n ; the first excited state of ^{48}Ca is 3.831 MeV and is expected to have a smaller R_n than ^{208}Pb . These relatively large first excited state energies allow the experimental apparatus to geometrically accept nearly all elastic scattered events and reject almost all inelastic events. This

2.10. MOTIVATIONS

is important because A_{PV} from inelastic scattering is essentially unknown.

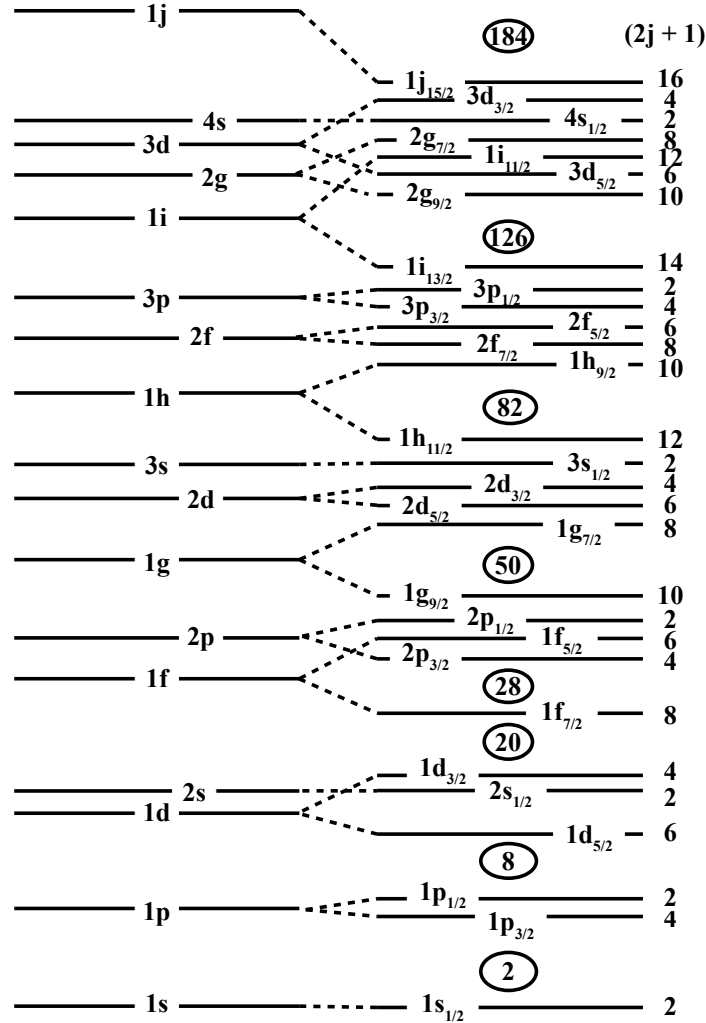


Figure 2.9: An example energy level diagram of single-particle nuclear spherical shell model. The magic numbers are shown within the ovals.

2.10.2 PVeS versus Other Approaches

Over the last few decades, PVeS has become a precision tool for scrutinizing neutron densities of neutron-rich nuclei. In contrast to the non-perturbative, model-dependent hadron scattering experiments involving, for example, protons [30, 31], anti-protons [32], or pions [33], PVeS can probe the weak charge form factors or weak charge

2.10. MOTIVATIONS

distributions in a model-independent⁵ way with overall uncertainty dominated by statistics. PVeS is free from large uncertainties related to the *strong* interaction, and is thus a relatively clean way to study neutron distributions within nuclei.

2.10.3 Choice of Kinematics

The choice of kinematics is important when considering the desired precision in the neutron skin measurement with minimum running time. It is chosen such that the product $R \times A^2 \times \epsilon^2$ is optimum (this product is called the Figure Of Merit, FOM). Here, R is the detected scattering rate, A is the measured A_{PV} , and $\epsilon = \frac{dA}{A} = \frac{A_1 - A}{A}$, where A is the asymmetry calculated from a Mean Field Theory and A_1 is the asymmetry from the Mean Field Theory calculation such that the neutron radius is increased by 1 %.

2.10.4 Neutron Skin (R_{skin}) Calculation

Assuming the weak charge density of ^{208}Pb , $\rho_W(r)$, in a Wood-Saxon form, [34]

$$\rho_W(r) = \frac{\rho_W^0}{e^{\frac{r-c}{a}} + 1}, \quad (2.31)$$

where ρ_W^0 , c , and a are the normalization factor, radius parameter and surface thickness, respectively. The surface thickness is optimized using various density functional models. The RMS weak radius, R_W , of a nucleus is related to Eq. 2.31 by

$$R_W^2 = \frac{1}{Q_W} \int r^2 \rho_W(r) d^3r, \quad (2.32)$$

⁵We use various relativistic and non-relativistic density functional models to extract the neutron distribution from the measured A_{PV} . These models are extremely precise and pose negligibly small model error (see Sec. 4.11).

2.10. MOTIVATIONS

where Q_W is the weak charge of the nucleus.

The relationship between the point proton radius, R_p , and the measured charge radius, R_{ch} , is given by (see [34] and the reference therein)

$$R_{ch}^2 = R_p^2 + \langle r_p^2 \rangle + \frac{N}{Z} \langle r_n^2 \rangle + \frac{3}{4M^2} + \langle r^2 \rangle_{so}, \quad (2.33)$$

where $\langle r_p^2 \rangle = 0.769 \text{ fm}^2$ is the mean-square charge radius of a single proton, $\langle r_n^2 \rangle = -0.116 \text{ fm}^2$ is the mean-square charge radius of a single neutron, $\langle r^2 \rangle_{so} = -0.028 \text{ fm}^2$ is the contribution of spin-orbit currents to R_{ch} , and M is the nucleon mass. Using these values and the understanding that the value of $\frac{3}{4M^2}$ is small, Eq. 2.33 becomes [34]

$$R_{ch}^2 = R_p^2 + 0.5956 \text{ fm}^2. \quad (2.34)$$

The point neutron RMS radius, R_n , is related to the weak radius, R_W , as [34]

$$R_n^2 = \frac{Q_W}{q_n N} R_W^2 - \frac{q_p Z}{q_n N} R_{ch}^2 - \langle r_p^2 \rangle - \frac{Z}{N} \langle r_n^2 \rangle + \frac{Z + N}{q_n N} \langle r_s^2 \rangle, \quad (2.35)$$

where $q_n = -0.9878$ is the radiatively corrected weak charge of the neutron, $q_p = 0.0721$ is the radiatively corrected weak charge of the proton, and $\langle r_s^2 \rangle$ is the square of the nucleon strangeness radius. The weak charge of ^{208}Pb is

$$Q_W = \int d^3r \rho_W(r) = Nq_n + Zq_p = -118.55. \quad (2.36)$$

Using these values in Eq. 2.35, [34] shows that R_n can be obtained from R_W with a small correction from $\langle r_s^2 \rangle$ as

2.10. MOTIVATIONS

$$R_n^2 = 0.9525R_W^2 - 1.671\langle r_s^2 \rangle + 0.7450 \text{ fm}^2, \quad (2.37)$$

where $\langle r_s^2 \rangle = 0.02 \pm 0.04 \approx \pm 0.04 \text{ fm}^2$ [34]. Using the experimentally measured $R_{ch} = 5.503 \text{ fm}$ and Eq. 2.32 in Equations 2.34 and 2.37, one can calculate the neutron skin, $R_{skin} = R_n - R_p$ in ^{208}Pb .

2.10.5 Importance of PREX-2/CREX measurements

- As a relatively smaller nucleus, the ^{48}Ca result is more influenced by surface effects, and thus the PREX-2 and CREX results together can give complementary information [35, 36] while individually providing unique data sets on high and medium Z -targets, respectively. Both experiments use the same technique and apparatus to measure the neutron skin, which further emphasizes the fact that a consistent measurement between the two experiments would further reinforce their results.
- Using the equations in Sec. 2.10.4, PREX-1 reported the neutron skin in ^{208}Pb [34] as

$$R_{skin} = R_n - R_p = 0.30 \pm 0.18 \text{ fm} \quad (2.38)$$

with 3 % uncertainty on R_n . On the other hand, $R_{skin} = 0.15 \pm 0.03_{-0.03}^{+0.01} \text{ fm}$ (the first error is statistical, and the second is systematic) was reported from an analysis of the coherent π^0 photoproduction from ^{208}Pb at Mainz, Germany [4], and is in close agreement with various independent measurements, including: electron dipole polarizability α_D [9], giant quadrupole resonances [37], proton elastic scattering [38], and an x-ray cascade of antiprotonic atoms [39]. The theoretically “clean” PREX-2 endeavor provides a definitive measurement to

2.10. MOTIVATIONS

be used for calibration of the facility for radioactive isotope beams (FRIB), heavy-ion collisions, atomic parity-violation experiments, as well as probing the formation and structure of neutron stars. It turns out that the size of a neutron star is directly related to the neutron skin thickness of a heavy nucleus [5].

- R_{skin} for medium-sized nuclei, such as ^{48}Ca , are now predicted from *ab initio* calculations, while we only have the results from nuclear Density Functional Theory (DFT) for heavy nuclei like ^{208}Pb . Studying the neutron skins for ^{208}Pb and ^{48}Ca using PVeS will provide an important bridge between medium- and heavy-sized nuclei. The *ab initio* calculations for ^{48}Ca , by G. Hagen et al. [10], suggest that its R_{skin} is significantly smaller than the DFT estimation. According to [10], the *ab initio* calculation of ^{48}Ca is $0.12 \text{ fm} < R_{skin} < 0.15 \text{ fm}$, while the reported DFT prediction [35] is $R_{skin} = 0.176 \pm 0.018 \text{ fm}$. However, different DFT models are not in close agreement with each other. The PREX-2/CREX results will provide an important crosscheck of the predictions from various models and calculations.
- The three-nucleon (3N) force is, in the first approximation, the dominant explanation for measurement deviations from theory predictions which only incorporate two-nucleon (2N) forces. The role of the 3N force is important for probing nuclear structure [40, 41, 42]. Indeed, the equation of state suggests that 3N forces increase the pressure, or energy per nucleon, as a function of the density. For a medium-sized nucleus, such as ^{48}Ca , there exist microscopic model calculations; these include coupled cluster [43], or the no-core shell model [44], which incorporate 3N forces. In contrast, there are no microscopic models for ^{208}Pb . A better understanding of the role of 3N forces in nuclear structure is an important motivation for CREX. Its measurement result will scrutinize predictions of neutron densities from microscopic models which incorporate 3N

2.10. MOTIVATIONS

forces [45].

Chapter 3

Experimental Setups

3.1 Jefferson Lab

PREX-2 and CREX each make precision, statistics-limited measurements of a parity-violating asymmetry of order 10^{-6} or 1 part per million (ppm). This is not easy to achieve without stringent control over all possible sources of systematic error and, most importantly, without the “parity-quality” beam of the CEBAF at Jefferson Lab. The “Thomas Jefferson National Accelerator Facility (TJNAF),” now commonly known as “Jefferson Laboratory (JLab),” with the “Continuous Electron Beam Accelerator Facility (CEBAF),” has established itself as one of the premier polarized electron beam facilities in the world for parity-violation experiments. A sketch of the lab is shown in Fig. 3.1.

The experimental site can be grouped into three major components: injector, accelerator, and four experimental halls. It also consists of two separate cryogenic plants in the Central Helium Liquefier (CHL) building. We conduct PREX-2/CREX in Hall A. PREX-2 runs from June to September 2019, while CREX runs from December 2019 to September 2020. CREX takes longer than expected because it is

3.1. JEFFERSON LAB

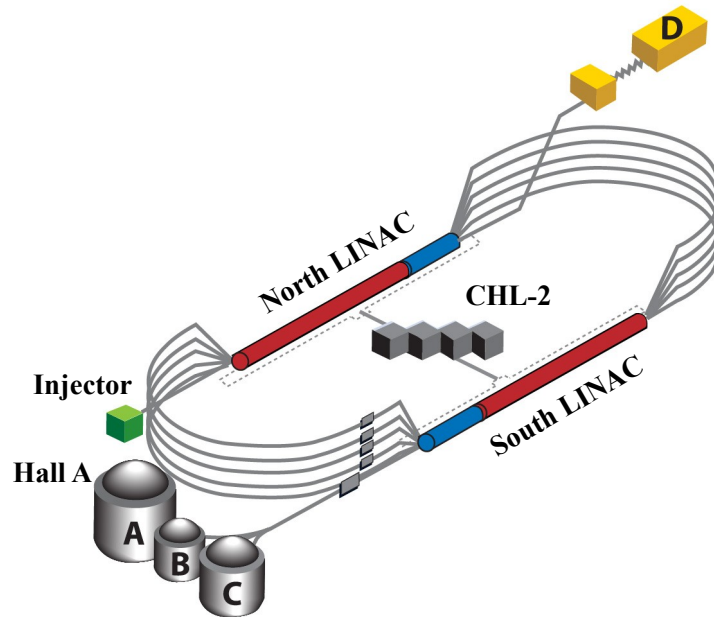


Figure 3.1: Sketch of JLab accelerator site and four experimental halls: A, B, C, and D (reproduced from [46]). The injector serves as the polarized electron beam source. The North and South LINACs provide the necessary acceleration to the electron beam, providing it with the desired energy. Each LINAC consists of twenty original (from 6 GeV era) cryo-cooled, superconducting radio-frequency (SRF) modules, as shown in the red-colored regions, and five more modules added after the 12 GeV upgrade shown in blue.

interrupted for four months (from March to July of 2020) due to the worldwide pandemic (COVID-19). In this chapter, we will discuss the various pieces of equipment and setups used during the experiments.

Following the 12 GeV upgrade, which effectively took place from $\sim 2012 - 2015$, the CEBAF is capable of delivering up to 12 GeV electrons as needed by experiments in the four different halls¹. The upgrade not only expanded the lab's energy range but also added a new hall (Hall D). It also added five more cryo-cooled, superconducting radio-frequency (SRF) modules in addition to the existing twenty cryo-modules in each LINAC (linear accelerator), and one new arc² to pass 12 GeV electrons through

¹By design, Hall D is the only hall which can receive the maximum 12 GeV beam energy. The beam delivered to the other experimental halls can only have as high as 11 GeV energy.

²The new arc allows the electrons to gain further acceleration (one more pass) through the North

3.2. INJECTOR

the North LINAC to Hall D.

3.2 Injector

The injector is the source or beginning of the polarized electron beam at JLab. It is mainly comprised of a laser, attenuator, insertable half-wave plate (IHWP), RTP Pockels cell, rotatable half-wave plate (RHWP), and photocathode. These components are collectively capable of delivering the parity quality beam (PQB) required by PREX-2/CREX. The major components of the injector along with their operational sequence are shown in Fig. 3.2.

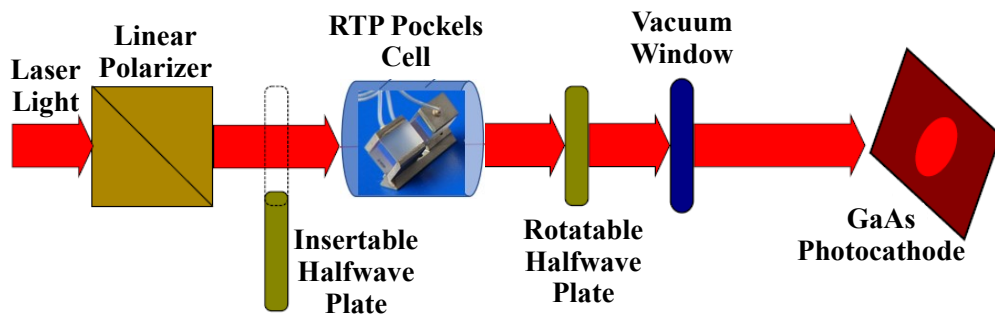


Figure 3.2: Simple cartoon of the JLab injector setup (reproduced from [47]).

The light originating from the laser source is first linearly polarized before going through the IHWP and then the RTP Pockels cell. The Rubidium Titanyl Phosphate (RTP) cell is designed especially for PREX-2/CREX and is discussed in Sec. 3.2.2. A high DC voltage is applied to the RTP cell and is controlled, in such a way, to convert the linearly polarized incident light into left(right) circularly polarized light; this conversion occurs at a tunable “flip” frequency (240 Hz for PREX-2 and 120 Hz for CREX). The left(right) circular polarization state of the light determines the left(right) handed helicity state of the electrons emitted from the Gallium Arsenide (GaAs) photocathode—further discussed in Sec. 3.2.5. A detailed schematic of the LINAC before being extracted into Hall D.

3.2. INJECTOR

JLab injector is shown in Fig. 3.3. In addition to the fast helicity reversal provided by the RTP cell, there are two other mechanisms of, so-called, slow helicity reversal: toggling the IHWP state “IN” and “OUT”, and changing the double Wien settings (this is discussed in Sec. 3.2.6). The production of a polarized electron beam is a complex, multi-stage process carried out by the collective and optimal functioning of each of the injector subsystems. In short, the Hall A source laser light (780 nm) propagates through a series of optical elements before hitting the photocathode, where a “bunch” of longitudinally polarized electrons is produced by means of optical excitation.

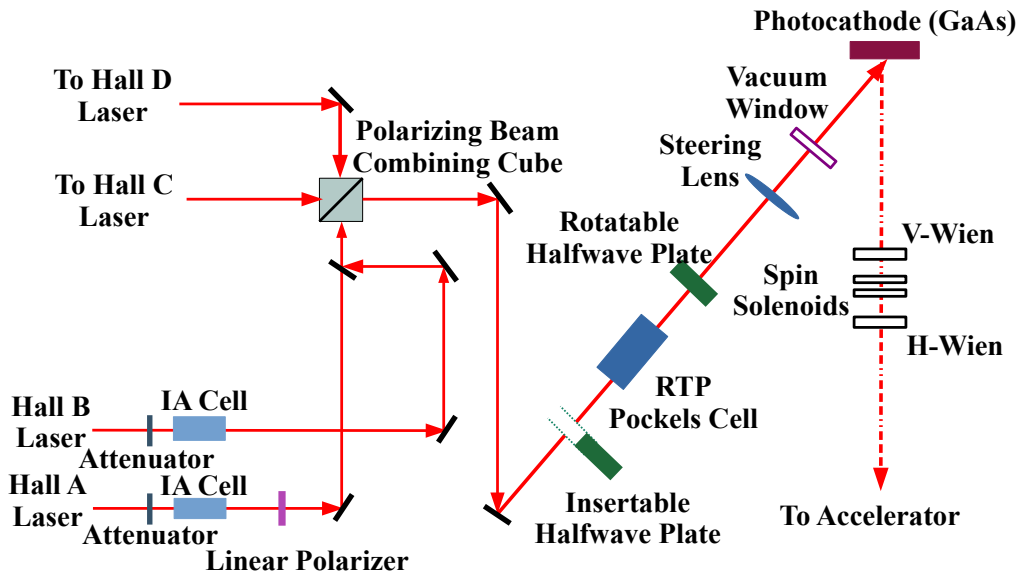


Figure 3.3: Detailed schematic of JLab polarized electron source (reproduced from [48] and [49]). The IHWP is periodically inserted in, and taken out of, the laser beam path providing helicity reversals to cancel potential helicity-correlated false asymmetries. A new RTP Pockels cell is used to convert linearly polarized laser light to left(right) circularly polarized light. The photocathode produces electron bunches in a left or right helicity state based on the left or right circular polarization state of laser light from the Pockels cell.

3.2.1 Intensity Attenuator (IA) System

Intensity attenuation is a process used to control the amount of laser light that traverses the optical elements in the injector. Ultimately, it also has overall control of

3.2. INJECTOR

the beam intensity in the hall. The IA system is shown in Fig. 3.3. Linear polarizers are used before and after the system to clean up the linear polarization.

3.2.2 RTP Pockels cell

PREX-2 and CREX use a newly designed RTP Pockels cell. It is made of two RTP (Rubidium Titanyl Phosphate) crystals and is designed by the University of Virginia (UVa) parity group. It performs two essential tasks in one: it converts the linearly polarized light into circularly polarized light, and it provides the fast helicity reversal capability.

Any change in the polarized beam characteristics at the target can introduce a helicity-correlated beam asymmetry (HCBA), which is a potential source of false asymmetry in our data. Such an asymmetry may appear in the form of an intensity asymmetry (charge asymmetry), position (and angle), and energy differences, as well as a potential spot-size asymmetry. The raw measured asymmetry, A_{raw} , is given by

$$A_{raw} = A_{det} - A_q + \sum_i \alpha_i \Delta M_i, \quad (3.1)$$

where A_{det} is the asymmetry measured by the main integrating detector, A_q is the charge asymmetry, and the last term contains the helicity-correlated position and energy differences (HCPD) contamination, where the ΔM_i are the beam position, angle, and energy differences, and α_i are the detector responses or “slopes” corresponding to those beam changes. The HCPD analysis and correction are detailed in Sections 4.2.4 and 4.2.5, respectively. Measurement of the raw asymmetry is performed from the charge normalized main detector signal. Therefore, A_q is subtracted from A_{det} in Eq. 3.1. The basic physical constructs underlying these helicity-correlated false asymmetries are depicted in Fig. 3.4.

3.2. INJECTOR

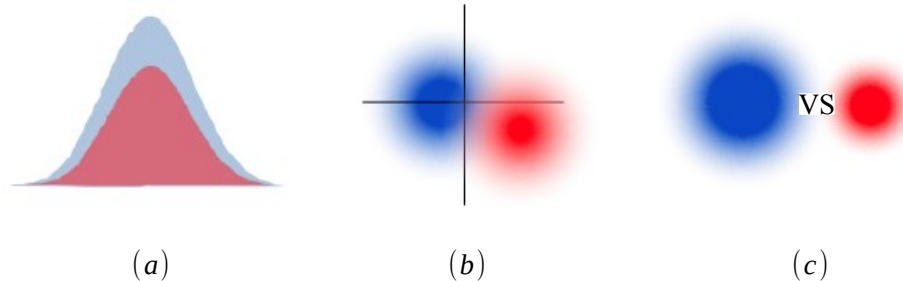


Figure 3.4: Illustration of various sources of helicity-correlated false asymmetries. (a) Intensity asymmetry from laser polarization asymmetry. (b) Position difference from polarization gradient. (c) Spot-size asymmetry. Figure taken from [50]. The two colors represent hypothetical beam monitor distributions from right vs. left handed beam helicity states. The (design) performance of the Pockels cell, and its precise alignment with the laser beam, play a critical role in minimizing these false asymmetries.

The novel design of the ultra-fast switching RTP cell is tested and found to provide rigorous control over beam intensity asymmetry, position differences, and spot-size asymmetry. Each crystal consists of two high voltage (HV) plates (so a total of four HV plates in the Pockels cell made of two RTP crystals) plus grounded side-panels; the design allows for independent control of each HV plate (using eight independent HV settings, four for each helicity state). A positive or negative HV is applied to the RTP cell, using a pseudo-random flip pattern, which in turn produces left or right circularly polarized light in the same pattern. The RTP Pockels cell is temperature sensitive and suffers from slow fluctuation in the temperature difference between its two RTP crystals; this slow fluctuation induces a drift or change in the beam intensity asymmetry. This effect can be corrected by adjusting the Parity Induced Transport Asymmetry (PITA) voltage [50] which effectively offsets the analyzing power on the photocathode due to residual linear polarization of the incident laser light, see Sec. 3.2.4.

Many of the systematic effects and noise, associated with slow drifts in properties of the experimental apparatus, can be removed (or at least brought under control) by performing the asymmetry measurements on two helicity states that are close together

3.2. INJECTOR

in time. For this reason, the helicity of the electron beam is rapidly flipped at a frequency which is an integer multiple of 60 Hz. This strategy is referred to as AC-line-sync, and it helps to remove noise associated with the AC power-line. The mechanism for generating the rapid helicity reversal and integration of the detector/monitor signals corresponding to a single helicity window is discussed in Sec. 3.10.

3.2.3 Insertable Halfwave Plate (IHWP)

The main purpose of the IHWP is to flip (or reverse) the circular polarization state of the laser light, by rotating the incident linear polarization state by 90° , just before it reaches the Pockels cell. During the experiments, the IHWP is inserted and removed on a regular basis. This occurs on a timescale of 1 shift to 1 day depending on the running efficiency. Ideally, the overall effect of this is to change the sign of the measured asymmetry without altering its size. In practice, any change in the size of a measured asymmetry, due to the change in the IHWP state, is an indication of helicity-correlated systematic contamination. By taking an equally weighted (statistically), and sign-corrected, average of the two IHWP state data sets, the helicity-correlated systematic cancels out.

3.2.4 Rotatable Halfwave Plate (RHWP)

The orientation of linearly polarized light impinging on the GaAs photocathode affects its quantum efficiency (QE). This in turn creates an analyzing power on the photocathode with respect to an axis lying in the plane of the cathode surface. While striking the photocathode, equal intensities of the residual linear polarization in the two helicity states produce asymmetric photo-currents [47]; this asymmetric response is referred to, generally, as analyzing power. A detailed mathematical explanation of the intensity asymmetry, its dependence on the analyzing power, and PITA slope cor-

3.2. INJECTOR

rections are presented in [51]. Any residual linearly polarized light exiting the Pockels cell, that is aligned with the photocathode’s analyzing power axis, can effectively lead to a helicity-correlated intensity asymmetry. To minimize this effect a RHWP is used downstream of the Pockels cell to rotate the residual linear polarization to be 45° with respect to the direction of the analyzing power axis of the photocathode [52]. The RHWP angle is adjusted such that the PITA slope is small but non-zero. The non-zero PITA slope is needed for the charge feedback³ system to work. During the experiments, PITA scans are performed periodically. During these scans, the PITA voltages are systematically changed, making larger charge asymmetries. We then measure the response (asymmetry signal) from various detectors and monitors, as a function of the PITA slope, in order to estimate the systematic contribution from possible non-linear detector/monitor responses.

3.2.5 Gallium Arsenide (GaAs) Photocathode

The circularly polarized laser light exiting the Pockels cell illuminates the surface of a strained “super-lattice” Gallium Arsenide (GaAs) photocathode. A fraction of the incident light excites electrons from the valance band to the conduction band via photo-emission. This process is shown in Fig. 3.5. Finally, the photo-ejected longitudinally polarized electrons from the cathode surface are collected, using a well-tuned accelerating potential, and then transported to the accelerator. This process effectively creates a continuous wave (CW) electron beam. The state-of-the-art design of JLab’s CEBAF can provide up to $\sim 90\%$ beam polarization. The “Left” or “Right” handedness of the electron’s helicity is determined by the polarization state of the circularly polarized light as explained in Sec. 3.2.2.

³This is an active feedback system that regularly monitors the intensity asymmetry (A_q) and automatically adjusts the Pockels cell voltage to minimize it.

3.2. INJECTOR

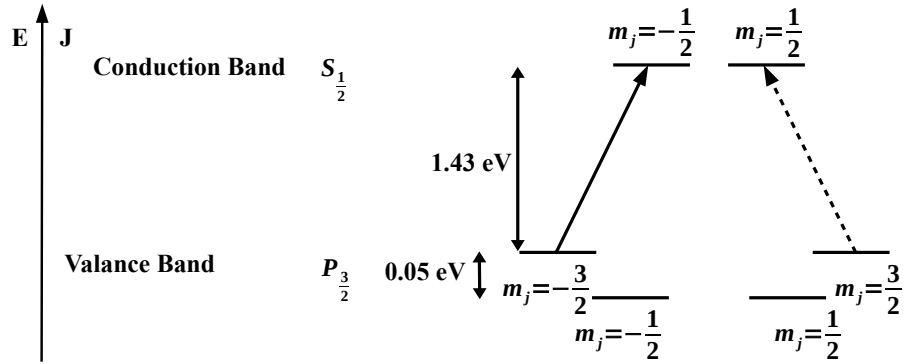


Figure 3.5: Photo-emission process in a strained GaAs photocathode. Circularly polarized laser light illuminates the surface of the cathode and ultimately produces longitudinally polarized electrons. The transition shown by the dotted(solid) line is triggered by the left(right) circularly polarized photons.

3.2.6 Double Wien

Similar to the IHWP, a double Wien filter is the second method of slow helicity reversal. It is located just downstream of the photocathode and consists of a vertical Wien, two solenoids, and a horizontal Wien, as shown in Fig. 3.6. The sequence of magnetic fields in the double Wien filter precesses the electron's spin in such a way that ultimately, the helicity of the beam as it enters the accelerator is opposite of what it was during the previous Wien setting. The Wien settings (the magnetic and electric fields) are adjusted such that the system behaves in one of two ways: so-called Wien-Right or Wien-Left configuration. During PREX-2 the Wien setting is changed roughly every two to three weeks, while during CREX it is changed only twice. Since the DAQ system is immune to (or unaware of) the process of altering the helicity by changing the Wien settings, the effect should only be seen in the sign of the asymmetry. When used in combination with the IHWP system, the double Wien filter greatly improves cancellation of helicity-correlated systematic errors. This is accomplished by simply averaging the asymmetries measured during a pair of opposite Wien states that have roughly equal amounts of data.

3.3. THE ACCELERATOR

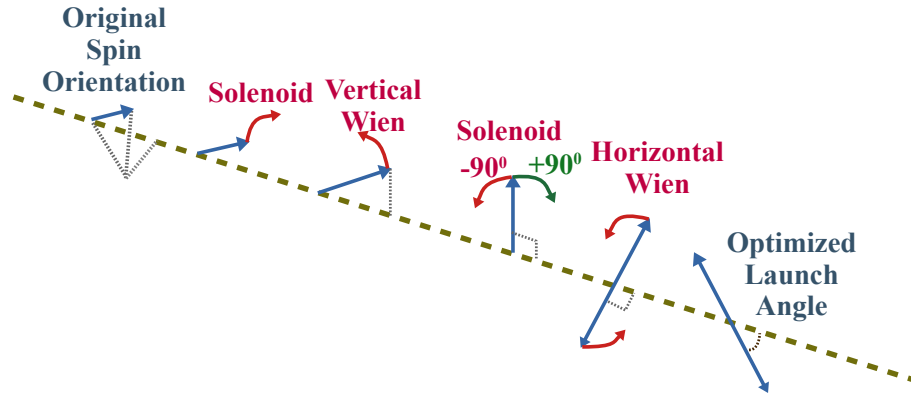


Figure 3.6: JLab injector Wien filter setup (reproduced from [52]). The magnetic and electric fields are adjusted as needed such that it provides a second method of slow helicity reversal.

3.3 The Accelerator

The accelerator consists of two superconducting radio-frequency (SRF) linear accelerators (LINACs), named the North and South LINAC. Each LINAC has 25 helium-cooled cryogenic modules. Each module is made of 8 superconducting niobium cavities. The two LINACs are connected by 180° arcs as shown in Fig. 3.1. The polarized electrons from the injector are first pumped into the North LINAC and kept circulating around the accelerator until the desired energy is reached. The accelerator is capable of providing beam energy of up to 12 GeV. The amount of energy each hall receives depends on the number of passes the electrons make in the accelerator before being extracted into the experimental halls using RF (radio-frequency) extractors and septum magnets.

3.4 Hall A Beamline

The Beam Switch Yard (BSY), located just downstream of the South LINAC, is where the electron beam is separated for distribution into experimental Halls A, B, and C. This is where the Hall A beamline begins, extending through the center of Hall A

3.4. HALL A BEAMLINE

(approximately 10 ft above the floor), and terminating at the Hall A beamdump. The Hall A beamline includes: beam modulation (or dithering) system, beam energy monitors, beam position monitors (BPMs), beam current monitors (BCMs), target scattering chamber, high resolution spectrometers (HRSs), and many more. The major components of Hall A are shown in Fig. 3.7.

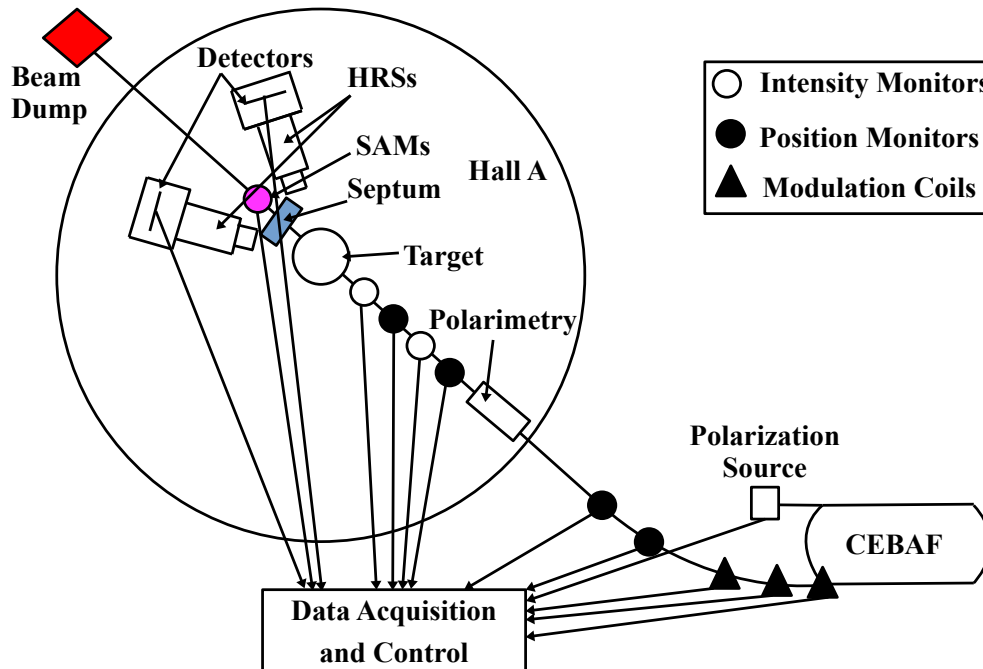


Figure 3.7: Schematic view (not to scale) of Hall A, CEBAF, HRSs, and target scattering chamber with beam monitoring and dithering system components shown along the beamline. The monitors shown are only some examples; not all monitors are shown here.

3.4.1 Beam Modulation (or Dithering)

The beam modulation or dithering system is used to purposefully change (or modulate) the beam's position, angle, and energy on target in order to quantify the response of beam monitors and main detectors to these changes. These responses, e.g. helicity window pair position differences and slopes-measured asymmetry change per position difference, are then used to make corrections to the measured asymmetry, reducing

3.4. HALL A BEAMLINE

contamination from helicity correlated false beam asymmetries. Note the size of this contamination can be more than an order of magnitude larger than A_{PV} and is parity conserving in nature. The source of this asymmetry comes from small fluctuations in the beam's position, energy, and angle as it hits the target, and these can be correlated with the beam's helicity state. As a result, the measured asymmetry requires a correction, and that is provided primarily by the beam modulation system. To calculate this correction, the invasive beam modulation or dithering technique is used approximately 10 % of the running time in order to purposefully mis-steer the beam while analyzing its effect on the measured asymmetry and monitors. In this way, the effects of helicity-correlated beam motion (and energy fluctuation) are corrected for, on a helicity window pair-by-pair basis, using correction slopes from the dithering analysis (see Sec. 4.2.5).

The dithering system makes use of seven magnetic beam-steering coils located several meters upstream of the main bend into Hall A. These include three \hat{x} -modulation coils, three \hat{y} -modulation coils, and one energy vernier. Dithering is set to repeat automatically every 10 min and lasts approximately 1 minute. Each complete cycle, referred to as a super cycle, constitutes the complete modulation of the seven coils in sequence. A schematic view of the locations of various coils along with several other beam-monitors is given in Fig. 3.8.

3.4.2 Harp Scan and Beam Raster

An appropriate or large enough intrinsic beam spot-size is crucial for maintaining target health. In particular, the Pb target is required to have a spot-size of at least $100 \times 100 \mu\text{m}^2$, otherwise nonuniform density changes in the target thickness or possibly melting could occur. The spot-size should be optimized because too small a spot-size at high beam currents may lead to excessive local heating, which can

3.4. HALL A BEAMLINE

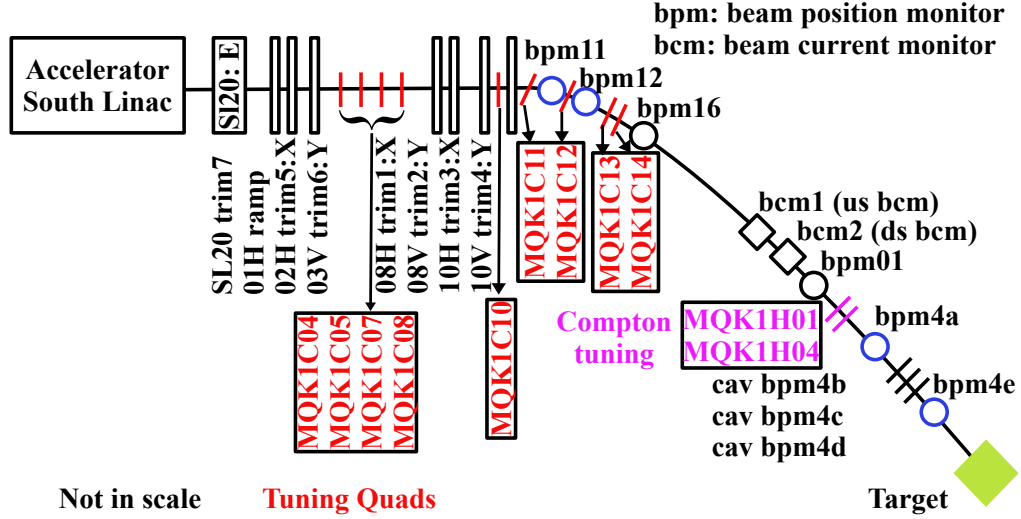


Figure 3.8: Schematic view of dithering coils. Several modulation coils, tentative location of the tuning magnets, and other beam-monitors are also shown; trim1, trim3, and trim5 modulate the beam horizontally, trim2, trim4, and trim6 modulate the beam vertically, and trim7 modulates the beam energy. The bpm11 and bpm12 are located in the dispersion arc (a bending arc that directs electrons into the hall’s transport line), and their \hat{x} -wires are sensitive to the beam energy and are used as beam energy monitors.

effectively cause target melting, while too large a spot-size may introduce extra noise in the main detector signals. To make sure the spot-size is appropriate, a harp scan is done at the beginning of the experiment, as well as intermittently when resuming back from downtime that lasts more than a few hours, or if there has been any change in the beam properties upstream of the target, or a change in the target type. It is an invasive procedure and is performed at low currents, usually at or below $5 \mu\text{A}$ tuned (low duty cycle) beam, and with no raster. To prevent the target from density fluctuations due to overheating and potential damage, the beam is systematically swept over the target face in a repeating square or rectangular pattern, called a raster pattern.

It is also crucial to use a proper raster size to distribute the beam’s heat load over an area (defined by the raster size) of the target. These sizes are $4 \text{ mm} \times 6 \text{ mm}$ for Pb targets and $2 \text{ mm} \times 2 \text{ mm}$ for Ca targets. Furthermore, for a temperature-

3.4. HALL A BEAMLINe

sensitive target, such as Pb, the raster pattern is synchronized with the helicity flip rate. This means the raster pattern completes one cycle (in the exact same way every time) during each helicity window. This greatly eliminates integrated signal fluctuations caused by large-scale density variations that develop over time due to localized beam heating (melt/refreeze cycling) of the Pb target. The raster system uses two magnetic coils located several meters upstream of the target. One magnet steers the beam vertically, while the other steers it horizontally. The raster size and pattern are checked regularly using dedicated, so-called, spot++ counting mode runs. These are counting mode DAQ runs (as opposed to integration mode runs) and can be performed in two different ways.

To perform the raster size and pattern checks, first, a high current run is used to check the raster size on the target. This is a non-invasive procedure and can be performed during production data taking; no HRS trigger scintillators are used, but instead, a clock pulser trigger is used. Second, a low current run allows us to image the raster size on the target, as well as the density fluctuations by plotting the detected scattering rates as a function of raster current in \hat{x} and \hat{y} directions. The raster size check is often performed using a carbon-hole target. Figures 3.9 and 3.10 show the raster patterns for typical spot++ runs during PREX-2 and CREX, respectively. This process is invasive and is performed using the HRS scintillator triggers and the counting mode DAQ at low beam currents. Beam currents are chosen such that the scintillator rates are of order 100 kHz. Additionally, these checks also give us an indication of any accidental misalignment of the beam and possible interception on the target frame.

3.4. HALL A BEAMLINE

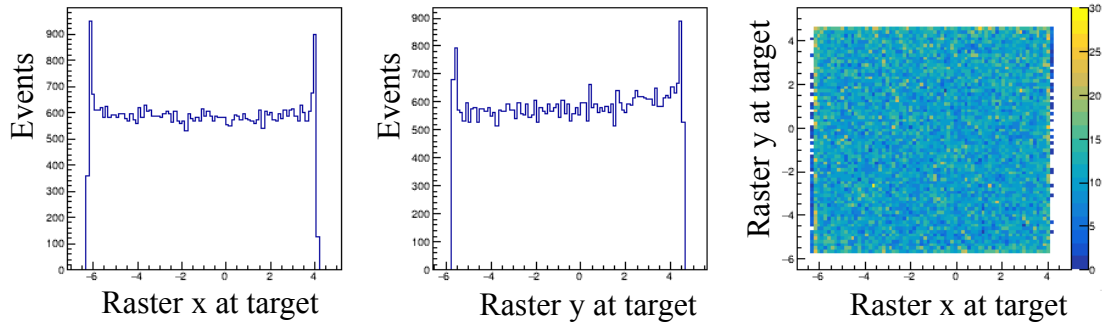


Figure 3.9: Typical spot++ run on a ^{208}Pb target during PREX-2.

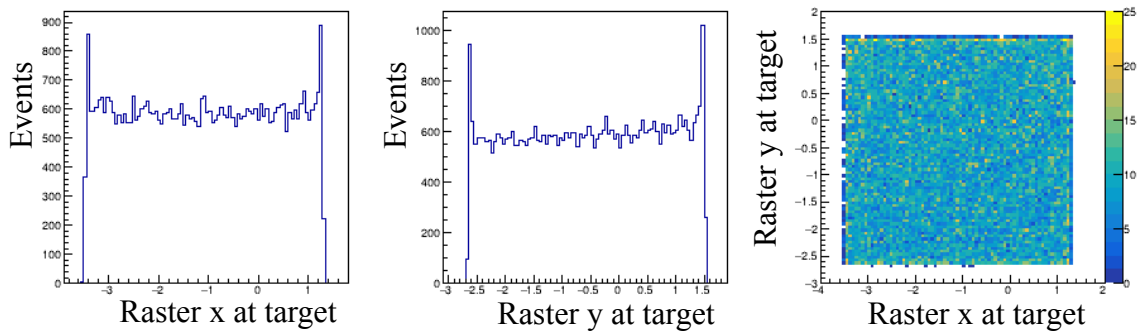


Figure 3.10: Typical spot++ run on a ^{48}Ca target during CREX.

3.4.3 Beam Position Monitors (BPMs)

The actual scattering angles accepted by the spectrometers are correlated with the precise position (and angle) of the beam when it impinges on the target, and this is continuously changing due to the raster as well as natural and helicity-correlated beam motion. As a result, precise and continuous measurement of beam position and intensity are required when measuring a considerably small asymmetry with high precision. PREX-2 and CREX use the standard set of Hall A beam position monitors (BPMs) and energy monitors at various locations upstream of the target. The approximate (not to scale) location of each of these monitors was shown in Fig. 3.8.

Each BPM is composed of four wire-antennas: X_+ , X_- , Y_+ , and Y_- , oriented symmetrically at $\pm 45^\circ$ with respect to the horizontal and vertical planes intersecting

3.4. HALL A BEAMLINER

at the beamline as shown in Fig. 3.11. The signal from each wire is proportional to the beam intensity times the distance between the wire and the beam. During data taking, the signals are digitized and integrated. The integrated signal size for each channel is maintained approximately constant by setting the Hall A BPMs to auto-gain mode—where the channels switch their gain based on beam intensity. However, the energy BPMs in the arc are used in forced-gain mode, which keeps their gain fixed at a constant value, so that their measured signal gives a measure of the beam energy and its deviation from nominal. The Hall A coordinate system beam positions recorded by a particular BPM are determined by

$$\begin{pmatrix} x \\ y \end{pmatrix} = \begin{pmatrix} \cos 45^\circ & -\sin 45^\circ \\ \sin 45^\circ & \cos 45^\circ \end{pmatrix} \begin{pmatrix} X_{rotated} \\ Y_{rotated} \end{pmatrix}, \quad (3.2)$$

where $X_{rotated}$ and $Y_{rotated}$ give the beam position along the axis of the wires, and are given by

$$X_{rotated} = k \left(\frac{X_P - X_M}{X_P + X_M} \right) \quad \text{and} \quad Y_{rotated} = k \left(\frac{Y_P - Y_M}{Y_P + Y_M} \right), \quad (3.3)$$

where X_P , X_M , Y_P , and Y_M are the integrated signals measured by each antenna, and $k = 18.76$ mm [25].

The standard stripline BPMs are used throughout both PREX-2 and CREX. A special set of magnets is used to lock the beam position on the target. The beam position lock, which normally works above a couple of μA beam current, is achieved using the readouts of the target BPMs: bpm4a and bpm4e. These are the most important BPMs in the sense that we use them to measure the helicity-correlated position and angle differences on the target. During PREX-2, when we have to run various counting mode DAQ diagnostics and HRS optics calibrations at very low beam currents (usually a few tens of nA), cavity BPMs are used to lock the beam

3.4. HALL A BEAMLINE

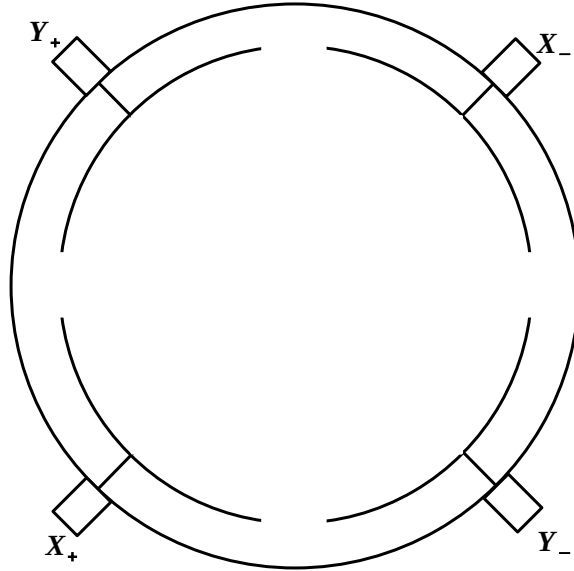


Figure 3.11: Schematic diagram of the four wire-antennae of a stripline BPM, looking downstream along the beam axis (reproduced from [50, 53]).

position on the target. This is needed because the stripline BPMs do not give accurate readings at such low currents. However, the cavity BPMs are not used during CREX running because the scattering rate from the calcium target during CREX is ~ 80 times lower than for the PREX-2 Pb target. This allows the beam current to be a few hundred nA during CREX counting runs, giving reliability to the stripline BPM readout.

Located in the Hall A arc, the \hat{x} wires of bpm11 and bpm12 are highly sensitive to beam dispersion and hence are used to measure beam energy. The differences in the beam positions, for opposite helicity states measured by these BPMs in the horizontal plane of the arc, ΔX , are used to measure the beam energy differences. Due to the high correlation between the energy difference measurements from the two BPMs, we form a linear combination of them for the asymmetry correction during offline analysis. More about the combination and applied correction is discussed in Chapter 4. Along with the above-mentioned BPMs, several other Hall A BPMs are also added to the data stream during parity or integrating mode DAQ running. In addition to

3.4. HALL A BEAMLINE

these standard Hall A BPMs, various BPM signals in the injector are also acquired and used for diagnostic purposes and systematic checks.

3.4.4 Beam Current Monitors (BCMs)

Figure 3.12 shows a schematic diagram of the Hall A BCM system. It consists of three main devices: the UNSER, upstream beam current monitor (US BCM), and downstream beam current monitor (DS BCM). The UNSER is a parametric⁴ current transformer (PCT) device and has an unstable output over a few minute period making it unreliable at continuous measurement of the beam current. However, it is very linear at shorter time scales and is used to calibrate the US BCM and DS BCM. The UNSER itself is calibrated by passing a known current through a wire inside the beam pipe [55].

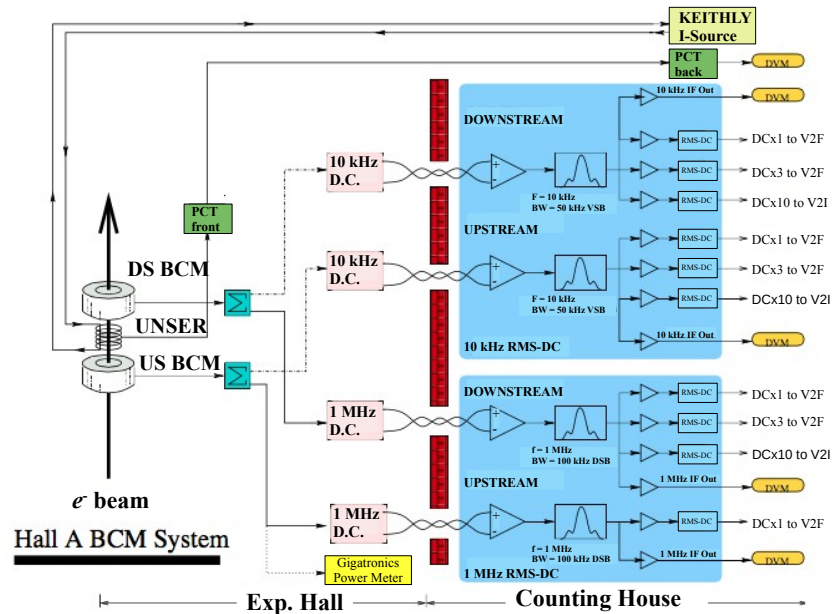


Figure 3.12: Schematic of the Hall A beam current monitoring system (reproduced from [55]). The 1 MHz channel is used during PREX-2/CREX.

The US BCM and DS BCM are resonant radio-frequency (RF) cavities made of

⁴It is called parametric because the magnetic modulator provides parametric amplification in the low frequency channel, up to a transition frequency [54].

3.4. HALL A BEAMLINER

stainless steel cylindrical waveguides. The cavities are tuned to the beam-frequency, or beam pulse repetition rate, which is 1497 MHz. Each cavity outputs a voltage signal level proportional to the beam intensity. The output signals are then split into two parts, one down-converted to 10 kHz and the other to 1 MHz, and sent to the DAQ system via RMS-DC converters. To be more precise, we use the 1 MHz channels during PREX-2 and CREX. The BCMs used in precision experiments, like parity experiments, should be highly reliable and linear as they measure the beam intensity asymmetry—a helicity-correlated beam asymmetry that requires monitoring and correction. Also, their calibration needs to be accurate, and their performance stable, because their signals directly impact the main detector rates and noise. In addition, other BCM signals located in the injector are also fed into the parity DAQ and are used for injector source studies and other diagnostic purposes.

3.4.5 Polarimetry

PVeS experiments measure the elastically scattered flux of a longitudinally polarized electron beam from unpolarized (fixed) targets at the desired kinematics. Although these experiments require a perfect (to the highest degree possible) longitudinally polarized electron beam in order to maximize the measured A_{PV} , in practice it is not possible to achieve 100 % polarization. In addition, these experiments also require nulled transverse beam polarization components in order to minimize potentially large transverse (parity-conserving, false) asymmetries, referred to as A_T . Therefore, the beam polarization direction and magnitude are measured precisely—making sure that the uncertainties are within the experiment’s systematic error budget.

The experimental asymmetries are scaled by the measured beam polarization to obtain the physics asymmetries. PREX-2 and CREX measure the beam polarization using two independent, standard Hall A polarimeters referred to as the Møller and

3.4. HALL A BEAMLINe

Compton polarimeters. The proposed systematic uncertainty from polarization measurement is 1 % for PREX-2 and 0.8 % for CREX. Furthermore, as an additional diagnostic, we construct and use special auxiliary detectors to monitor possible A_T contamination, and to help limit its contribution to the total systematic error. See Sections 3.6.3 and 4.5 for details about the design, operation, and performance of the auxiliary (“A_T”) detectors.

Møller Polarimeter

The Møller polarimeter is a Hall A standard polarimeter located approximately 17.5 m upstream of the target scattering chamber center. Schematic top and side views of the polarimeter are shown in Fig. 3.13. Polarization measurements are carried out using Møller scattering ($e + e \rightarrow e + e$) of longitudinally polarized beam electrons scattering off the polarized electrons in the pure iron target foil. The polarimeter uses a 4 T superconducting Helmholtz magnet, and precision alignment capability of the ferromagnetic target foil, to saturate the foil’s electron polarization to its theoretically known limit. The measured Møller asymmetry is given by

$$A_{Møller} = \langle A_{ZZ} \rangle \times P_b \times P_t, \quad (3.4)$$

where P_b is the beam polarization, P_t is the target polarization, and $\langle A_{ZZ} \rangle$ is the system’s average analyzing power (a measure of the system’s sensitivity to changes in beam and target polarization on scattering cross-sections) which is obtained from simulation. The precise P_t is obtained from calculation given the precise foil location and magnetic field size and direction. The Møller measurements are made using a $\pm 20^\circ$ orientation of the target foil, and the average from several measurements is used. This helps cancel any transverse component of beam polarization, and other false backgrounds, since the asymmetries associated with these backgrounds cancel

3.4. HALL A BEAMLINE

out when averaged. $A_{M\ddot{o}ller}$ is measured in dedicated counting (Møller) runs at low beam current. Then, given knowledge of all the parameters, the beam polarization is calculated from the measurement using Eq. 3.4.

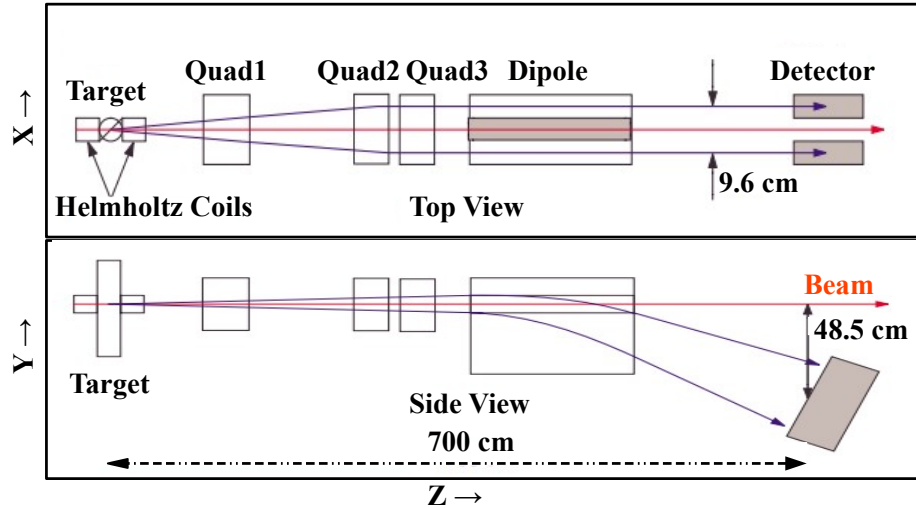


Figure 3.13: Top-view and side-view schematic of the Hall A Møller polarimeter (reproduced from [56]). It is located along the beamline inside Hall A. The distance from the Møller target to its detector is approximately 7 m.

The Møller measurements require a special setup for its transport/spectrometer magnets (quads and dipoles), which are also Hall A beamline magnets. The measurements also require lower beam current, usually well below $1 \mu\text{A}$, therefore it is an invasive measurement which interrupts production running. PREX-2 and CREX perform Møller measurements every one to two weeks, and each measurement takes one to two shifts depending on the efficiency of accelerator beam delivery.

Compton Polarimeter

The Compton polarimeter measures electron beam polarization using the nearly head-on Compton scattering of polarized beam electrons off polarized laser photons ($e + \gamma \rightarrow e' + \gamma'$). One can perform an asymmetry measurement (A_{meas}) on the integrated Compton scattering signals between left and right helicity states:

3.4. HALL A BEAMLINER

$$A_{meas} = \frac{S_+ - S_-}{S_+ + S_-}, \quad (3.5)$$

where S_+ and S_- are the detected Compton signals for the two opposite helicity states. The Compton asymmetry is related to the electron beam polarization (P_b) and the laser circular polarization, P_γ , through the relation

$$A_{meas} = P_b P_\gamma \langle A_s \rangle, \quad (3.6)$$

where $\langle A_s \rangle$ is the Compton analyzing power, which is defined as the asymmetry that would be measured if the electron and photon beams are perfectly polarized, and it is obtained from simulation. P_γ is measured using a quarter-wave plate upstream of the resonant cavity containing the photon target. Unlike Møller polarimetry, Compton polarimetry is a non-invasive measurement which does not interrupt production data taking.

The Compton polarimeter is located within a magnetic chicane that runs parallel to and ~ 1 m below the Hall A beamline. A simple drawing of the Compton polarimeter in Hall A at JLab is shown in Fig. 3.14. It mainly consists of four chicane dipoles (D_1 , D_2 , D_3 , and D_4), a scattering region (Fabry-Perot Cavity), and detectors. The first two dipoles (D_1 and D_2), when energized, bend the full electron beam into the Compton beamline and through the interaction region of the laser cavity. Only a small fraction of beam electrons (one out of $\sim 10^9$) scatter from the photons. To increase the intensity of the laser light and Compton scattering rates, light from a seed laser is sent into a Fabry-Perot resonant Cavity, where the light undergoes multiple reflections between two well-positioned mirrors at either end of the cavity; the cavity is designed to have a finesse or amplification factor of approximately 4000 and was first designed and used for PREX-1. The electrons not involved in Compton

3.4. HALL A BEAMLINE

scattering are steered back into the main beamline using the second pair of chicane dipoles (D_3 and D_4). The Compton scattered electrons and photons are detected in the electron and photon detector, respectively.

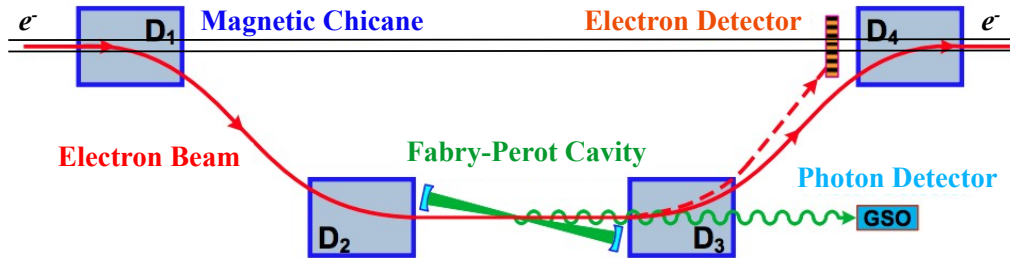


Figure 3.14: Simple schematic of the Compton polarimeter in Hall A at JLab [57].

While the Compton electron detector does not work well during PREX-2/CREX, the photon detector does. The Compton photon detector uses a single GSO crystal scintillator (0.5 % Ce-doped Gd_2SiO_5 manufactured by Hitachi Chemical) dry-mounted flush (no grease) against a 2 inch PMT window. The GSO crystal is 6 cm diameter \times 15 cm long and capable of large light yields via scintillation. The detector is placed on a computer controlled table, as shown in Fig. 3.15, which can be moved in \hat{x} and \hat{y} dimensions (transverse to the beam direction). A lead collimator with fixed apertures, along with thin lead sheets (0.25 mm - 8 mm thick), is used to reduce synchrotron and bremsstrahlung backgrounds from beam electrons bending through the Hall A arc and upstream chicane dipoles. An additional variable aperture Tungsten collimator, whose aperture can be controlled remotely from 1 mm to 5 cm, is used to center the detector on the Compton scattered photons. A pair of Tungsten finger scintillators are also used to align the detector.

3.4.6 Scattering Chamber and Targets

The PREX-2/CREX target scattering chamber is an aluminum vessel comprised of two target ladders: one that can slide in and out of the beam horizontally, along the

3.4. HALL A BEAMLINE

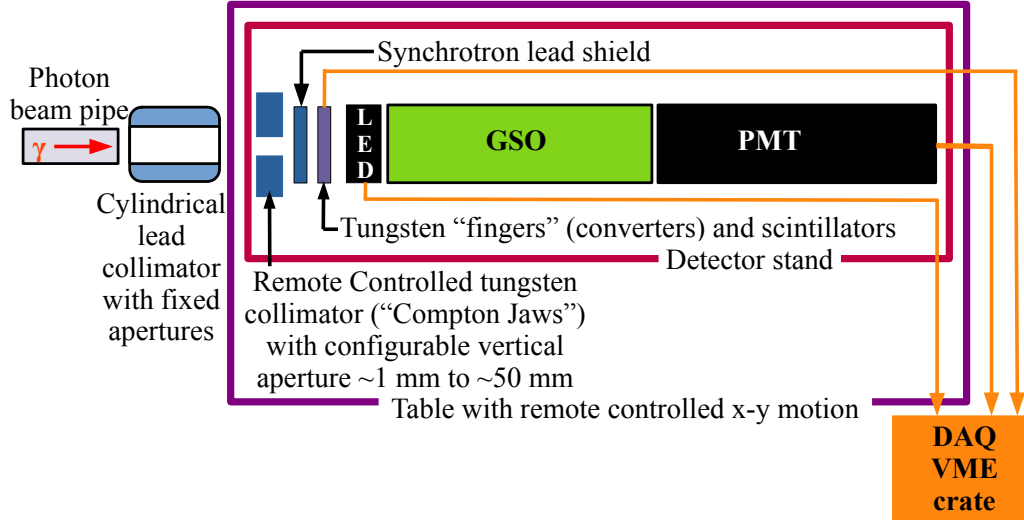


Figure 3.15: Compton photon detector table (reproduced from [58]). The GSO crystal and PMT are the major components of the detector. LEDs are used for in-situ PMT non-linearity monitoring.

\hat{x} -axis of the hall coordinate system, and the other which slides at an angle of 45° with respect to the \hat{x} -axis. The horizontal ladder (“cold” ladder) consists of sixteen cryo-cooled targets used for production running. The 45° ladder (“warm” ladder) consists of five optics targets maintained at room temperature which are used for spectrometer optics calibrations at low beam currents. A CAD drawing of the chamber is shown in Fig. 3.16. Simple drawings of the cold and warm ladders are shown in Figures 3.17 and 3.18, respectively, while the details of each target are given in Table 3.1. Slot 1 (the place holder for the ^{48}Ca CREX target) in the cold ladder is the left-most ladder slot (looking downstream with beam) and is left empty during PREX-2 running.

PREX-2 runs at three different beam currents. In the beginning phase it runs at $50 \mu\text{A}$ (for a few days), then most of the time it runs at $70 \mu\text{A}$, and for a few days at the end, it runs at $85 \mu\text{A}$. Running at higher beam intensity accumulates more statistics in a given time, but the low thermal conductivity and melting point of the Pb target limits the possible run time at the higher current. Toward the end of PREX-2 running, we still have four unused targets and therefore decide to run at

3.4. HALL A BEAMLINE

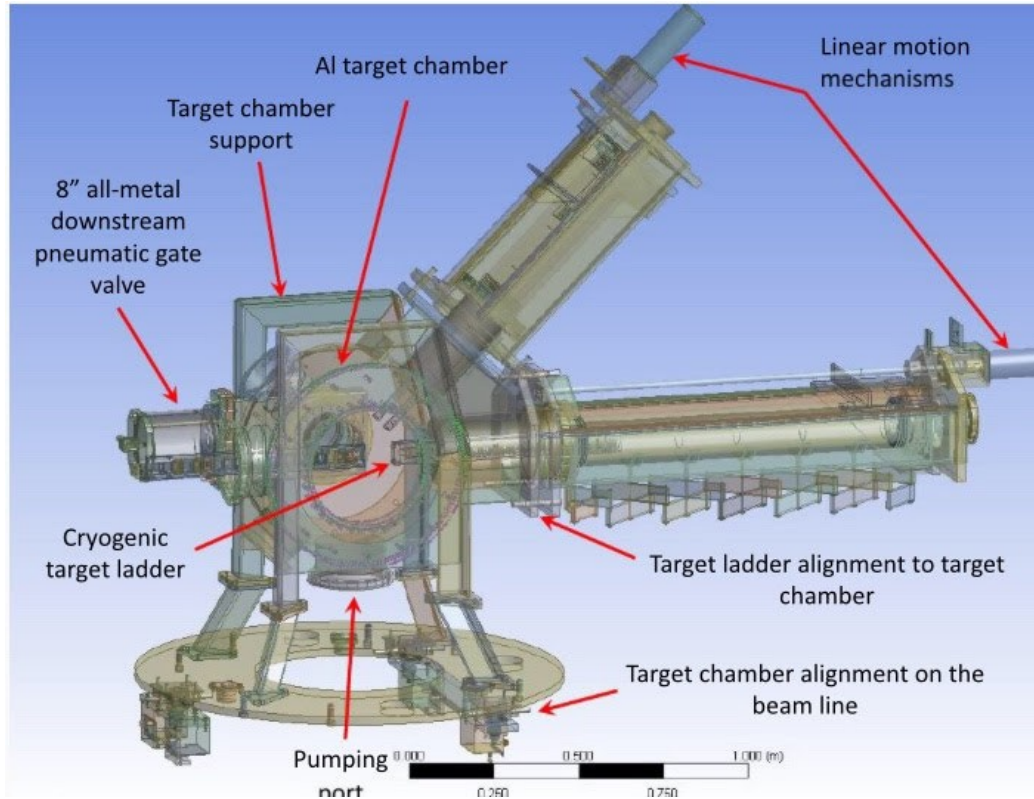


Figure 3.16: PREX-2/CREX scattering chamber [59]. The chamber is maintained at $\sim 10^{-7}$ torr internal pressure. These are newly designed target ladders and chamber, specifically for PREX-2 and CREX.

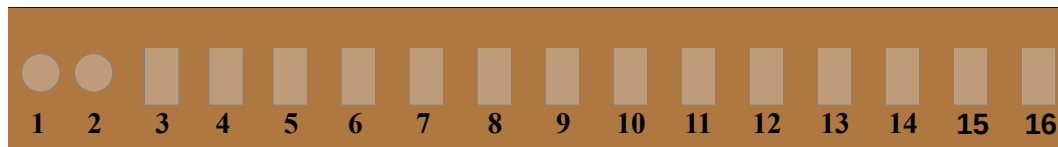


Figure 3.17: PREX-2/CREX production target ladder sketch (not to scale). The ladder is cryo-cooled with liquid helium at 15 K. There are a total of sixteen targets: ten PREX-2 production targets, one CREX production target, and five other auxiliary targets as given in the text.

85 μA which helps us improve our statistical precision.

The PREX-2 production targets each have a 0.553 mm thick ($0.10X_0$) isotopically pure ^{208}Pb foil sandwiched between two 250 μm thick diamond layers. The Pb foil is in thermal contact with the diamond “wafers” which are each in thermal contact with a copper frame cooled by liquid helium; this is required to keep the Pb foil below

3.4. HALL A BEAMLINE

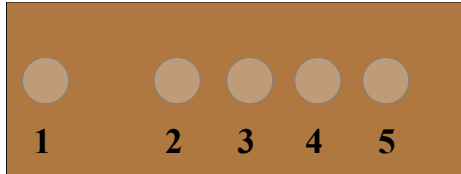


Figure 3.18: PREX-2/CREX optics target ladder sketch (not to scale). This ladder holds a total of five targets which are used for spectrometer optics calibrations. This ladder is kept at room temperature.

its melting point and prevent it from potential damage. Even with proper thermal contact and cooling, the diamond eventually degrades due to beam damage, which in turn causes non-uniformity in the lead target thickness and ultimately leads to target melting. For this reason, the production target ladder is installed with several ^{208}Pb targets. The duration of time a single lead target can be used depends on the thickness of the diamond sheets, thermal contact with the copper frame, raster size, and beam intensity. Of the ten PREX-2 ^{208}Pb targets, one of them uses graphite and the rest use diamond backing; we never took production data on the target with graphite backing. There are also two additional natural lead targets, one with diamond backing and the other with graphite backing—which are slightly used in the beginning, during the commissioning of the experiment. PREX-2 uses seven production targets before the end of the experiment. The Pb target labeled DE-208Pb4-DF is used only for the dedicated transverse asymmetry measurements performed during CREX. During PREX-2 running, the ^{208}Pb targets are changed roughly every ten days, following the first signs of its degradation.

The most reliable indicator of target degradation is a sudden increase in the measured main detector asymmetry widths. In short, target degradation happens when the diamond's thermal conductivity significantly degrades due to beam damage. When this occurs, it is hypothesized that the Pb target begins to undergo a melting/re-freezing process which leads to possibly dynamic local thickness varia-

3.4. HALL A BEAMLINER

Production (cold) ladder		
S.N. ^a	Target	Comment
1	⁴⁸ Ca	CREX production target ^b
2	⁴⁰ Ca	Used for transverse asymmetry measurements ^b
3	Carbon Hole	Used for raster size check and other diagnostics
4	D9-208Pb10-D10	Isotopically pure ²⁰⁸ Pb target ^c
5	D7-208Pb9-D8	Isotopically pure ²⁰⁸ Pb target ^c
6	D5-208Pb8-D6	Isotopically pure ²⁰⁸ Pb target ^c
7	D3-208Pb7-D4	Isotopically pure ²⁰⁸ Pb target ^c
8	D1-208Pb6-D2	Isotopically pure ²⁰⁸ Pb target ^c
9	DG-208Pb5-D20	Isotopically pure ²⁰⁸ Pb target ^c
10	DE-208Pb4-DF	Isotopically pure ²⁰⁸ Pb target ^d
11	DC-208Pb3-DD	Isotopically pure ²⁰⁸ Pb target
12	DA-208Pb2-DB	Isotopically pure ²⁰⁸ Pb target ^c
13	Carbon 1 %	Used during transverse asymmetry measurements
14	C-208Pb1-C	Isotopically pure ²⁰⁸ Pb target
15	DI-Pb-DJ	Natural Pb target
16	C-Pb-C	Natural Pb target
Optics (warm) ladder		
1	Water Cell	Used for scattering angle measurements
2	Tungsten	Not used
3	Pb	Natural Pb
4	Carbon 0.2 %	Used for spectrometer optics calibrations
5	Carbon Hole	Used for optics calibration and other diagnostics

^a This sequence is the same as the numbering used in Figures 3.17 and 3.18.

^b In the beginning of CREX, position-1 is occupied by ⁴⁰Ca and position-2 is occupied by ⁴⁸Ca. ⁴⁸Ca target melts due to an accident on January 18, 2020. Later it is replaced by a stack of 3 separate wafers or pucks. Furthermore, during the replacement the position of ⁴⁸Ca and ⁴⁰Ca are swapped.

^c Used during PREX-2 running.

^d Used during CREX transverse asymmetry measurements.

Table 3.1: A complete list of targets installed on the production and optics ladders during PREX-2 and CREX. The position-1 is left empty and position-2 is installed with ⁴⁰Ca during PREX-2 running. In the beginning of CREX, ⁴⁰Ca is installed in position-1 and ⁴⁸Ca is installed in position-2. ⁴⁸Ca position is swapped with ⁴⁰Ca after the accidental melting of the initial ⁴⁸Ca target during CREX. D1, D2, ..., D10, and D20 represent thermal diamond foils, DA, DB, ..., DJ represent optical diamond foils, and C represents graphite.

tions. This causes an overall reduction in the scattered flux rates in the focal plane⁵

⁵The HRS optics are tuned to focus the elastically scattered electrons onto the focal plane

3.4. HALL A BEAMLINe

(main) detectors and hence an increased RMS width of the measured asymmetry. Figure 3.19 gives an instance of a Pb target failure during PREX-2, showing the abrupt jump in the focal plane detector widths (indicating the failure), and a photograph of the damaged and partially melted target. The target failure can also be observed by monitoring increased power deposition in the upstream collimator, which increases the radiation (thermal neutrons) levels inside the hall and causes an increase in Compton background rates—due to neutron capture in the Gadolinium of the GSO crystal. As another check, often when we see a jump in detector widths, we switch to low current counting mode and check the rate distribution on the target as a function of raster current or position (spot++ runs). Using the counting mode DAQ setup with trigger scintillators and VDCs, the raster current distribution on target can be plotted, and any nonuniform distribution indicates target degradation. Figure 3.20 gives a comparison of raster current distributions for a good (or undamaged) target and a degraded target.

CREX runs mostly at $150\ \mu\text{A}$ on isotopically pure ^{48}Ca target with a 6 % radiation length for production running. The initial ^{48}Ca target (95.99 % ^{48}Ca , 3.84 % ^{40}Ca , and a small fraction of other isotopes) is 5.72 mm thick with 1.2938 g mass, mounted in a copper frame. At the beginning of CREX, ^{40}Ca target is located in the far left position of the target ladder (looking downstream the beamline), while the next position to the right is occupied by a ^{48}Ca target. Due to an operational accident, the beam is mis-steered during production running on January 18, 2020, causing the beam to hit the copper frame (target holder) near the ^{48}Ca target, and in turn creates a runaway thermal event which quickly leads to catastrophic melting of the initial ^{48}Ca target puck. Figure 3.21 shows the damage caused in the copper frame due to the accident. The damaged target is replaced by another ^{48}Ca target, which is a stack of three separate pucks each with roughly 12.7 mm diameter. Details about

detectors.

3.4. HALL A BEAMLINE

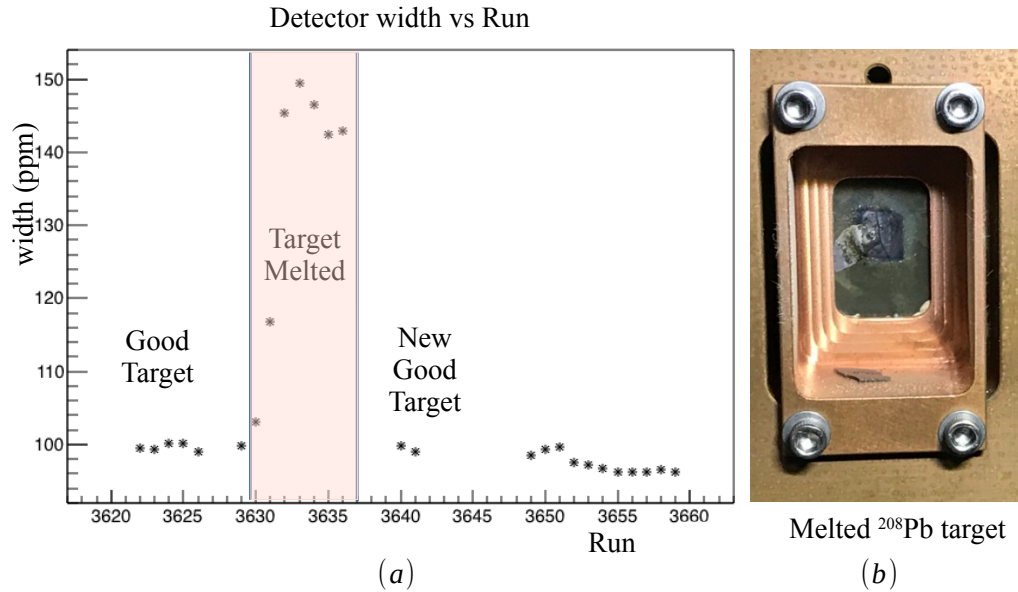


Figure 3.19: Evidence of target degradation during production running. (a) Focal plane detector width of measured asymmetry versus run number. A sudden jump in the measured asymmetry widths starting near run 3630 indicates target degradation. The widths return to the nominal range starting at run 3640, when a new target is used. (b) A photograph of a melted ^{208}Pb target; noticeable cracks are present within the rectangular region of the raster.

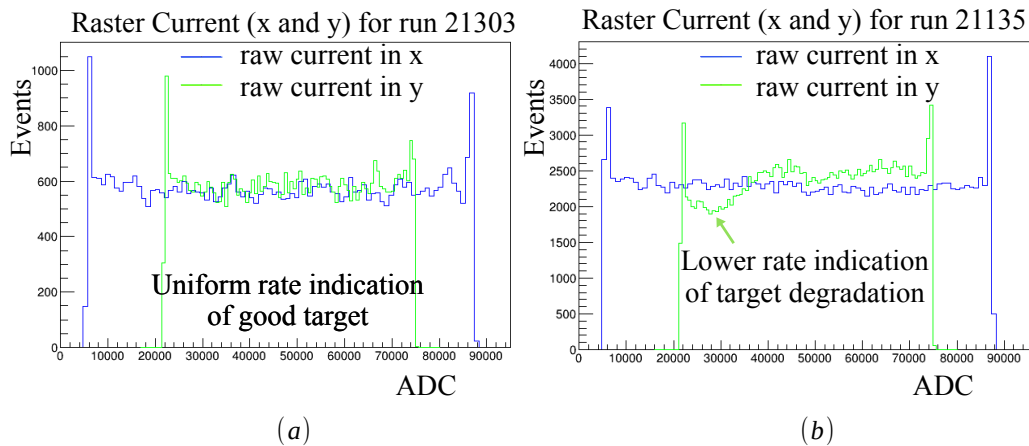


Figure 3.20: Evidence of target degradation from counting mode raster checks. (a) Raster current (raw) distributions for an undamaged Pb target, and (b) for a degraded Pb target. Note the raster currents are directly proportional to the raster positions on target.

the new composite ^{48}Ca target are given in Table 3.2. Following the accident, the ^{40}Ca and ^{48}Ca target positions are swapped and are installed with a small protective

3.4. HALL A BEAMLINE

(upstream) collimator made of tungsten (90.0 %), nickel (6.0 %), and copper (4.0 %).

Foil	Thickness (mm)	Mass (g)	Isotopic %
upstream	0.511	0.1067	95.99
middle	1.118	0.2461	95.99
downstream	4.094	0.9116	90.04

Table 3.2: Details about the three foils or pucks used in the new composite ^{48}Ca target. The majority of the impurity is ^{40}Ca ($\approx 8\%$ averaged over the three foils), and the fraction of other isotopes is negligibly small.



Figure 3.21: Photograph of accidental damage to ^{48}Ca target. An accidental mis-steering of the beam causes it to hit the copper frame of the ^{48}Ca target, causing the target to melt (photo taken from Dave Meekins’s logbook).

3.4.7 Collimator and Septum Magnet

PREX-2 and CREX use two essential collimator systems: one centered on the beam-line between target chamber and septum, and the other at the entrance of Q_1 (the first quadrupole) of each spectrometer. The beamline collimator, made of Cu/W (30 %/70 %) alloy, is critical for reducing the radiation load in the hall due to forward scattering electrons that can neither make it into the HRS nor to the beam dump. The collimator design consists of a spiraling water channel for cooling as shown in Fig. 3.22. The front face of the collimator is ≈ 0.85 m downstream of the target as shown in Fig. 3.24, and intercepts electrons with scattering angles greater than 0.78° ;

3.4. HALL A BEAMLINER

symmetric custom vacuum beampipe feed-throughs, on either side of the collimator, pass the $\sim 5^\circ$ scattered electrons from target chamber to the septum entrance.

The collimators at the Q_1 entrances are made of lead and act as the HRS acceptance-defining collimators for the experiments. These collimators are custom-designed, curved apertures installed symmetrically on the left and right sides of the beamline. The two apertures need to have a high degree of both left/right and up/down symmetry with respect to the beamline to maximize systematic error cancellations. Figure 3.23 shows a photograph of the acceptance defining collimators installed just upstream of Q_1 .

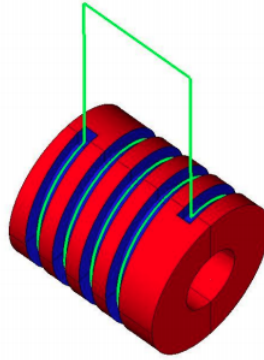


Figure 3.22: PREX-2/CREX beamline collimator. The spiraling water channel for cooling is shown. This collimator is located on the beamline just downstream of the scattering chamber in between the sieve box and septum (see Fig. 3.24).

PREX-2 and CREX measure A_{PV} on elastically scattered flux at approximately 5° . Due to the original design of the Hall A HRS system, the spectrometers can only reach a minimum angle of 12.5° with respect to the beamline. Therefore, we use a septum magnet just downstream of the collimator (and before the Q_1 's) to bend the electrons scattered at $\sim 5^\circ$ to 12.5° . Figure 3.24 shows a CAD view of the septum and beamline collimator used in PREX-2 and CREX. The septum is composed of two non-superconducting magnetic dipoles with three coils each. For high luminosity experiments, like PREX-2/CREX, the use of superconducting magnet coils near the beamline can be problematic due to radiation heating and damage from the beam.

3.4. HALL A BEAMLINE



Figure 3.23: Photograph during installation of the PREX-2/CREX acceptance-defining collimators for the left and right HRSSs. The left and right collimators are symmetric with respect to the beamline which is shown in between the two collimators.

The coils located on the left and right sides of the septum induce dipole fields up and down, respectively, which bend the $\sim 5^\circ$ scattered electrons out to 12.5° . The unscattered and scattered electrons at much smaller angles pass through the central beamline to the dump. The temperature of the septum is maintained using a water-cooling (“chiller”) system. The current set-point for the septum during PREX-2 running is 333.000 A, while it is 801.248 A during CREX; CREX requires higher current density because of the higher beam energy, and it also requires a higher water flow rate due to higher beam intensity.

3.4.8 Radiation shielding

During PREX-1, excessive radiation inside the hall caused damage to electronics and soft rubber O-ring seals in the scattering chamber. This resulted in long periods of downtime during PREX-1 and consequently very low collected statistics [60].

3.4. HALL A BEAMLINE

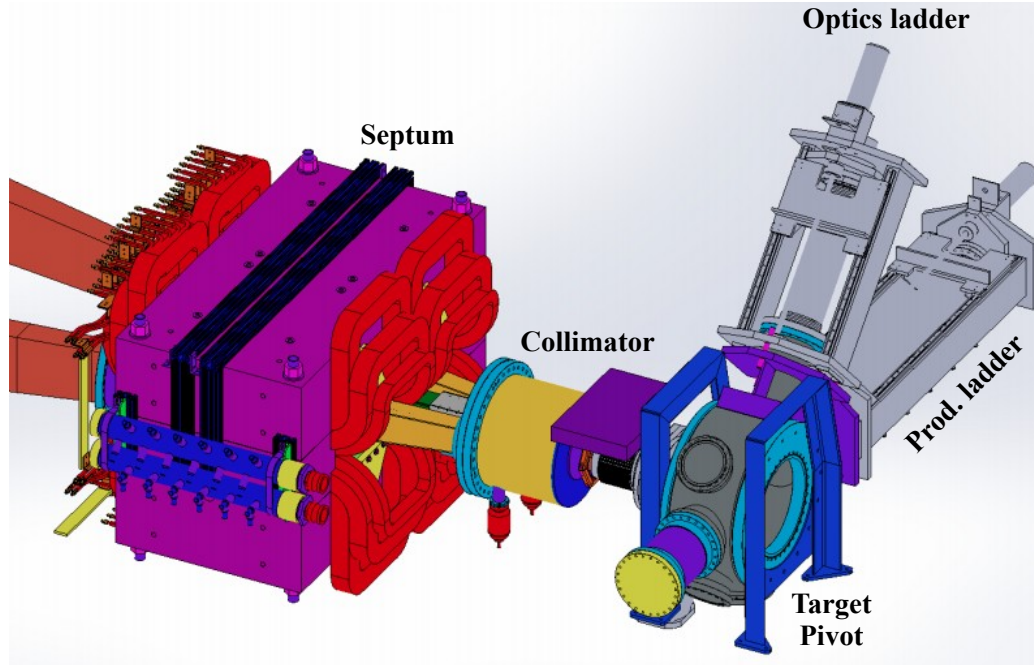


Figure 3.24: PREX-2/CREX septum drawing shown in context with the beamline collimator and scattering chamber at the target pivot (hall center) with optics and production target ladder assemblies.

Therefore, it was a challenge for the PREX-2/CREX collaboration to understand the possible sources of that radiation, and implement effective control measures to ensure the radiation dose levels are well below JLab’s yearly radiation budget. The soft O-rings are replaced by metal O-rings; the inner bore diameter of the collimator is made smaller and tapered to intercept more unwanted scattered electrons. The intercepted particles in the collimator become new sources of radiation, particularly neutrons, and thus high-density polyethylene (HDPE) neutron shielding encases the collimator region. For site-boundary dose considerations, a set of concrete “sky-shine” shielding blocks is placed over the beamline collimator and target-pivot region. The new improvements result in PREX-2 producing only $\approx 6\%$ of the yearly site boundary radiation budget for the lab.

3.5 High Resolution Spectrometers (HRSs)

PREX-2 and CREX use the standard Hall A HRSs. There are two identical HRSs in Hall A, and each includes (in order) two quadrupole magnets or quads (Q_1 and Q_2), a large dipole magnet, and a final quad (Q_3). The series of magnets are tuned to achieve a momentum resolution of $\sim 10^{-4}$, when used in conjunction with the VDCs, over its full range of accepted momenta (0.8 - 4.0 GeV/c). A sketch of a single Hall A HRS is presented in Fig. 3.25. The angular range of the left(right)-HRS is $12.5^\circ - 150^\circ$ ($12.5^\circ - 130^\circ$). For PREX-2 and CREX, each HRS is set to its minimum angle of 12.5° . The particles scattered at $\sim 5^\circ$, after being bent to 12.5° by the septum, are focused using two superconducting quads (Q_1 and Q_2). The particles are then transported through a 6.6 m long dipole, which bends the particles up at 45° toward the hall ceiling; note there is also some additional focusing from the dipole's field gradient [61]. The third quad (Q_3) provides further focusing of the scattered particles onto the focal plane detectors. Q_2 and Q_3 of each spectrometer have similar field and size requirements [61]. Each magnet is custom-tuned during the commissioning phase at the beginning of both PREX-2 and CREX to provide better resolution and focusing of the elastic peak onto the main quartz detectors. These experiments require high resolution to separate the elastic flux from the inelastic background.

The fields of each HRS magnet are measured regularly and fed into the EPICS (or “slow-controls”) data stream. The quadrupole fields are measured using a Hall probe while the dipole fields are measured using both NMR field probes and Hall probes placed inside the magnets [61]. A point to note here is that the NMR locking system for the left-HRS dipole does not work during CREX, so we have to rely only on the Hall probe. But the Hall probe loses stability over the long-term [61], therefore we have to perform detector alignment checks regularly to verify the position of the elastic peak on the quartz. Given stable beam position and energy on target, any

3.6. PREX-2/CREX DETECTOR SYSTEM

shift in the elastic peak position in the detector plane indicates a possible drift in the dipole field.

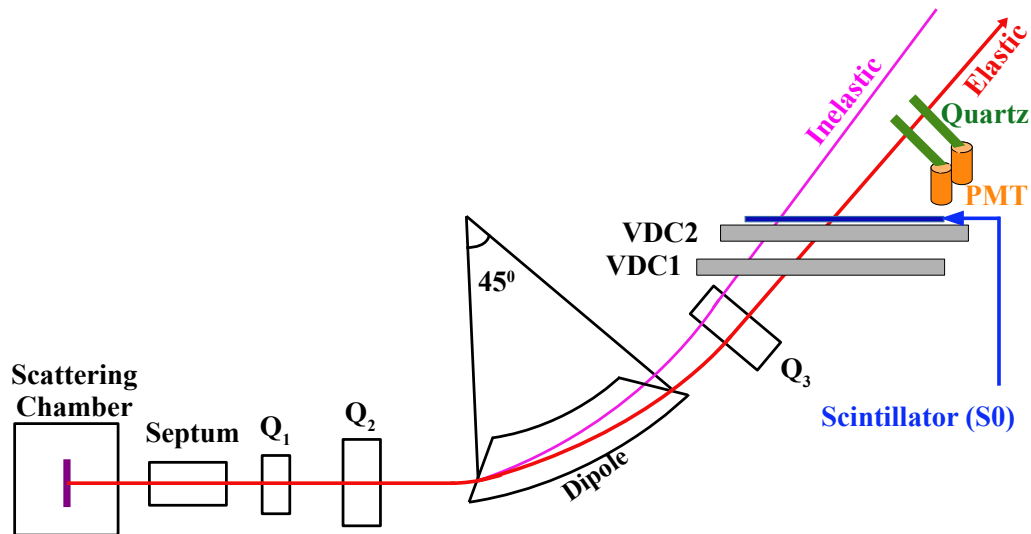


Figure 3.25: Side-view drawing of a Hall A HRS showing the layout of magnets and focal plane detectors (not to scale). Relative positions and orientations of Q_1 , Q_2 , Dipole, Q_3 , VDC planes, scintillator, and main quartz detectors are shown. Also illustrated are the locations of the elastic peak ray (central ray) and first inelastic state ray.

3.6 PREX-2/CREX Detector System

PREX-2 and CREX use the same HRS detector packages (same exact hardware). In each HRS, the detector package is composed of i) integrating quartz detectors (mains and auxiliary A.Ts), ii) Gas Electron Multiplier (GEM) chamber tracking system, iii) motion control systems for the quartz detectors, and iv) standard Hall A Vertical Drift Chamber (VDC) tracking system with scintillator paddles for triggering. A CAD view of the major components of the PREX-2 and CREX detectors mounted in the HRS detector hut framing is shown in Fig. 3.26. While the main focal plane detectors are primarily dedicated to the integration mode physics asymmetry measurements, they are also used in counting mode together with the standard Hall A

3.6. PREX-2/CREX DETECTOR SYSTEM

detector system (VDC and trigger scintillators) for HRS optics calibration, elastic peak quartz alignment checks, and Q^2 measurements—all of which require precision particle tracking. The focal plane detector package is detailed in Sec. 3.6.3.

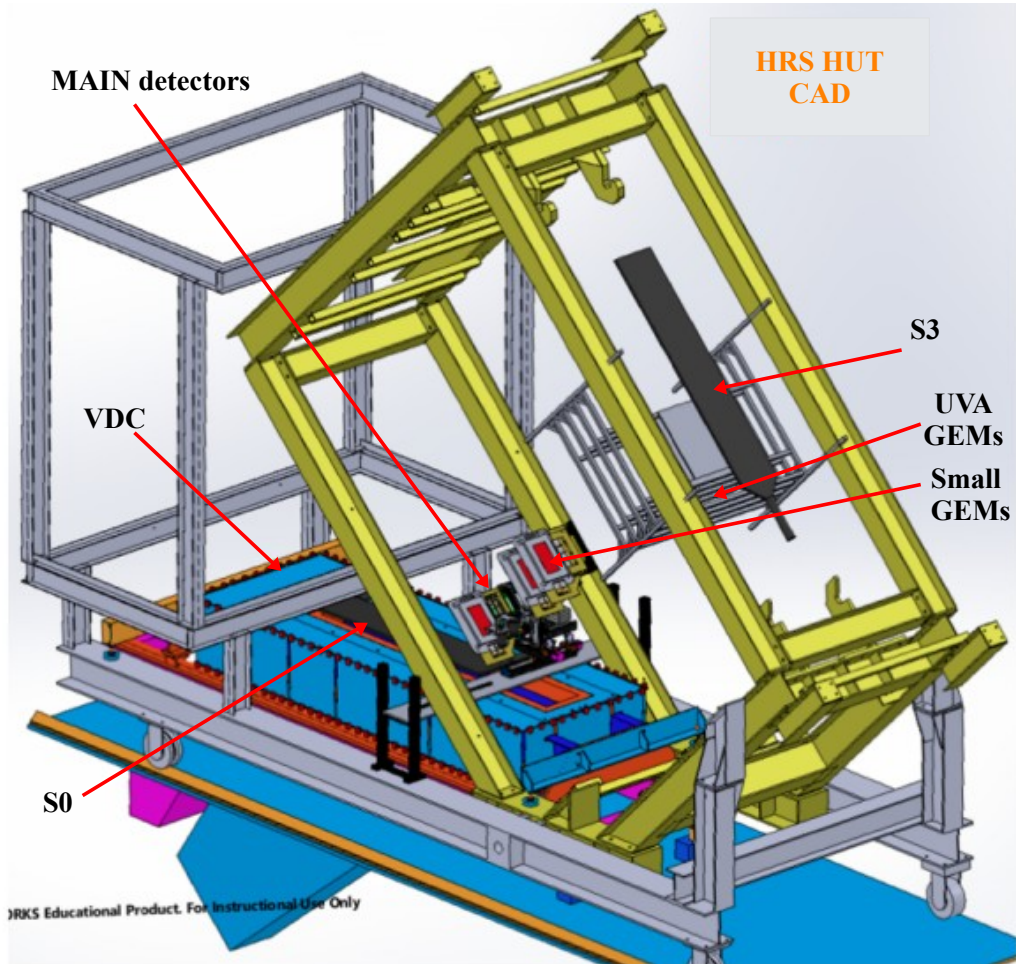


Figure 3.26: CAD view of the PREX-2 and CREX detectors shown within the I-beam framing of the HRS detector hut. Scattered electrons enter the hut from the bottom left of the figure. The relative positions of the various detectors are shown. The auxiliary detectors are missing in the drawing.

3.6.1 Vertical Drift Chamber (VDC)

Hall A has two VDCs in each HRS. PREX-2/CREX made use of VDCs for various purposes, for example, tracking the position of electrons in the focal plane, reconstructing the particle trajectories through the detectors, locating the detected

3.6. PREX-2/CREX DETECTOR SYSTEM

electron's hit position and angle on the target, Q^2 measurements, and so on. Each VDC is a $2.118\text{ m} \times 0.288\text{ m}$ active area wire chamber—made of two criss-crossing wire-planes. The planes in each HRS are named u1 and v1 for the upstream VDC and u2 and v2 for the downstream VDC. The separation between the two “u” wire planes or the two “v” wire planes is 0.335 m . Each plane has 368 sense wires which are separated regularly by 0.424 cm . The wires of two successive planes (u and v) are oriented at 90° with respect to each other as shown in Fig. 3.27. The wires make a 45° angle with respect to the \hat{x} and \hat{y} directions of the detector coordinate system (see Fig. 4.6 for the coordinate system) in such a way that the central ray of accepted particles intercepts the planes at an angle of 45° [62]. The HRS transport (and detector) coordinate systems are defined such that the origin lies approximately in the middle of the bottom or most upstream VDC in each HRS. The signal from each wire is pre-amplified and discriminated to provide a logical hit/no-hit differential ECL signal that is passed to LeCroy 1877 FastBus TDCs via sixteen conductor, twisted-pair ribbon cables. Each chamber is constantly flushed with an equal mixture of argon and ethane (50/50 % by volume). Each VDC is operated at -3500 V high voltage and uses a 3 V discriminator threshold for PREX-2 and CREX. The high voltage is supplied by remote-controllable LeCroy HV modules.

3.6.2 Scintillators

PREX-2 and CREX use two plastic scintillators in each HRS to produce event triggers while running the counting mode DAQ. The scintillators are named S0 and S3. S0 is a $185\text{ cm} \times 25\text{ cm} \times 1\text{ cm}$ organic plastic scintillator paddle with two PMTs, one on each 25 cm side as shown in Fig. 3.28 (details about its construction can be found in [53]). It is installed just above the VDC in each HRS, with its long side parallel to the VDC box, as shown in Fig. 3.26. For PREX-2, S3 is a plastic paddle

3.6. PREX-2/CREX DETECTOR SYSTEM

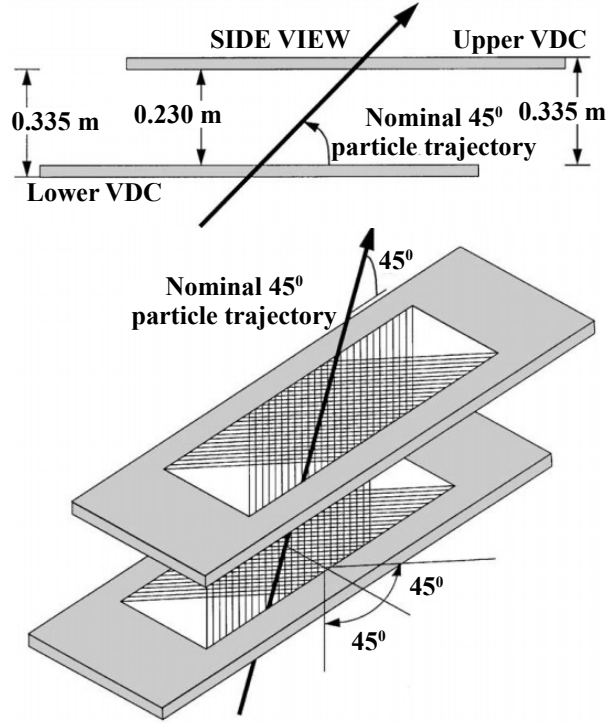


Figure 3.27: Schematic views of the Hall A VDCs (not to scale) [62].

(71 cm \times 9 cm \times 1 cm) with a single PMT on one side along its length installed downstream of all the detectors, as shown in Fig. 3.26. The scintillators are always turned off when the counting mode DAQ is not in use. During PREX-2 running we leave S0 in the acceptance region (with HV off) for a long time. This causes a “hole” or dead-spot in the plastic, at the elastic peak location in both HRS S0s, because the intercepted electron rate is too high (≈ 2.2 GHz/HRS) for too long. Figure 3.29 shows \hat{x} and \hat{y} distributions of left-HRS VDC tracks projected to the main detector plane for both a typical run with good S0 (S0 with no dead-spot in the acceptance), and another run with damaged S0. After the damage, we move S0 in both HRSs slightly downstream toward $+\hat{x}$ (in the detector coordinate system) and toward the beamline to pass the relatively small scattered flux peak through an undamaged part of the scintillator. We could have used S3 instead of S0 here, but S3 is small in size and is far downstream of the VDC (~ 3 m), so we could possibly miss VDC tracks due to de-focusing or dispersion of the scattered flux envelope. For this reason, as a backup

3.6. PREX-2/CREX DETECTOR SYSTEM

plan, we decide to redesign S3 to be larger for CREX running. S3 is redesigned by combining three PREX-2 S3 type scintillators lengthwise (with 1 cm overlap between adjacent paddles) to make a single large detector using a logical (OR) combination of the three PMT signals. A photograph of the redesigned S3 used during CREX is shown in Fig. 3.30.

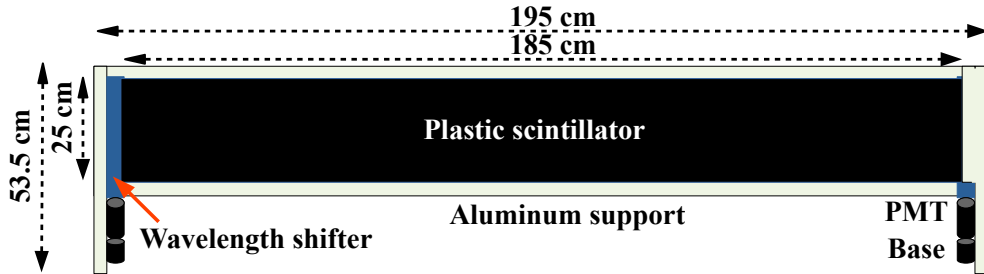


Figure 3.28: Schematic drawing of the S0 scintillator used in PREX-2 and CREX (not to scale). The whole body of the scintillator is carefully wrapped with black Kapton and electrical tape to make it light-tight.

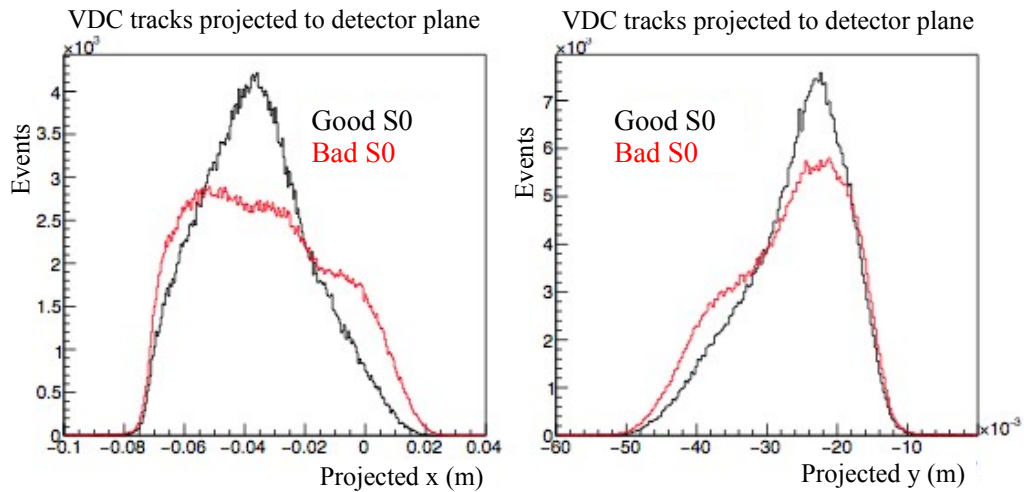


Figure 3.29: An indication of S0 damage. VDC track \hat{x} and \hat{y} distributions projected to the main detector plane. Black histograms are from a run taken with good S0, while red histograms belong to a run with damaged S0. Clear distortion is seen in the recorded spectra with bad s0.

An electron traversing the plastic causes the emission of isotropic scintillation radiation. The radiation propagates towards each 25 cm side of S0 simultaneously, and is absorbed and re-emitted by a wavelength shifter attached to the PMT window.

3.6. PREX-2/CREX DETECTOR SYSTEM



Figure 3.30: Photograph of S3 scintillator used in CREX. It is a combination of three PREX-2 style S3 scintillators. Signals from the three PMTs are combined using logical OR so that the combination works as a single body.

The gain setting (HV) of each PMT is adjusted carefully during commissioning, so we can achieve clear separation of signal from the pedestal and set the proper trigger discriminator threshold; this is accomplished with much guidance from Hall A staff scientist, Bogdan Wojtsekhowski. The discriminator threshold is calibrated such that no noise (pedestal) is accepted, and no signal is cut out. To do this the PMT signal is monitored with an oscilloscope, and the average muon counting rate⁶ is achieved in a standard cosmic setup. The PMT signals are sent to the counting DAQ electronics to provide triggering. More about the counting mode trigger setup is given in Sec. 3.9.

3.6.3 Focal Plane Detector Package

PREX-2 and CREX measure a tiny A_{PV} (ppm level) with high precision. Achieving this goal in a relatively short time requires high scattered flux rates on the main integrating detectors. This requires the focal plane detectors to have a radiation-hard design and be constructed of radiation hard materials. The main integrating detectors primarily consist of radiation-hard, optically polished, high-purity Spectrosil 2000 artificial fused-silica (quartz) as an active Čerenkov medium dry-butted (with no optical grease or glues) directly to a photosensitive device (PMT) window. The focal plane detector package in each HRS includes a tandem-mount quartz detector

⁶At sea level, the average flux is ~ 1 muon per square centimeter per minute for a horizontal detector[63].

3.6. PREX-2/CREX DETECTOR SYSTEM

system (that is, two main quartz detectors with approximately identical acceptances), three $10\text{ cm} \times 20\text{ cm}$ active area GEM tracking planes for Q^2 normalization, and two auxiliary quartz detectors (A.T background monitors) for monitoring parity-conserving (false) asymmetry backgrounds primarily from any residual transverse polarization of the electron beam. The tandem quartz detectors and the GEMs are mounted in a single frame so that they can be moved together during commissioning. A CAD render of the right-HRS focal plane detector system, with GEMs and motion system (x , y , and θ degrees of freedom) is shown in Fig. 3.31. The left-HRS detector package is approximately a mirror image of the right-HRS package.

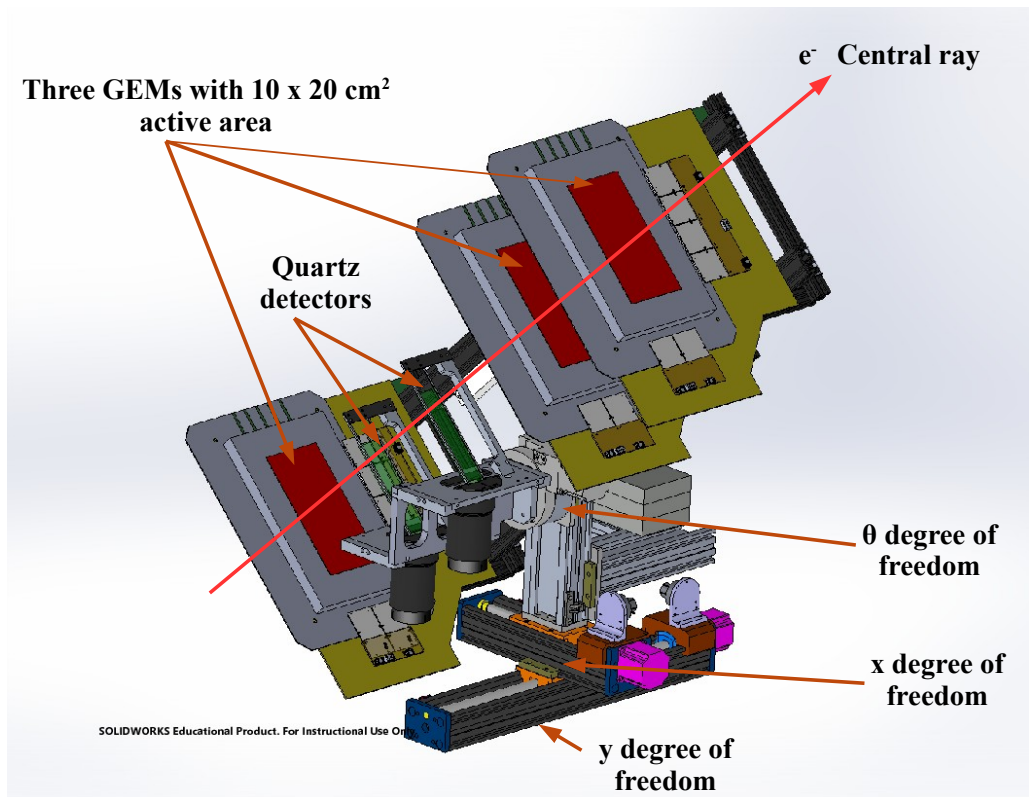


Figure 3.31: CAD render of the right-HRS PREX-2/CREX focal plane main detector package. The light-tight quartz covers have been removed for viewing the quartz tiles inside; the quartz are colored green for viewing clarity.

Each quartz is covered with a 3D printed Acrylonitrile butadiene styrene (ABS) plastic case, except for the electron interception region, which is covered with 3 mil

3.6. PREX-2/CREX DETECTOR SYSTEM

thick black polyimide Kapton film. The PMT is also kept inside a 3D printed plastic case which is fitted with a mu-metal shield to eliminate the possible influence of external magnetic fields on the PMT. We take great care to ensure that each quartz detector has a light-tight seal and that it is maintained. Figure 3.32 shows a photograph of a complete focal plane detector package (including the quartz detectors with their light-tight shells); also shown are the auxiliary A-T detectors and the larger UVa GEM array. Furthermore, the focal plane detector system is installed in each HRS such that the upstream quartz detector is 1.3 m downstream of the upstream VDC plane. Each of the two auxiliary A-T detectors in each HRS is installed about 2 m downstream of the upstream VDC plane, and their positions in transport \hat{x} and \hat{y} are controlled independently with dual, 2-axis motion systems in each HRS. The focal plane detector packages for the left- and right-HRS are designed and constructed by the ISU parity group. Further details of the design and operation of each of the detectors are given below.

Each quartz detector uses a Hamamatsu R7723Q 2-inch PMT as a photodetector. The detector is oriented in such a way that the incoming scattered electrons have \sim normal incidence on the quartz face; the quartz bar (or tile) is effectively oriented at 45° relative to the horizontal VDC plane. This is different than for PREX-1—where the quartz was parallel to the VDC plane such that electrons intercepted the quartz face at 45° . A comparison between the PREX-1 and PREX-2/CREX detector designs, illustrating the modification to the quartz (and PMT) orientation, is shown in Fig. 3.33. The new design is less sensitive to extra noise from delta-ray⁷ production within the quartz. This modification allows us to effectively capture all sides of the Čerenkov light cone, nearly doubling the detector’s light yield, which in turn improves the $\frac{RMS}{Mean}$ in the detected signal by $\sim\sqrt{2}$. Another design modification is related to the

⁷Secondary electrons created from hard scattering interactions in the quartz. These electrons are relativistic and also create Čerenkov light which gives more fluctuation in the detector response and thus worsens its resolution.

3.6. PREX-2/CREX DETECTOR SYSTEM

use of light guides. PREX-1 used an air-core, aluminum-mirror channel light guide to direct Čerenkov photons from quartz to PMT, while the PREX-2/CREX design uses total internal reflection (TIR) inside the quartz as the light guide.

Each individual quartz detector uses a single piece of quartz that is 5 mm thick, 3.5 cm wide, and 16 cm long. These are fairly small pieces of quartz whose size has been carefully chosen to be no larger than needed. Note for comparison that PREX-1 used 6 mm (10 mm) thick, 3.5 cm wide, and 14 cm long quartz pieces in the upstream (downstream) positions of the main tandem detectors. During commissioning, the detectors are precisely positioned in the focal plane such that only elastically scattered events are intercepted. Details about the detector commissioning are given in Sec. 4.1. The focal plane detector incorporates a tandem design in each HRS in order to provide independent redundant A_{PV} measurements that can be used to cross-check each other, or as a backup if one detector fails. In order to perform more frequent alignment checks, to make sure we are not accepting too much inelastics, the downstream detectors are always left in counting mode configuration during CREX. This way we can perform the alignment checks without requiring hall access. This greatly reduces the time needed for the checks which are invasive to production running. Detailed studies of expected flux rates and detector photo-electron yields, through simulations and several beam-tests at MAMI and SLAC, have been carried-out before the experiments. PMT gain measurements as well as precision non-linearity characterizations have also been done to help minimize the systematic uncertainties associated with the detector's operation at the very high ≈ 2.2 GHz rates of PREX-2.

Čerenkov Radiation and the Quartz

Čerenkov radiation is observed when a charged particle, like an electron, traverses a medium with a velocity faster than the phase velocity of light in that medium. This

3.6. PREX-2/CREX DETECTOR SYSTEM

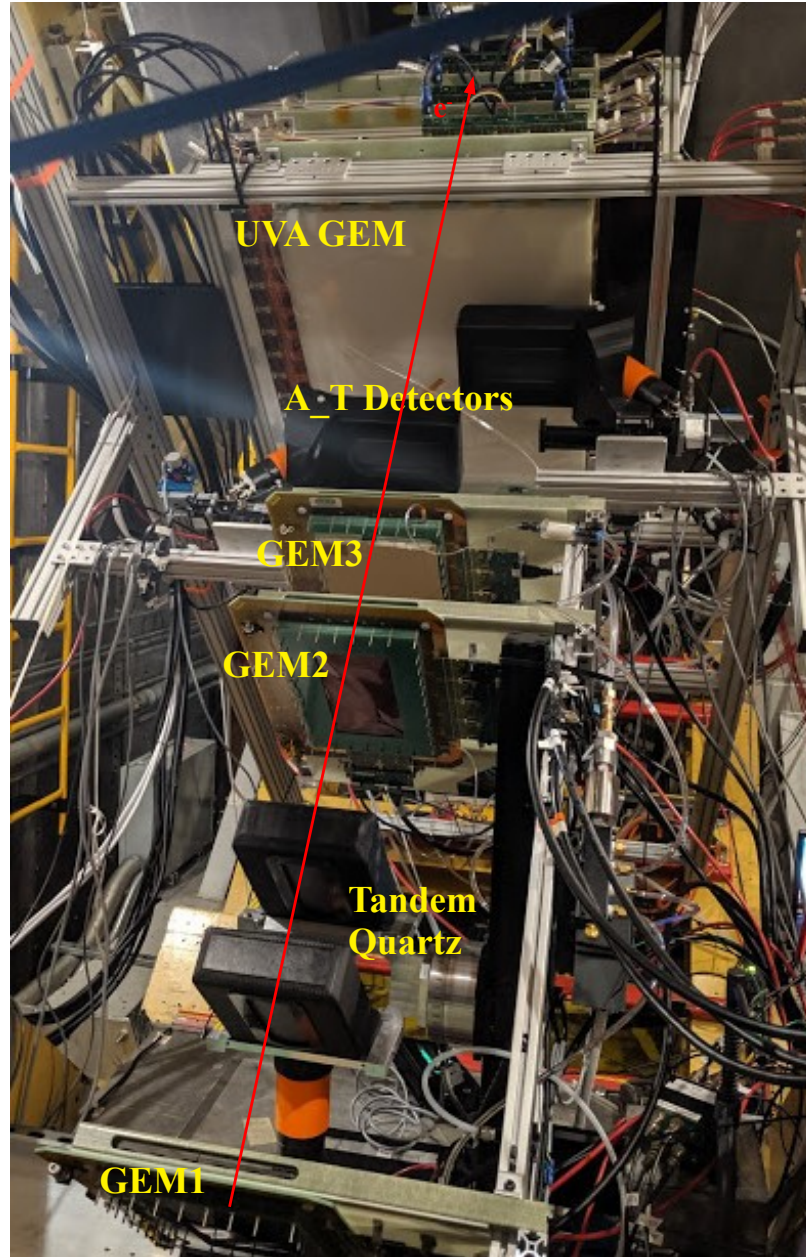


Figure 3.32: Photograph of the left-HRS focal plane detector package. Three small ($10 \times 20 \text{ cm}^2$) active area GEM chambers are mounted in the same frame with the tandem (main) detectors. Two auxiliary detectors (A_T background monitors) are shown downstream of this frame. There are another three larger ($50 \times 60 \text{ cm}^2$ active area) GEMs from the University of Virginia (UVa). The quartz and PMT in each detector are enclosed inside a light-tight ABS plastic 3D printed shell and Kapton film.

phenomenon is an optical cousin of a sonic boom, and the photons are emitted as a result of successive excitation and de-excitation of the molecules in the electrically

3.6. PREX-2/CREX DETECTOR SYSTEM

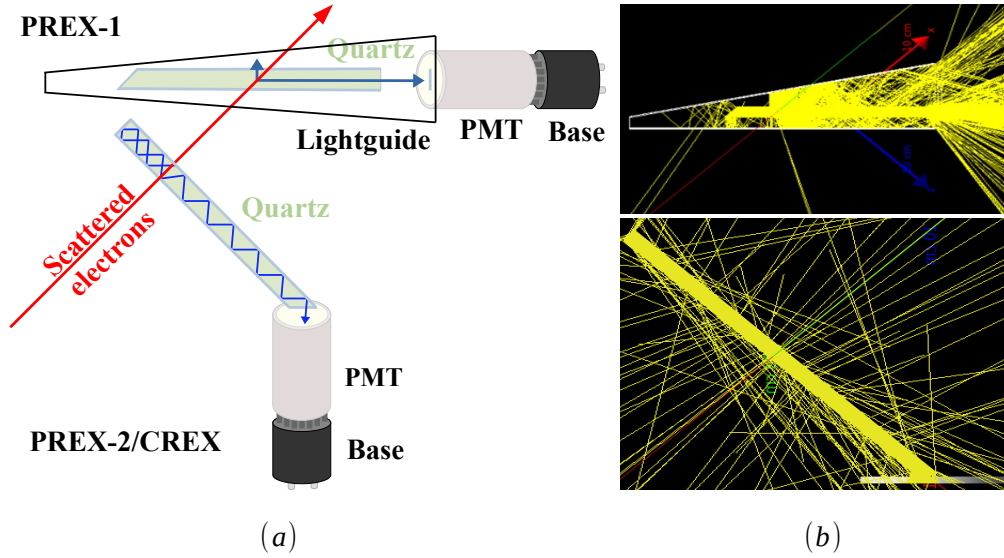


Figure 3.33: (a) Main detector quartz and PMT orientation change from PREX-1 to PREX-2/CREX. (b) G4 visualizations of a single event (electron traversing quartz) for PREX-1 (top image) and for PREX-2/CREX quartz (bottom image). The PREX-2/CREX design gives nearly double the light yield and improved resolution. Yellow rays are optical (UV and visible) photons, electrons are red, and gamma rays green.

polarizable medium. A schematic of a Čerenkov cone is given in Fig. 3.34. For an electron with velocity v_e , traversing a medium with refractive index n , the emission angle of the Čerenkov light is given by $\cos \theta = \frac{1}{n\beta}$, where $\beta = \frac{v_e}{c}$. The minimum electron velocity required to induce the Čerenkov phenomenon is given by $\beta = \frac{v_e}{c} > \frac{1}{n}$ (with $\theta = 0^\circ$). This corresponds to an electron energy threshold of $E_e^{\text{th}} = m_0c^2 \frac{n}{\sqrt{n^2-1}}$, where m_0c^2 is the rest energy of the electron.

As mentioned earlier, the PREX-2 and CREX focal plane detectors use Spectrosil 2000 artificial fused-silica (quartz) as the Čerenkov medium or radiator. Each surface of the quartz tile is cut extremely parallel to its opposite surface, and perpendicular to adjacent surfaces, except for one of the short ends (see Table 3.3 for a list of quartz factory specifications). This end is cut and polished at a 45° angle and is referred to as the bevel. The bevel feature of the tile is where, theoretically for the PREX-2/CREX design, all the Čerenkov light exits the quartz and immediately impinges on the PMT window. For the PREX-1 design, the situation was quite different. Figure

3.6. PREX-2/CREX DETECTOR SYSTEM

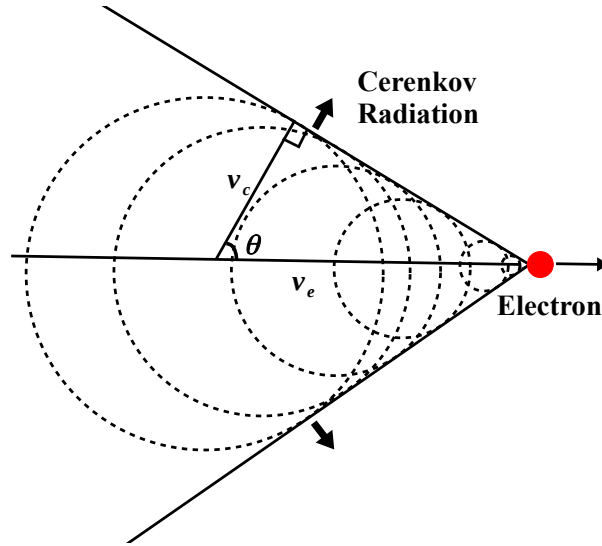


Figure 3.34: Schematic representation of a Čerenkov cone. At the velocity of JLab electrons, that is, very close to the speed of light ($\beta \approx 0.99999$), the emission angle of the Čerenkov radiation, θ , is approximately 46.6° .

3.33(a) shows a simple drawing contrasting the design modifications from PREX-1 to PREX-2/CREX. Figure 3.33(b) gives G4 event visualizations corresponding to the two designs. Notice the relative quartz orientation with respect to both the incoming scattered electron and the PMT have changed between the two designs. Also, the quartz tiles are flipped—so the bevel was facing away from the PMT for PREX-1. However, given the different orientation of quartz and scattered electron for the PREX-1 design, \sim half the light-cone travels toward the PMT and exits the non-beveled end of the quartz, as shown in the top visualization of Fig. 3.33(b); the other half of the Čerenkov cone is lost out the downstream face (and other faces) where its incident angle is less than critical for TIR. The light guide for PREX-1 was employed to recover some of these lost photons. Note that quartz wrappings are not used for PREX-1 or PREX-2/CREX because, while these were found to increase light and PE yields, they cause the resolution to get worse [64]. The stray optical photons (yellow rays) exiting the quartz randomly come from the non-perfect polish that is part of the simulation. Each quartz piece is optically polished at the 25 Angstrom level, and its stringent geometric properties are chosen to give the best total internal

3.6. PREX-2/CREX DETECTOR SYSTEM

reflection for the Čerenkov light. Roughly 8 cm of the quartz length is intercepted by the elastic flux envelope during PREX-2, while the interception is about 5 cm long for CREX. The remaining portion of the quartz length acts as a light guide to direct the Čerenkov photons to the PMT photocathode. Details of this are given in Sec. 4.1. As mentioned, PREX-2/CREX quartz is only 5 mm thick while PREX-1 quartz was 6 mm and 10 mm thick. For a given design, the thicker quartz produces more light yield resulting in more photoelectrons (PEs), but it also introduces extra noise in the detected signal due to increased delta-ray production within the quartz. For this reason, the downstream tandem detectors have larger noise (or integrated asymmetry widths) than the upstream ones; they are picking up extra delta-rays produced in the upstream quartz. The overall effect of thicker quartz is a larger $\frac{RMS}{Mean}$ in the PE distribution, due to the larger Landau tail (or bright light tail) in the pulse height distribution, which causes increased excess noise beyond pure counting statistics in the measured asymmetry. The effective error or statistical width of A_{PV} is inflated by this excess noise according to

$$\sigma_{A_{PV}} = \frac{\sigma_{meas}}{\sqrt{1 + \left(\frac{RMS}{Mean}\right)^2}}, \quad (3.7)$$

where σ_{meas} is the width of the measured asymmetry. $\sigma_{A_{PV}}$ is the pure statistical width in A_{PV} related only to counting statistics (N) by

$$\sigma_{A_{PV}} = \frac{1}{\sqrt{N}}, \quad (3.8)$$

where N is the number of particles detected per helicity multiplet pattern (see Sec. 3.10 for the definition of helicity multiplet pattern). If t_w is the time duration of a helicity window and n is the number of windows used to calculate an asymmetry (or the number of windows in a helicity multiplet pattern), the detected rate, R , is

3.6. PREX-2/CREX DETECTOR SYSTEM

given by

$$R = \frac{N}{n \times t_w}, \quad (3.9)$$

which in terms of σ_{APV} is given by

$$R = \frac{1}{n \times t_w \times (\sigma_{APV})^2}. \quad (3.10)$$

More information about the sampling techniques of the integration (physics) mode DAQ and details of the helicity windows are given in Sec. 3.10.

Specification	Quantity
Length	160 ± 0.127 mm
Width	35 ± 0.127 mm
Thickness	5.0 ± 0.127 mm
Ok scratch/dig	20 angstroms or better
Clear aperture	80 %
45° polished angles	± 30 arc min
Parallelism	3 arc min (primary faces)
Perp	15 arc min
Polished bevel	0.5 REF on all edges exception to print

Table 3.3: Factory specifications for the quartz used in PREX-2/CREX detectors. The quartz manufacturer is Heraeus.

PMT Selection and Operation

A PMT is a photosensitive device that converts optical (UV/Visible) photons into an electronic signal (a current pulse). When photons of a given wavelength, λ , impinge on the PMT cathode, electrons get emitted via photoelectric emission. The probability for any incident photon of a given wavelength to eject a photoelectron from the cathode is termed the quantum efficiency (QE) and is given by [65]

3.6. PREX-2/CREX DETECTOR SYSTEM

$$QE(\nu) = (1 - R) \times \frac{P_\nu}{k} \times \frac{kL}{1 + kL} \times P_s, \quad (3.11)$$

where ν is the photon frequency, R is the cathode's reflectivity, P_ν is the probability that the absorbed light excites electrons to a level greater than the vacuum level, k is the absorption coefficient of photons, L is the mean escape length of excited electrons, and P_s is the probability that electrons reaching the photocathode surface release into the vacuum. Hamamatsu R7723Q PMTs are used for the focal plane (main and auxiliary) detectors. The PMTs consist of a bialkali photocathode and 8 electron-multiplying stages (dynodes) housed in borosilicate glass under vacuum. The cathode window is made of artificial fused silica to allow UV light transmission to the cathode. This greatly increases PE yields since most of the Čerenkov light is in the UV spectrum. The secondary emission ratio of each dynode, the collection efficiency of each dynode (and anode), the overall gain, and the linearity of the PMT greatly depend on the supplied high voltage and the design of the voltage divider. A custom voltage divider is used with ratios of relative potential difference between the cathode, successive eight dynodes, and anode of 6:1:2:1:1:1:1:2:1. This divider is designed to provide better linearity⁸. In short, the gain of a PMT depends on the dynode multiplicity (μ , which is the number of secondary electrons emitted per primary electron incident on a dynode) and the number of dynodes (n), and is given by μ^n . All the PMTs used during the experiments have well characterized gain curves [66] and non-linearity (refer to Sec. 3.6.4 for details of the PMT non-linearity characterization).

For production running (at high beam current), the gain of each PMT is set by adjusting the high voltage (HV) supply at the beginning of the experiments. The current-based signal coming directly from the PMT anode is converted into a voltage

⁸The larger voltage drop between the cathode and first dynode increases (and stabilizes) the collection efficiency of the most important first stage and hence improves linearity.

3.6. PREX-2/CREX DETECTOR SYSTEM

using a custom “I-to-V” pre-amplifier, and the voltage signal from the pre-amplifier is then sent to a custom VME 6U ADC (vQ_{wk} ADC). The wiring diagram for the main quartz detectors is similar to the one for the SAM system, shown in Fig. 3.42, except the “fat Twinax” cable is replaced with a BNC cable, and no converter boxes are used. The main detectors use 210 k Ω (SNS) and 2 M Ω (MAIN) pre-amplifier gain settings for PREX-2 and CREX, respectively. The pre-amplifiers were designed by TRIUMF, originally for the Qweak experiment, as were the vQ_{wk} ADCs.

The PREX-2 charge normalized yield from the tandem main detectors as a function of time is given in Fig. 3.35. It shows the yields from slug 1 to slug 96⁹. The PREX-2 slug number starts at 1 and ends at 96. The two large discontinuous yield jumps early in the experiment, high-lighted in Fig. 3.35, occur because the left- and right-HRS detectors are initially installed with 10 mm thick quartz, but are replaced with 5 mm thick quartz near run 3600 (before slug 12) for the left-HRS, and near run 3750 (before slug 21) for the right-HRS. When using the thicker quartz, the PMTs are operated at different (generally lower) gain/HV settings which causes the bigger yield changes that are not target-failure related. Starting at slug 21, no detector configuration is changed until the end of PREX-2. It is clear from these plots that the detector yields degrade over time irrespective of the target change. For the time scale shown in the plot, the left-HRS detector’s yield degrades $\sim 20\%$ while the right-HRS detectors see a $\sim 30\%$ yield reduction. It is important to investigate the cause of this decay. The only possible explanations are 1) excessive radiation damage to the quartz can cause internal light transmission losses and reduce the overall Čerenkov light and PE yield over time, 2) a change or degradation in the PMTs photocathode characteristics, resulting in a gradual decrease in its QE, or 3) the gain of the PMT dynodes degrades over time causing an overall decrease in PMT gain and thus we observe lowering yields over time.

⁹A slug is a collection of runs within a given IHWP and Wien state for about one shift (8 hours)

3.6. PREX-2/CREX DETECTOR SYSTEM

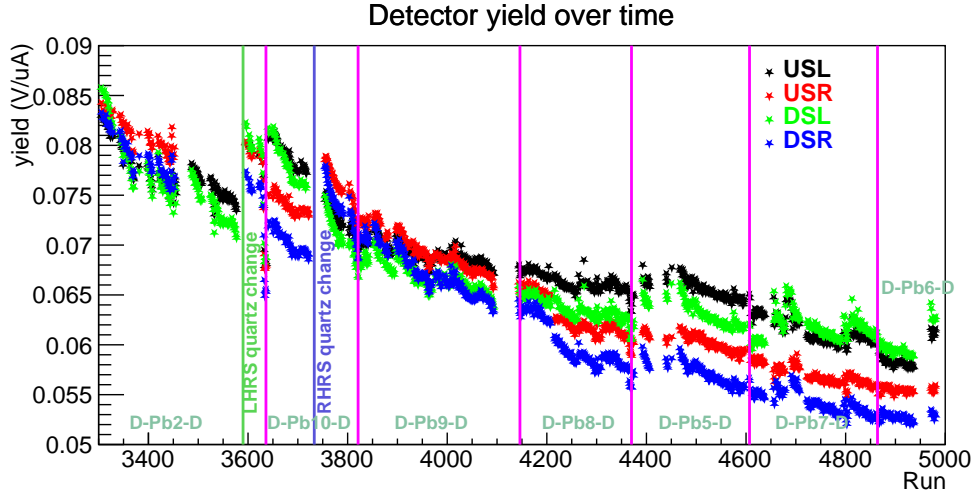


Figure 3.35: PREX-2 detector yields over time—approximately two months total time scale. This is equivalent to ~ 17 days of continuous running at $70 \mu\text{A}$ beam current, which is ~ 43 million octets. Plot shows the charge-normalized main detector yields versus run number. These are the voltage signals (yields) of the detectors normalized to beam intensity. Each magenta colored vertical line marks the run when a target is changed (typically due to failure). USL and DSL are the upstream and downstream main detectors in the left-HRS tandem detector, while USR and DSR are those detectors in the right-HRS. Further details are given in the text.

It has been shown in [67] that the PREX-2 quartz should have at most ~ 0.6 % light transmission loss due to the radiation dose accumulated by the end of the experiment. Therefore this does not explain the observation and rules out the first possibility. After the completion of PREX-2, we re-calibrate the light level (LL, see the footnote of Sec. 3.6.4 for the details of LL) sensed by each PMT cathode using a calibrated amount of 405 nm LED light. The post-experiment calibrations are done with the same exact apparatus as the pre-experiment calibrations. The two results are compared, and no change in the QE of any PMT is observed. This rules out the second option—degradation in the PMT photocathode. As another check, we measure the anode current¹⁰ (I_a) at 10 nA LL setting, and at a specific HV setting, and compare it with the anode currents at the same settings prior to PREX-2. The comparison is shown in Table 3.4. The reduction in I_a we observe from this comparison is in the

worth of “good” data. See Sec. 4.2 for the definition of good data.

¹⁰Anode current is the PMT output signal that depends on gain and cathode current (light level).

3.6. PREX-2/CREX DETECTOR SYSTEM

range of yield degradation we see in PREX-2 (Fig. 3.35). For the PMT used in the DSL detector, we see $\approx 7\%$ larger decrease in anode current as compared to the yield degradation from Fig. 3.35; this is the largest discrepancy in the test results; the other three PMTs are in agreement with Fig. 3.35 at the couple percent level. A potential reason for the discrepancy is that the DSL PMT was used for a much longer time than other PMTs during the non-linearity bench tests. So it has been exposed to more 405 nm light, and responds with a steeper degradation curve to the bench test compared to the actual Čerenkov light. In summary, the yield reduction observed over the experiment is likely from a reduction in the dynode’s secondary emission (multiplicity) leading to a decrease in gain (PMT aging due to use). Furthermore, the right-HRS PMTs experience a larger reduction in yield because the PMTs used there are comparatively older PMTs from PREX-1.

Detector	PMT	HV	I_a before	I_a after	Difference
USL	ZK5370	-600 V	20.05 μA	16.27 μA	-18.9 %
USR	ZK5401	-680 V	27.92 μA	19.05 μA	-31.8 %
DSL	ZK5407	-690 V	26.60 μA	19.47 μA	-26.8 %
DSR	ZK4033	-720 V	28.41 μA	20.40 μA	-28.2 %

Table 3.4: Anode current (I_a) comparison of PMTs used in PREX-2 detectors before and after the experiment. Results indicate an average degradation in PMT gain of around 25 %, consistent with Fig. 3.35.

Gas Electron Multipliers (GEMs)

The Hall A standard HRS tracking systems, VDCs, are used extensively for spectrometer optics reconstruction and Q^2 measurements, but their efficiency can potentially sag if the rate density is too high (as potentially during PREX-2) causing the measured Q^2 distributions to get distorted (or sag) in the peak rate region. To prevent the distortion, the VDCs are operated with rate densities at or below (~ 10 kHz/cm²). To achieve this requires very low beam currents, especially during PREX-2. As discussed

3.6. PREX-2/CREX DETECTOR SYSTEM

in Sec. 3.4.3, for PREX-2, the stripline BPMs do not work at the needed low currents. For this reason, the cavity BPMs are installed to monitor the beam positions at the low currents, and the high-rate capable Gas Electron Multiplier (GEM) chamber tracking system is installed within each HRS detector hut as a backup and also as a check of the VDC distributions. The GEMs can handle high rates (~ 100 MHz/cm²). However, this is not a problem for CREX because the CREX rate is low enough to satisfy the operational limits of the VDCs and stripline BPMs. The ISU parity group takes the lead in developing the GEM tracking system for the PREX-2 experiment.

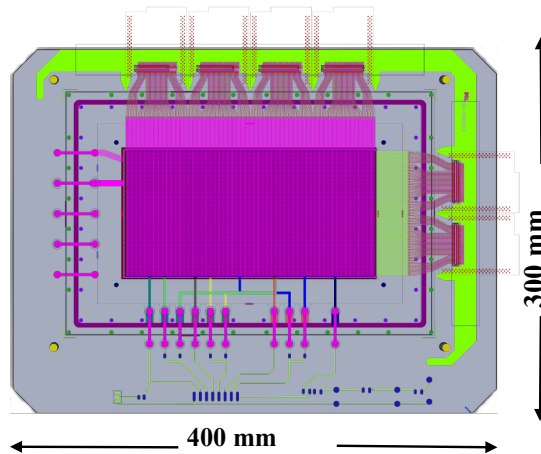


Figure 3.36: CAD drawing of a PREX-2 GEM chamber. The dark magenta rectangle represents the 10×20 cm² active area of the chamber.

Figure 3.36 shows a single 10×20 cm² GEM chamber schematic. One GEM is mounted just upstream of the tandem detector and two are mounted just downstream, as shown in Figures 3.31 and 3.32. These GEMs translate in \hat{x} and \hat{y} , along with the tandem detector, using the motion system described in the following subsection, but do not have a rotational degree of freedom like the tandem detector. Each chamber consists of a cathode (or drift) layer followed by three GEM foils and finally a readout plane. All the layers are 10×20 cm² and with various thicknesses. The material budget for each GEM, including all layers as well as glass epoxies and closing skin (125 μ m Kapton), is $\sim 0.64 X_0$. At one end of the GEM is the drift electrode, which is

3.6. PREX-2/CREX DETECTOR SYSTEM

a 5 μm copper layer on 50 μm Kapton; the Cu faces the inside of the chamber. On the opposite end of the chamber is the readout layer (again made of Cu on Kapton) with 400 μm pitch with XY (90° 2-dimensional) stereo angle. The spacing between the drift layer and first foil is 3 mm, while the foils and readout planes are each separated by 2 mm; this is a standard CERN GEM configuration with 3/2/2/2 spacing. The GEM foils are perforated every 140 μm with conical or hourglass-shaped holes with 50 μm inner and 70 μm outer diameters (also a CERN standard). The foils are made of a 50 μm layer of electrically insulating Kapton with 5 μm layers of copper coating on each side. The chambers are filled with a mixture of argon (Ar) and carbon dioxide (CO₂), at a nominal 3:1 ratio. During operation, the top and bottom of each foil are set to a ≈ 400 V potential difference. There are also potential differences (or accelerating voltages) between the drift and first GEM foil, as well as in between each foil. When an electron zips through the chamber, it produces a trail of ionized electrons from Ar gas (quenched by the CO₂), as well as strikes the thin, but dense layers of copper. The electrons released from the copper drift electrode dominate the cascade of electrons that get successively amplified through the three GEM foil stages. After the last foil, the cascading avalanche of electrons strike the readout plane. Depending on the precise details of the GEM's voltage divider circuit and gas mixture, each incident electron can create up to a few times 10^4 electrons that strike the readout plane in a "cluster." This system is capable of providing sub 100 μm position resolution on the cluster centroids at very high rate densities and with little dead time.

Each HRS uses three GEM chambers that make up the tracking system. Since the chambers are custom designed and purchased from CERN, the largest R&D effort for the project has been how to readout the GEM signal and acquire it by a CODA (JLab) DAQ system. The PREX-2 GEM readout scheme is based on the INFN/UVa SBS rear-tracker system. It uses custom VME Multi Purpose Digitizer (MPD) cards

3.6. PREX-2/CREX DETECTOR SYSTEM

for the ADC. The MPD is a 16 channel, 12-bit, 40 - 100 MHz voltage sampling digitizer. The MPDs are connected with HDMI signal and control cables to ISU-designed printed circuit boards (PCBs), referred to as “back-planes”, which connect directly to APV25 front-end cards that are connected directly to the GEM readout strips via 128 pin panasonic connectors. The APV (amplifier) cards were designed at CERN for use in the CMS experiment at the LHC and are made of radiation-hard components. Each APV card services 125 adjacent strips; each $10 \times 20 \text{ cm}^2$ GEM uses 2 by 4 APV cards, respectively, as shown in Fig. 3.36. The signals from the groups of APVs on each GEM are bused together using the back-plane PCBs and passed through a single HDMI cable to the MPD. Each ADC channel is responsible for one APV card (125 strips).

Auxiliary Detectors (Background Monitors)

In addition to the main quartz detectors for the A_{PV} measurement, each HRS consists of two auxiliary quartz detectors for monitoring any parity-conserving asymmetry backgrounds from residual transverse polarization of the electron beam or any other possible false asymmetry backgrounds. These detectors or monitors have the same exact design and components as the main detectors, and are installed approximately 2 m downstream of the Hall A detector (HRS) coordinate system origin. The position of these detectors relative to the main focal plane detectors is shown in Fig. 3.32. The quartz in the auxiliary detectors is oriented at 90° relative to the main detector quartz, such that the scattered flux intercepts its width (3.5 cm) along the dispersive \hat{x} -direction (of the transport coordinate system—refer to Fig. 4.6). The scattered flux rate integrated by each of the auxiliary detectors is roughly one fifth of the main detector rate. Therefore, the PMTs are operated at gain settings approximately five times higher than the main detector PMTs. The signal from each PMT is sent to the DAQ via an I-to-V pre-amplifier, just like the main detector signal, and each uses

3.6. PREX-2/CREX DETECTOR SYSTEM

a $0.3 \text{ M}\Omega$ (KDPA) and $4 \text{ M}\Omega$ (MAIN) I-to-V (pre-amplifier) gain for PREX-2 and CREX, respectively.

Detector Motion Control System

The main components of the detector motion control system are the Velmex BiSlides and rotary stages. These provide \hat{x} , \hat{y} , and $\hat{\theta}$ motion, have position transducers and optical encoders for position readback validation, and use a LabJack USB ADC for the encoder readouts and a Raspberry Pi connected to ethernet for remote computer control. The Pi runs a custom Qt based control GUI written by ISU undergraduates, and incorporates pi-cameras with live-streaming views of the main and auxiliary detectors. The tandem-mount (main) detectors and GEMs are installed in a single extruded aluminum frame, so they can be moved together (in HRS detector coordinate system \hat{x} and \hat{y}), while each auxiliary detector is controlled independently and moves in \hat{x} and \hat{y} transport. The detectors are positioned remotely using the Qt based GUI. The main detectors can be moved up to 5 inches along the \hat{x} direction of the HRS detector coordinate system (see Fig. 4.6 for detector and transport coordinate systems) and 15 inches along the transverse \hat{y} direction. They can also be rotated using the rotatory stage to tweak (make $\approx 90^\circ$) the angle between the intercepted central ray and the quartz plane. The auxiliary detectors are installed with 2 inches of travel along \hat{x} and 4 inches along \hat{y} directions in the HRS detector coordinate system. The position transducer signals are digitized and fed into the control software to give user feedback of all four detector positions.

3.6.4 Detector Non-linearity

Detector non-linearity is an important systematic error and must be well understood before the start of any precision parity experiment. The ISU parity group is respon-

3.6. PREX-2/CREX DETECTOR SYSTEM

sible for this task for PREX-2 and CREX. The main contribution to the detector non-linearity error is the PMT non-linearity—which is essentially a non-linear gain (output) response of the PMT over a given range of input light intensity. Due to the high flux rate in PREX-2 during integration mode, the PMTs need to be operated at a lower gain (HV) setting than for a typical PMT application; at lower gains, the PMT signal output can behave non-linearly with respect to either the light received by the photocathode and/or the dynode amplification stages. Ideally, it is desired to find a sweet spot for a given PMT, where it can produce anode current as a highly linear function of its cathode current and gain. In practice, however, most of the electronics that we use in our labs suffer from some degree of non-linearity.

For a PMT, the non-linearity is a measure of a systematic balance between the divider *supply* current, which flows through the voltage divider circuit, and the amount of *signal* current flowing along the array of dynodes due to the continuous flow of a cascading shower of amplified PEs. The working principle of the PMTs used in PREX-2/CREX, and the design of their modified bases for improved linearity, are given in Sec. 3.6.3. At the end of PREX-2, we see 20 - 30 % degradation in the PMT anode current as mentioned in Sec. 3.6.3. For this reason, we repeat the linearity bench-tests for the main detector PMTs after completing PREX-2 and before starting CREX. The idea behind the bench-test system is to produce a PMT signal asymmetry using two LEDs, and then see how well the PMT measures that same asymmetry over a broad range of incident light intensities for different settings of LED light and PMT gain. Details of the non-linearity characterization apparatus, procedures, and the results are presented in this section.

3.6. PREX-2/CREX DETECTOR SYSTEM

Bench-test Setup

Prior to the experiments, we performed a complete characterization of the non-linearity of our PMTs in order to determine their optimal HV settings for the anticipated incident light levels (LLs)¹¹ of the experiments. Where,

$$\text{LL (nA)} = N_{PE} \times \text{Rate (GHz)} \times 1.6 \times 10^{-19} \text{ (C)}. \quad (3.12)$$

As given in Chapter 4, the Rate_{PREX-2} is approximately 2.2 GHz, Rate_{CREX} is approximately 28 MHz, and N_{PE} is ≈ 28 . This calculation gives $LL_{PREX-2} \approx 10$ nA and $LL_{CREX} \approx 0.13$ nA. During the non-linearity bench-testing, the LL on each PMT is individually calibrated by operating the PMT in unity gain mode. This is accomplished with a special unity gain voltage divider which directs the ejected PEs directly to the anode, and the current is then measured with a Keithley pico-ammeter.

The bench-tests use two LEDs: one flashing dimly at a specific frequency and the other relatively bright and constantly glowing; all parameters are independently adjustable for the two LEDs. This arrangement creates a small constant LED asymmetry which is measured by the PMT over a range of incident intensities. The constant LED is powered through a HAPPEX timer board 16 bit DAC (digital to analog converter) and is responsible for establishing the LL of the test. Use of the DAC for setting the LED voltage provides highly reproducible LLs; the LED driver circuits use only a simple 100 Ω resistor. These tests use an integrating mode DAQ with identical hardware as used during the experiment. The DAQ's "Trigger" and "Gate" timing signals are generated and controlled through the HAPPEX timer board. A Struck SIS3610 I/O VME card is used for triggering. The intensity of the flashing LED

¹¹The light level is a measure of the PE current produced by the PMT photocathode. Typically measured in nA, the LL results from the flow of electrons emitted via photoelectric emission. It not only depends on the number of photons (and their wavelength) reaching the photocathode, but also on the unique cathode properties of an individual PMT.

3.6. PREX-2/CREX DETECTOR SYSTEM

and the DAQ frequency are controlled using a synchronized square wave from a two-channel RIGOL 100 MHz arbitrary function generator. For most of the bench tests, the LED is flashed at 120 Hz, and DAQ integrates at 240 Hz. Note that the PMT's non-linearity performance is independent of the LED flash frequency. The synchronized timing of the DAQ/LED signals, trigger, and gate, as sketched in Fig. 3.37, are constantly monitored using an oscilloscope. Once the flashing LED changes its on/off state, the trigger signal, for reading out the previous window, occurs after a delay of $t_1 = 45 \mu\text{s}$. The gate signal, used for initiating the next integration window, occurs after $t_{\text{settle}} = t_1 + t_2 = 140 \mu\text{s}$ from the LED change. $t_3 = 5 \mu\text{s}$ is the logic pulse width and $t_4 = 2.5 \mu\text{s} + 2 \mu\text{s} \times (vQ_{wk}\text{-}GATE_DELAY)$, where $2.5 \mu\text{s}$ is an intrinsic delay related to the ADC hardware design, $2 \mu\text{s}$ is the ADC's sampling rate (i.e. the ADC samples voltages at 500 kHz), and $vQ_{wk}\text{-}GATE_DELAY$ is the user-defined delay which is the number of 500 kHz clock cycles the DAQ waits before starting to sample. For example, for our 240 Hz integration window, we use $vQ_{wk}\text{-}GATE_DELAY = 100$ giving $t_4 = 202.5 \mu\text{s}$. The DAQ collects 400 samples per block, and each integration window has four blocks giving 1600 total samples in $t_{\text{meas}} = 2 \mu\text{s} \times 1600 = 3200 \mu\text{s}$. At 240 Hz DAQ rate, the ADC stops sampling $t_5 = \frac{10^6}{240} - 45 - 95 - 5 - 202.5 - 3200 = 619.17 \mu\text{s}$ before the flashing LED changes its state.

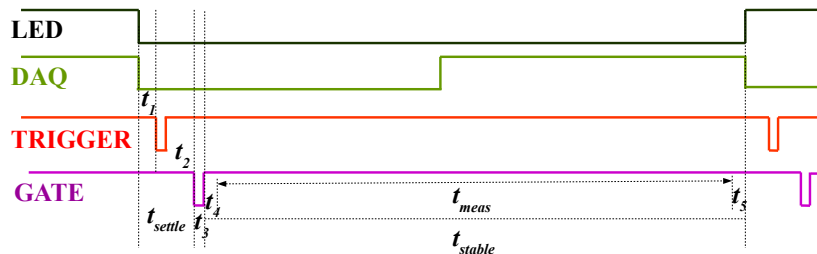


Figure 3.37: Timing diagram for PMT non-linearity bench tests. The ADC samples the data only during the t_{meas} time window. See text for details.

The light from the LEDs is collimated, passed through an electronic shutter,

3.6. PREX-2/CREX DETECTOR SYSTEM

a computer-controlled filter wheel with eight transmission settings, then through a diffuser, and finally to the PMT's photocathode. The different transmission settings are provided by neutral density filters with 1 %, 10 %, 25 %, 40 %, 50 %, 63 %, 79 %, and 100 % transmission and are randomly arranged around the wheel. The whole system is housed inside a light-tight dark box and is shown in Fig. 3.38. The response of the PMT is converted to a voltage signal using a pre-amplifier (as usual) and sent to an integrating DAQ system that uses a vQ_{wk} ADC. For each run, the filter wheel is rotated through 20 cycles; data is collected for 10 seconds at each filter position. Also, just before the filter changes to the next position, an automated electronic shutter (the shutter is installed just after the LEDs, when turned off it blocks the light from LEDs before reaching the PMT) is turned off for 2 seconds and turned back on once the filter moves to the new position. This allows for frequent monitoring of the ADC pedestal. After every complete cycle, the shutter is kept off for 5 seconds. The filter wheel and shutter are controlled using a Raspberry Pi with a very simple automated bash script. The pedestal signals are measured using the events from the closed shutter periods, and are subtracted from the shutter-open signal before extracting the LED asymmetries. The events recorded by the DAQ are analyzed using a root/C macro.

Data Analysis

The DAQ integrates and records the events in four different blocks with 400 samples per block and $2 \mu s$ per sample (500 kHz rate). The first order (dominant) non-linear effect on the asymmetry can be expressed as

$$A_{LED} = \frac{N_{pmt}^+ - N_{pmt}^-}{N_{pmt}^+ + N_{pmt}^-} \approx A_{true}(1 + \beta N_{avg}), \quad (3.13)$$

where $N_{pmt}^\pm = N^\pm(1 + \beta N^\pm)$ is the number of ADC channels (corresponding to the

3.6. PREX-2/CREX DETECTOR SYSTEM

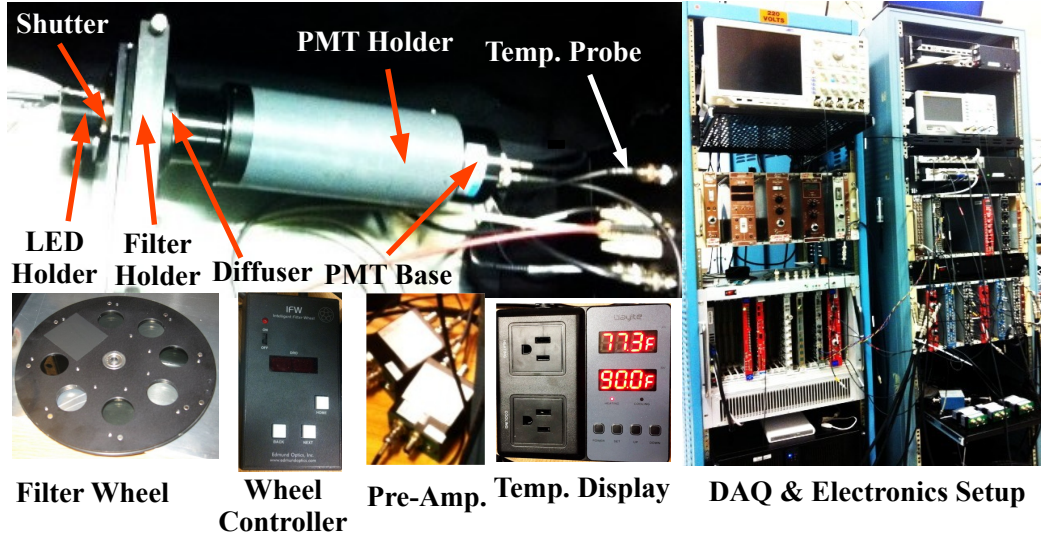


Figure 3.38: Experimental setup for PMT non-linearity bench-tests. The PMT within the holder is a Hamamatsu R7723Q, 2 inch PMT. The various components shown are described in the text.

PMT signal output) for two consecutive integration windows¹² and $N_{avg} = \frac{N_{pmt}^+ + N_{pmt}^-}{2}$. The integration window is adjusted to be one over the anticipated helicity flip frequency during the experiments. Therefore, N^+ is the signal that corresponds to the integration window when both constant and flashing LEDs are energized, while N^- is the signal corresponding to the integration window when only the constant LED is on. This creates a signal asymmetry, A_{LED} , measured by the PMT. The combined light from the LEDs passes through the different filters which changes the overall intensity on the PMT but not the asymmetry. During a measurement (or run), each filter setting is repeated twenty times, and the average is computed giving a single asymmetry for each filter-transmission setting. The measured average asymmetry, A_{LED} , is linearly fitted against N_{avg} . The two parameters from the straight line fit, \hat{y} -intercept and slope, are related to A_{true} and $A_{true} \times \beta$, respectively, according to Eq. 3.13. The β parameter can then be determined and used to calculate the amount of non-linearity, $\beta \times N_{max}$, where N_{max} is N_{avg} for the no filter (100 % transmission)

¹²Integration window is a time interval during which the ADC acquires (samples and integrates) the input signal to give a single digital output (actually four digital outputs, one for each block). The length of this window depends on the DAQ frequency.

3.7. SMALL ANGLE MONITORS (SAMS)

setting. For the main detector PMTs, the PREX-2 light level is ≈ 10 nA, while for CREX it is ≈ 0.13 nA. Figure 3.39 shows the non-linearity for a typical run. We performed measurements over a wide range of high voltages and various light levels. Figure 3.40 gives a nice summary of the non-linearity test results for the PMTs used in the PREX-2 main detectors. The high voltage settings for the PMTs used during PREX-2 and CREX are shown in Table 3.5. The measured non-linearities for all the tested PMTs are given in Appendix A.

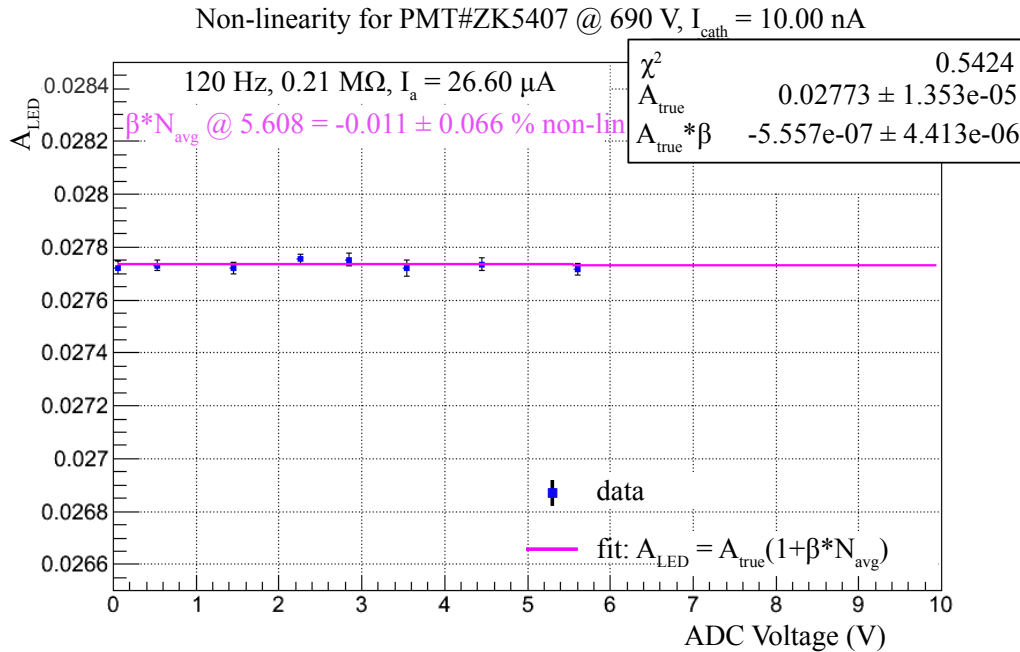


Figure 3.39: Results from a single non-linearity measurement (or run) for PMT ZK5407 (Hamamatsu R7723Q) at a typical high voltage of -690 V and at a 10 nA light level.

3.7 Small Angle Monitors (SAMs)

New Hall A SAMs, designed to have improved performance, have replaced the Hall A Luminosity Monitors (which were used during previous parity experiments in Hall A). The SAM apparatus measures the rate of charged particles emerging from the target at small ($\approx 0.5^\circ$) angles during the experiment. The SAMs constitute a powerful

3.7. SMALL ANGLE MONITORS (SAMS)

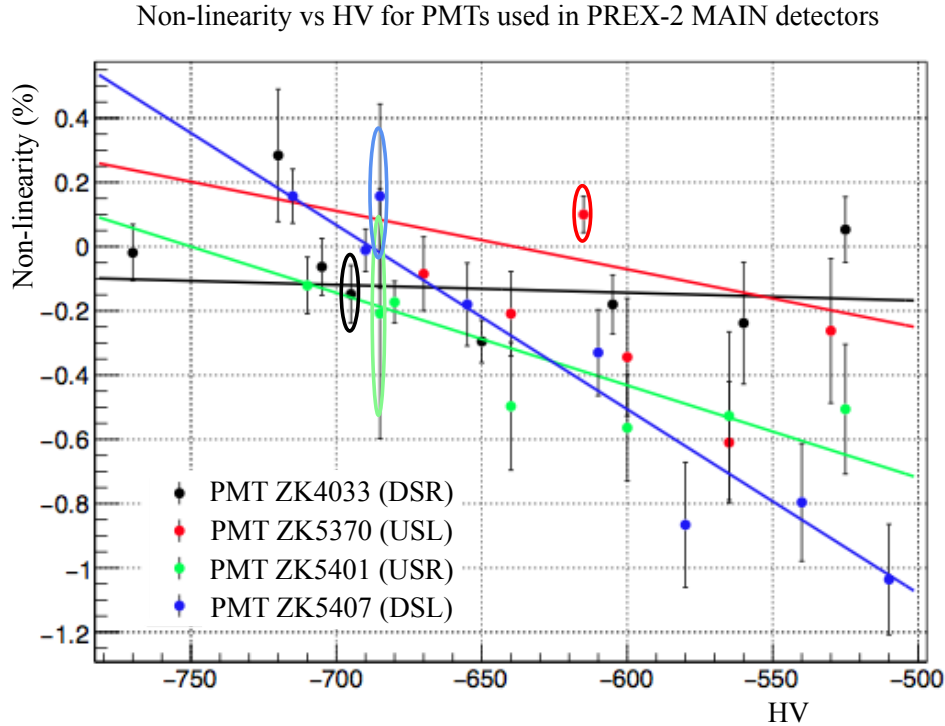


Figure 3.40: Summary of non-linearity test results of the various PMTs used in the PREX-2 main detectors. Data are shown as a function of high voltage and the light level is 10 nA. We run PREX-2 at the HVs listed in Table 3.5. The data points enclosed by ovals indicate the HV values and non-linearities for PREX-2.

Experiment	PREX-2		CREX	
	Detector	PMT	HV	PMT
USL	ZK5370	-615 V	ZK5370	-905 V
USR	ZK5401	-685 V	ZK5363	-910 V
DSL	ZK5407	-685 V	ZK5407	–
DSR	ZK4033	-705 V	ZK5365	–

Table 3.5: PMT and HV settings for PREX-2 and CREX main detectors during integration mode. The downstream detectors are always connected to the counting mode DAQ during CREX running. During counting mode runs the detectors are operated at ~ -2000 V.

parity-quality beam-monitoring instrument that is designed to monitor a (theoretical) null asymmetry at extremely high rates (and extremely small Q^2). The detected rates are so high that the SAM asymmetry widths give a measure of the electronics “noise-floor” in the hall—which can be understood as coming from the quadrature sum of

3.7. SMALL ANGLE MONITORS (SAMS)

various contributing noise sources and can serve as a confidence-building cross-check for understanding beam noise. The SAMS are a necessary diagnostic tool to monitor and possibly help correct for any beam-related false asymmetries.

The ISU parity group designed, constructed, and installed multiple generations of SAMS in the Hall A beamline between 2015 and 2019. The SAMS are located approximately 7 m downstream of the target, and positioned symmetrically around the beamline in four diametrically opposing pairs. During the SAM design process, there were two stages of prototyping followed by test beam studies to ensure that we fully understand the detector's light yield and resolution performance. Figure 3.41 gives a collage of SAM drawings and photos.

Each SAM consists of an air-core, mirrored-aluminum light guide fitted with a 2 inch diameter PMT at one end, and an optically polished piece of fused-silica (quartz) at the other end. Several light guide materials are studied on the bench and in beam-tests. The material named Miro-silver 4270, from the manufacturer Anomet, is found to work best and give more photo-electrons. During operation, the SAM light guides are constantly flushed with dry air to remove moisture and help prevent corrosive damage to inner mirrored surfaces, as well as help quench scintillation light backgrounds from the charged particles that traverse the light guides. Charged particles that scatter at small angles and traverse the quartz will produce Čerenkov radiation, which escapes the quartz bevel and is directed to the PMT with the light guide.

3.7.1 SAM Installation

The SAMS are redesigned versions of the original Hall A Luminosity Monitors (LUMIs)—which were designed and installed in Hall A around 2002. The new SAMS (first generation) were installed in Hall A in December 2015 following the completion of the 12 GeV upgrade. Historically, the Lumi system never worked well. It was plagued

3.7. SMALL ANGLE MONITORS (SAMS)

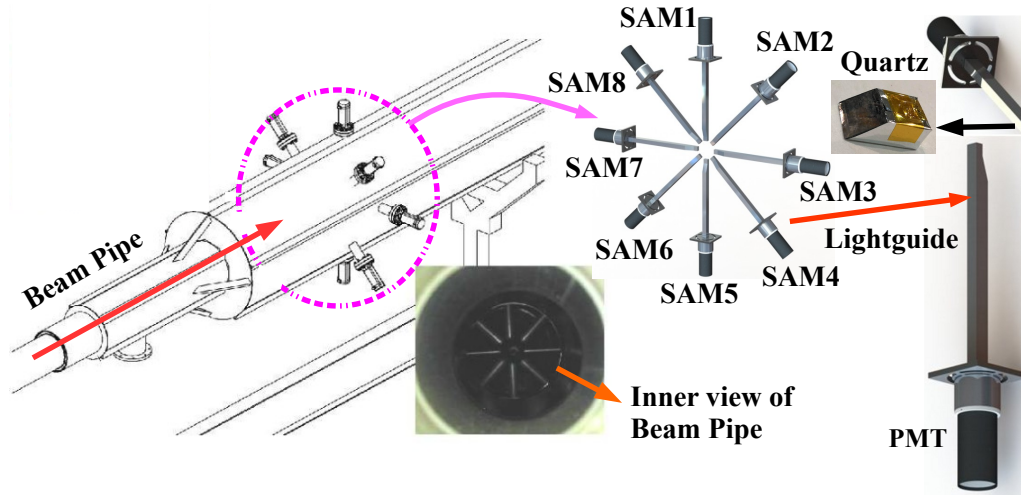


Figure 3.41: Collage of drawings and photos for the SAM system. Working clockwise starting at the top left, the images are: beamline CAD with SAMs installed, CAD drawing of eight SAM array (looking downstream with beam), close-up photo of the SAM quartz which is wrapped with aluminized mylar, a couple of CAD views of an individual SAM, and a photograph inside the beampipe looking downstream at the SAM insertion tubes.

with very large non-linearities due primarily to the PMT setup. These detectors have low PEs per electron but are potentially exposed to ~ 100 GHz rates which creates large LLs on the cathode, and requires too low a high voltage for proper PMT function. The LUMIs also had other design flaws, such as quartz size (too long) and light guide geometry (not optimized), that were addressed in the redesign. However, before PREX-2, due to anticipated excessive radiation loads in the Hall, the first generation SAMs had to be redesigned with thinner quartz radiators, new light guides, and new vacuum insertion tubes. The redesigned SAMs for PREX-2 have shorter light guides (14.2" instead of 15.6"), thinner radiators (6 mm instead of 13 mm), and new vacuum insertion tubes with thin domed endcaps (0.012" thick instead of previously used flat 0.065" endcap). Geant4 optical simulations of the SAM performance were benchmarked using several beam-tests performed prior to installation. A detailed explanation of the comparison between beam-test and simulation using QSIM, an application of Geant4 dedicated to the simulation of the quartz Čerenkov detectors,

3.7. SMALL ANGLE MONITORS (SAMS)

can be found in [64].

Each SAM consists of a 2 inch Hamamatsu R375 PMT as its photosensitive device. At the expected ~ 100 GHz rates, SAM signals can suffer from a high degree of non-linearity when operated at “normal” (or so-called high) gain settings. Therefore, as a test, only one of four SAM pairs (two PMTs total) use the high gain mode, while the others use “unity” gain mode. Note that special voltage divider bases are designed and used for unity gain mode. Some of the SAM PMTs are tested for their linearity in dedicated bench-tests before installation. The non-linearity should only be a concern for the high gain SAMs, and it is demonstrated to be within a few percent for the range of expected LL and HV/pre-amp combination. Details about the bench-tests are given in Sec. 3.6.4. All quartz detector non-linearities are regularly monitored during the experiments through both PITA scans and stepped beam current ramps. The signal integration technique for the SAMs is the same as for the main detectors. Table 3.6 gives the gain and I-to-V settings for each SAM during PREX-2 and CREX. The wiring configuration for a single SAM detector is shown in Fig. 3.42. However, while running PREX-2, we discover that the new SAM light guides are too short, keeping the quartz in the shadow of the beamline collimator. This prevent the SAMs from intercepting enough rate as well as induce more rate fluctuation over the square raster pattern. Therefore, for CREX, we reinstall the original light guides and quartz from 2015, but with new, longer domed endcap insertion tubes to get the quartz closer to the beamline and out of the collimator shadow.

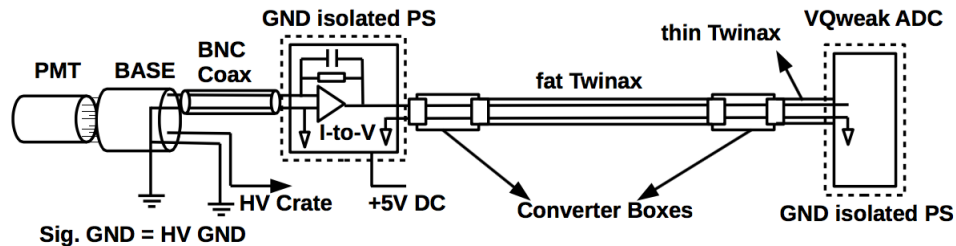


Figure 3.42: Wiring configuration of a SAM detector.

3.7. SMALL ANGLE MONITORS (SAMS)

SAM	Gain	I-to-V (PREX-2)	I-to-V (CREX)
1	Unity	25 M Ω	10.1 M Ω
2	Unity	25 M Ω	25 M Ω
3	High	0.5 M Ω	0.1 M Ω
4	Unity	25 M Ω	10.1 M Ω
5	Unity	25 M Ω	10.1 M Ω
6	Unity	4 M Ω	4 M Ω
7	High	0.5 M Ω	0.1M Ω
8	Unity	4 M Ω	4 M Ω

Table 3.6: SAM system PMT gain and pre-amplifier (I-to-V gain) settings during PREX-2 and CREX.

At the beginning of PREX-2, we install an electronic shutter just in front of each SAM’s PMT window. The shutters are remote-controllable using a python based GUI installed on a dedicated Raspberry Pi, and the purpose is to check for possible light (PE) generation from radiation striking the PMT window or cathode directly; these PMTs are mostly unshielded and fairly close to the beamline downstream of the target. The shutter study is performed to give a better understanding of SAM backgrounds and data quality. The study (data collection phase) lasts only about one hour and takes place during commissioning, before the SAM area of the beamline becomes restricted due to high-radiation. The study includes a few SAM runs during production commissioning, with shutters open and again with them closed. The beam conditions are not changed during the short tests. We find that with the shutter closed, the SAM’s signal output is negligibly small. After this test, the shutters are uninstalled.

3.7.2 SAM Performance

The SAMs are sensitive to fluctuations in beam current, position, energy, angle, and many other subtle helicity correlated effects. Furthermore, the SAMs can also give a quick response to any target density fluctuation or change. SAM pairs, positioned on

3.8. DATA ACQUISITION SYSTEMS (DAQS)

opposite sides of the beamline, tend to be highly correlated and have nearly equal and opposite responses to changes in beam position. For instance, SAM3 and SAM7 rates are highly influenced by beam motion in the \hat{x} (horizontal) direction, while SAM1 and SAM5 respond more to beam position fluctuation in the \hat{y} (vertical) direction. Since CREX is a relatively low rate experiment (in the focal plane, but not in the beampipe), the main detectors have a much larger statistical width than the SAMs, so any small fluctuation in detected rate would not be readily observed in the main detectors but would be seen by the SAMs. The SAMs serve as a powerful tool for helping ensure high-quality data collection during the experiments.

3.8 Data Acquisition Systems (DAQs)

PREX-2/CREX use different data acquisition (DAQ) systems for various purposes. The main physics asymmetry measurement is performed using a dedicated integrating DAQ, commonly known as the parity DAQ. For particle tracking, Q^2 measurement, some background studies, and other HRS optics-related commissioning tests, a counting DAQ is used. The Møller polarimetry measurement uses an independent counting DAQ, while the Compton polarimeter uses an independent integrating DAQ.

3.9 Counting DAQ

The counting DAQ is a Hall A standard data acquisition system, which uses the standard Hall A “Podd” analyzer for data analysis. The DAQ includes various electronic modules such as VME and NIM signal processing modules (Amplifier, Logic FIFO, Discriminator, Logic Unit, etc), ADCs, TDCs, and scalers. The triggers for the counting DAQ for PREX-2/CREX are provided by various logical combinations of the S0 and S3 scintillator signals. A clock pulser trigger is occasionally used for

3.9. COUNTING DAQ

diagnostic purposes, for example counting mode pedestal studies performed parasitically with the integrating DAQ at higher beam intensities. As long as the DAQ's data transfer rate can keep up with the detected rate, the scaler rate is proportional to the incident flux; the scalers count scintillator trigger signals that are above voltage threshold. Above a certain rate threshold, the DAQ can not handle the data transfer at the same speed as the trigger rate, because the DAQ is still processing the previous trigger. This causes the trigger to be counted, but the signals do not get digitized; this effect is commonly known as DAQ dead-time. To avoid this, the counting DAQ is normally operated at lower beam currents and with appropriate prescaling (the DAQ digitizes a subset of the total triggers) of the triggers.

Various independent triggers are created by logical "AND" and "OR" combinations of S0 and S3 signals. Such a combination is shown in Fig. 3.43. The most important trigger is the T1 trigger, which is formed by the logical "AND" between S0's two PMT (S0_A and S0_B) signals. The formation of triggers during CREX is slightly different than during PREX-2, because the PREX-2 S3 uses a single plastic scintillating paddle with a single PMT, while the CREX S3 uses two more additional paddles as shown in Fig. 3.30. All of these triggers are sent to the trigger supervisor (TS) VME module, which starts and controls the DAQ readout. The selection of a trigger and prescale setting can be done remotely.

At the beginning of PREX-2, we try using triggers generated from the quartz signals as well. This requires us to make several copies of a quartz signal, by passing it through a linear Fan IN/Fan OUT (FIFO), which introduces extra noise in the signal making it harder to separate the signal from the pedestal. Therefore, after a couple of days of running during PREX-2 commissioning, we connect the quartz signal directly to the FastBus ADC. Therefore, no quartz trigger is available. But this type of "self-trigger" would be used only for diagnostic purposes since it constitutes a biased trigger, which causes the acquired focal plane data distributions to be incomplete,

3.10. INTEGRATING DAQ

possibly skewed, and biased toward only events that traverse the quartz.

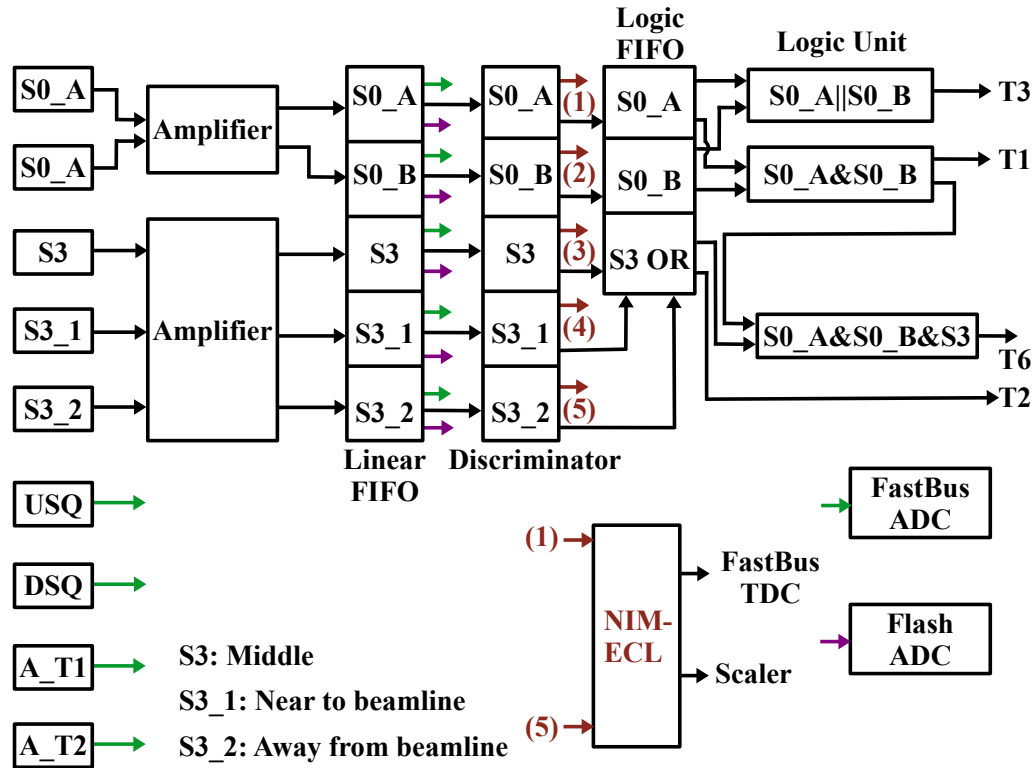


Figure 3.43: DAQ flowchart of counting mode triggers in use during CREX. PREX-2 and CREX use S0 and S3 plastic scintillator’s signals to create various triggers in the data stream. An appropriate trigger can then be chosen later during offline data analysis. CREX triggers are different than PREX-2 triggers only in that the PREX-2 S3 is a single scintillating paddle with a single PMT, but CREX S3 is made by adding two new such paddles S3.1 and S3.2 on either side of the PREX-2 S3.

3.10 Integrating DAQ

Parity experiments such as PREX-2 and CREX require running at extremely high rates to collect the needed statistics in a relatively short time. Counting individual hits on a detector does not make sense because of DAQ dead-time. This requires us to implement an integration technique. In this technique, we integrate the detected signal over a specified time window, with a fixed and sufficiently low trigger rate such that there is no DAQ dead-time. Additionally, while this technique removes the

3.10. INTEGRATING DAQ

possibility of DAQ dead-time, it also is nearly 100 % efficient at collecting all experimental production data. For these reasons, the physics asymmetry measurement is performed using an independent integrating DAQ, well known in the parity group as the “Parity DAQ.” The Helicity Control Board (HCB), Happex Timer Board (HTB), SIS3801 Scaler, FlexIO, Voltage to Frequency Converter (V2F), and vQ_{wk} ADC are the key modules used in the integrating DAQ.

The parity DAQ consists of VME crates located at four different locations: Injector, left-HRS, right-HRS, and the Counting House (CH). The signals from various beam-monitors in the injector site are sent to the Injector crate, the signals from the various beam-monitors in the Hall A beamline are sent to the CH crate, and the detector’s signals in the HRSs are sent to the crates located in their respective detector hut. Using the crates at various locations helps keep the detected signals from being attenuated before digitizing. The data taken by the parity DAQ is analyzed using “Just Another Parity ANalyzer (JAPAN)”—an independent analyzer software package developed for PREX-2 and CREX. Note that the analyzer for the previous HAPPEX and PREX-1 experiments was named “Parity ANalyzer (PAN).”

The helicity frequency is controlled using the HCB, where the helicity patterns are created pseudo-randomly and fed into the Pockels cell system for electron-helicity reversal patterns. The helicity signal that is sent to the Pockels cell is not sent to the other crates directly, but is instead delayed by 8 (16) helicity windows for 120 (240) Hz helicity frequency. This delay, combined with the pseudo-random helicity window pair pattern sequence, eliminates the systematic effects of possible cross talk through ground loops for example. The timing scheme of the DAQ is similar to the one shown in Fig. 3.37. The integration timing for the helicity windows is controlled using the HTB, and the SIS3801 Scaler is used for triggering. The length of the integration window, t_{meas} , is adjusted according to the helicity flipping frequency (of the Pockels cell). The t_{settle} is adjusted to account for the time needed for the Pockels

3.10. INTEGRATING DAQ

cell to transition from one helicity state to another. Normally, t_{settle} is $100 \mu\text{s}$, and if we are running at 120 Hz flipping rate, the fraction of time (and events) lost due to electron-helicity reversal is $100 \mu\text{s} \times 120 \text{ Hz} = 1.2 \%$. PREX-2 takes most of its production runs at 240 Hz flipping frequency with pseudo-randomly generated octet patterns (+ - - + - + + - or - + + - + - - +), and CREX flips at a frequency of 120 Hz with pseudo-random quartet patterns (+ - - + or - + + -). Each octet (at 240 Hz flipping) and quartet (at 120 Hz flipping) is called a helicity multiplet pattern (or simply multiplet pattern). The asymmetry and position differences are performed in each octet or quartet pattern, depending on flip frequency. The pattern combination of octet or quartet is needed to properly cancel out the 60 Hz noise of the power-line as shown in Fig. 3.44. Following the pattern combinations, these quartets (at 120 Hz) and octets (at 240 Hz) contain complementary measurements at the same phase relative to the 60 Hz noise, which averages out to zero [25] upon integration.

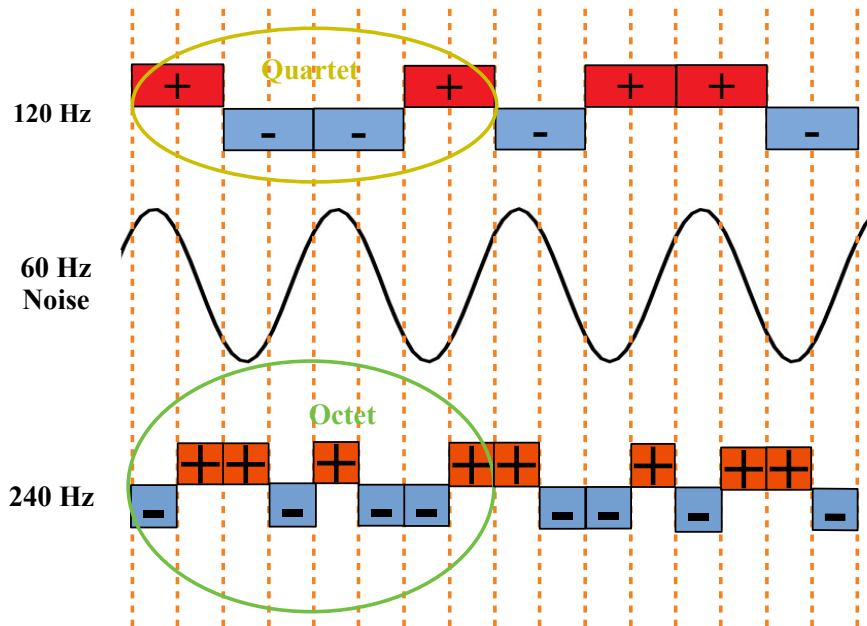


Figure 3.44: Helicity pattern train combinations and 60 Hz power-line phase cancellation. PREX-2 uses (mostly) 240 Hz flipping with octet patterns and CREX uses 120 Hz flipping with quartet patterns.

Chapter 4

Data Analysis

The PREX-2 and CREX measurements use an electro-weak interaction probe at a single, but low Q^2 kinematic setting. The choice of kinematics is driven by optimizing the Figure Of Merit (FOM). The scattering angle and hence Q^2 are chosen to be low enough, such that the weak form factor (F_W) excludes, or is far from, the first diffractive minima. This ensures a very high (near perfect) correlation between F_W and R_n as shown in Fig. 2.7. In order to make a precise measurement of such a tiny quantity, it is extremely important to rigorously understand and control all sources of systematic error and backgrounds. These include helicity-correlated beam asymmetries (intensity, energy, and position differences) and false asymmetry due to residual transverse beam polarization, to name a few. In this chapter we will highlight: the performance of the PREX-2/CREX integrating detectors, the corrections to the measured raw asymmetry, Q^2 measurements, beam polarization measurements, various sources of backgrounds, and finally report the PREX-2 final results for A_{PV} , R_n , and R_{skin} . While the CREX analysis is still not concluded at the time this document is finalized, whenever possible various sources of systematic and asymmetry backgrounds for CREX will also be discussed.

4.1 Focal-Plane Detector Alignment

The focal plane detector package (in each HRS) consists of two main detectors, two auxiliary detectors, and three small ($10\text{ cm} \times 20\text{ cm}$) GEM tracking planes. Details about the R&D preparation, design, and installation of the detectors are given in Sec. 3.6.3. This section is mostly focused on the performance of the main detectors. We will discuss the performance of the auxiliary detectors in Sec. 4.5. There are three more larger GEMs downstream of the auxiliary detectors with an active area ($50\text{ cm} \times 60\text{ cm}$). Though these GEMs and the smaller ones are designed, installed, and used for cross-checking the Q^2 measurements, particularly at higher rates during PREX-2, the final Q^2 measurements are obtained from the VDCs. The electron hit distributions on the three smaller GEMs in the right-HRS are shown in succession from left to right in Fig. 4.1. The Xstrip is along the \hat{x} -axis, and Ystrip is along the \hat{y} -axis of the transport coordinate system. Figure 4.2 gives example plots showing the performance of track reconstruction using the GEMs as compared to VDCs.

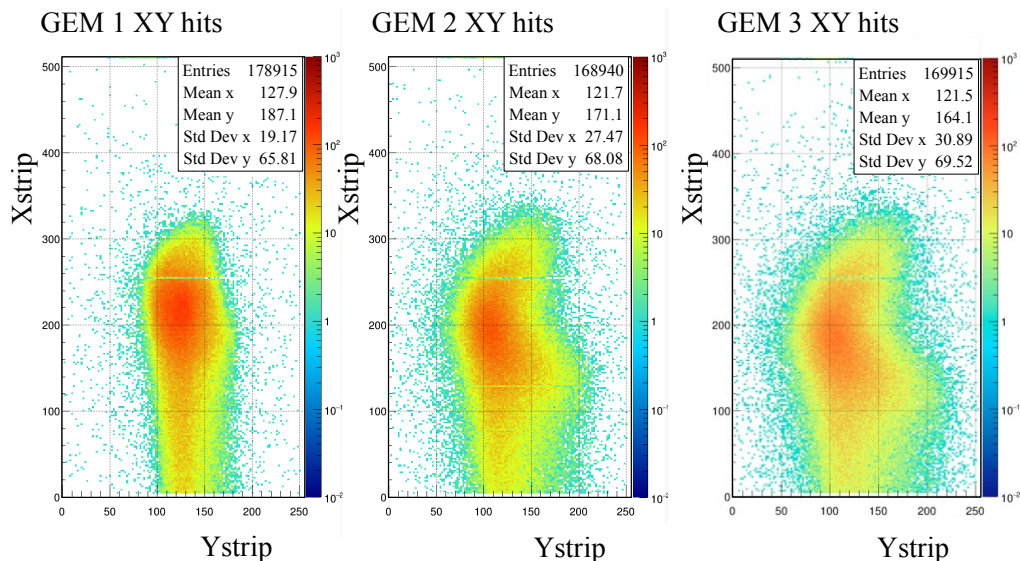


Figure 4.1: Electron hit distributions on the three small GEMs in the right-HRS [68].

At the beginning of each experiment, the detectors are aligned using a few hours of dedicated counting mode DAQ running. The counting runs are taken nominally

4.1. FOCAL-PLANE DETECTOR ALIGNMENT

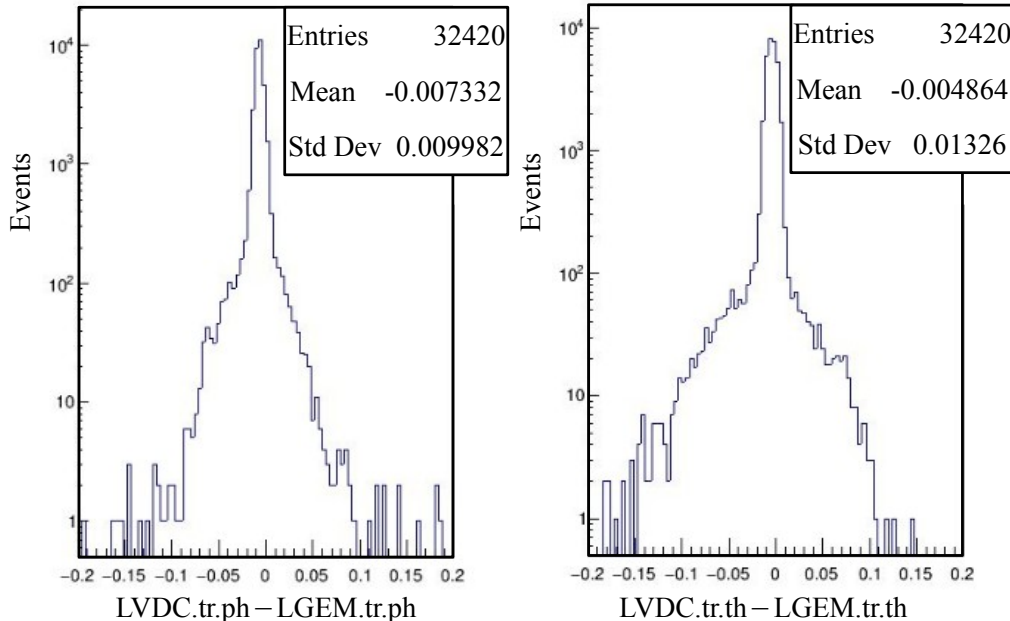


Figure 4.2: Comparison of the reconstructed track variable distributions using GEM and VDC. Left-hand side plot: Difference between VDC and GEM system reconstructed track ϕ variable (tangent of track ϕ angle). Right-hand side plot: The difference between VDC and GEM track θ variable (tangent of track θ angle) [68].

at ~ 30 nA beam current during PREX-2 and ~ 0.3 μ A during CREX. The limiting factor for the beam current size is determined by the recommended operating range of rates on the VDCs. Some details of the VDCs are given in Sec. 3.6.1. The essential purpose of the main detector alignment procedure is to maximize the acceptance of elastically scattered electrons, into the quartz radiator, while rejecting the inelastic electrons.

The first step in the alignment is to look at the detector’s ADC spectrum. As explained in Sec. 3.9, there are many combinations of triggers to choose from, but we use the T1 trigger created from the logical “AND” between S0_A and S0_B PMTs of the S0 scintillator. The S0 scintillator is more reliable than S3 simply because of its size and proximity to the VDCs and main quartz detectors. If an electron hits the S0 scintillator and creates a signal in both of its PMTs, then it is counted as a trigger. If the same electron also hits the quartz, then it produces a signal in the

4.1. FOCAL-PLANE DETECTOR ALIGNMENT

quartz detector. On the other hand, if an electron creates a trigger signal but misses the quartz, then there is no signal from the quartz detector (only pedestal). A typical pulse-height distribution of an upstream quartz detector is shown in Fig. 4.3(a). The blue histogram is data, and the red curve is a Gaussian fit to the pedestal portion of the distribution. The ADC cut (pedestal cut) is shown as the vertical magenta-colored line. Figure 4.3(b) shows the pedestal-corrected ADC distribution with the ADC cut applied. σ_{cor}^2 is the quadrature difference between the width of the LanGau fit (a Landau tail convoluted with a Gaussian function) and the width of the Gaussian fit to the pedestal distribution, and MPV is the most probable value from the LanGau fit denoting the peak location. The fit, combined with a purely statistical model for what dominates the width of the Gaussian component of the spectra, allows one to extract the peak photoelectrons to be $PE = \frac{MPV^2}{\sigma_{cor}^2} = 28$.

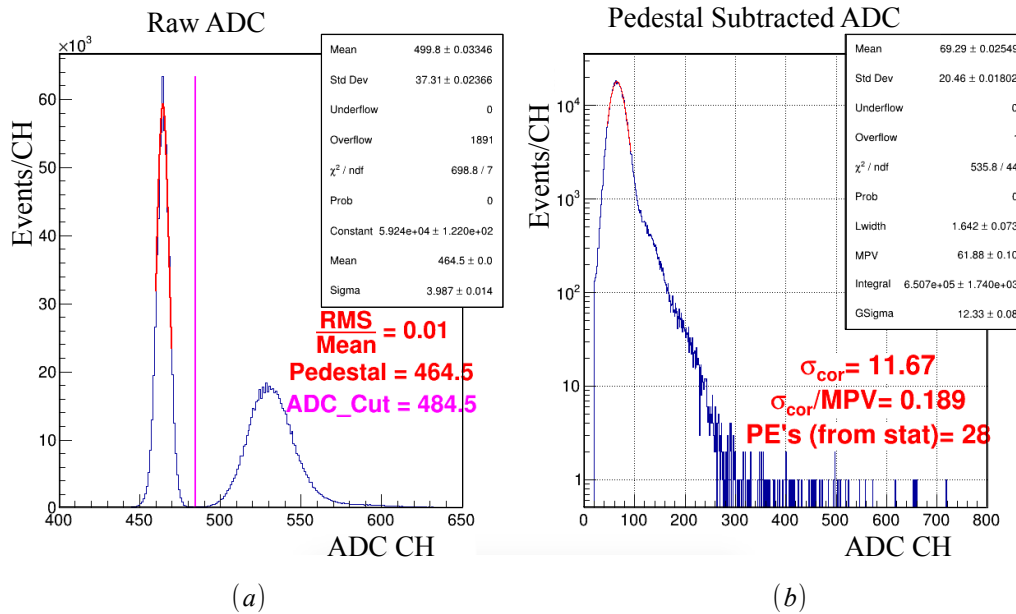


Figure 4.3: (a) Sample pulse-height distribution for the left-HRS upstream main detector. Data is shown in blue, and the Gaussian fit to the pedestal in red. The vertical magenta line shows the ADC pedestal cut location. (b) Pedestal subtracted ADC distribution with ADC cut applied. The blue histogram is data, and the red fit is the LanGau fit—a Landau tail convoluted with a Gaussian function.

4.1. FOCAL-PLANE DETECTOR ALIGNMENT

4.1.1 HRS Dispersion and Quartz Acceptance

The main quartz detector’s scattered flux acceptance, as well as any possible shifts in the beam energy, are regularly monitored using the counting mode DAQ. Given that the inelastic scattering parity-violating asymmetries associated with the excited states of ^{48}Ca are more unknown, frequent alignment checks are more important for CREX. To monitor possible shifts in beam energy during CREX, the downstream main detectors are always connected in counting mode throughout the experiment. We take great care in maintaining a large enough gap between the quartz edge and the focal plane positions of the inelastic peaks throughout the experiments. The positions of the various low-lying excited states, relative to the elastic peak position, are calibrated by estimating the HRS dispersion constant.

Figure 4.4 shows a profile distribution of reconstructed tracks, for the transport \hat{x} coordinate versus $\frac{dp}{p}$ on the VDC plane and projected to the detector plane. Each profile distribution is fitted with a straight line. Figure 4.4(a) shows that the dispersion constant at the VDC detector plane is approximately 12.48 m per 1 % change in the momentum, in close agreement with what is listed in [61]. Recall the transport \hat{x} coordinate is along the dispersive direction in the HRS. $\frac{dp}{p}$ is the fractional change in spectrometer momentum. As shown in Fig. 4.4(b), the dispersion constant at the main detector plane is approximately 15.31 m per 1 % change in beam momentum. This figure comes from a typical counting mode run in the left-HRS during CREX. The slopes of the fits give the shift in the spectrum, on the corresponding plane, per unit change in momentum (the so-called dispersion constant). As a cross-check, the dispersion constant can also be calculated from a “ dp ” scan which artificially moves the elastic peak on the focal plane by changing the HRS dipole field settings. For example, see Fig. 4.5(a), which shows the $\frac{dp}{p}$ distribution for run 2977 at the nominal dipole setting, and run 2987 at -2 % dipole setting (dipole current reduced by 2 %).

4.1. FOCAL-PLANE DETECTOR ALIGNMENT

The 2 % decrease in dipole current results in a 1.9 % shift in $\frac{dp}{p}$. Figure 4.5(b) shows the corresponding shift in the spectrum in the VDC plane transport \hat{x} . We observe a 0.237 m shift in the spectrum corresponding to the 1.9 % shift in $\frac{dp}{p}$. This gives 12.47 cm of dispersion per 1 % change in beam momentum, again, in close agreement with [61].

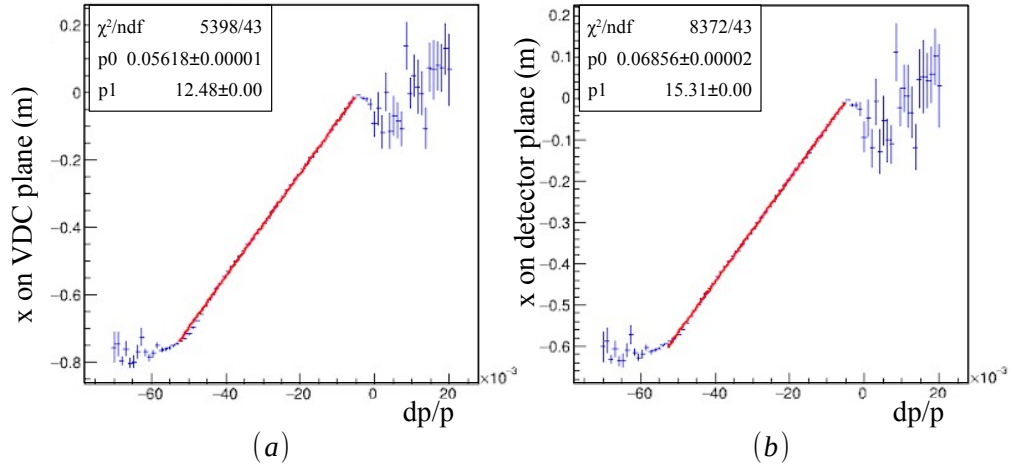


Figure 4.4: Estimating the dispersion constant in the left-HRS. (a) Transport \hat{x} -distribution versus $\frac{dp}{p}$ for VDC tracks at the VDC detector plane, and (b) for those same tracks projected to the focal plane (main quartz detector).

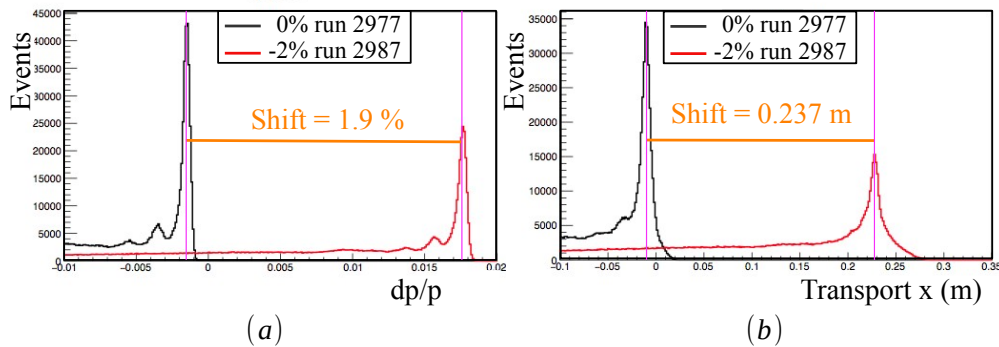


Figure 4.5: Dispersion constant in the left-HRS via dp scan (CREX runs). (a) $\frac{dp}{p}$ distribution for nominal and -2 % HRS dipole settings. (b) Transport \hat{x} (dispersive direction in the HRS) distribution on the VDC plane for nominal and -2 % dipole settings.

4.1. FOCAL-PLANE DETECTOR ALIGNMENT

4.1.2 Rejecting Inelastic Flux from the Acceptance

Using the dispersion constant from the previous section, we can determine the spatial location of various low-lying excited states relative to the elastic peak position. This gives us an idea of where to position the “quartz edge” (which is on the radiative tail side of the tile as shown in Fig. 4.6)—making sure that minimal inelastic events traverse the quartz. While performing the alignment, one must also take care not to position the quartz edge too far up the side of the elastic peak, otherwise the energy slope correction introduces relatively large fluctuations in the measured asymmetry.

The focal plane detectors are installed within the HRS detector hut such that the upstream quartz is approximately 1.3 m downstream from the origin of the transport coordinate system. A not-to-scale sketch of the transport coordinate system, detector coordinate system, and the relative position of quartz is presented in Fig. 4.6.

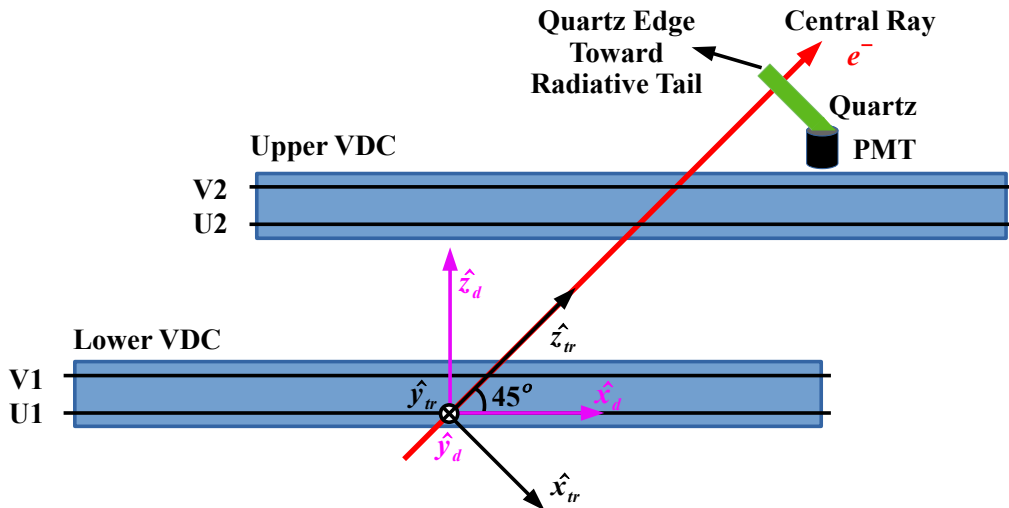


Figure 4.6: Schematic of transport (black) and detector (magenta) coordinate systems. The upstream quartz is ~ 1.3 m downstream (along transport \hat{z}) of the origin of the coordinate systems. The auxiliary detectors (not shown) are approximately 2 m downstream of the origin, traveling along transport \hat{z} (the Central Ray).

The transport \hat{x} and \hat{y} distributions projected to the quartz plane, during PREX-2 for a typical counting mode run, are shown in Fig. 4.7. The black histograms are for

4.1. FOCAL-PLANE DETECTOR ALIGNMENT

all the events triggered (by the S0 scintillator), the red(blue) histograms are for those events which are accepted(missed) by the upstream main detector using the ADC cut threshold. The intersection point between the accepted and missed histograms gives the quartz edge position in both \hat{x} and \hat{y} distributions (see the left and center plots of Fig. 4.7). The accepted events spread over an approximately 8 cm length and 3.5 cm width—which is the full width of the quartz radiator. The locations of the first four excited states relative to the elastic peak are shown by the colored vertical lines in the figure. The location, x_{ex} , of a general excited state (labeled ex) is obtained using

$$x_{ex} = \frac{E_{ex}}{E_{beam}} \times DC, \quad (4.1)$$

where E_{ex} is the energy of the excited state relative to the elastic peak, E_{beam} is the beam energy, and DC is the dispersion constant. Similar alignment plots for CREX are given in Fig. 4.8.

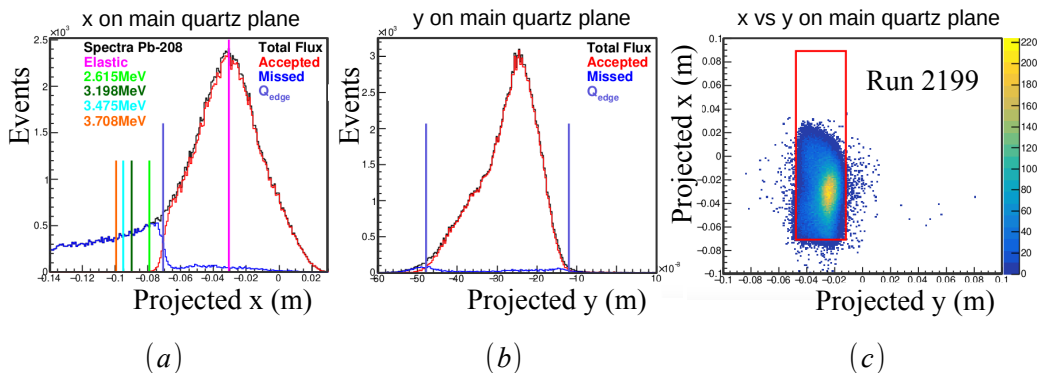


Figure 4.7: Left-HRS main detector alignment plots during PREX-2. (a) Transport \hat{x} projected to the upstream tandem quartz plane. The black, red, and dark blue histograms give the total flux, the flux accepted by the quartz, and the flux missed by the quartz, respectively. The elastic peak and the quartz edge are shown by the (taller) magenta and the light blue colored vertical lines, respectively. The positions of the first four excited states are shown. (b) Transport \hat{y} projected to the quartz plane. The quartz edges are shown by vertical light blue colored lines. (c) Transport \hat{x} vs. \hat{y} projected to the quartz plane. The red box shows the relative dimension of the quartz.

4.2. ASYMMETRY ANALYSIS

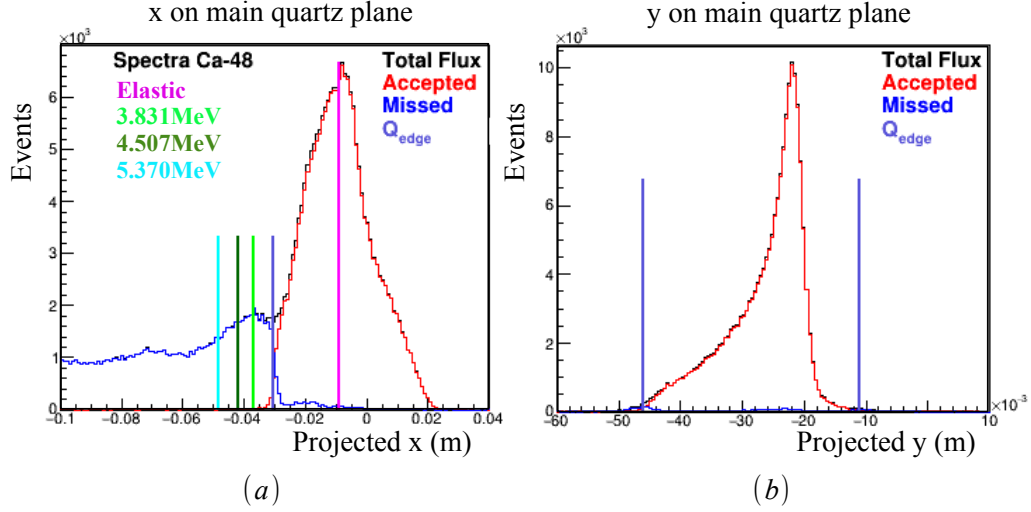


Figure 4.8: Left-HRS main detector alignment plots during CREX, similar to Fig. 4.7(a) and (b). A broad bump in the spectra is clearly seen in the region of the inelastic states.

4.2 Asymmetry Analysis

PREX-2 collects production data at 50 - 85 μA beam currents. Most of the runs are 30 min long, and each run is divided into several miniruns, such that each minirun contains 5 minutes worth of “good” data (or 9000 good multiplet patterns). Here, good data means those events which pass all the event cuts (see the next section for the cuts used for production data). One multiplet pattern is a group of 8 helicity windows (octet: + - - + - + + - or - + + - + - - +) at 240 Hz of helicity flipping, or 4 helicity windows (quartet: + - - + or - + + -) at 120 Hz helicity flipping. Both multiplet patterns last a total of ≈ 33 ms and repeat at a rate of 30 Hz. PREX-2 collects a total of 5084 miniruns. The IHWP state is toggled every 5 - 6 hours of good data. The runs for each IHWP state are grouped into larger data-set intervals called “slugs.” PREX-2 collects a total of 96 slugs. After collecting roughly two weeks worth of good data under smooth running conditions, the Wien state is changed. By the end of PREX-2, we have changed the Wien setting three times. As mentioned in the previous chapter, the two mechanisms of slow helicity reversal, the IHWP and

4.2. ASYMMETRY ANALYSIS

Wien systems, help cancel helicity-correlated false asymmetries when averaged with roughly an equal statistical weighting.

4.2.1 Cuts

For each production run, we need to make sure that the data we are considering for the final analysis does not have unacceptably large beam fluctuations, any electronic hardware failure, synchronization mismatch between different ROCs (VME crate Read Out Controllers), etc. A global error flag is created for each event, and several cut categories are entered into the flag. Some of the important cuts applied in the final analysis are listed below. Occasionally, because of equipment malfunction, such as HRS magnet failure, DAQ failure, etc., special cut conditions have to be defined on a run-by-run basis.

- Beam current threshold cut
- Beam current stability cut
- Beam position excursion cut
- Beam position stability (burp) cut
- Beam energy excursion cut
- Beam energy stability (burp) cut
- Detector/Monitor hardware failure cut
- DAQ synchronization cut

4.2. ASYMMETRY ANALYSIS

4.2.2 Pedestal Calibration

The quartz detectors (PMTs) and beam monitors (BCM cavities and BPM wires), which we use to detect signals, have dark currents associated with them. These dark currents, together with the ADC design and preAmp settings, define the pedestal (or zero signal baseline) of the detector or monitor; the pedestals are subtracted from the signals acquired during production data taking. The pedestal is independent of the electron beam helicity state, so it theoretically remains the same for both. If $F_R(F_L)$ is the flux detected in a detector for right(left) helicity states, and S_{ped} is the pedestal signal, the signal recorded by the ADC can be expressed as

$$S_{R(L)} = F_{R(L)} + S_{ped}. \quad (4.2)$$

Therefore, the detector asymmetry is given by

$$A = \frac{S_R - S_L}{S_R + S_L} = \frac{F_R - F_L}{F_R + F_L + 2S_{ped}}. \quad (4.3)$$

Note the $2S_{ped}$ term in the denominator affects our physics asymmetry. This is why we need to calibrate the detector, BCM, and BPM pedestals regularly. A new pedestal calibration is performed whenever there is any change in detector configuration, for example, high voltage change or detector alignment change. The first step in the pedestal calibration procedure is to calibrate the UNSER. Once the UNSER is calibrated, it is used to calibrate the normalizing BCM. The normalizing BCM (the BCM which is used to charge normalize the detector signal) is then used to calibrate the other BCMS, BPMs, and detector pedestals. All pedestal calibrations are performed with dedicated current-ramp calibration runs. The pedestal calibration plots for the upstream main (tandem) detectors for a typical current-ramp calibration run are shown in Fig. 4.9.

4.2. ASYMMETRY ANALYSIS

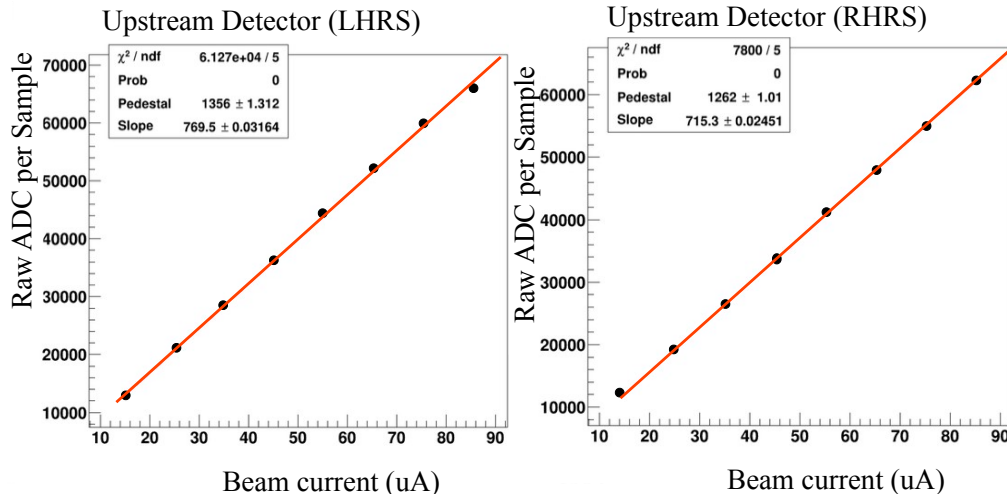


Figure 4.9: Pedestal calibration for upstream main detectors for a typical current-ramp calibration run. The detector’s raw ADC value per sample is plotted against beam current, where the beam current is increased in steps of $10 \mu\text{A}$. The data points are fitted with a first-order polynomial. Under ideal conditions, the raw ADC value per sample should be a linear function of beam current, and thus the detector pedestal is given by the y -intercept of the fit.

4.2.3 Raw Asymmetry and Charge Normalization

The measured asymmetry arises from the integrated rate differences of the main detectors between opposite helicity states of the beam. Refer to Sec. 3.10 for a discussion of the integrating DAQ technique. The raw asymmetry measured by each detector is given by

$$A_{raw} = \frac{\frac{F_R}{I_R} - \frac{F_L}{I_L}}{\frac{F_R}{I_R} + \frac{F_L}{I_L}}, \quad (4.4)$$

where F_R and F_L are the flux measured by the detector during a consecutive pair of right and left helicity window states, and I_R and I_L are the corresponding beam intensities. To first order, Eq. 4.4 can be simplified to

$$A_{raw} = A_{det} - A_q, \quad (4.5)$$

4.2. ASYMMETRY ANALYSIS

where $A_{det} = \frac{F_R - F_L}{F_R + F_L}$ is the asymmetry measured by a detector, and $A_q = \frac{I_R - I_L}{I_R + I_L}$ is the charge (or intensity) asymmetry measured by the BCM. We measure the asymmetry in both spectrometers and take an average of the two. Taking the average of the two spectrometers is important because it helps cancel any potential false background due to beam motion along the horizontal direction (left and right of the beam axis). The cancellation occurs because the signal detected in one spectrometer is correlated with beam position, while the signal detected in the other spectrometer is anti-correlated with the beam position. The fast helicity reversal and its frequency are discussed in Sec. 3.10. The blinded¹ average raw asymmetry from the two HRSs and the charge (intensity) asymmetry measured by PREX-2 are given in Table 4.1. Using a 1.0 % non-linearity factor in the measurement’s BCM normalization², the systematic error contribution to A_{PV} from A_q (the charge or intensity asymmetry) is 0.04 % relative (0.25 ppb absolute).

	Mean (ppb)	Error (ppb)	RMS (ppm)
A_{raw}	431.64	44.01	350.28
A_q	20.68	25.80	176.79

Table 4.1: Average raw asymmetry (blinded) and charge asymmetry during PREX-2.

4.2.4 Helicity-correlated Position Differences (HCPD)

The beam position monitors (BPMs) used in the experiments are discussed in Sec. 3.4.3. The pattern-wise beam position and energy differences between pairs of opposite helicity states give rise to a potential false asymmetry background. As we will discuss in Sec. 4.2.5, bpm4a, and bpm4e are the main BPMs used for determining the beam

¹To avoid human bias on the measured asymmetry, a random blinding offset is applied to the true asymmetry. It is implemented in the analyzer software, “JAPAN,” using a “secret” supplied character string as the seed for generating a random number. The random number defines a blinding offset which is added to the calculated asymmetry before any human can see it. The blinding offset is extracted and removed only after all the analysis projects are completed.

²The BCM non-linearity is monitored regularly in-situ using current ramp calibration runs.

4.2. ASYMMETRY ANALYSIS

fluctuation corrections. Each of these BPMs records the beam position along the \hat{x} and \hat{y} axes of the hall coordinate system. For the energy fluctuation correction (for all data except slugs 1 and 2), PREX-2 uses a linear combination of the x -position measured by the two energy monitors bpm11 and bpm12 (referred to as $bpm11X$ and $bpm12X$, respectively), and it is defined as

$$bpmE = bpm11X + 0.4 \times bpm12X. \quad (4.6)$$

Slugs 1 and 2 use only $bpm12X$ for the energy fluctuation correction (bpm11 is not functional until slug 3). If $X_{L(R)}$ is the beam position for the left(right) helicity states in a multiplet pattern, then the position difference, ΔX , is calculated using

$$\Delta X = \frac{X_R - X_L}{2}. \quad (4.7)$$

The differences are then weighted by the statistical errors of the left-right HRS average asymmetry (after beam corrections are applied). The weighted, slug-average position difference is given by

$$\langle \Delta X \rangle = \frac{\sum_i w_i \Delta X_i}{\sum_i w_i}, \quad (4.8)$$

and the weighted slug-average position difference error is given by

$$\langle \sigma_{\Delta X} \rangle = \sqrt{\frac{\sum_i w_i^2 \sigma_{X_i}^2}{(\sum_i w_i)^2}}, \quad (4.9)$$

where $w_i = \frac{1}{\sigma_{A_i}^2}$, σ_{A_i} is the error on the left-right HRS average asymmetry measured by the upstream main detectors, and i runs over the miniruns in the corresponding

4.2. ASYMMETRY ANALYSIS

slug. The (weighted) “grand³” averages of the position differences for PREX-2 are given in Table 4.2.

ΔX	Mean (nm)	Error (nm)	RMS (μm)
$\Delta bpm4eX$	-0.66	1.45	10.21
$\Delta bpm4eY$	1.34	0.61	4.25
$\Delta bpm4aX$	0.48	0.24	1.74
$\Delta bpm4aY$	1.91	0.95	6.52
$\Delta bpmE$	2.33	1.09	7.85

Table 4.2: Helicity-correlated position and energy differences during PREX-2. These are the statistically weighted grand averages (analysis done by Tao Ye).

The position and angle differences on the target can be obtained using bpm4a and bpm4e as follows:

$$\Delta X_{targ} = \frac{\Delta bpm4eX - \Delta bpm4aX}{D/L} + \Delta bpm4aX, \quad (4.10)$$

$$\Delta Y_{targ} = \frac{\Delta bpm4eY - \Delta bpm4aY}{D/L} + \Delta bpm4aY, \quad (4.11)$$

$$\Delta \theta_X = \frac{\Delta bpm4eX - \Delta bpm4aX}{D}, \quad (4.12)$$

and

$$\Delta \theta_Y = \frac{\Delta bpm4eY - \Delta bpm4aY}{D}, \quad (4.13)$$

where $D = 4.083$ m is the distance along the beamline between bpm4e and bpm4a, while $L = 5.725$ m is the distance between the target and bpm4a. The grand-averaged position and angle differences at the target for the PREX-2 data set are given in Table

³The average over the entire PREX-2 experiment.

4.2. ASYMMETRY ANALYSIS

4.3.

	Mean	Error
ΔX_{targ}	-1.3 nm	2.0 nm
ΔY_{targ}	1.1 nm	0.5 nm
$\Delta\theta_X$	-0.28 nrad	0.32 nrad
$\Delta\theta_Y$	-0.14 nrad	0.09 nrad

Table 4.3: The grand-averaged, helicity-correlated beam position and angle differences at the target for PREX-2 (analysis done by Tao Ye and Caryn Palatchi).

4.2.5 Beam Fluctuation-corrected Asymmetry (A_{cor})

The physics asymmetry measurement arises from the difference in the detected scattered flux between left and right polarization states of the incident electron bunch on the target. We call each of these polarization states a helicity window. Any systematic change in the beam characteristics, such as position, energy, and angle caused by this helicity reversal, accounts for a potential false asymmetry. We call this helicity-correlated false asymmetry, which requires correction or removal from the asymmetry measured by our detectors. The beam position and energy jitter (noise) RMS is several times greater than the measured asymmetry counting statistics (RMS width), which can pose a potentially large systematic uncertainty in our measurement if not corrected for properly. This statement is true for all the quartz detectors, including main detectors, auxiliary detectors, and SAMs. The asymmetry after beam corrections is given by

$$A_{cor} = A_{raw} - A_{false}, \quad (4.14)$$

where $A_{false} = \sum_i \alpha_i \Delta M_i$ is the helicity-correlated beam asymmetry (note the charge asymmetry A_q is already corrected while calculating A_{raw}). A_{false} comes from natural

4.2. ASYMMETRY ANALYSIS

fluctuations in beam position and energy. ΔM_i is the helicity-correlated position, angle, or energy difference of the i^{th} monitor and α_i is the regression slope of A_{raw} to ΔM_i . We use three different techniques to make this correction. This allows for consistency cross checks between the different methods. The techniques are: linear regression, dithering, and the so-called Lagrange multiplier method. Figure 4.10 shows the power of the beam fluctuation corrections for a typical run. The correction techniques help cancel beam jitter and lower the statistical width of the asymmetry distribution from ≈ 269 ppm to ≈ 92 ppm (which is close to the statistical width limit).

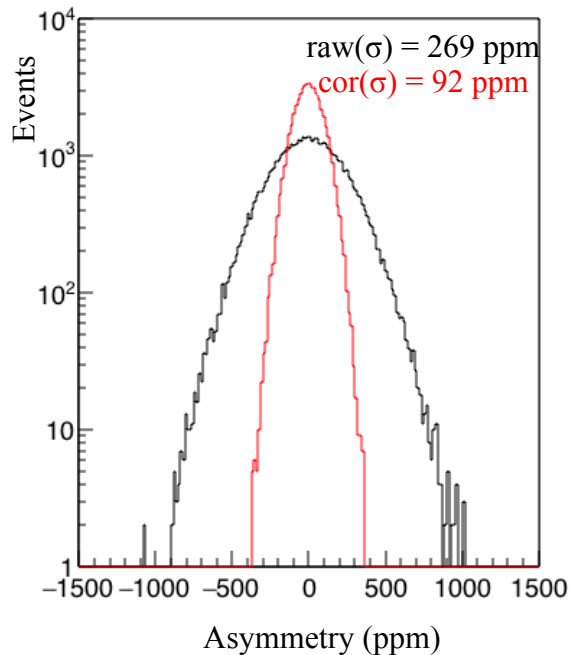


Figure 4.10: Demonstration of the power of beam corrections for a typical run during PREX-2. The natural fluctuations in the beam cause the measured asymmetry width (before beam corrections) to be roughly 3 times worse than the theoretical counting statistics width. Recall that counting statistics widths go as $\frac{1}{\sqrt{N}}$, where N is the number of detected electrons in the helicity multiplet pattern.

Linear Regression

The linear regression (or just regression) beam correction technique uses the measured correlation slopes of the raw asymmetry versus position, angle, and energy differences

4.2. ASYMMETRY ANALYSIS

due to natural beam motion during production data taking; it simply uses the natural beam motion to calculate the slopes, which is in contrast with the beam modulation correction technique discussed in the next subsection. To get the regression slopes, the asymmetries are plotted against the position differences, and the slopes are extracted. Example correlation plots between the upstream main detector asymmetries and position differences of $bpm4eX$, $bpm4eY$, and $bpm12X$ for a typical run are shown in Fig. 4.11.

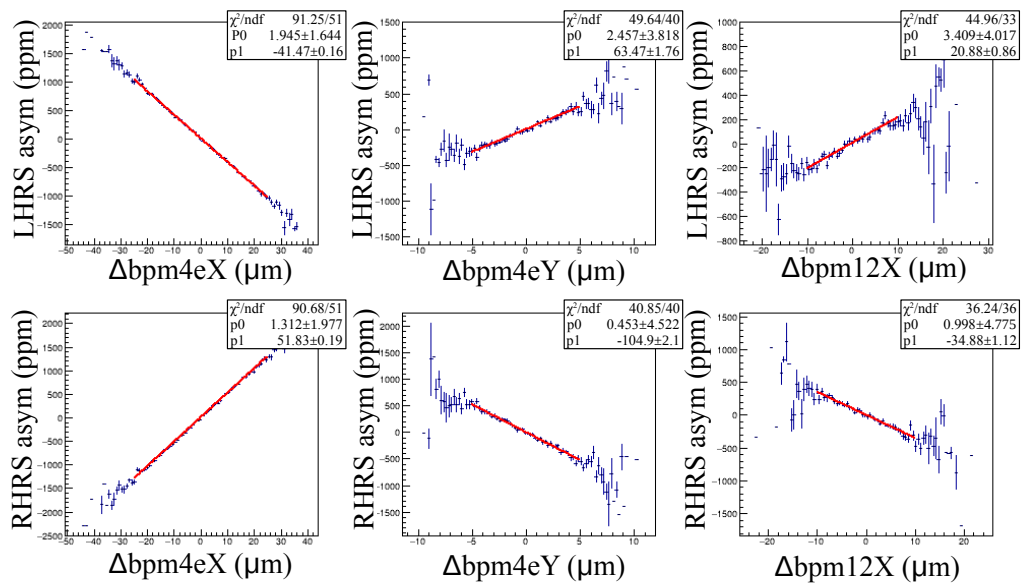


Figure 4.11: Correlation between raw asymmetry and beam position difference ($\Delta X = \frac{X_R - X_L}{2}$) for $bpm4eX$, $bpm4eY$, and $bpm12X$ during PREX-2. Recall $bpm12X$ is sensitive to beam energy.

In this method, the slope of each beam parameter is determined using a least-squares fit, which minimizes the χ^2 . In the multivariate regression equation, detector raw asymmetries are the dependent variables, while the position differences measured by the twelve different monitors ($bpm11X$, $bpm11Y$, $bpm12X$, $bpm12Y$, $bpm16X$, $bpm16Y$, $bpm1X$, $bpm1Y$, $bpm4aX$, $bpm4aY$, $bpm4eX$, and $bpm4eY$) are the independent variables. The idea is to minimize

4.2. ASYMMETRY ANALYSIS

$$\chi^2 = \sum_j \left(A_{raw_j} - \sum_i \alpha_i (\Delta M_i)_j \right)^2, \quad (4.15)$$

where $(\Delta M_i)_j$ is the j^{th} measurement of the i^{th} independent variable. The χ^2 is then minimized for each α_i , i.e. $\frac{\partial \chi^2}{\partial \alpha_i} = 0$. This equation is solved for the regression coefficients α_i using a matrix inversion algorithm.

Beam Modulation (or Dithering)

The beam modulation technique uses controlled, induced excursions of the beam position, angle, and energy on target. It then determines the responses of the detectors $\left(\frac{\partial D}{\partial C_k}\right)$ and monitors $\left(\frac{\partial M_i}{\partial C_k}\right)$, where C_k represents the modulation coils (seven total), D represents the detector responses, and M_i represents the position (and energy) monitor responses (twelve total). Figure 4.12 shows example detector and monitor sensitivities for a typical modulation cycle. The beam modulation or dithering correction technique is an invasive procedure which energizes the modulation coils, as explained in Sec. 3.4.1, at a 15 Hz frequency and with $\sim 100 \mu\text{m}$ amplitude position swings. On longer time scales, the 15 Hz frequency helps cancel 60 Hz electronic noise and random beam fluctuations. There are seven total modulation coils available, five of them are used in the final analysis and the remaining two are used for redundancy checks.

The normalized detector sensitivity to the k^{th} modulation coil, $\frac{\partial D}{\partial C_k}$, is expressed in terms of the beam position monitors' sensitivity to the same modulation coil $\left(\frac{\partial M_i}{\partial C_k}\right)$ as

$$\frac{\partial D}{\partial C_k} = \sum_i \frac{\partial D}{\partial M_i} \frac{\partial M_i}{\partial C_k}. \quad (4.16)$$

This equation can be rewritten in matrix form as $\mathbf{D}_C = \mathbf{D}_M \mathbf{M}_C$, from which the

4.2. ASYMMETRY ANALYSIS

normalized detectors' slope to the i^{th} position monitor, $\alpha_i = \frac{\partial D}{\partial M_i}$, is extracted using the inversion matrix method, provided that the matrix \mathbf{M}_C is non-singular.

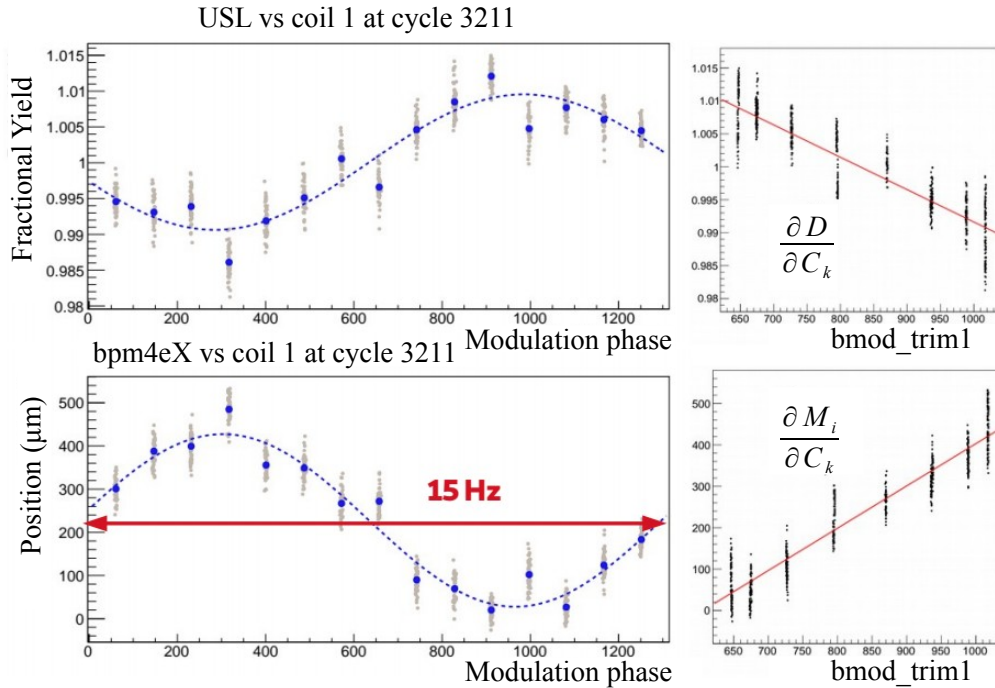


Figure 4.12: An example of beam modulation for a typical modulation cycle [69]. The detector sensitivity $\frac{\partial D}{\partial C_k}$ and monitor sensitivity $\frac{\partial M_i}{\partial C_k}$ for the k^{th} modulation coil (or trim) are used in Eq. 4.16 to calculate the correction slope ($\frac{\partial D}{\partial M_i}$).

Lagrange Multipliers

The Lagrange multipliers technique is a hybrid of the regression and beam modulation techniques. It calculates the correction slopes and performs χ^2 minimization (as in linear regression) of the Lagrangian defined by

$$\mathcal{L} = \chi^2 + \sum_k \lambda_k \left(\frac{\partial D}{\partial C_k} - \sum_i \alpha_i \frac{\partial M_i}{\partial C_k} \right), \quad (4.17)$$

where λ_k is a Lagrange multiplier for the k^{th} modulation coil, where k runs over the chosen five modulation coils, and i runs over the twelve monitors/eigenvectors (see next paragraph). The slopes are extracted solving Eq. 4.17 with the constraints

4.2. ASYMMETRY ANALYSIS

$$\frac{\partial \mathcal{L}}{\partial \lambda_k} = 0 \quad \text{and} \quad \frac{\partial \mathcal{L}}{\partial \alpha_i} = 0. \quad (4.18)$$

Direct comparison between regression with other beam correction techniques, e.g. beam modulation, can be overwhelmed by the effects of parameter correlation causing the errors to (artificially) inflate. To get rid of the parameter correlation effect, the Lagrange multiplier method diagonalizes the 12×12 BPM covariance matrix by eigenvalue decomposition, then it calculates the helicity correlated differences and correction slopes in the eigenvector basis⁴.

The largest correction slope comes from the energy jitter. The uncertainty in each slope measurement is within 3 %, and we assume a global 3 % uncertainty in all slope calculations. So the quoted uncertainty in A_{false} is assigned based on the 3 % uncorrelated uncertainty (added in quadrature) in the correction from each of the five beam parameters, which is consistent with cross-checks among various regression and beam-modulation analyses [70]. The total correction to the asymmetry due to beam fluctuation is:

$$A_{false} = -60.38 \pm 2.50 \text{ ppb}, \quad (4.19)$$

where the uncertainty on A_{false} contributes 0.54 % relative (2.98 ppb absolute) to the A_{PV} systematic error tally. The beam-corrected blinded asymmetry as a function of slug number (or time) is shown in Fig. 4.13. The average corrected asymmetry after removing the blinding offset is given by

$$A_{cor} = 492.55 \pm 13.52 \text{ ppb}, \quad (4.20)$$

where the quoted error is purely statistical.

⁴The beam correction and associated systematic uncertainty analysis is led by Tao Ye.

4.2. ASYMMETRY ANALYSIS

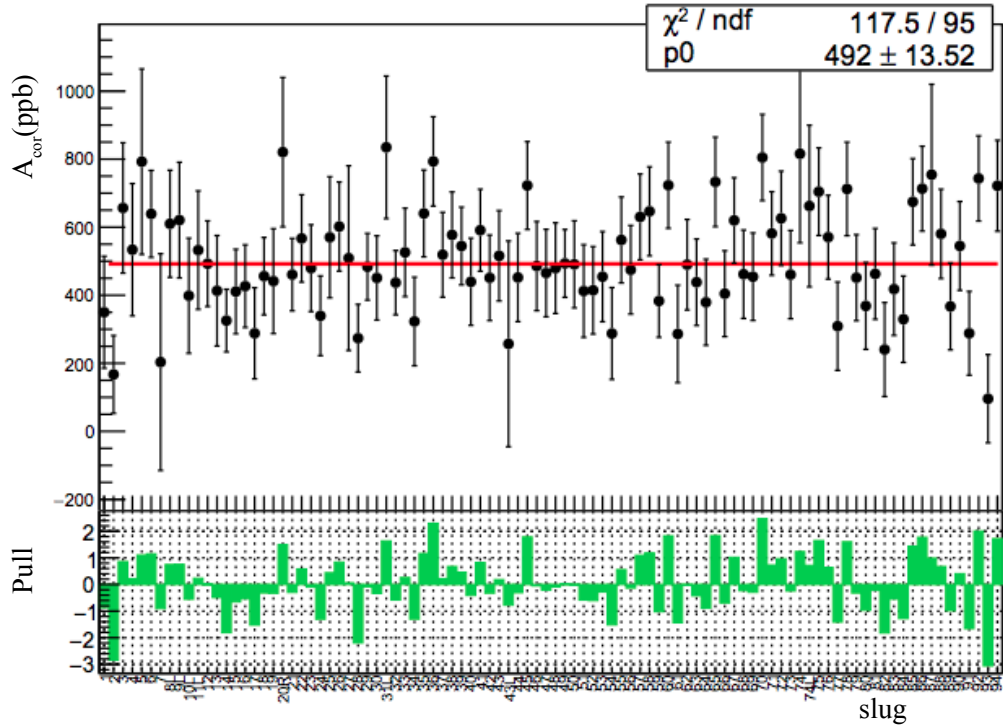


Figure 4.13: PREX-2 Lagrange-corrected (blinded) asymmetry as a function of slug number (or time). The slug number with L(R) means the slug is taken with only the left(right) HRS and all other slugs are taken with both HRSs. The bar graph in the lower panel shows the “pull” distribution, which is defined as $\text{Pull} = \frac{A_i - \langle A \rangle}{\sigma_{A_i}}$, where A_i is each asymmetry data point, σ_{A_i} is the error bar of that data point, and $\langle A \rangle$ is the average asymmetry obtained from zeroth order polynomial fit (red line). (Plot taken from Tao Ye).

4.2.6 Helicity-correlated Pedestal Asymmetry (HCPA)

One of the potential sources of systematic uncertainty is the helicity-correlated pedestal asymmetry. In this section, we discuss the HCPAs which are measured when the beam is off. Any asymmetry measured by the detectors, when there is no physics signal in the quartz, comes from a helicity-correlated electronics signal (noise). Ideally, an asymmetry between the opposite helicity windows should be null when there is no beam. If “ a ” and “ b ” are the measured signals, for the opposite helicity states in a multiplet pattern, for a beam-off pedestal run, then:

4.2. ASYMMETRY ANALYSIS

$$\text{HCPA} = \frac{(a - b)/2}{\text{production_yield}}, \quad (4.21)$$

where `production_yield` is the average measured signal (for a helicity multiplet pattern) during production running.

The HCPA measured by the upstream main detector for a typical beam-off run in each HRS is shown in Fig. 4.14. The RMS of this asymmetry distribution gives the level of electronic noise. Figure 4.15 shows the grand aggregated HCPA for both detectors. For this analysis we chose a sample of beam-off runs from various times during PREX-2 running. The colors in the data points represent different combinations of IHWP and Wien settings, as shown in the legend. Table 4.4 gives the grand aggregated HCPA and pedestal noise, which are found to be too small to pose any problem with interpreting the physics asymmetry.

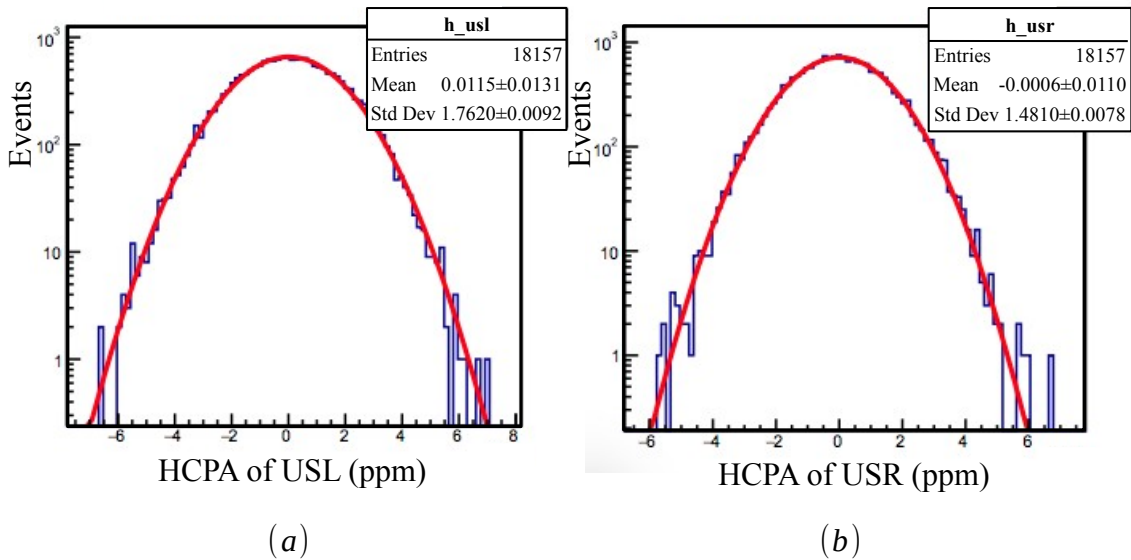


Figure 4.14: Helicity-correlated pedestal asymmetry for a typical beam-off run during PREX-2; blue histogram data is shown with red Gaussian fit. (a) Left-HRS upstream main detector, and (b) right-HRS upstream main detector.

4.3. BACKGROUNDS AND POSSIBLE CORRECTIONS

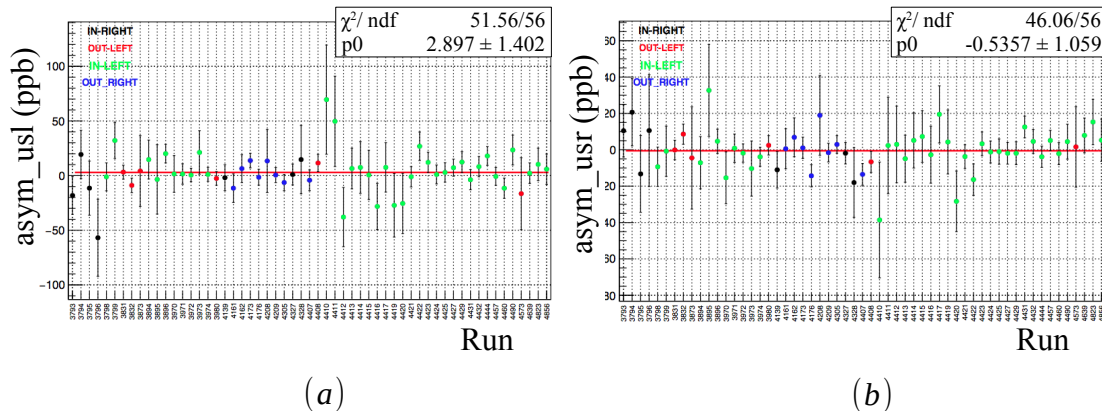


Figure 4.15: Grand aggregated helicity-correlated pedestal asymmetry for selected beam-off runs from various dates during PREX-2 running. (a) Left-HRS upstream main detector, and (b) right-HRS upstream main detector.

Detector	HCPA (ppb)	χ^2/NDF	Noise (ppm)
USL	2.9 ± 1.4	51.6/56	2.0
USR	-0.5 ± 1.1	46.1/56	1.5

Table 4.4: Grand aggregated helicity-correlated beam-off asymmetries and pedestal noise for PREX-2.

4.3 Backgrounds and Possible Corrections

In contrast to hadronic-based scattering probes (e.g. proton, pion, α -particle, etc.), PVeS measurements are relatively clean (both experimentally and theoretically) and allow a model-independent approach for extracting the neutron skin thickness in neutron-rich nuclei. PVeS uses state-of-the-art equipment and measures A_{PV} , which arises from the peculiar, parity-violating nature of the weak interaction. The measurement is relatively clean, in the sense that a detailed study has been done on the various possible corrections, and it has been shown over time that the systematic uncertainties corresponding to such corrections are negligible. An extensive study of those corrections has been done by Horowitz et al. [23] (see Appendix B). If a background contribution is significant, we need to correct for it. If it is small, we may not correct for it, but instead choose to add its full contribution to the system-

4.3. BACKGROUNDS AND POSSIBLE CORRECTIONS

atic uncertainty tally. The physics A_{PV} after applying background corrections to the beam-corrected asymmetry, A_{cor} , is given by

$$A_{PV} = \frac{A_{cor} - P_b \sum_i f_i A_i}{P_b(1 - \sum_i f_i)}, \quad (4.22)$$

where f_i is the contamination fraction of the i^{th} background source, A_i is the asymmetry of the background, and P_b is the beam polarization. In the following subsections we describe some of the possible backgrounds and corrections.

4.3.1 Coulomb Distortion

Coulomb distortion comes from the repeated electromagnetic interactions of incident electrons off a target nucleus. Figure 4.16(b) shows the basic mechanism of Coulomb distortion. This effect significantly reduces A_{PV} and scales with nuclear charge number Z as $\frac{\alpha Z}{\pi}$ [23]. Therefore, for ^{208}Pb , the correction is $\approx 20\%$, while for ^{48}Ca , it is $\approx 5\%$. The Coulomb distortion corrections have been calculated by [22] with an accuracy better than our expected experimental precision goal. This is done by solving the Dirac equation numerically for an electron in an axial-vector weak and Coulomb potential.

4.3.2 Beam Polarization

The uncertainty in beam polarimetry is perhaps the most critical systematic error to control during a PVeS experiment. To ensure accuracy, two independent methods for monitoring beam polarization, referred to as the Møller and Compton polarimeters, are utilized. Details about the hardware and working mechanism of these polarimeters are given in Sec. 3.4.5. Due to the lower beam energy of PREX-2, the Compton polarimeter's photon detector has a low signal-to-noise ratio and the measured

4.3. BACKGROUNDS AND POSSIBLE CORRECTIONS

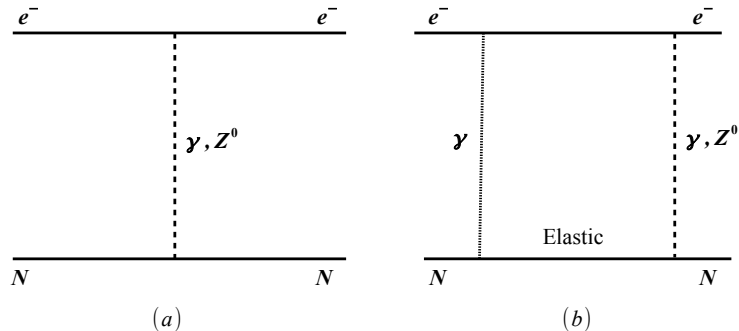


Figure 4.16: (a) Electroweak interaction in the Born approximation. (b) Coulomb distortion effect. In the context of an electroweak interference probe (γ, Z^0), the extra γ -exchange here depicts the Coulomb distortion mechanism, which can involve repeated interactions of beam electrons off the target nucleus—which remains in its ground state. This effect can significantly alter the measured asymmetry and must be taken into account.

asymmetry (or analyzing power) is small. This makes the Compton measurements for PREX-2 very challenging, and it is difficult to bound its systematic uncertainty. Therefore, PREX-2 does not include Compton results in the final analysis (only the Møller results are used). The beam polarization measured by the Møller polarimeter averaged over the entire PREX-2 running is

$$P_b = 89.67 \pm 0.80 \%. \quad (4.23)$$

The beam polarization correction contributes 5.23 ppb absolute (0.95 % relative) in the A_{PV} final systematic uncertainty.

4.3.3 Detector Non-linearity

Detector non-linearity is another important source of systematic uncertainty that needs to be understood and controlled. The non-linearity is studied in bench tests before and after the experiments and in-situ during the experiments. Details about the bench test studies are given in Sec. 3.6.4. From the LED bench tests, the non-

4.3. BACKGROUNDS AND POSSIBLE CORRECTIONS

linear response of each PMT is found to be less than 0.3 % at PREX-2/CREX gain settings and light levels. The beam-based non-linearity is monitored via PITA scans and current-ramp calibration runs. PITA scans are limited by beam corrections and can not give a precise measurement of non-linearity. As we mentioned in Sec. 4.2.2, the detector pedestals are calibrated using the normalizing BCM, while the normalizing BCM pedestal is calibrated using the UNSER BCM. The current-ramp pedestals match the beam-off (bench test) pedestals within 0.5 %. Therefore, we do not make any non-linearity correction to A_{PV} , but assign a relative systematic uncertainty due to non-linearity equal to 0.49 % (2.69 ppb absolute).

4.3.4 Target Backing and Impurity Correction

The purity of the target material plays an essential role in the interpretation of the measured asymmetry. A target such as ^{208}Pb requires a backing material to help protect it from melting while running at high beam currents. Even with a proper (large) beam raster, a pure lead target without backing does not last long because of its poor thermal conductivity and relatively low melting point. Therefore, finding a material that can be used to help transfer heat—keeping the target from being overheated—is a challenge. But the concern is that the backing material should be one that does not contaminate our physics asymmetry too much, and we must have knowledge of its asymmetry. Keeping this in mind, we construct PREX-2 targets with Pb foils sandwiched between thin diamond foils. Details of the target design are given in Sec. 3.4.6. The parity-violating asymmetry of ^{12}C is known that its contamination to the measured asymmetry can be easily corrected. The target backing- or dilution-corrected asymmetry of ^{208}Pb , A_{PV} , is calculated using

$$A_{PV} = \frac{A_{cor} - P_b f_C A_C}{P_b(1 - f_C)}, \quad (4.24)$$

4.3. BACKGROUNDS AND POSSIBLE CORRECTIONS

where A_{cor} is the beam fluctuation-corrected asymmetry, P_b is the beam polarization, f_C is the carbon dilution fraction, and A_C is the parity-violating asymmetry of carbon.

Carbon Dilution Fraction (f_C)

The dilution fraction (f_C) is the fractional contamination of the detected signal coming from the ^{12}C nuclei. It is given by

$$f_C = \frac{R_C}{R_{Pb} + R_C}, \quad (4.25)$$

where R_C and R_{Pb} are the rates detected by our detectors from ^{12}C and ^{208}Pb nuclei, respectively. The rates are obtained from GEANT4 simulations in order to calculate f_C . From these simulations for PREX-2, $R_C = 0.129$ GHz and $R_{Pb} = 1.93$ GHz giving

$$f_C = 0.0629 \pm 0.0046, \quad (4.26)$$

where the uncertainty comes from the 5 % uncertainty in the thickness measurement of each diamond and lead foil. This result is cross-checked with other methods, such as using known cross-sections:

$$f_C = \frac{t_C \times \sigma_C}{m_C} \left(\frac{t_{Pb} \times \sigma_{Pb}}{m_{Pb}} + \frac{t_C \times \sigma_C}{m_C} \right)^{-1}, \quad (4.27)$$

where t_C (t_{Pb}), σ_C (σ_{Pb}), and m_C (m_{Pb}) are the thickness, cross-section, and mass of the diamond (lead) foil, respectively. Another cross-check is performed using the available form factors for ^{12}C and ^{208}Pb as follows:

4.3. BACKGROUNDS AND POSSIBLE CORRECTIONS

$$f_C = \frac{t_C \times Z_C^2 \times FF_C^2}{m_C} \left(\frac{t_{Pb} \times Z_{Pb}^2 \times FF_{Pb}^2}{m_{Pb}} + \frac{t_C \times Z_C^2 \times FF_C^2}{m_C} \right)^{-1}, \quad (4.28)$$

where Z_C (Z_{Pb}) and FF_C^2 (FF_{Pb}^2) are the nuclear charge number and form factor squared for ^{12}C (^{208}Pb), respectively. The results obtained from these various approaches agree within the error given in Eq. 4.26.

^{12}C Asymmetry (A_C) and Correction

The carbon asymmetry is also obtained from the GEANT4 simulation using a cross section table generated by Chuck Horowitz. The carbon asymmetry is found to be ≈ 539 ppb. The uncertainty on A_C is taken as 4 % (21.56 ppb), the experimental uncertainty of the HAPPEX-He4 experiment. Using A_C and f_C from Eq. 4.26, the asymmetry correction due to the diamond backing is 0.69 ppb. The absolute systematic uncertainty contribution to A_{PV} due to this correction is 1.45 ppb (0.26 % relative).

Target Impurity Correction for CREX

For CREX, target heating is not as big an issue as it is for PREX. CREX uses a 1 gm/cm² isotopically pure ^{48}Ca target. The melting point of such a target is 842 °C. Computational Fluid Dynamic (CFD) calculations performed by the collaboration indicated a raster size of 2×2 mm² is sufficient to keep the target temperature well below its melting point, therefore no thermal backing is needed. Following the ^{48}Ca target accident, the original target is replaced with a ^{48}Ca composite target with ≈ 8 % ^{40}Ca composition (see Sec. 3.4.6 for details). Also, the pure calcium targets are highly oxidizing, and special care must be taken to limit any accidental exposure to

4.3. BACKGROUNDS AND POSSIBLE CORRECTIONS

the atmosphere. Any asymmetry associated with such an impurity can contribute systematic background in the measured asymmetry and needs correction.

4.3.5 Inelastic Contributions

If one knows the parity-violating asymmetry for low-lying excited states (from inelastic scattering), then practically speaking, it could be desirable to accept some fraction of inelastic flux and then make corrections in the offline analysis. This increases the detected rate, and can be done either by increasing the target thickness or by placing the detectors in such a way that they can accept the inelastic scattered flux. However, increasing the target thickness results in more radiative losses, and in turn, results in worse detector (energy) resolution. One can also think about measuring A_{PV} for different Q^2 or different scattering angles. But there is a catch to all these ideas or possibilities: changing these parameters not only affects the detected rate (R) but also the measured asymmetry (A) and the *sensitivity* (ϵ , see Sec. 2.10.3) of the asymmetry to the extracted neutron radius (R_n). It is always desirable to optimize the Figure Of Merit ($FOM = R \times A^2 \times \epsilon^2$) which minimizes the error in R_n for a given runtime. For a sufficiently large separation of the inelastic events from the elastic peak, one needs to use a spectrometer with high resolution. The HRSs in Hall A at JLab meet this requirement and provide $\sim 10^{-4}$ (~ 0.01 %) momentum resolution.

The target nuclei considered for PREX-2 (^{208}Pb) and CREX (^{48}Ca) have large first excited states, that is, a relatively large amount of energy is required to excite the nuclei from the ground state. The first inelastic peak in ^{208}Pb is at 2.615 MeV (energy loss of the inelastically scattered beam electron) with spin-parity 3^- , while in ^{48}Ca it is at 3.831 MeV and with spin-parity 2^+ . The extreme momentum resolution of the HRS combined with precision alignment of the main quartz detectors, helps us identify and geometrically exclude most of the inelastic events from the quartz

4.3. BACKGROUNDS AND POSSIBLE CORRECTIONS

measurement.

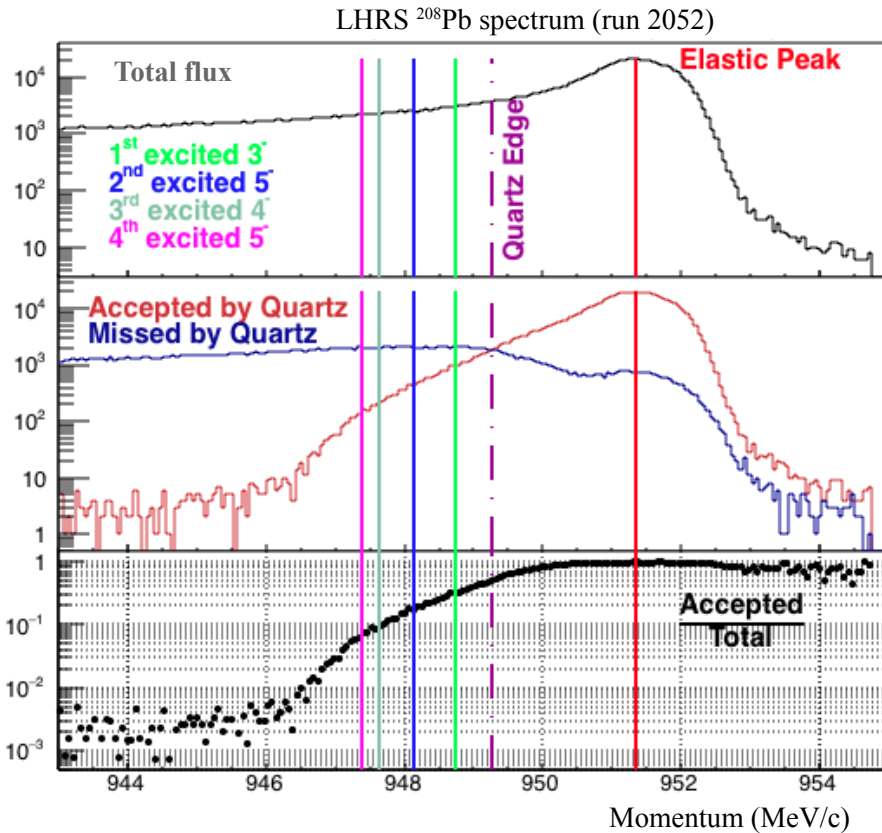


Figure 4.17: Energy or momentum distribution for ^{208}Pb during PREX-2. The black histogram in the top plot shows all the events. The middle plot shows the events accepted by the quartz (red histogram), and the events missed by the quartz (blue histogram). The bottom plot shows the accepted events (from middle plot) divided by the total events (from top plot). The elastic peak, quartz edge, and first four excited state positions (in momentum space) are shown and labelled using different colored vertical lines.

The energy or momentum spectrum of ^{208}Pb for a typical counting mode run is shown in Fig. 4.17. The histogram at the top is for all the events that reached the focal plane with some general cuts such as VDC single cluster and T1 trigger. The red and blue histograms in the middle plot are subsets of the top histogram; the red histogram is for the events which pass the upstream main detector’s ADC cut, while the blue histogram shows the events which fail the ADC cut; the intersection of these two histograms indicates the quartz edge position (in terms of momentum) shown as

4.3. BACKGROUNDS AND POSSIBLE CORRECTIONS

the dashed vertical line. The bottom histogram in the figure shows the ratio of the red histogram (in the middle) and the black histogram at the top. This plot gives the probability for each of the energy bins to be accepted by the quartz detector. The location of the elastic peak, quartz edge, and the first four excited states are shown by different colored lines. The beam energy for PREX-2 is 953.4 MeV, while the elastic peak is at 951.4 MeV. This corresponds to a 2.0 MeV energy loss, which accounts for radiation, collisional, recoil, and ionization energy losses in the target. Focal plane electrons having energy greater than 950 MeV have approximately 100 % probability of being accepted (see bottom plot of Fig. 4.17), while the probability drops gradually for electrons with lower energy. The acceptance probability for the energy bins corresponding to the elastic peak and the excited states of ^{208}Pb during PREX-2 are given in Table 4.5.

State	Acceptance (%)
Ground (Elastic)	100
1 st excited (3^-)	30
2 nd excited (5^-)	20
3 rd excited (4^-)	10
4 th excited (5^-)	5

Table 4.5: Acceptance probability of the elastic peak and first four excited states of ^{208}Pb during PREX-2.

To calculate the background fraction for each of the inelastic states, we need to multiply the probabilities given in Table 4.5 by their relative cross-sections. As can be seen in the upper plot of Fig. 4.17, there is no visible peak in the spectrum for any of the Pb excited state locations; approximately all of the events beyond the quartz acceptance are radiative tail events. Table 4.6 gives the cross-sections, relative to the size of the elastic cross section, for the first (3^-) excited state as a function of the effective four momentum transfer, q_{eff} . The effective four momentum transfer is given by

4.3. BACKGROUNDS AND POSSIBLE CORRECTIONS

$$q_{eff} = q \left(1 + \frac{4Z\alpha}{3E_i R_{RMS}} \right), \quad (4.29)$$

where $R_{RMS} = R_0 A^{\frac{1}{3}}$.

q_{eff} (fm ⁻¹)	$\frac{\sigma_{3^-}}{\sigma_{elastic}}$ (%)
0.550	0.123
0.692	0.804
0.837	1.066
0.974	0.954
1.117	2.226
1.226	6.380
1.258	6.309
1.436	3.867
1.631	7.347

Table 4.6: Cross-sections, relative to the elastic cross section, of the first excited state of ²⁰⁸Pb as a function of the effective four momentum transfer (q_{eff}) [71].

For PREX-2, $Q^2 = 0.00616$ (GeV/c)² leads to $q = 0.40$ fm⁻¹, which gives q_{eff} much smaller than 0.550 fm⁻¹ (the lowest value in Table 4.6). Thus, for PREX-2 kinematics, $\frac{\sigma_{3^-}}{\sigma_{elastic}}$ is estimated to be 0.1 %. The background fraction (f) due to the first excited state is given by the product of the acceptance probability and the relative strength, i.e. $f_{3^-} = 0.0003$. [23] has shown that the asymmetry of the 3⁻ state in ²⁰⁸Pb is

$$A_{3^-} \approx 1.25 \times A_{elastic}. \quad (4.30)$$

Using $A_{cor} = 492.6$ ppb we obtain $A_{3^-} = 615.8$ ppb, and we assume 50 % uncertainty in it. Using the values of f_{3^-} , A_{3^-} , and P_b in Eq. 4.22, we get a negligibly small correction due to the first excited state. Other excited states are farther away from the quartz acceptance, and hence their contamination is also negligible. Although no correction is applied to the physics asymmetry, the uncertainty associated with

4.3. BACKGROUNDS AND POSSIBLE CORRECTIONS

the calculation of f_{3-} and A_{3-} is propagated to the final systematical uncertainty calculation. Table 4.7 gives the correction and systematic uncertainty in A_{PV} due to the inelastic contribution.

Quantity	Correction (ppb)	Absolute Error (ppb)	Rel. Error (%)
f_{3-}	0	0.04	0.01
A_{3-}	0	0.11	0.02

Table 4.7: Corrections and systematic errors on A_{PV} for PREX-2 due to the inelastic background from the first excited state.

An analysis of the inelastic background for CREX is given in Appendix C.

4.3.6 Rescattering during HRS Transport

This background comes from inelastically scattered electrons and/or radiative tail events which are accepted into the HRS collimator, but whose energy is sufficiently low that they do not transport correctly to the focal plane. This background is not the same as the inelastic background described in the previous section. The inelastic electrons discussed here are ones far from the elastic peak, which “rescatter” off the spectrometer wall (thus the name). These electrons can possibly reach the quartz detector acceptance and get integrated with the physics signal. Thus we must correct the asymmetry measurement or bound the error associated with this background.

The strength of the accepted background signal, B_{rs} , is given by the integral over the scattered energies from the inelastic threshold E_{thr} to the maximum energy loss E_{max} , and is expressed as

$$B_{rs} = \int_{E_{thr}}^{E_{max}} dE P_{rs}(E) R(E), \quad (4.31)$$

where the rescattering function, $P_{rs}(E)$, is given by

4.3. BACKGROUNDS AND POSSIBLE CORRECTIONS

$$P_{rs}(E) = \tau \times \left(\frac{E_{dep}}{E_0} \right), \quad (4.32)$$

and $R(E)$ is the ratio of the inelastic to elastic cross-section given by

$$R(E) = \frac{\left(\frac{d\sigma}{d\Omega dE} \right)_{inelastic}}{\left(\frac{d\sigma}{d\Omega} \right)_{elastic}}. \quad (4.33)$$

E_{dep} , E_0 , and τ in Eq. 4.32 are energy deposited by rescattered electrons on the detector, energy deposited by elastically scattered electrons, and the probability for the inelastic electrons to rescatter inside the spectrometers, respectively. For all intents and purposes, $\frac{E_{dep}}{E_0} \approx 1$, therefore, $P_{rs}(E) \approx \tau$.

Measurement of $P_{rs}(E)$ is performed by increasing the fields of the HRS magnets (dipole and quads)–forcing trajectories of the elastic electrons to follow the trajectories of the inelastic events during the production field setting (ramming most of them into the wall at the dipole bend). We take integrating mode runs both with septum magnets kept at nominal production settings, and with the septum field increased by the same fraction as the other magnets. We also take the runs at two different gain settings of the quartz detector PMTs, and both sets of gain are higher than production settings to produce a reasonable signal level in the ADC (since rescattering rates are very low). The test is performed only in the left-HRS due to the right-HRS dipole’s extremely slow behavior, but much past experience has shown the two HRSs to be highly symmetric. The rescattering probability as a function of the fractional momentum change is shown in Fig. 4.18.

Since we change the magnet dp settings in discrete steps (i), Eq. 4.31 can be simplified to

$$B_{rs} = \sum_i P_{rs}(E)_i \times [R(E)dE]_i, \quad (4.34)$$

4.3. BACKGROUNDS AND POSSIBLE CORRECTIONS

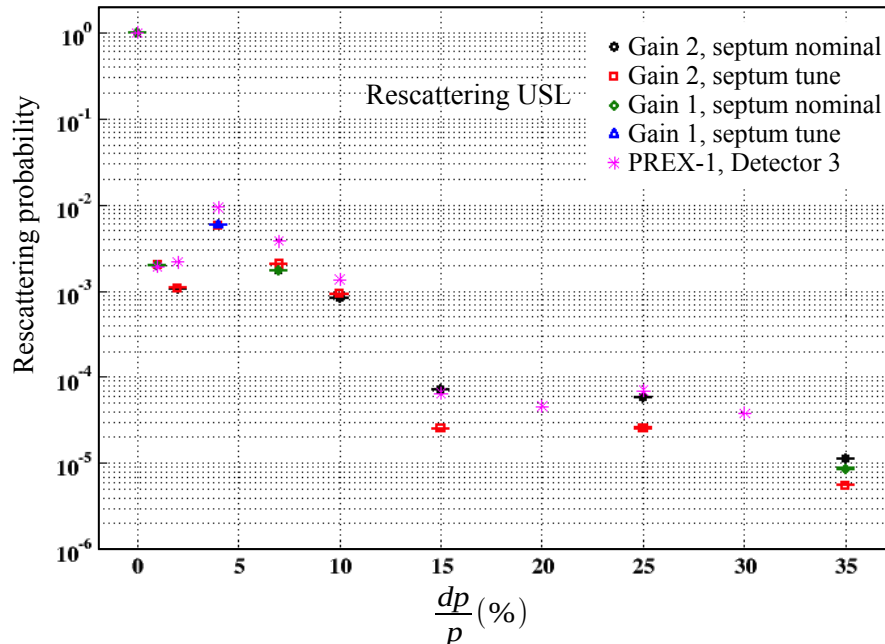


Figure 4.18: Rescattering probability plotted against the fractional change in the HRS dipole setting, $\frac{dp}{p}$, in percent from nominal. Gain 1 and Gain 2 are two different gain settings of the quartz PMT. Septum nominal means the septum field is kept at the production setting, while septum tune means the septum field is changed by the same fraction as the other magnets. PREX-1 measurements of the rescattering probability are taken from [72] and are displayed in the figure for comparison.

where the relative rate, $R(E)dE$, is obtained from simulation using the Hall A Monte Carlo (HAMC), and is shown in Fig. 4.19. To obtain the background fractions we need to multiply the rescattering probability by the relative cross-section for each dp setting. From this, we get $\sum_i f_i = B_{rs} = 1.67 \times 10^{-4}$. Now, to estimate the asymmetry of the electrons with each of these energies, we assume a simplistic first-order model, where the asymmetry is a linear function of Q^2 .⁵ Again, $Q^2 = 2EE'(1 - \cos \Theta)$ is different for different dp settings. This is because each spectrometer dp setting transports a different range of E' events. In this way, we have $\sum_i f_i A_i = 0.0877$ ppb. Using these values in Eq. 4.22 gives a negligibly small correction to A_{cor} . Therefore,

⁵To first order, the asymmetry can be approximated as a linear function of Q^2 , i.e. $A_i = A_0 Q_i^2$, where, i represents each of the dp settings and A_0 is a constant to be calibrated using the PREX-2 physics A_{PV} and Q^2 . Since $Q^2 = 2EE'(1 - \cos \Theta)$, it varies with E' as we change the dp settings.

4.3. BACKGROUNDS AND POSSIBLE CORRECTIONS

we do not make any correction, but as before we include the systematic uncertainties from $\sum_i f_i$ and $\sum_i A_i$, as given in Table 4.8, into the total systematic error for the measurement.

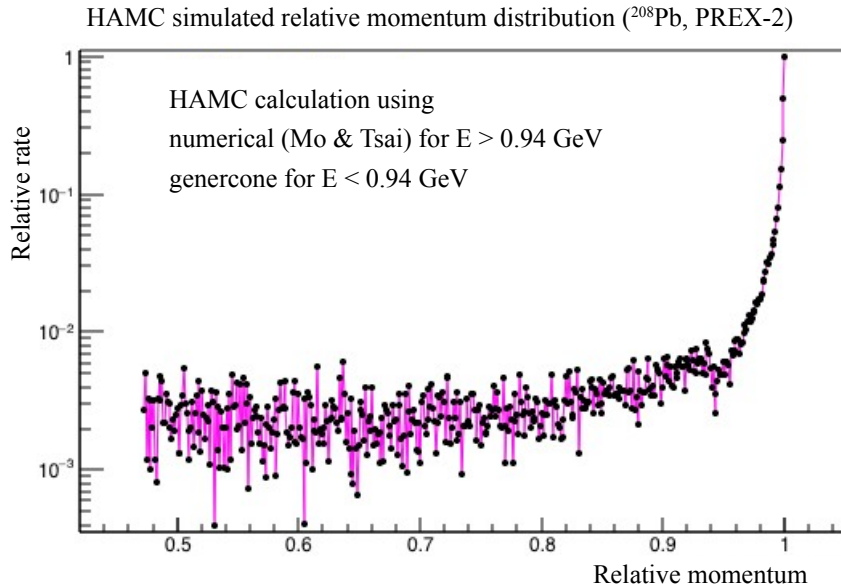


Figure 4.19: Relative focal plane rate for ^{208}Pb as a function of momentum relative to the elastic peak. To handle radiative losses (or corrections) in the simulation, a numerical method from Mo & Tsai, and a long-standing JLab package called “genercone” are used for small and large energy losses, respectively.

Quantity	Correction (ppb)	Absolute Error (ppb)	Rel. Error (%)
$\sum_i f_i$	0	0.10	0.02
$\sum_i A_i$	0	0.00	0.00

Table 4.8: Corrections and systematic errors on A_{PV} due to the rescattering background for PREX-2.

By changing dp we are effectively scanning the HRS E' acceptance over the radiative tail region which has different Q^2 . In reality, radiative effects, such as Bremsstrahlung emission/absorption, can happen before the main physics scattering vertex, at the vertex, or after the vertex (see Fig. 4.20). For example, external radiation emitted before the vertex results in a decrease in E and hence Q^2 . These types

4.4. BLINDED TUBE/STUBBY QUARTZ TEST

of effect would need simulation to quantify, but to the order of the contamination we are dealing with (very low), our simple linear model of Q^2 and the asymmetry of the radiative tail events should still be valid.

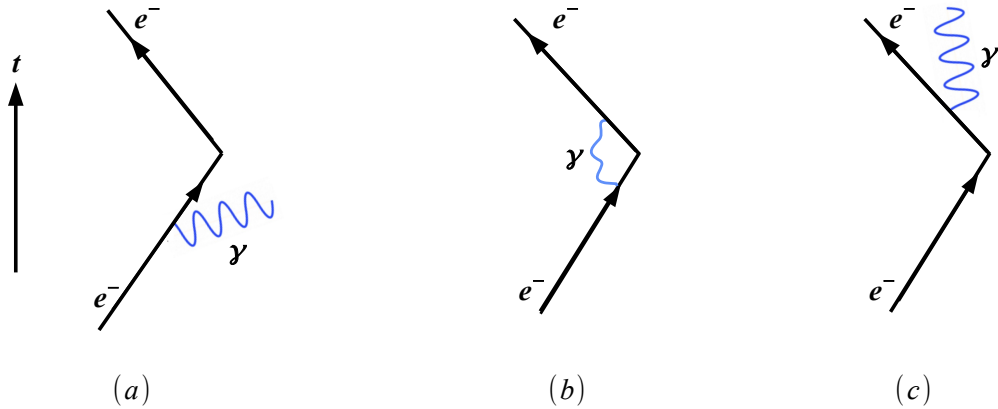


Figure 4.20: Simple diagram of radiative effects (a) before the vertex, (b) at the vertex, and (c) after the vertex.

4.4 Blinded Tube/Stubby Quartz Test

As another background test, we physically “blind” the downstream main detector in the left-HRS and the upstream main detector in right-HRS, while the other two main detectors are installed with a “stubby” quartz radiator. These tests are done to quantify possible backgrounds from electrons (mostly stray, rescattered, etc.) that can strike the photocathode or PMT window directly, or traverse the light guide portion of the quartz.

We do the stubby quartz test only during PREX-2 because CREX shares the same detector setup and spectrometer⁶. So this background, if any, should stay the same between the two back-to-back experiments. In order to install the stubby quartz, we have to disturb the main detector alignment, so these tests are costly with respect

⁶But the blinded tube test is repeated during CREX in a non-invasive way. This is done by installing the A_T2 detectors (PMTs) nearly in between the upstream and downstream main quartz detectors as discussed in this section.

4.4. BLINDED TUBE/STUBBY QUARTZ TEST

to time and clearly invasive. Note that each production quartz is 16 cm long. As mentioned in Sec. 4.1.2, the focal plane foot-print of the elastic signal spans ≈ 4 cm from quartz edge to elastic peak, and then extends another 4 cm beyond the elastic peak toward the PMT (the so-called “super-elastic” side). Thus, the other ≈ 8 cm of the quartz is effectively a light guide and not a radiator. The stubby quartz pieces are 6 cm long Spectrosil 2000 with the same width, thickness, and other exact specifications as the production quartz. The shorter length means that there is a ≈ 2 cm gap between the elastic signal flux envelope and the stubby quartz edge during the test. We expect no signal from the stubby quartz during the full beam current, integrating mode test. For the blinded tube tests, we completely cover the PMT window/photocathode using black Kapton polyimide film, a rubber factory PMT endcap, and black electrical tape. Figure 4.21 shows photographs of the stubby quartz installed in the left-HRS upstream main detector and the blinded downstream main PMT.

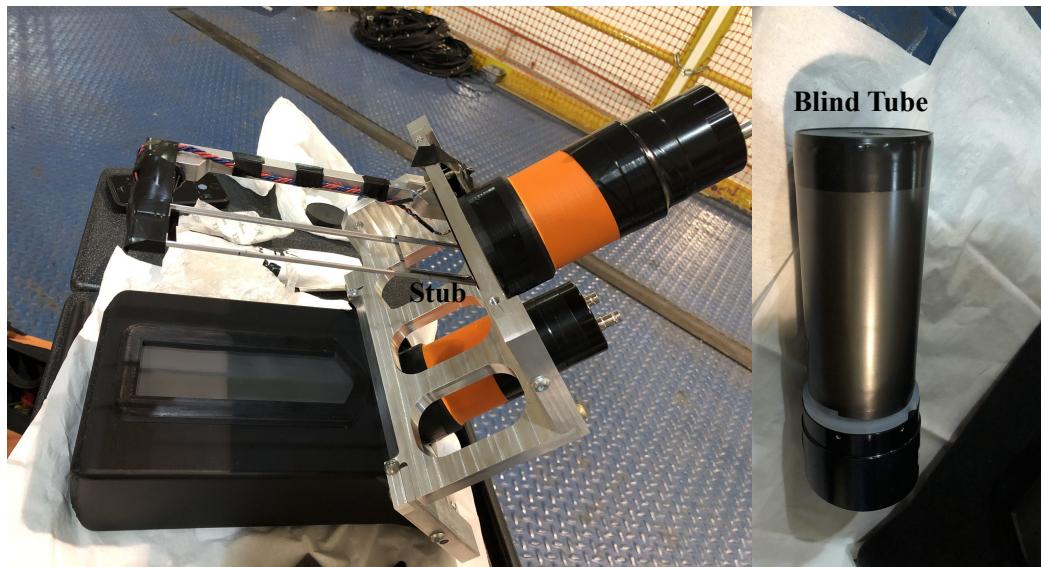


Figure 4.21: Photographs of left-HRS upstream main detector fitted with stubby quartz (left-side image) and blinded downstream main PMT (right-side image) using black Kapton, a rubber PMT endcap, and black electrical tape.

Both integrating and counting mode data are taken in this configuration. Again,

4.4. BLINDED TUBE/STUBBY QUARTZ TEST

if “ a ” and “ b ” are the charge normalized signals for the opposite helicity states in a multiplet pattern, for an integrating mode run (with blinded/stubby setup), then:

$$\text{asymmetry}_{\text{blinded/stubby}} = \frac{(a - b)/2}{\text{production_yield}} \quad (4.35)$$

where `production_yield` is the average measured charge normalized signal in a single detector (for a helicity multiplet pattern) during production running.

Table 4.9 lists the helicity-correlated asymmetry due to the blinded fraction. The blinded fraction is the fractional detected signal yield of the blinded/stubby quartz relative to the nominal unblinded main detector yield. Figure 4.22 compares the pulse-height distributions for a typical counting mode run (with full-size quartz and unblinded tube) to a run with blinded/stubby detectors. For comparison, an equal number of events (500k) are plotted for each run. The pedestal subtracted distributions (right-hand side plots) use the standard ADC cut and show that the detected rate of the blinded/stubby detectors is extremely low. We take only one run each of counting and integrating mode.

Detector	Asymmetry (ppb)	Noise (ppm)
USL (S)	-54.9 ± 63.0	11.6
DSL (B)	3.2 ± 42.2	7.8
USR (B)	-22.5 ± 59.7	11.0
DSR (S)	36.0 ± 65.5	12.1

Table 4.9: Helicity-correlated asymmetries due to blinded/stubby fraction. The “S” or “B” within parenthesis means “stubby” or “blinded.” The “Noise” column is the RMS of the asymmetry distribution.

Toward the end of PREX-2, we decide to collect more statistics of the blinded tube configuration in a non-invasive way. To this end, we uninstall the auxiliary A.T2 detectors from both HRSs, blind their PMTs as explained above, and install only their PMTs (with μ -metal shields) approximately in between the upstream and

4.4. BLINDED TUBE/STUBBY QUARTZ TEST

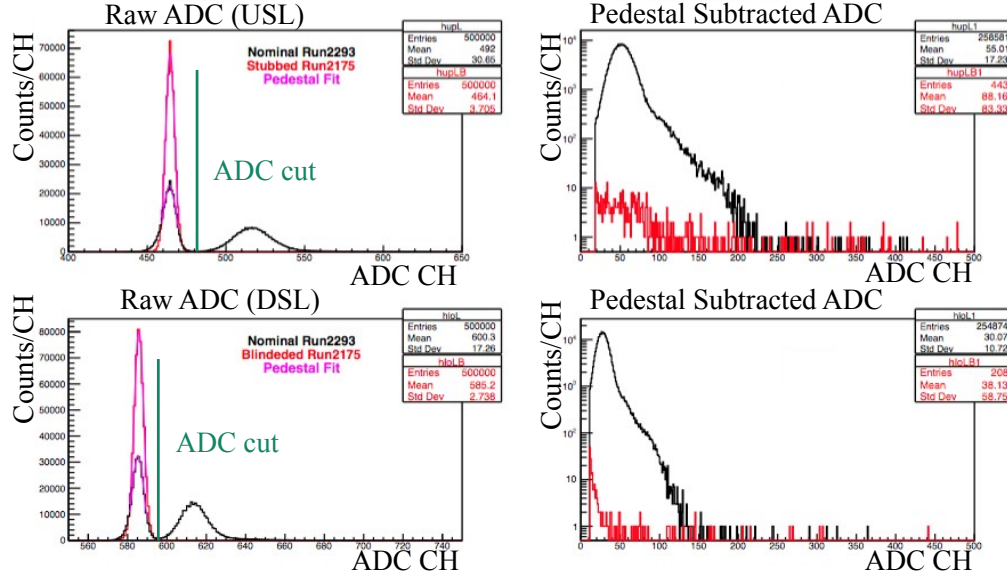


Figure 4.22: Normal detector vs blinded/stubby detector ADC distributions in the left-HRS during PREX-2. The upper plots are for the upstream main detector, while the bottom plots are for the downstream detector. Plots on the right show the pedestal subtracted distributions for the events within the detector acceptance. Note the blinded/stubby rates are extremely low compared to the standard production detector rates.

downstream main detector PMTs. The idea is to get the helicity-correlated false asymmetry background (if any) in the measured asymmetry over an extended time— to improve the precision of the tiny background measurement. We note that 12 out of 96 total slugs are run in this configuration. The statistics in each slug are maintained at roughly equal levels to make sure that each IHWP (also note these slugs are taken during a Wien-Left configuration) state has comparable statistical weight for best cancellation of HCBA. The asymmetry measured by each A_T2 in this configuration is properly scaled by the main detector blinded fraction of its respective HRS. In this way, the measurements of these PMTs give an estimate of a false asymmetry background due to the blinded fraction of the main detectors. The results are given in Table 4.10. This table shows that the helicity-correlated, blinded-tube asymmetry is very small, and poses no complications in presenting the physics asymmetry. The minirun-wise asymmetry distribution for the right-HRS blinded tube

4.4. BLINDED TUBE/STUBBY QUARTZ TEST

is shown in Fig. 4.23. Recall each minirun is a subset of a run with a collection of 5 min worth of good events; each minirun constitutes a collection of 9000 helicity multiplet patterns, i.e. 9000 counts of asymmetry measurements. The one-dimensional (1D) *Pull* plot histogram on the right-hand side is obtained by

$$Pull = \frac{A_i - \langle A \rangle}{\sigma_{A_i}}, \quad (4.36)$$

where A_i is each asymmetry data point, σ_{A_i} is the error bar of that data point, and $\langle A \rangle$ is the average asymmetry.

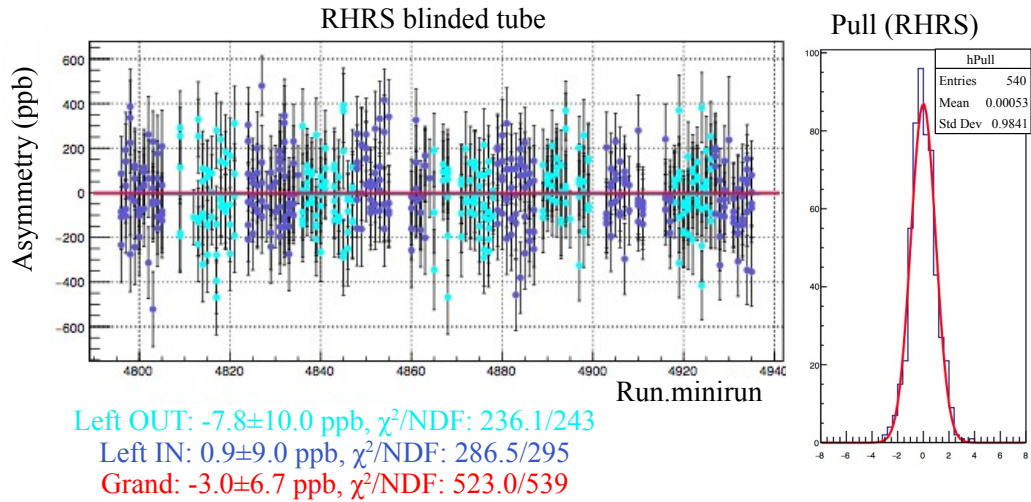


Figure 4.23: Helicity-correlated false asymmetry due to the blinded fraction in right-HRS. The 2D plot on the left-hand side shows the asymmetry versus minirun; different colors represent various Wien and IHWP states. The 1D plot on the right-hand side is the *Pull* distribution where data is blue, and Gaussian fit is red.

Detector	Asymmetry (ppb)	Noise (ppm)
Left-HRS	0.5 ± 3.9	9.0
Right-HRS	-3.0 ± 6.7	15.4

Table 4.10: Helicity-correlated false asymmetries due to the blinded fraction averaged over 12 slugs. The “Noise” column is the RMS of the asymmetry distribution. These two blinded PMTs are installed very close to main detectors in each HRS, roughly in between the upstream and downstream main detectors.

4.5 Auxiliary Detectors (Background Monitors)

In addition to the main detectors, dedicated to the physics asymmetry measurements, each HRS consists of two auxiliary quartz detectors for monitoring parity conserving asymmetry or other possible false asymmetry backgrounds. As previously discussed, the dominant source of this background could originate from any residual transverse polarization of the electron beam. Although we use the polarized beam to measure A_{PV} , even a small fraction of transversely polarized electrons can give a sizeable parity-conserving asymmetry background. The size of this asymmetry can be over an order of magnitude larger than A_{PV} . The auxiliary detectors are designed to be sensitive to the horizontal transverse beam polarization component. Due to the configuration of the injector, it is relatively easy to nullify the vertical transverse component. In order to bound the potential size of the parity-conserving asymmetry, dedicated vertical transverse asymmetry (A_T) measurements are made with the main detectors during both PREX-2 and CREX on various targets. These targets include: ^{208}Pb , ^{12}C , ^{48}Ca , and ^{40}Ca . The analyses of these measurement are given in Sec. 4.8.

The relative positions of the four auxiliary detectors with respect to the beamline are shown in Fig. 4.24. The auxiliary detectors are finally aligned for their desired acceptance, with optimized A_T sensitivity, after about the first quarter of PREX-2 and almost from the beginning of CREX. The measured asymmetries of the auxiliary detectors during PREX-2 are shown in Table 4.11. These results are corrected for beam position and energy fluctuations using linear regression analysis and are weighted by the A_{PV} error. Similar results are obtained when correcting for beam fluctuations using the dithering (beam modulation) system. Since the electrons hitting the auxiliary detectors first pass through the main detectors, the measured asymmetry would be $A_{PV} \pm A_T$, where A_T is the possible transverse asymmetry. While the A_{PV} for PREX-2 is expected to be of order 500 ppb, A_TL1 (see Fig. 4.24) measures an

4.5. AUXILIARY DETECTORS (BACKGROUND MONITORS)

asymmetry approximately 3σ larger than A_{PV} , but the rest of the auxiliary detectors measure asymmetries roughly equal to A_{PV} within their errors. Therefore, A_TL1's signal requires extra investigation.

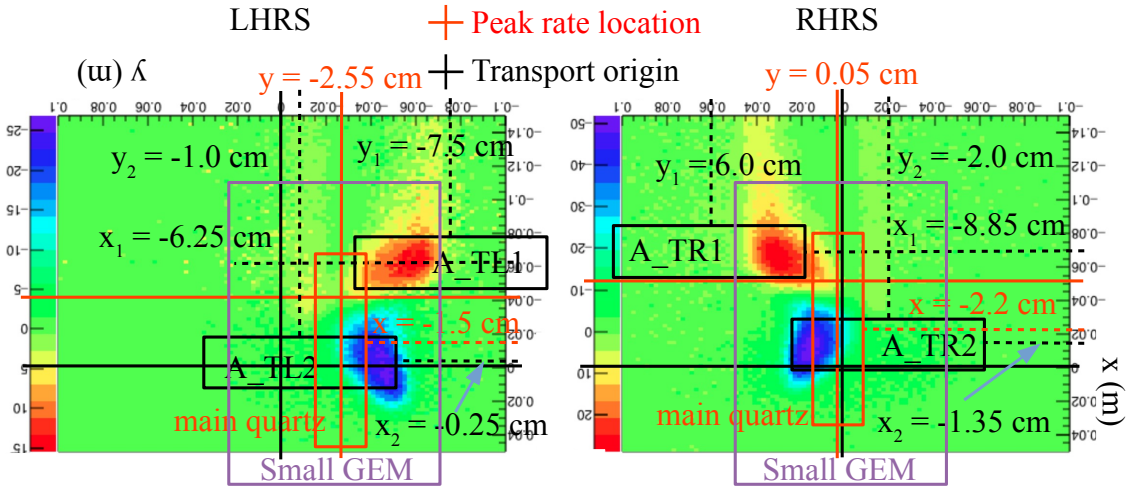


Figure 4.24: Beam's Eye view of relative positions of auxiliary detectors in the HRSs. VDC tracks are projected 2.0 m downstream of the $z = 0$ transport plane to the location of the auxiliary detectors. The relative positions of the detectors in the left and right HRS are shown. The red rectangle in each HRS is the shadow of the main quartz; the shadow of the small GEM active area is also shown. Note that the plots' vertical and horizontal axes have been flipped and rotated to give the beam's eye view for each focal plane. The scatter plot color scale represents events with opposite sign A_T analyzing power. These are events that scatter at azimuthal angles that are either above or below the horizontal scattering plane. Note that the red and blue events (all electrons) traverse the main quartz which is approximately 0.7 m upstream of the auxiliary detector plane; after passing through the quartz, these rays continue to defocus, distort, and separate by the time they reach the auxiliary detectors.

An idea for investigating the large A_TL1 signal asymmetry is to develop a procedure to map-out and quantify the location and size of the background asymmetry in the vicinity of A_TL1. The hope is that this can give us clues as to the source of the background. In the following subsections, we will discuss the results from a set of investigations, and possible explanations, for understanding the large A_TL1 signal asymmetry. The itemized list of studies performed includes:

1. Systematically reposition the A_TL1 detector to sample different acceptances.

4.5. AUXILIARY DETECTORS (BACKGROUND MONITORS)

Detector	Asymmetry (ppb)	χ^2/NDF	RMS (ppm)
A_TL1	892.2 ± 116.5	31.6/26	466.5
A_TL2	464.7 ± 92.9	20.6/26	375.2
A_TR1	377.0 ± 120.4	23.4/26	486.3
A_TR2	523.2 ± 95.6	26.9/26	386.8

Table 4.11: Asymmetries measured by auxiliary detectors during PREX-2 (weighted by the A_{cor} error-error on the left-right HRS average asymmetry measured by the upstream main detectors). Data is aggregated from slug 26 to slug 54. The RMS column shows that the detected rate in each A_T1 detector is roughly the same, at approximately $1/13^{\text{th}}$ of the rate in the main detectors, while each A_T2 sees approximately $1/8^{\text{th}}$ of the main detector rate.

2. Blind the PMTs in the auxiliary detectors for a few slugs and monitor the helicity-correlated asymmetry due to their blinded fractions.
3. Consider possible large pedestal noise pickup as the cause of the large signal asymmetry and monitor the helicity-correlated beam-off asymmetry.
4. Check if the regression correction has some problem, which can cause the large asymmetry to emerge from the application of beam corrections.
5. Detector non-linearity

4.5.1 Position Scan

It is clear from Table 4.11 that the acceptance, or correct positioning of the auxiliary detectors, is not a problem because they all have roughly the same rate. However, following the idea of item number one above, about halfway through PREX-2, we decide to move the A_TL1 detector in 1 cm or 2 cm steps to measure the background asymmetry for different acceptances. We move it either in the dispersive \hat{x} or transverse \hat{y} direction, and left it there for a few slugs. We repeat this for five different positions, but we do not see any evidence to support that the acceptance or position

4.5. AUXILIARY DETECTORS (BACKGROUND MONITORS)

of A_TL1 is somehow a problem; there is no statistically significant variation in its asymmetry for the different positions we tested.

4.5.2 Blinded Tube Test

After a couple of weeks of position scans, we decide to blind the PMTs and investigate if there is any significant helicity-correlated beam asymmetry due to the blinded fraction. Recall that this is the fraction of detected blinded-yield relative to the detector's unblinded-yield. For these tests, we blind all the auxiliary detectors over a few day period using the same technique explained in Sec. 4.4. The asymmetries are calculated using Eq. 4.35, and the results are presented in Table 4.12. The auxiliary detector asymmetries from the blinded fractions are very small, similar to the main detector blinded fractions.

Detector	Asymmetry (ppb)	RMS (ppm)
A_TL1	-28.0 ± 43.5	76.6
A_TL2	49.7 ± 24.2	42.7
A_TR1	35.8 ± 45.4	80.1
A_TR2	-80.6 ± 28.1	49.5

Table 4.12: Blinded tube test results for auxiliary detectors. For these tests, all the auxiliary detector PMTs are blinded using Kapton foil, rubber endcaps, and black electrical tape to completely cover their PMT window and photocathode, as explained in Sec. 4.4.

4.5.3 HCPA for Auxiliary Detectors

The helicity-correlated pedestal asymmetry (HCPA) analysis for the auxiliary detectors is the same as that discussed in Sec. 4.2.6 for the main detectors. The asymmetries are calculated using Eq. 4.21. The auxiliary detector's beam-off asymmetry distribution for a typical beam-off run, such as run 4209, is shown in Fig. 4.25. The grand aggregated results for 57 beam-off runs taken over various dates are shown in

4.5. AUXILIARY DETECTORS (BACKGROUND MONITORS)

Table 4.13. The HCPA for each auxiliary detector is extremely small, and the pedestal noise is only a couple of ppm, which is also too small to motivate a correction.

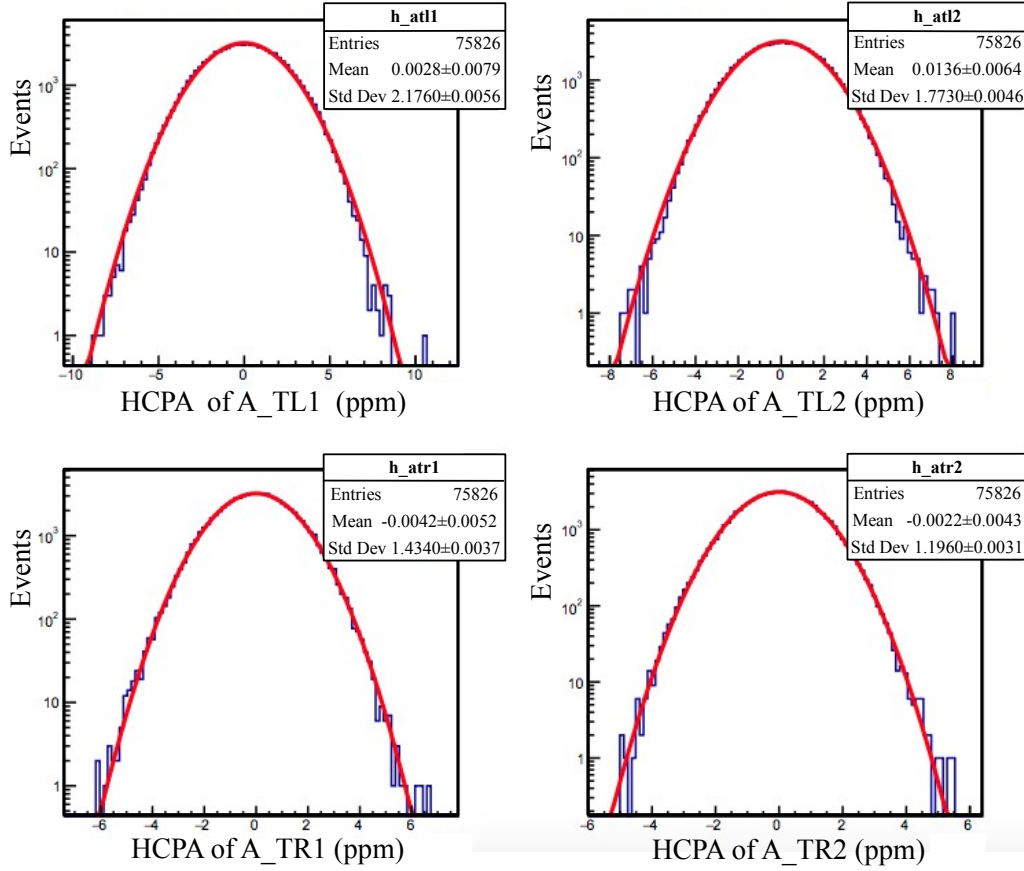


Figure 4.25: Pedestal asymmetry distribution for a typical beam-off run; data are in blue with red Gaussian fits.

Detector	Asymmetry (ppb)	RMS (ppm)
A_TL1	1.5 ± 1.9	3.0
A_TL2	2.4 ± 1.3	2.0
A_TR1	1.9 ± 1.2	1.8
A_TR2	0.5 ± 0.9	1.3

Table 4.13: Helicity-correlated pedestal asymmetries measured by auxiliary detectors during PREX-2. These results are aggregated from 57 beam-off runs over various dates during the run.

4.5. AUXILIARY DETECTORS (BACKGROUND MONITORS)

4.5.4 HCPD and Correction Slopes for Auxiliary Detectors

The general approach for analyzing HCPDs is given in Sec. 4.2.4. The helicity-correlated position (and energy) differences for the auxiliary detector data set considered here are shown in Table 4.14.

Monitor	Difference (nm)	χ^2/NDF	RMS (μm)
<i>bpm4aX</i>	0.12 ± 0.39	19.9/26	1.57
<i>bpm4aY</i>	1.74 ± 2.01	24.7/26	8.12
<i>bpm4eX</i>	-1.20 ± 2.41	32.9/26	9.81
<i>bpm4eY</i>	1.40 ± 1.21	25.6/26	4.88
<i>bpmE</i>	0.65 ± 1.81	25.7/26	7.37

Table 4.14: Helicity-correlated position differences (weighted by left-right HRS upstream main detectors average asymmetry error) relevant for the auxiliary detectors. The position monitors are *bpm4aX*, *bpm4aY*, *bpm4eX*, and *bpm4eY*, while the energy monitor is labelled *bpmE*.

The regression slopes (α_i) of the auxiliary detectors for the data set (slug 26 to slug 54) are shown in Table 4.15. All the slopes are reasonable. Indeed, A_TL1 which measures quite larger asymmetry has smaller slopes compared to the others, suggesting regression is not a suspect for causing the larger asymmetry. As a cross check of the applicability of the regression analysis, one can also look into the residual slopes. For this, we calculate the residual sensitivity or slopes of the A_T detector asymmetries to the monitor position and energy differences at the slug level. We weight the asymmetries and position differences by the upstream left and right HRS main detector’s average statistics (using Eq. 4.8 for the average and Eq. 4.9 for the error) to calculate the slug level average and error bars. The results are shown in Table 4.16. The residual slopes are all null within error—reinforcing the validity of linear regression. All these results are more or less consistent with the results obtained from dithering.

4.5. AUXILIARY DETECTORS (BACKGROUND MONITORS)

Det.	A_TL1	A_TL2	A_TR1	A_TR2
<i>bpm4aX</i>	-38.65 ± 0.21	157.14 ± 0.47	81.31 ± 0.37	131.43 ± 0.47
<i>bpm4aY</i>	-1.03 ± 0.16	30.13 ± 0.35	23.14 ± 0.28	31.02 ± 0.35
<i>bpm4eX</i>	101.97 ± 0.04	-202.66 ± 0.08	-178.94 ± 0.06	-94.61 ± 0.08
<i>bpm4eY</i>	-20.70 ± 0.27	36.09 ± 0.58	-6.14 ± 0.47	46.18 ± 0.58
<i>bpmE</i>	48.61 ± 0.04	-264.17 ± 0.09	-136.47 ± 0.07	-317.76 ± 0.09

Table 4.15: Position and energy slopes for auxiliary detectors. Again, *bpmE* is the energy monitor while the rest are position monitors. The units are ppm/ μm .

Det.	A_TL1	A_TL2	A_TR1	A_TR2
<i>bpm4aX</i>	-59.49 ± 64.33	22.06 ± 51.45	-25.64 ± 66.16	-5.77 ± 53.41
<i>bpm4aY</i>	-7.04 ± 11.95	10.24 ± 9.56	-10.42 ± 12.27	-5.22 ± 9.85
<i>bpm4eX</i>	-5.50 ± 8.18	-6.39 ± 6.48	-10.94 ± 8.43	-2.81 ± 6.68
<i>bpm4eY</i>	-14.11 ± 19.26	17.36 ± 15.47	-8.03 ± 19.91	-7.67 ± 15.95
<i>bpmE</i>	-5.55 ± 12.78	1.28 ± 10.16	2.97 ± 13.20	8.40 ± 10.45

Table 4.16: Residual position and energy slopes for auxiliary detectors. The units are ppm/ μm .

4.5.5 Non-linearity

Under normal operating conditions, an ideal detector's signal should be a linear function of beam intensity. But a realistic detector can have significant non-linearity depending on the beam intensity. The main source of detector non-linearity, if any, is the photo-sensitive device (PMT). As the intensity of light hitting a PMT photocathode goes beyond a certain threshold, constrained by the characteristics of the PMT components and design, the PMT anode signal starts saturating and no longer behaves linearly. The PMTs used in all the quartz detectors are carefully studied in bench tests to find their best linear operating conditions (see Sec. 3.6.4 for details of the bench test). The non-linearity is also monitored regularly via current scans and PITA scans.

The bench tests are conducted at several light levels covering both PREX-2 and CREX signal levels, and over a wide range of high voltages (gain settings). During

4.5. AUXILIARY DETECTORS (BACKGROUND MONITORS)

PREX-2, A_TL1 is set in such a way that its anode current (I_a) is $\approx 15 \mu\text{A}$. The non-linearity from the bench test for the PMT ZK5363 used in A_TL1 during PREX-2 is shown in Fig. 4.26. For the level of anode currents during PREX-2, the bench test results show that A_TL1 should have $\approx 0.3 \%$ non-linearity. We observe that all the auxiliary detectors have $\approx 1 \%$ non-linearity from the current scan during pedestal calibrations. Therefore, non-linearity is not a problem for the auxiliary A_TL1 detector.

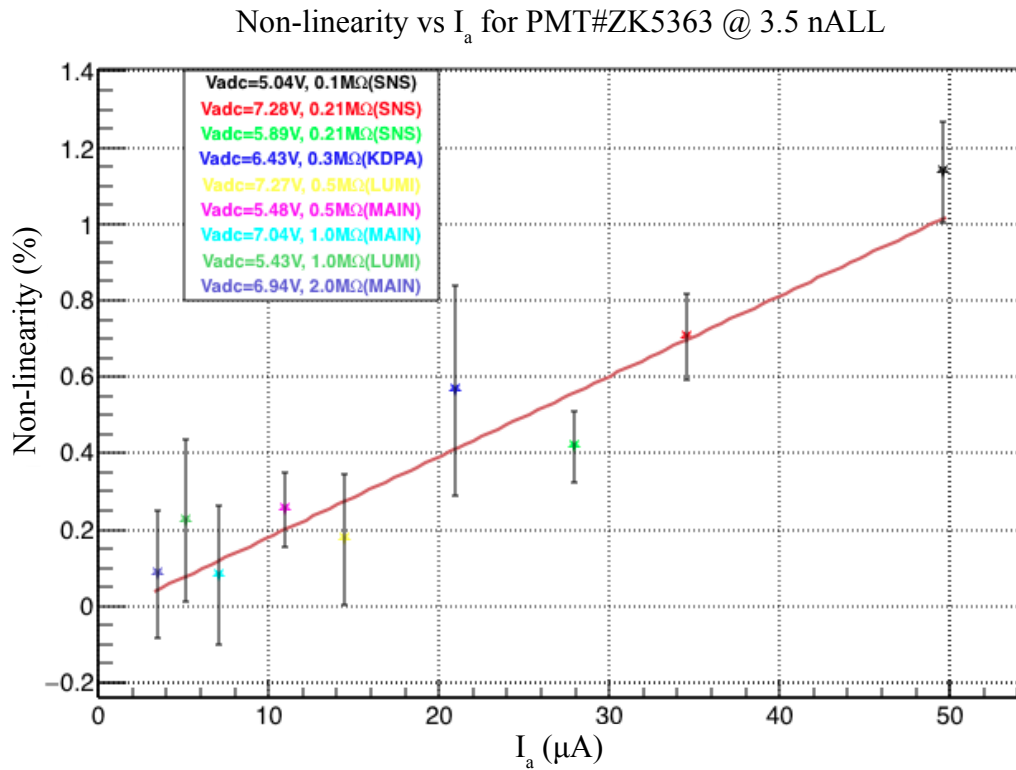


Figure 4.26: Non-linearity plotted against anode current for PMT ZK5363 (used in A_TL1 during PREX-2) from bench test. $V_{adc} = I_a \times G$ is the voltage per helicity window integrated by the ADC for the given anode current, where G is the gain setting of the I-to-V converter.

4.5.6 Summary of Auxiliary Detectors

Each HRS focal plane detector package is installed with a pair of complementary (auxiliary) detectors. The geometry, quality, and performance of the quartz used in these detectors are the same as those used in the main detectors. The idea behind the design of these detectors is to monitor the parity non-violating background or false asymmetry from any residual transverse beam polarization. With the ideal HRS tune and alignment of the focal plane main detectors, the possible transverse asymmetry contamination is naturally cancelled. This happens because of the “complete” or symmetric left-right and up-down acceptance of the target scattering. The horizontal-transverse asymmetry is cancelled individually within each main detector, while the vertical-transverse asymmetry cancels when averaging the left- and right-HRS main detectors.

Under the ideal condition of perfectly longitudinal (no transverse component) beam polarization, any asymmetry measured by an auxiliary detector should be equivalent to the physics asymmetry. All the auxiliary detectors, except A_TL1, do not show any considerable false asymmetry contamination. The lone and statistically weak observation of A_TL1’s large asymmetry is difficult to study, and we would need a starting hypothesis to build upon. Our two main ideas, a problem with regression or a quirk in the acceptance, have been effectively ruled out; A_TL1 has smaller slopes compared to the others, and its kinematics match those of the other auxiliary and main detectors. The other listed ideas (non-linearity, or pedestal pickup) seem easily ruled out. So, without a viable hypothesis, this observation goes in the category of a statistical fluke. We have tried, but we do not have a model for how it could show a false asymmetry, and the signal is too weak to demonstrate a clear problem.

4.6 Q^2 Measurement

The square of the four-momentum transferred by a scattered electron to the target depends on the electron’s incoming energy, E , its outgoing energy, E' , and the scattering angle, Θ , and is given by

$$Q^2 = 2EE'(1 - \cos \Theta). \quad (4.37)$$

The importance of the Q^2 measurements is given in Sec. 2.8. The following subsections describe the PREX-2 Q^2 measurements and give the associated systematic uncertainties.

4.6.1 Energy Measurement

The incident energy (E) is continuously measured using the “Tiefenbach” method, which has been calibrated using an ARC energy measurement, and it uses the readout of Hall A BPMs. The Tiefenbach method is non-invasive to production data taking, while the ARC energy measurement is invasive and requires dedicated runs. The ARC energy measurement uses the magnetic field integral of the dipole magnets ($\int \vec{B} d\vec{l}$) that bend the electron beam from the LINAC to the Hall A beamline through a bend angle (Φ). The bend angle, obtained from the 2018 survey, is found to be 34.26° . The average beam energy measured during PREX-2 is 953.4 ± 1 MeV. This energy uncertainty contributes 0.15 % relative uncertainty to A_{PV} .

The energy of the outgoing, scattered electron is measured by the HRSs. The expression to calculate E' is given in Eq. 2.29. It is recorded for every event and saved in the data stream.

4.6. Q^2 MEASUREMENT

4.6.2 Scattering Angle Measurement

The scattering angle is calculated from the spectrometer central angle (Θ_0), and the angles subtended by the reconstructed trajectories of the electrons to the \hat{z} -axis along xz - and yz -planes of the “transport” coordinate system (θ_{tg} and ϕ_{tg}). The scattering angle, Θ is given by

$$\Theta = \arccos \left(\frac{\cos \Theta_0 - \phi_{tg} \sin \Theta_0}{\sqrt{1 + \theta_{tg}^2 + \phi_{tg}^2}} \right), \quad (4.38)$$

where Θ_0 is the angle between the spectrometer axis and the nominal beamline. It is obtained from the “pointing” measurement using the standard Hall A water cell target. The pointing measurement technique allows us to calculate the central angle using the difference in E' for ^1H and ^{16}O nuclei in the water cell target, which is given by

$$\Delta E' = E'_O - E'_H = E \left(\frac{1}{1 + \frac{E}{M_O}(1 - \cos \Theta)} - \frac{1}{1 + \frac{E}{M_H}(1 - \cos \Theta)} \right). \quad (4.39)$$

Furthermore, the pointing technique with the water cell is crucial because it cancels out the energy loss before and after scattering. The cancellation occurs by using the energy separation between the two peaks, thus knowledge of the absolute vertex energy is not necessary (it cancels out). This helps minimize the uncertainty in the angle measurement. For a consistency check, the pointing measurement is performed with three different momentum settings. The momentum settings are adjusted by keeping the spectrometer magnets at their nominal settings (i.e. $dp = 0$ %), and changing the magnet settings by ± 1 % (i.e. $dp = \pm 1$ %). The central angle (Θ_0) is obtained by minimizing the square of the difference between $\Delta E'$ from calculation

4.6. Q^2 MEASUREMENT

(using Eq. 4.39) and from the measured energy difference between the ^1H and ^{16}O peaks, i.e. $(\Delta E'_{calc} - \Delta E'_{meas})^2$. The central scattering angles measured for PREX-2 for the two spectrometers are given in Table 4.17. The 0.02° uncertainty in the pointing measurement contributes 0.60 % relative uncertainty to A_{PV} .

HRS	Θ_0 ($^\circ$)	$\Delta\Theta_0$ ($^\circ$)
Left-HRS	4.78	0.02
Right-HRS	4.76	0.02

Table 4.17: Spectrometer central scattering angles measured for PREX-2.

4.6.3 Average Q^2

The physics production runs of PREX-2/CREX are taken at very high beam currents, and hence the counting rates are above the operational limit of the VDCs. The VDCs are only capable of measuring rate densities of approximately 10 kHz/cm^2 , and they suffer from pileup issues and give distorted distributions at higher rate densities. In order to measure Q^2 , dedicated low current counting runs are needed. The PREX-2 Q^2 runs are usually taken at $\sim 30 \text{ nA}$ beam current. To make counting runs possible at such low beam currents, cavity BPMs are installed and used in Hall A. These BPMs are important because the standard stripline BPMs do not work at such low currents (see Sec. 3.4.3 for details). As a backup, we also install and use tracking GEM chambers for Q^2 measurements, which can handle significantly higher rates than the VDCs. We have discussed the GEM system in Sec. 3.6.3. As previously mentioned, we take many Q^2 runs using both the GEMs and VDCs, but the final Q^2 analysis uses only the VDC data.

The Q^2 runs are taken every 1-2 weeks. PREX-2 uses multiple production targets, so the Q^2 data is taken with both pristine and damaged targets, and their measurements are compared later during the offline analysis. As mentioned in Sec. 3.6.2, we

4.6. Q^2 MEASUREMENT

discovered a hole in S0 about halfway through the PREX-2 run. Many of our Q^2 runs, taken near that time frame, suffer from this damage; all these runs are excluded from the final analysis. Although we have many trigger combinations available, we only use the T1 trigger, which is made from the logical “AND” between the two PMT signals of the S0 scintillator. In addition, only events with a single cluster in the VDC are passed to the main detector ADC cuts. The Q^2 distributions measured in the left and right spectrometer for typical runs are shown in Fig.4.27.

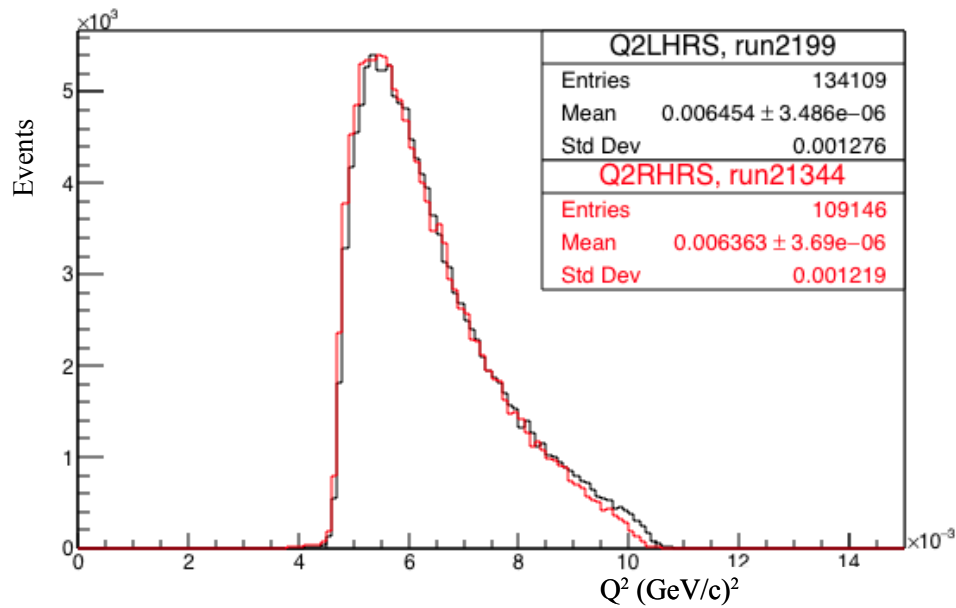


Figure 4.27: PREX-2 Q^2 distributions in left and right HRS for typical runs. Black histogram is for left HRS, and red histogram is for right HRS. Note that while the left- and right-HRS data have different run numbers, those runs occur at the same time.

All the cuts remained the same for each run except the main detector ADC cut. The ADC cut is adjusted slightly for each run such that it lies at the minimum of the valley between the pedestal and signal peak as shown in Fig. 4.3. The Q^2 measurements for all runs (excluding the S0 scintillator damage period) during PREX-2 are shown in Fig. 4.28. The average PREX-2 Q^2 for the left HRS is 0.006475 ± 0.000004 (GeV/c)², and for the right HRS is 0.006369 ± 0.000002 (GeV/c)². These

4.6. Q^2 MEASUREMENT

uncertainties are purely statistical.

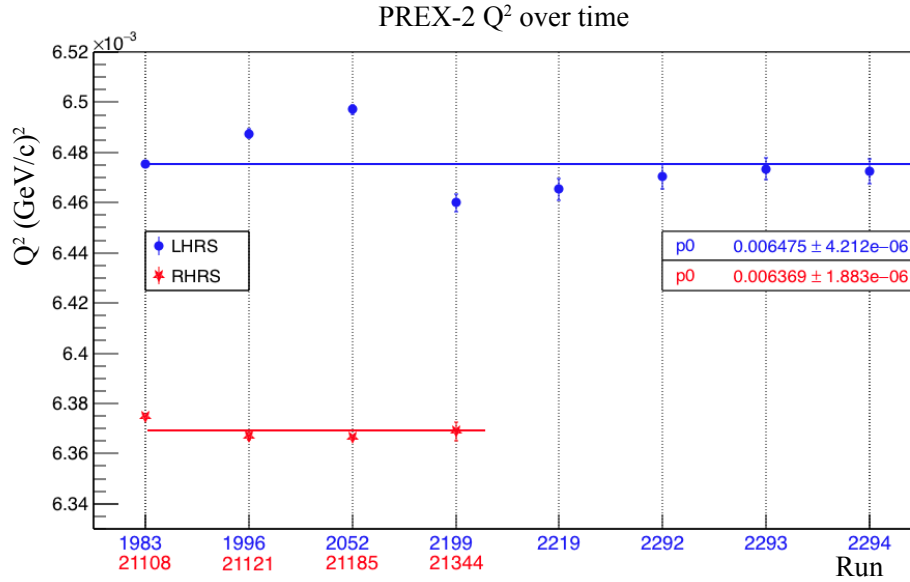


Figure 4.28: PREX-2 Q^2 measurement results as a function of time. The run numbers progress chronologically in time order throughout the experiment. The blue-colored data are for the left HRS and the red are for the right HRS. The error bar in each point is purely statistical. The zeroth-order polynomial fit assumes an equal statistical weight for each data point.

4.6.4 Other Systematic Uncertainties on Q^2 Measurement

There are some additional sources of systematic uncertainties associated with the Q^2 measurement. These come from variations in the measurements over time, variation with ADC cut, trigger dependence, and variation in the quartz acceptance (alignment).

As can be seen in Fig. 4.28, there is a slight variation in Q^2 over time. To estimate the systematic uncertainty due to this variation, we calculate the difference between each Q^2 data point and the average Q^2 (p_0 value of the fit). The standard deviation of these differences divided by the average Q^2 gives this uncertainty. For PREX-2 data, this variation is calculated to be 0.17 % in the left HRS and 0.05 % in the right HRS. Therefore, in the final analysis, we assign 0.20 % uncertainty for the time variation

4.7. FINITE ACCEPTANCE

of the Q^2 measurement. This contributes 0.15 % relative uncertainty to A_{PV} . We observe negligible systematic contributions related to the ADC cut and variations in the quartz acceptance. The trigger dependence contributes 0.1 % relative uncertainty. Adding the uncertainties in quadrature from energy measurements, pointing measurement, time variation in average Q^2 , and its trigger dependence, the total systematic error contribution to A_{PV} from the Q^2 measurement is 3.54 ppb absolute (0.64 % relative).

4.7 Finite Acceptance

The extraction of the neutron distribution, R_n , is effectively made at a single Q^2 , but the measured A_{PV} is averaged over a range of HRS acceptance. As discussed in Sec. 3.4.7, the acceptance is defined by the collimator placed just upstream of the first HRS quadrupole (Q_1) magnet, at the entrance of each spectrometer. The effect of this finite acceptance must be understood in order to make a theoretical interpretation of the measured asymmetry and Q^2 . The acceptance function ($\epsilon(\theta)$) is a function of the scattering angle (θ). It gives the probability for an elastically scattered electron at an angle θ to reach the detector. The asymmetry averaged over the acceptance is given by [73]

$$\langle A \rangle = \frac{\int d\theta \sin \theta A(\theta) \frac{d\sigma}{d\Omega} \epsilon(\theta)}{\int d\theta \sin \theta \frac{d\sigma}{d\Omega} \epsilon(\theta)}, \quad (4.40)$$

where $A(\theta)$ is the asymmetry within the acceptance as a function of θ , and $\frac{d\sigma}{d\Omega}$ is the differential scattering cross-section. The PREX-2 acceptance function is shown in Fig. 4.29. The uncertainties in calculating the acceptance function are studied carefully. Several acceptance models are examined for this, for example, collimator position, target position, septum field settings, etc. are varied in simulation to under-

4.7. FINITE ACCEPTANCE

stand the acceptance function sensitivities. At the end, we bounded the acceptance function with 2.87 ppb uncertainty which is equivalent to 0.52 % relative uncertainty on A_{PV} .

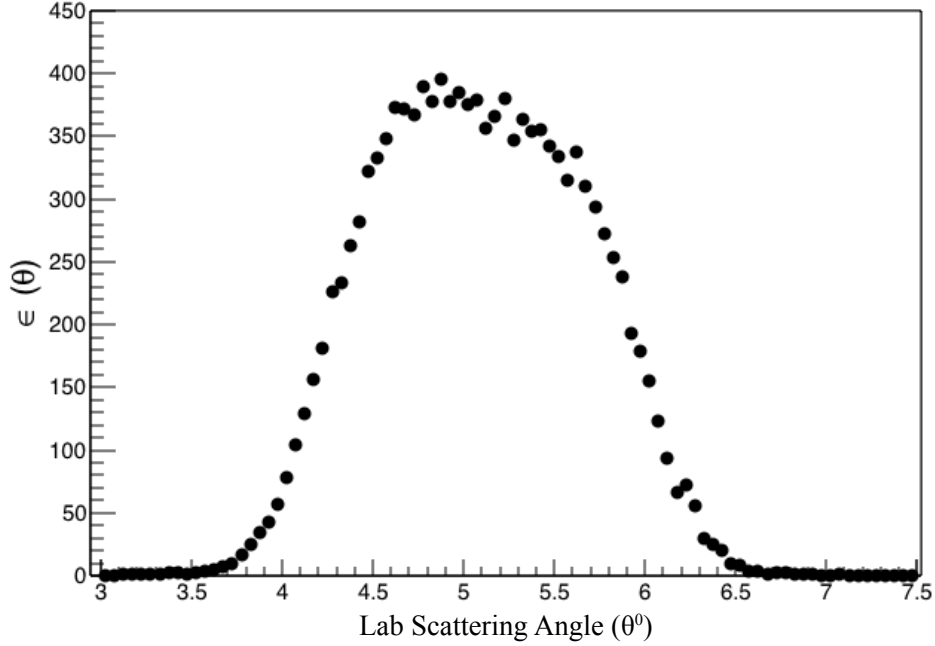


Figure 4.29: PREX-2 acceptance function versus lab scattering angle (θ). The function is arbitrarily normalized to sum to unity over the full acceptance, i.e. $\sum_i \epsilon(\theta_i) \sin(\theta_i) \Delta\theta = 1$, with $\Delta\theta = 0.05^\circ$ [70].

Additionally, the measured Q^2 is slightly different than the vertex Q^2 primarily due to multiple scattering and radiative corrections. The vertex Q^2 is obtained from a Geant4 based Monte Carlo simulation, such that the simulated Q^2 at the detector plane agrees with the experimentally measured Q^2 . Finally, the average Q^2 at the vertex and corresponding acceptance function ($\epsilon(\theta)$) are incorporated into the existing theoretical models to extract the neutron radius (R_n). After the finite acceptance correction, the Q^2 at the vertex for PREX-2 is 0.00616 ± 0.00005 (GeV/c) 2 .

4.8 Transverse Asymmetry Measurements

The transverse asymmetry, also called beam normal single-spin asymmetry (A_T), stems from a non-zero component of beam polarization in a direction transverse to the beam direction. It is a relative measure of the detected rate difference between scattered electrons having spin parallel and anti-parallel to the normal vector of the scattering plane, $\hat{n} = \frac{\vec{k} \times \vec{k}'}{|\vec{k} \times \vec{k}'|}$ (see Fig. 4.30), and is given by

$$A_T = \frac{\sigma_{\uparrow} - \sigma_{\downarrow}}{\sigma_{\uparrow} + \sigma_{\downarrow}}, \quad (4.41)$$

where $\sigma_{\uparrow(\downarrow)}$ is the elastic scattering cross-section for beam electrons with spin parallel (antiparallel) to the normal vector; \vec{k} and \vec{k}' are the initial and final momenta of the scattered electron, respectively. We perform dedicated measurements of the transverse asymmetries, for all physics-related targets during PREX-2 and CREX, by using a \sim fully transverse-polarized electron beam. For these dedicated measurements, the beam polarization is changed from longitudinal to vertical (transverse) by adjusting the double Wien filter settings. For PREX-2, the actual measurements take a total of a few hours, while for CREX the measurements span several shifts; this is due to the much lower CREX rates as well as the addition of the ^{48}Ca measurement.

The A_T measurements are carried out using the focal plane (main) detectors, the same detectors that are used to measure A_{PV} with the longitudinally polarized beam. The measurement is made for ^{208}Pb , ^{40}Ca , and ^{12}C targets during PREX-2. CREX also measures these same three targets as well as ^{48}Ca . A_T for ^{12}C has been studied extensively and is well-constrained theoretically [74]. The new measurement for ^{12}C provides a cross-check for existing results, theoretical models, and most importantly to provide a systematic correction to A_{PV} due to possible transverse asymmetry contamination from the ^{208}Pb target's diamond backing. PREX-1 reported a ^{208}Pb

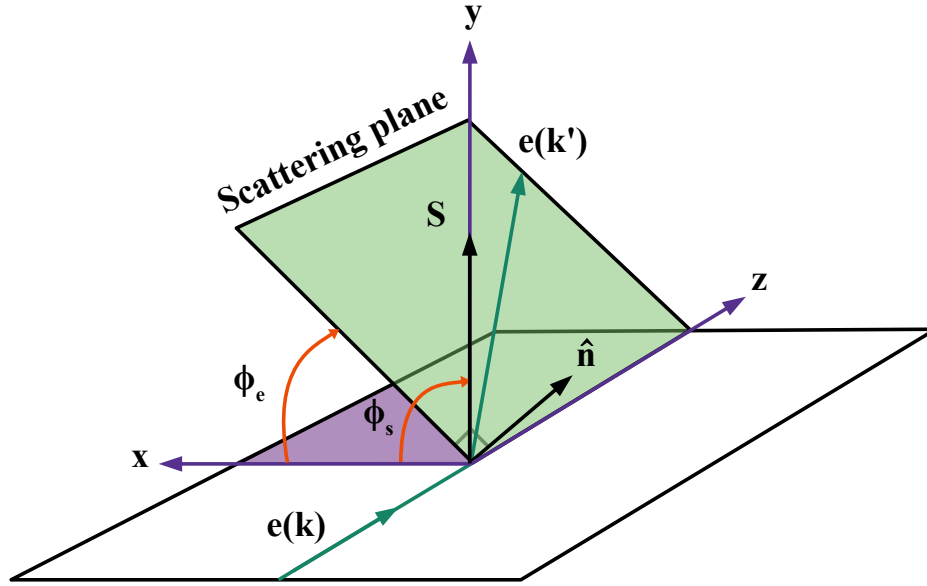


Figure 4.30: Scattering plane relative to the hall coordinate system.

transverse asymmetry measurement near zero in complete disagreement with its theoretical prediction [75]. The new PREX-2 measurement of the same quantity, and at nearly the same kinematics, verifies the PREX-1 result. It is important to note here that the transverse asymmetry for Pb is theoretically expected to be huge (negative), and thus should require extensive systematic study to correct. However, PREX-1, PREX-2, (and CREX) measure A_T asymmetries for Pb that are nearly null within error. Thus the largest contribution to the transverse asymmetry background for the PREX-2 A_{PV} potentially comes from the target's diamond backing. The dedicated A_T measurements of ^{208}Pb and ^{12}C during PREX-2 provide critical inputs into the transverse asymmetry background correction to A_{PV} . Furthermore, the new (never been measured before) measurement of A_T for the intermediate nucleus, ^{40}Ca , can help understand the surprisingly tiny ^{208}Pb A_T results.

The measured transverse asymmetry, $A_{meas}(\phi)$, can be expressed in terms of A_T as

4.8. TRANSVERSE ASYMMETRY MEASUREMENTS

$$A_{meas}(\phi) = A_T P_b \cos \phi, \quad (4.42)$$

where \vec{P}_b is the electron's polarization vector, and ϕ is the angle between \vec{P}_b and \hat{n} . Note that for the small and symmetric out-of-plane target scattering acceptance centered around $\phi = 0^\circ$, the horizontal-transverse asymmetry, $A_T P_b \sin \phi$ (with up-down rate dependence, instead of left-right), is extremely small relative to Eq. 4.42. As mentioned previously, potential background asymmetries from any transverse-horizontal beam polarization component are monitored by the dedicated auxiliary detectors during production running.

In the first Born approximation, A_T should vanish and thus its measurement provides a direct probe of higher-order photon exchange effects [75]. The size of the asymmetry is therefore very small and difficult to measure for most experimental setups. However, for parity violation experiments, the size of A_T is relatively quite large and “easy” to measure. For the running conditions and experimental apparatus of PREX-2 and CREX, the asymmetry comes from the vertical component of the transverse polarization and should have the same size, but with opposite sign, between the two HRSs (according to Eq. 4.42). Therefore, by taking the average A_{PV} measurement between the two HRSs during production, the vertical-transverse asymmetry contamination naturally cancels. In practice, any form of asymmetric alignment of the acceptance between the left and right HRS focal plane detectors gives rise to a parity conserving transverse asymmetry contamination to A_{PV} and requires correction.

4.8.1 Beam Corrections

For the vertical-transverse polarization data, corrections to the raw asymmetry (A_{raw}) are performed using both dithering and linear regression techniques to get A_{cor} . Re-

4.8. TRANSVERSE ASYMMETRY MEASUREMENTS

call that $A_{cor} = A_{raw} - \sum_i \alpha_i \Delta M_i$, where ΔM_i is the position or the energy difference of the i^{th} monitor, and α_i is the detector's sensitivity to the i^{th} monitor. This would correct for helicity-correlated false beam asymmetries. The corrections from the two methods produce similar results; therefore, the results reported in this and the following sub-sections are taken from the dithering correction. The raw asymmetries, beam-corrected asymmetries, and average Q^2 for all the targets are shown in Table 4.18. The dither corrected transverse asymmetry distributions for PREX-2 vertical polarization data are given in Appendix D.

Exp.	Target	A_{raw} (ppm)	A_{cor} (ppm)	Q^2 (GeV/c) ²
PREX-2	¹² C	-5.268 ± 0.741	-5.494 ± 0.330	0.006715 ± 0.000003
	²⁰⁸ Pb	0.196 ± 0.672	0.000 ± 0.129	0.006403 ± 0.000004
	⁴⁰ Ca	-4.439 ± 1.219	-5.295 ± 0.290	0.006729 ± 0.000004
CREX	¹² C	-7.614 ± 1.040	-8.167 ± 0.880	0.03309 ± 0.00001
	²⁰⁸ Pb	-2.414 ± 1.741	-2.765 ± 1.610	0.03203 ± 0.00002
	⁴⁰ Ca	-8.363 ± 1.198	-8.405 ± 0.926	0.03076 ± 0.00001
	⁴⁸ Ca	-7.784 ± 1.075	-7.917 ± 0.839	0.03056 ± 0.00001

Table 4.18: Asymmetries and corresponding Q^2 measurements for various targets during PREX-2 and CREX dedicated transverse running.

4.8.2 Target Impurity Corrections

Each ²⁰⁸Pb target is a composite target with 0.553 mm thick, isotopically pure ²⁰⁸Pb foil sandwiched between two 0.250 mm thick diamond (pure ¹²C) foils. Similarly, the ⁴⁸Ca target is a stack of 3 foils from 2 different sources. The first source has a total mass of 0.3528 gm with 95.99 % purity and the second source has a total mass of 0.9116 gm with 90.04 % purity. The impurity in the ⁴⁸Ca target is mostly ⁴⁰Ca isotope (see Sec. 3.4.6). Therefore, the measured asymmetries for ²⁰⁸Pb and ⁴⁸Ca need corrections to account for their impurities. If f is the rate ratio (ratio of detected rates from impurity to the rates from target material) for the target impurity, the

4.8. TRANSVERSE ASYMMETRY MEASUREMENTS

measured asymmetry (A_{meas}) following this correction to A_{cor} , the beam-corrected asymmetry, becomes

$$A_{meas} = A_{cor}(1 + f) - fA_{cor}^B, \quad (4.43)$$

where A_{cor}^B is the asymmetry of the corresponding impurity or background species B . This equation is mathematically equivalent to Eq. 4.24 except beam polarization normalization.

The rate ratios for PREX-2 ^{208}Pb target, CREX ^{208}Pb target, and CREX ^{48}Ca target are 6.71 ± 0.57 %, 60.89 ± 6.09 %, and 9.07 ± 0.18 %, respectively. These are obtained from simulation for the final analysis, but agree with the values obtained using multiple techniques based on both theory and our measured detector widths. The asymmetries after the target impurity corrections are given in Table 4.19.

4.8.3 Correction for Imperfect Beam Polarization

As mentioned above, we make the transverse asymmetry measurements with a dedicated vertical polarization setup in the injector. We use two independent polarimeters to measure the beam polarization during a longitudinal setup. The Mott polarimeter in the injector gives another method of polarimetry during longitudinal and transverse beam setups. As usual, the measured asymmetry, A_{meas} , is normalized for beam polarization (P_b) and $\langle \cos \phi \rangle$ acceptance to obtain the physics asymmetry. Rearranging Eq. 4.42, we find

$$A_T = \frac{A_{meas}(\phi)}{P_b \cos \phi}, \quad (4.44)$$

where P_b for PREX-2 is 89.67 ± 0.80 %, and for CREX is 86.90 ± 0.78 %.

4.9. SUMMARY OF CORRECTIONS TO A_{PV}

4.8.4 Summary of A_T Measurements

The values of $\cos \phi$ and A_T for all the targets are given in Table 4.19. As given in the table, PREX-2 and CREX A_T results for ^{208}Pb and ^{12}C agree with the previous measurements. Since the A_T for the ^{208}Pb is nearly zero within experimental error, we do not make any correction to A_{PV} . From these measurements we include 0.30 ppb absolute (0.06 % relative) uncertainty to the final systematic error table for PREX-2 A_{PV} .

Exp.	Target	A_{meas} (ppm)	$\cos \phi$	A_T (ppm)
PREX-2	^{12}C	-5.49 ± 0.33	0.967	$-6.34 \pm 0.38 \pm 0.09$
	^{208}Pb	0.37 ± 0.14	0.966	$0.43 \pm 0.16 \pm 0.07$
	^{40}Ca	-5.30 ± 0.29	0.964	$-6.12 \pm 0.33 \pm 0.25$
CREX	^{12}C	-8.17 ± 0.88	0.969	$-9.70 \pm 1.05 \pm 0.17$
	^{208}Pb	0.52 ± 2.65	0.969	$0.62 \pm 3.14 \pm 0.75$
	^{40}Ca	-8.41 ± 0.93	0.970	$-9.97 \pm 1.10 \pm 0.05$
	^{48}Ca	-7.87 ± 0.92	0.970	$-9.34 \pm 1.09 \pm 0.12$

Table 4.19: Beam normal single spin asymmetry (A_T) results for various targets. The first and second uncertainties in A_T are statistical and systematic, respectively. The systematic uncertainties in this table are preliminary.

4.9 Summary of Corrections to A_{PV}

A summary of all the corrections to A_{PV} and their associated systematic uncertainties are given in Table 4.20. The total systematic uncertainty for PREX-2, which is a quadrature sum of individual uncertainties, is $\approx 1.5\%$ (or ≈ 8.2 ppb absolute) [70].

4.10 Parity-Violating Asymmetry (A_{PV})

The physics A_{PV} , after all corrections and normalization, is given by

4.10. PARITY-VIOLATING ASYMMETRY (A_{PV})

	A_{PV} correction \pm uncertainty	
	Absolute (ppb)	Relative (%)
Polarization	56.76 ± 5.23	10.32 ± 0.95
Q^2	0.00 ± 3.54	0.00 ± 0.64
Acceptance function	0.00 ± 2.87	0.00 ± 0.52
Beam correction	-60.38 ± 2.98	-10.98 ± 0.54
Non-linearity	0.00 ± 2.69	0.00 ± 0.49
Carbon dilution	0.69 ± 1.45	0.13 ± 0.26
Transverse asymmetry	0.00 ± 0.30	0.00 ± 0.06
Charge correction	20.68 ± 0.25	3.76 ± 0.04
Inelastic contamination	0.00 ± 0.12	0.00 ± 0.02
Rescattering	0.00 ± 0.10	0.00 ± 0.02
Total	17.75 ± 8.16	3.23 ± 1.48

Table 4.20: Summary of PREX-2 A_{PV} corrections and systematic uncertainties. The total uncertainty is the quadrature sum of individual terms. Several error sources have no correction associated with them as discussed in previous sections.

$$A_{PV} = R_{radcor} \times R_{acceptance} \times R_{Q^2} \times \frac{A_{cor} - P_b \sum_i f_i A_i}{P_b(1 - \sum_i f_i)}, \quad (4.45)$$

where R_{radcor} , $R_{acceptance}$, and R_{Q^2} are the normalization fractions for radiative correction, HRS acceptance, and Q^2 , respectively. Each of these fractions is equal to 1. The corrected asymmetry, A_{cor} , is given by

$$A_{cor} = A_{raw} - A_{false} - A_{nonLin} - A_T - A_{blind} \quad (4.46)$$

where A_{false} , A_{nonLin} , A_T , A_{blind} are the asymmetry corrections due to beam fluctuations, detector non-linearity, transverse polarization, and blinding offset. Recall A_{raw} includes the A_q correction. Since we do not make any correction for non-linearity

4.11. WEAK CHARGE RADIUS (R_W) OF ^{208}Pb

and transverse polarization, the expression for A_{cor} reduces to Eq. 4.14 (but with the blinding offset). With the overall normalization fraction being unity, and A_{cor} given by Eq. 4.14, one gets Eq. 4.22. Following all background and beam fluctuation corrections, the physics asymmetry measured by PREX-2 [70] is

$$A_{PV} = 550.00 \pm 16.09 \text{ (stat.)} \pm 8.16 \text{ (syst.) ppb.} \quad (4.47)$$

The errors are equivalent to 2.93 % statistical and 1.48 % systematic relative uncertainties. Finally, adding these two uncertainties in quadrature, the PREX-2 A_{PV} measurement has an overall relative uncertainty of 3.28 % (18.04 ppb absolute).

4.11 Weak Charge Radius (R_W) of ^{208}Pb

After measuring A_{PV} , the next step is to calculate the weak form factor (F_W) of the target nuclei at the experimental Q^2 . In Eq. 2.25, $(1 - 4 \sin^2 \theta_W) \approx 0.07$ is the weak charge of a proton (Q_p), which is very small compared to the weak charge of a neutron ($Q_n \approx -1$). Thus, Eq. 2.25 can be rewritten as

$$A_{PV} = \frac{G_F Q^2 |Q_W| F_W(Q^2)}{4\pi\alpha\sqrt{2}Z F_{ch}(Q^2)}, \quad (4.48)$$

where Q_W is the weak charge of the ^{208}Pb nucleus, $F_{ch}(Q^2)$ is the Fourier transform of the known charge density distribution. F_W is the Fourier transform of the weak charge density distribution, ρ_W , of the nucleus and is given by [34]

$$F_W(Q^2) = \frac{1}{Q_W} \int d^3r \frac{\sin(qr)}{qr} \rho_W(r). \quad (4.49)$$

The weak form factor measured by PREX-2 [70] is

4.11. WEAK CHARGE RADIUS (R_W) OF ^{208}Pb

$$F_W(Q^2 = 0.00616 \text{ (GeV/c)}^2) = 0.368 \pm 0.013 \text{ (exp.)} \pm 0.001 \text{ (model)}, \quad (4.50)$$

where the first uncertainty is experimental, and the second uncertainty is associated with assumed theoretical models. The model uncertainty is obtained by fitting several relativistic and non-relativistic density functional models [76] (theoretical models), where the fit function is the ρ_W described as a two-parameter Fermi function [77].

$$\rho_W(r, c, a) = \rho_W^0 \frac{\sinh(c/a)}{\cosh(r/a) + \cosh(c/a)}, \quad (4.51)$$

where c and a are the parameters defining nuclear size and surface thickness (corresponding to a given model), respectively, and the normalization constant ρ_W^0 is given by [78]

$$\rho_W^0 = \frac{3Q_W}{4\pi c(c^2 + \pi^2 a^2)}. \quad (4.52)$$

Using this equation, one can express the weak charge radius (R_W) as [78]

$$R_W^2 = \frac{1}{Q_W} \int r^2 \rho_W(r) d^3r = \frac{3}{5}c^2 + \frac{7}{5}\pi^2 a^2, \quad (4.53)$$

which gives

$$\rho_W^0 = \frac{27Q_W}{4\pi(5R_W^2 - 4\pi^2 a^2)\sqrt{15R_W^2 - 21\pi^2 a^2}}. \quad (4.54)$$

R_W of ^{208}Pb as a function of A_{PV} for various theoretical models is shown in Fig. 4.31. The value of R_W measured by PREX-2 is obtained by interpolation using the PREX-2 A_{PV} result.

4.11. WEAK CHARGE RADIUS (R_W) OF ^{208}Pb

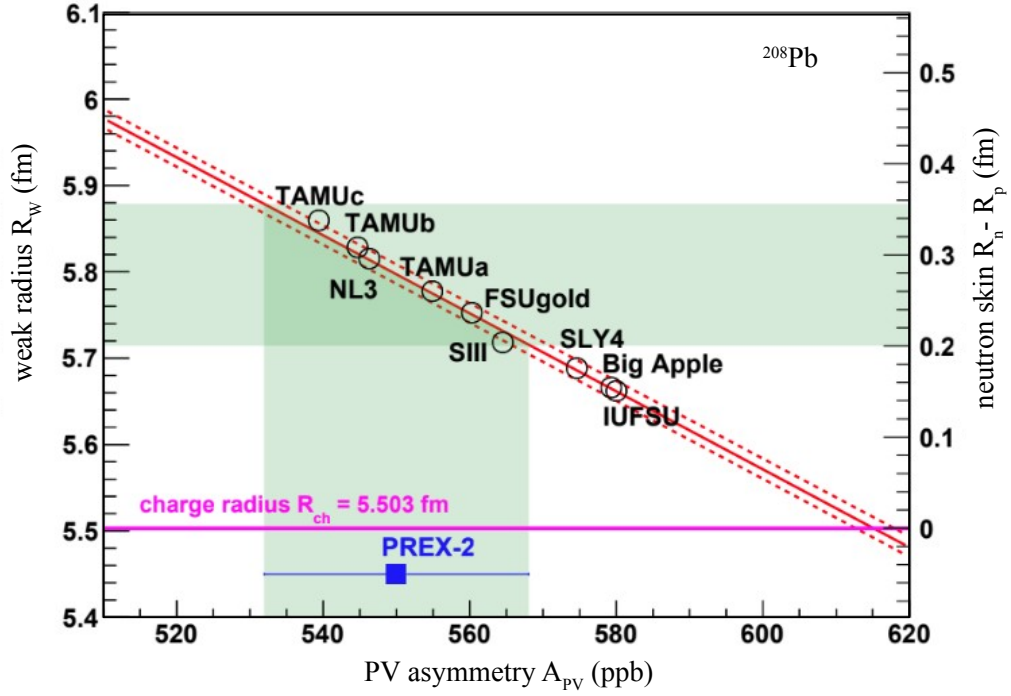


Figure 4.31: Weak charge radius (R_W) and neutron skin ($R_{skin} = R_n - R_p$) of ^{208}Pb as a function of A_{PV} for various theoretical models. The PREX-2 measurement is shown by the blue rectangular data point with the green vertical band showing the total experimental uncertainty. The dotted (red) lines give the model uncertainty. The nuclear electromagnetic charge radius for ^{208}Pb is shown by the magenta-colored line [70]. The intersection of the vertical green band with the span of theoretical models produces the horizontal green band of uncertainty in R_W and R_{skin} .

The weak charge radius in ^{208}Pb measured by PREX-2 [70] is

$$R_W = 5.795 \pm 0.082 \text{ (exp.)} \pm 0.013 \text{ (model) fm.} \quad (4.55)$$

Furthermore, Eq. 4.54 gives a measure of the ^{208}Pb interior weak density to be [70]

$$\rho_W^0 = -0.0798 \pm 0.0038 \text{ (exp.)} \pm 0.0013 \text{ (model) fm}^{-3}. \quad (4.56)$$

4.12 Neutron Skin (R_{skin}) of ^{208}Pb

After extracting the weak charge radius (R_W) from the measured A_{PV} , to get the weak charge skin, we need to subtract the known value of the charge radius (R_{ch}) of the target nucleus. R_{ch} has been previously determined experimentally to be 5.503 fm. Using Eq. 4.55, we determine the weak charge skin of ^{208}Pb to be

$$R_{skin}^W = R_W - R_{ch} = 0.292 \pm 0.082 \text{ (exp.)} \pm 0.013 \text{ (model) fm}, \quad (4.57)$$

where the exp. error comes from both statistical and systematic uncertainties in A_{PV} .

Finally, the neutron skin (R_{skin}), defined as the difference between point neutron and proton radii (i.e. $R_n - R_p$) is given by [79]

$$R_{skin} = R_n - R_p = \left(1 + \frac{Zq_p}{Nq_n}\right) (R_W - R_{ch}), \quad (4.58)$$

where Z is the nuclear charge number, N is the neutron number of the nucleus, $q_p = 0.0721$ is the radiatively corrected weak charge of a proton, and $q_n = -0.9878$ is that of a neutron. The ^{208}Pb neutron skin as a function of A_{PV} obtained from various theoretical models and the PREX-2 measurement is presented in Fig. 4.31. This gives the neutron skin for ^{208}Pb as [70]

$$R_{skin} = 0.278 \pm 0.078 \text{ (exp.)} \pm 0.012 \text{ (model) fm}. \quad (4.59)$$

Chapter 5

Result and Conclusion

The PREX-2 and CREX experiments took place in Hall A at JLab from Summer 2019 to Fall 2020. In this dissertation, we have presented the measurement concepts, the experimental apparatus design, commissioning and operation, and the ensemble of aggressive systematic controls achieved for these experiments. We also thoroughly explained the A_{PV} measurement and neutron skin extraction of ^{208}Pb from PREX-2 data, noting that a detailed analysis of CREX data is still in progress by the time this document is finalized. In this chapter, we summarize the PREX-2 measurement, and report the combined PREX-2 and PREX-1 result for the neutron skin of ^{208}Pb .

5.1 Parity-Violating Asymmetry A_{PV}

The physics asymmetry (A_{PV}) from the PREX-2 measurement [70] is

$$A_{PV} = 550.00 \pm 16.09 \text{ (stat.)} \pm 8.16 \text{ (syst.) ppb.} \quad (5.1)$$

The experiment successfully contains the systematic uncertainty to just under 1.5 %, which is about a factor of two smaller than the statistical uncertainty. The experi-

5.2. NEUTRON SKIN (R_{SKIN}) OF ^{208}Pb

mental uncertainties from various sources are summarized in Table 5.1.

		Uncertainty Contribution to A_{PV}	
		Absolute (ppb)	Relative (%)
	Polarization	5.23	0.95
	Q^2	3.54	0.64
Systematic	Acceptance function	2.87	0.52
	Beam correction	2.98	0.54
	Non-linearity	2.69	0.49
	Carbon dilution	1.45	0.26
	Transverse asymmetry	0.30	0.06
	Charge correction	0.25	0.04
	Inelastic contamination	0.12	0.02
	Rescattering	0.10	0.02
	Total Systematic	8.16	1.48
Statistical	16.09	2.93	
Total	18.04	3.28	

Table 5.1: Summary of experimental uncertainties from various sources [70]. The total uncertainty is the quadrature sum of statistical and systematic uncertainties.

5.2 Neutron Skin (R_{skin}) of ^{208}Pb

PREX-2 measures the weak charge radius (R_W) of ^{208}Pb , using an electroweak interaction probe [70], with the result

$$R_W = 5.795 \pm 0.082 \text{ (exp.)} \pm 0.013 \text{ (model) fm.} \quad (5.2)$$

Subtracting the known experimental R_{ch} from this R_W (with the appropriate correction for the proton weak charge as shown in Eq. 4.58), R_{skin} in ^{208}Pb is determined

5.3. IMPLICATIONS OF PREX RESULTS

to be [70]

$$R_{skin} = 0.278 \pm 0.078 \text{ (exp.)} \pm 0.012 \text{ (model) fm.} \quad (5.3)$$

The R_{skin} measured by PREX-2 is in very good agreement with the PREX-1 measurement (within the error bars). The combined ^{208}Pb neutron skin measurement result from PREX-2 and PREX-1 is [70]

$$R_{skin}^{comb.} = 0.283 \pm 0.071 \text{ fm,} \quad (5.4)$$

where the uncertainty includes both experimental and model contributions.

5.3 Implications of PREX results

Due to a strong correlation between the slope of the symmetry energy, $L(\rho)$, and the neutron skin measurement, as presented in Fig. 1.3, the combined PREX result favors a relatively large slope (recall that this is the slope of symmetry energy with respect to nuclear density) with $L(\rho = \rho_0) = 106 \pm 37 \text{ MeV}$ [7, 70]. This has important astrophysical implications and suggests a larger pressure (as discussed in Sec. 1.2) and stiffer equation of state in the core of neutron stars, and hence a larger possible size for the stars. This shows that the PREX observation provides an important input parameter for the equation of state (EOS). The size of R_{skin} in neutron rich matter, such as ^{208}Pb , can be used to infer the size of neutron stars because it is the same pressure in the core of neutron rich matter that determines both the thickness of the neutron skin in an atomic nucleus and the radius of a neutron star [77]. Recall that the size of a neutron star is ~ 18 orders of magnitude larger than the size of a atomic nucleus. Merging the combined PREX result with constraints from NICER (Neutron

5.4. CONCLUSIONS

Star Interior Composition Explorer), on a 1.4 solar mass neutron star, [7] sets upper and lower limits on R_{skin} for ^{208}Pb to be $0.21 \lesssim R_{skin} \text{ (fm)} \lesssim 0.31$, and upper and lower limits on a neutron star radius to be $13.25 \lesssim R_*^{1.4} \text{ (km)} \lesssim 14.26$.

The combined PREX neutron skin result corresponds to a ^{208}Pb interior weak charge density of [70]

$$\rho_W^0 = -0.0796 \pm 0.0038 \text{ fm}^{-3}. \quad (5.5)$$

Combining Eq. 5.5 with the well-measured interior electromagnetic charge density ρ_{ch} , [70] allows the ^{208}Pb interior baryon density to be reported as

$$\rho_b^0 = 0.1480 \pm 0.0038 \text{ fm}^{-3}. \quad (5.6)$$

Another important implication of the PREX result is the nuclear electric dipole polarizability (α_D). Figure 5.1 shows the correlation between $\alpha_D J$ (here J represents the nuclear symmetry energy) and R_{skin} of ^{208}Pb . Using R_{skin} from [70] and $J = 38.1 \pm 4.7 \text{ MeV}$ from [7], [80] reports α_D for ^{208}Pb as

$$\alpha_D = 21.8_{-1.4}^{+1.1} \text{ fm}^3. \quad (5.7)$$

5.4 Conclusions

PREX-2 extracts the neutron skin thickness of ^{208}Pb nuclei using the scattering of longitudinally polarized electrons from unpolarized targets. Electrons elastically scattered at $\sim 5^\circ$ are integrated using artificial fused-silica radiators (Spectrosil 2000). The experiment overcomes all the technical challenges that PREX-1 had encountered in

5.4. CONCLUSIONS

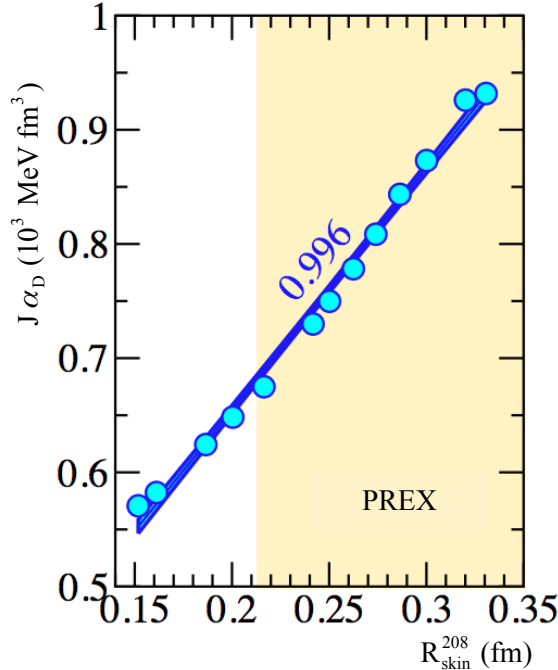


Figure 5.1: Electric dipole polarizability times symmetry energy plotted against R_{skin} of ^{208}Pb for various covariant energy density functionals. The number next to the fitting line shows the correlation coefficient. The yellow shaded region represents the PREX error band [80].

2010. Furthermore, PREX-2 is able to control the overall systematic uncertainty well below the proposed value, particularly the leading sources such as beam corrections, polarization, and detector non-linearity. We measure the parity-violating asymmetry $A_{PV} = 550.00 \pm 16.09$ (stat.) ± 8.16 (syst.) ppb, which results in a neutron skin, $R_{skin} = 0.278 \pm 0.078$ (exp.) ± 0.012 (model) fm, for ^{208}Pb . Combining the new neutron skin with the PREX-1 2010 measurement (which used the same approach), [70] reports the neutron skin in ^{208}Pb as given in Eq. 5.4 to be 0.283 ± 0.071 fm.

Following PREX-2 we run CREX and take A_{PV} data for the ^{48}Ca target. Since CREX shares the same set of equipment and setups as PREX-2, we expect a similar set of systematic uncertainty contributions. A preliminary asymmetry analysis has been performed by the PREX-2/CREX collaboration, and the detailed analysis is still ongoing as of the date this document is concluded. A future experiment MREX

5.4. CONCLUSIONS

has been proposed to measure the R_{skin} of ^{208}Pb at Mainz, Germany with a much better precision of ± 0.03 fm [3, 81].

Appendix A

Detector Non-linearity

The non-linearities for several PMTs are characterized in bench-tests both before and after the experiments. The measurement procedures are given in Sec. 3.6.4. The following tables show the non-linearities for the PREX-2/CREX quartz detector PMTs at several light levels and HV settings. The non-linearities below 0.3 % are marked as acceptable and are shown with a cyan-colored background. In the tables, I_a is the PMT anode current, and preAmp is the I-to-V gain setting of the pre-amplifier.

HV (V)	I_a (uA)	preAmp (M Ω)	non-Lin (%)
-765	49.78	0.10	0.581 \pm 0.182
-715	34.75	0.21	0.157 \pm 0.084
-690	26.60	0.21	-0.011 \pm 0.066
-685	19.30	0.21	0.157 \pm 0.287
-655	20.30	0.30	-0.180 \pm 0.129
-610	13.64	0.50	-0.330 \pm 0.134
-580	10.40	0.50	-0.866 \pm 0.195
-540	7.11	1.00	-0.796 \pm 0.183
-510	5.26	1.00	-1.036 \pm 0.172

Table A.1: Non-linearities for PMT ZK5407 at 10 nA light level.

HV (V)	I_a (uA)	preAmp (MΩ)	non-Lin (%)
-825	49.76	0.10	1.183 ± 0.201
-780	36.83	0.21	0.354 ± 0.107
-730	25.97	0.21	0.218 ± 0.172
-690	20.38	0.30	0.063 ± 0.215
-650	14.89	0.50	0.013 ± 0.140
-620	10.37	0.50	-0.217 ± 0.137
-565	7.04	1.00	0.106 ± 0.124
-530	5.01	1.00	0.173 ± 0.131
-500	3.64	2.00	-0.294 ± 0.122

Table A.2: Non-linearities for PMT ZK5407 at 7 nA light level.

HV (V)	I_a (uA)	preAmp (MΩ)	non-Lin (%)
-800	20.12	0.30	0.420 ± 0.166
-745	13.97	0.50	0.353 ± 0.134
-705	10.45	0.50	0.048 ± 0.214
-655	7.06	1.00	-0.008 ± 0.191
-620	5.03	1.00	0.220 ± 0.094
-580	3.63	2.00	0.045 ± 0.165
-555	2.88	2.00	0.203 ± 0.163
-510	1.82	4.00	0.130 ± 0.224

Table A.3: Non-linearities for PMT ZK5407 at 3.5 nA light level.

HV (V)	I_a (uA)	preAmp (MΩ)	non-Lin (%)
-900	3.52	2.00	0.156 ± 0.137
-860	2.81	2.00	0.235 ± 0.082
-795	1.86	4.00	0.246 ± 0.107
-750	1.38	4.00	0.174 ± 0.121
-660	0.71	10.00	0.111 ± 0.142
-615	0.49	10.00	0.172 ± 0.166

Table A.4: Non-linearities for PMT ZK5407 at 0.3 nA light level.

HV (V)	I_a (uA)	preAmp (M Ω)	non-Lin (%)
-755	49.23	0.10	0.486 \pm 0.195
-710	35.35	0.21	-0.121 \pm 0.088
-685	19.67	0.21	-0.208 \pm 0.389
-680	27.92	0.21	-0.173 \pm 0.065
-640	20.33	0.30	-0.497 \pm 0.199
-600	14.40	0.50	-0.564 \pm 0.165
-565	10.38	0.50	-0.527 \pm 0.262
-525	7.03	1.00	-0.506 \pm 0.202

Table A.5: Non-linearities for PMT ZK5401 at 10 nA light level.

HV (V)	I_a (uA)	preAmp (M Ω)	non-Lin (%)
-925	50.21	0.10	0.997 \pm 0.219
-865	34.77	0.21	0.616 \pm 0.129
-835	28.57	0.21	0.027 \pm 0.164
-785	20.31	0.30	0.034 \pm 0.166
-735	14.37	0.50	0.188 \pm 0.127
-640	6.88	1.00	0.273 \pm 0.243
-605	5.10	1.00	0.157 \pm 0.179
-565	3.51	2.00	-0.071 \pm 0.108
-545	2.89	2.00	-0.056 \pm 0.086
-500	1.80	4.00	0.101 \pm 0.186

Table A.6: Non-linearities for PMT ZK5401 at 3.5 nA light level.

HV (V)	I_a (uA)	preAmp (M Ω)	non-Lin (%)
-995	6.94	1.00	0.425 \pm 0.137
-940	5.14	1.00	0.349 \pm 0.138
-875	3.51	2.00	0.116 \pm 0.093
-840	2.83	2.00	0.072 \pm 0.090
-780	1.87	4.00	0.082 \pm 0.078
-740	1.41	4.00	0.227 \pm 0.095
-645	0.67	10.00	0.213 \pm 0.220
-615	0.52	10.00	0.010 \pm 0.058

Table A.7: Non-linearities for PMT ZK5401 at 0.3 nA light level.

HV (V)	I_a (uA)	preAmp (M Ω)	non-Lin (%)
-955	3.51	2.00	0.044 ± 0.087
-915	2.83	2.00	-0.045 ± 0.054
-845	1.82	4.00	0.113 ± 0.096
-805	1.41	4.00	0.045 ± 0.113
-700	0.66	10.00	0.282 ± 0.183
-670	0.53	10.00	0.120 ± 0.086

Table A.8: Non-linearities for PMT ZK5401 at 0.18 nA light level.

HV (V)	I_a (uA)	preAmp (M Ω)	non-Lin (%)
-980	3.52	2.00	-0.109 ± 0.138
-940	2.80	2.00	0.238 ± 0.055
-870	1.83	4.00	0.118 ± 0.100
-825	1.38	4.00	-0.075 ± 0.083
-720	0.67	10.00	0.030 ± 0.086
-690	0.53	10.00	0.049 ± 0.095

Table A.9: Non-linearities for PMT ZK5401 at 0.15 nA light level.

HV (V)	I_a (uA)	preAmp (M Ω)	non-Lin (%)
-825	49.76	0.10	0.499 ± 0.275
-770	34.68	0.21	-0.019 ± 0.088
-720	28.41	0.21	0.284 ± 0.206
-705	18.63	0.21	-0.063 ± 0.088
-695	20.63	0.30	-0.148 ± 0.090
-650	14.64	0.50	-0.295 ± 0.066
-605	10.19	0.50	-0.180 ± 0.092
-560	7.04	1.00	-0.238 ± 0.190
-525	5.07	1.00	0.053 ± 0.102

Table A.10: Non-linearities for PMT ZK4033 at 10 nA light level.

HV (V)	I_a (uA)	preAmp (M Ω)	non-Lin (%)
-870	50.52	0.10	0.485 ± 0.243
-810	34.99	0.21	0.010 ± 0.120
-740	20.75	0.30	-0.192 ± 0.155
-680	14.28	0.50	-0.138 ± 0.107
-645	10.86	0.50	-0.215 ± 0.084
-590	6.82	1.00	0.008 ± 0.264
-555	4.96	1.00	-0.341 ± 0.155
-500	2.89	2.00	-0.370 ± 0.092

Table A.11: Non-linearities for PMT ZK4033 at 7 nA light level.

HV (V)	I_a (uA)	preAmp (M Ω)	non-Lin (%)
-930	34.16	0.21	0.346 ± 0.129
-900	28.78	0.21	0.064 ± 0.146
-845	20.38	0.30	-0.031 ± 0.134
-790	14.53	0.50	-0.082 ± 0.120
-745	10.79	0.50	0.109 ± 0.150
-685	6.94	1.00	0.041 ± 0.123
-645	5.07	1.00	0.297 ± 0.239
-600	3.49	2.00	-0.281 ± 0.133
-575	2.79	2.00	0.075 ± 0.143
-530	1.81	4.00	0.011 ± 0.102

Table A.12: Non-linearities for PMT ZK4033 at 3.5 nA light level.

HV (V)	I_a (uA)	preAmp (M Ω)	non-Lin (%)
-955	3.48	2.00	-0.006 ± 0.066
-915	2.80	2.00	0.045 ± 0.114
-845	1.84	4.00	0.104 ± 0.105
-800	1.39	4.00	0.025 ± 0.068
-700	0.69	10.00	0.154 ± 0.193
-665	0.53	10.00	0.195 ± 0.088

Table A.13: Non-linearities for PMT ZK4033 at 0.3 nA light level.

HV (V)	I_a (uA)	preAmp (M Ω)	non-Lin (%)
-1000	2.69	2.00	0.129 ± 0.133
-930	1.85	4.00	0.071 ± 0.180
-880	1.40	4.00	0.008 ± 0.110
-765	0.69	10.00	0.113 ± 0.134
-725	0.52	10.00	0.182 ± 0.181

Table A.14: Non-linearities for PMT ZK4033 at 0.18 nA light level.

HV (V)	I_a (uA)	preAmp (M Ω)	non-Lin (%)
-955	1.82	4.00	0.090 ± 0.079
-905	1.38	4.00	-0.001 ± 0.123
-790	0.69	10.00	0.058 ± 0.114
-750	0.53	10.00	0.077 ± 0.123

Table A.15: Non-linearities for PMT ZK4033 at 0.15 nA light level.

HV (V)	I_a (uA)	preAmp (M Ω)	non-Lin (%)
-710	49.86	0.10	0.815 ± 0.189
-670	36.12	0.21	-0.085 ± 0.115
-640	28.16	0.21	-0.209 ± 0.131
-615	21.65	0.21	0.100 ± 0.056
-600	20.05	0.30	-0.344 ± 0.183
-565	14.30	0.50	-0.610 ± 0.189

Table A.16: Non-linearities for PMT ZK5370 at 10 nA light level.

HV (V)	I_a (uA)	preAmp (M Ω)	non-Lin (%)
-760	50.00	0.10	0.606 ± 0.098
-710	33.34	0.21	0.517 ± 0.203
-670	25.23	0.30	0.245 ± 0.161
-640	21.32	0.30	0.252 ± 0.192
-590	14.70	0.50	0.003 ± 0.131
-560	10.32	0.50	-0.008 ± 0.145
-520	6.90	1.00	-0.123 ± 0.167
-490	4.91	1.00	-0.474 ± 0.147

Table A.17: Non-linearities for PMT ZK5370 at 7 nA light level.

HV (V)	I_a (uA)	preAmp (M Ω)	non-Lin (%)
-865	49.07	0.10	0.927 ± 0.071
-820	35.69	0.21	0.675 ± 0.154
-775	25.54	0.21	0.306 ± 0.214
-735	20.18	0.30	0.281 ± 0.271
-690	14.36	0.50	0.117 ± 0.278
-650	10.42	0.50	0.186 ± 0.143
-605	7.10	1.00	0.162 ± 0.178
-570	5.14	1.00	0.072 ± 0.098

Table A.18: Non-linearities for PMT ZK5370 at 3.5 nA light level.

HV (V)	I_a (uA)	preAmp (M Ω)	non-Lin (%)
-950	6.84	1.00	0.287 ± 0.106
-900	5.37	1.00	0.228 ± 0.079
-850	3.73	2.00	0.064 ± 0.132
-800	2.88	2.00	-0.037 ± 0.204
-750	2.01	4.00	0.167 ± 0.066
-700	1.39	4.00	0.047 ± 0.053
-620	0.72	10.00	0.065 ± 0.172
-580	0.50	10.00	0.054 ± 0.146

Table A.19: Non-linearities for PMT ZK5370 at 0.3 nA light level.

HV (V)	I_a (uA)	preAmp (M Ω)	non-Lin (%)
-1000	5.1	1.00	0.140 ± 0.154
-940	3.82	2.00	0.025 ± 0.083
-905	2.85	2.00	0.228 ± 0.165
-900	3.03	2.00	-0.027 ± 0.114
-830	1.92	4.00	0.225 ± 0.136
-770	1.31	4.00	0.123 ± 0.179
-700	0.79	10.00	-0.012 ± 0.163
-650	0.53	10.00	0.070 ± 0.191

Table A.20: Non-linearities for PMT ZK5370 at 0.18 nA light level.

HV (V)	I_a (uA)	preAmp (M Ω)	non-Lin (%)
-745	51.34	0.10	1.070 ± 0.246
-690	35.15	0.21	0.284 ± 0.167
-660	27.67	0.21	0.450 ± 0.173
-625	20.82	0.30	0.313 ± 0.062
-580	13.88	0.50	0.068 ± 0.124
-550	9.93	0.50	0.198 ± 0.238
-510	7.02	1.00	-0.088 ± 0.251

Table A.21: Non-linearities for PMT ZK5365 at 10 nA light level.

HV (V)	I_a (uA)	preAmp (M Ω)	non-Lin (%)
-765	50.42	0.10	0.920 ± 0.212
-715	35.04	0.21	0.243 ± 0.117
-690	28.82	0.21	0.024 ± 0.287
-645	20.17	0.30	0.146 ± 0.234
-605	14.29	0.50	-0.285 ± 0.248
-570	10.35	0.50	0.105 ± 0.105
-530	7.03	1.00	-0.351 ± 0.174

Table A.22: Non-linearities for PMT ZK5365 at 7 nA light level.

HV (V)	I_a (uA)	preAmp (M Ω)	non-Lin (%)
-880	49.40	0.10	1.289 ± 0.185
-825	34.98	0.21	0.529 ± 0.134
-795	28.57	0.21	0.154 ± 0.219
-760	19.68	0.30	0.362 ± 0.123
-700	14.65	0.50	-0.009 ± 0.205
-670	10.39	0.50	0.039 ± 0.173
-610	6.99	1.00	0.090 ± 0.133
-575	5.09	1.00	0.206 ± 0.125
-535	3.47	2.00	0.112 ± 0.143

Table A.23: Non-linearities for PMT ZK5365 at 3.5 nA light level.

HV (V)	I_a (uA)	preAmp (M Ω)	non-Lin (%)
-960	7.11	1.00	0.158 ± 0.098
-900	5.13	1.00	0.205 ± 0.101
-840	3.57	2.00	0.092 ± 0.089
-800	2.76	2.00	-0.036 ± 0.060
-745	1.87	4.00	0.253 ± 0.113
-705	1.40	4.00	-0.052 ± 0.070
-615	0.67	10.00	0.022 ± 0.107
-590	0.54	10.00	0.026 ± 0.119

Table A.24: Non-linearities for PMT ZK5365 at 0.3 nA light level.

HV (V)	I_a (uA)	preAmp (M Ω)	non-Lin (%)
-985	5.20	1.00	0.248 ± 0.083
-915	3.54	2.00	0.132 ± 0.080
-875	2.79	2.00	0.044 ± 0.072
-810	1.83	4.00	0.084 ± 0.085
-770	1.39	4.00	0.296 ± 0.086
-670	0.66	10.00	-0.010 ± 0.125
-640	0.52	10.00	0.122 ± 0.106

Table A.25: Non-linearities for PMT ZK5365 at 0.18 nA light level.

HV (V)	I_a (uA)	preAmp (M Ω)	non-Lin (%)
-955	3.56	2.00	0.085 ± 0.061
-910	2.77	2.00	0.232 ± 0.160
-845	1.85	4.00	-0.075 ± 0.104
-800	1.39	4.00	-0.102 ± 0.116
-700	0.69	10.00	0.115 ± 0.140
-665	0.52	10.00	-0.058 ± 0.129

Table A.26: Non-linearities for PMT ZK5365 at 0.15 nA light level.

HV (V)	I_a (uA)	preAmp (MΩ)	non-Lin (%)
-840	49.73	0.10	1.116 \pm 0.233
-790	34.37	0.21	0.964 \pm 0.185
-760	28.20	0.21	0.554 \pm 0.112
-715	20.00	0.30	0.498 \pm 0.106
-675	14.32	0.50	0.808 \pm 0.264
-640	10.45	0.50	0.849 \pm 0.547
-595	7.00	1.00	0.550 \pm 0.228
-565	5.08	1.00	0.510 \pm 0.223
-530	3.51	2.00	0.265 \pm 0.122
-510	2.83	2.00	0.422 \pm 0.142

Table A.27: Non-linearities for PMT ZK5555 at 7 nA light level.

HV (V)	I_a (uA)	preAmp (MΩ)	non-Lin (%)
-895	49.34	0.10	1.371 \pm 0.162
-845	35.00	0.21	0.888 \pm 0.073
-815	28.25	0.21	0.676 \pm 0.105
-770	20.42	0.30	0.342 \pm 0.104
-725	14.35	0.50	0.532 \pm 0.090
-690	10.74	0.50	0.690 \pm 0.408
-640	6.64	1.00	0.637 \pm 0.223
-605	5.03	1.00	0.230 \pm 0.074
-570	3.53	2.00	0.399 \pm 0.143
-550	2.87	2.00	0.286 \pm 0.087
-500	1.64	4.00	0.353 \pm 0.190

Table A.28: Non-linearities for PMT ZK5555 at 3.5 nA light level.

HV (V)	I_a (uA)	preAmp (MΩ)	non-Lin (%)
-965	6.84	1.00	0.417 \pm 0.118
-915	5.04	1.00	0.263 \pm 0.080
-860	3.54	2.00	0.092 \pm 0.137
-825	2.78	2.00	0.202 \pm 0.104
-770	1.84	4.00	0.261 \pm 0.089
-735	1.40	4.00	0.184 \pm 0.102
-650	0.69	10.00	0.236 \pm 0.126
-620	0.52	10.00	0.154 \pm 0.197

Table A.29: Non-linearities for PMT ZK5555 at 0.3 nA light level.

HV (V)	I_a (uA)	preAmp (MΩ)	non-Lin (%)
-1000	5.23	1.00	0.430 ± 0.057
-930	3.47	2.00	0.233 ± 0.178
-895	2.77	2.00	-0.070 ± 0.252
-835	1.84	4.00	0.131 ± 0.091
-795	1.39	4.00	0.199 ± 0.053
-705	0.69	10.00	0.153 ± 0.177
-670	0.51	10.00	0.105 ± 0.125

Table A.30: Non-linearities for PMT ZK5555 at 0.18 nA light level.

HV (V)	I_a (uA)	preAmp (MΩ)	non-Lin (%)
-940	3.45	2.00	0.196 ± 0.111
-905	2.78	2.00	0.164 ± 0.147
-845	1.85	4.00	0.115 ± 0.148
-810	1.44	4.00	0.070 ± 0.079
-715	0.69	10.00	0.072 ± 0.092
-680	0.52	10.00	0.050 ± 0.166

Table A.31: Non-linearities for PMT ZK5555 at 0.15 nA light level.

HV (V)	I_a (uA)	preAmp (MΩ)	non-Lin (%)
-850	27.78	0.21	0.484 ± 0.156
-800	20.08	0.30	0.018 ± 0.135
-750	14.37	0.50	0.150 ± 0.080
-700	10.22	0.50	0.242 ± 0.161
-650	6.76	1.00	0.182 ± 0.282
-615	5.05	1.00	0.168 ± 0.151
-575	3.58	2.00	0.154 ± 0.092
-550	2.83	2.00	0.224 ± 0.092
-500	1.71	4.00	0.104 ± 0.170

Table A.32: Non-linearities for PMT ZK5553 at 7 nA light level.

HV (V)	I_a (uA)	preAmp (M Ω)	non-Lin (%)
-970	28.03	0.21	0.276 \pm 0.097
-910	20.14	0.30	-0.016 \pm 0.111
-855	14.43	0.50	0.230 \pm 0.075
-800	10.14	0.50	0.188 \pm 0.083
-745	6.95	1.00	0.276 \pm 0.136
-700	5.01	1.00	0.130 \pm 0.116
-655	3.53	2.00	0.116 \pm 0.143
-630	2.88	2.00	-0.027 \pm 0.092
-580	1.83	4.00	0.063 \pm 0.099
-550	1.38	4.00	0.004 \pm 0.098

Table A.33: Non-linearities for PMT ZK5553 at 3.5 nA light level.

HV (V)	I_a (uA)	preAmp (M Ω)	non-Lin (%)
-1000	2.88	2.00	0.051 \pm 0.110
-915	1.80	4.00	0.139 \pm 0.154
-870	1.38	4.00	0.100 \pm 0.069
-765	0.71	10.00	-0.044 \pm 0.165
-720	0.51	10.00	0.040 \pm 0.161

Table A.34: Non-linearities for PMT ZK5553 at 0.3 nA light level.

HV (V)	I_a (uA)	preAmp (M Ω)	non-Lin (%)
-990	1.82	4.00	0.244 \pm 0.108
-940	1.38	4.00	0.036 \pm 0.098
-830	0.71	10.00	-0.103 \pm 0.111
-780	0.52	10.00	0.154 \pm 0.165

Table A.35: Non-linearities for PMT ZK5553 at 0.18 nA light level.

HV (V)	I_a (uA)	preAmp (M Ω)	non-Lin (%)
-695	49.17	0.10	0.651 \pm 0.081
-655	35.60	0.21	-0.019 \pm 0.191
-630	28.81	0.21	-0.165 \pm 0.261
-600	22.00	0.30	-0.182 \pm 0.104
-555	14.48	0.50	-0.246 \pm 0.241
-520	10.21	0.50	-0.061 \pm 0.083

Table A.36: Non-linearities for PMT ZK5363 at 10 nA light level.

HV (V)	I_a (uA)	preAmp (MΩ)	non-Lin (%)
-750	49.80	0.10	0.844 ± 0.198
-685	34.94	0.21	0.391 ± 0.068
-660	28.70	0.21	0.036 ± 0.173
-620	20.50	0.30	0.017 ± 0.167
-580	14.33	0.50	0.185 ± 0.136
-545	10.26	0.50	0.473 ± 0.476
-505	6.85	1.00	0.487 ± 0.272

Table A.37: Non-linearities for PMT ZK5363 at 7 nA light level.

HV (V)	I_a (uA)	preAmp (MΩ)	non-Lin (%)
-855	49.60	0.10	1.136 ± 0.133
-800	34.50	0.21	0.704 ± 0.112
-770	27.93	0.21	0.417 ± 0.095
-730	20.98	0.30	0.565 ± 0.274
-680	14.44	0.50	0.175 ± 0.171
-635	10.94	0.50	0.253 ± 0.096
-585	7.03	1.00	0.081 ± 0.183
-560	5.12	1.00	0.225 ± 0.212
-520	3.45	2.00	0.084 ± 0.168

Table A.38: Non-linearities for PMT ZK5363 at 3.5 nA light level.

HV (V)	I_a (uA)	preAmp (MΩ)	non-Lin (%)
-875	5.11	1.00	0.462 ± 0.214
-815	3.52	2.00	0.142 ± 0.114
-780	2.79	2.00	-0.054 ± 0.067
-720	1.80	4.00	0.200 ± 0.092
-690	1.43	4.00	0.085 ± 0.148
-595	0.65	10.00	-0.065 ± 0.139
-570	0.52	10.00	0.094 ± 0.070

Table A.39: Non-linearities for PMT ZK5363 at 0.3 nA light level.

HV (V)	I_a (uA)	preAmp (M Ω)	non-Lin (%)
-955	5.20	1.00	0.171 ± 0.100
-910	3.65	2.00	0.298 ± 0.103
-890	3.57	2.00	0.205 ± 0.130
-850	2.80	2.00	0.059 ± 0.063
-790	1.87	4.00	0.083 ± 0.126
-750	1.42	4.00	0.060 ± 0.127

Table A.40: Non-linearities for PMT ZK5363 at 0.18 nA light level.

HV (V)	I_a (uA)	preAmp (M Ω)	non-Lin (%)
-990	5.27	1.00	0.346 ± 0.196
-920	3.59	2.00	0.125 ± 0.094
-875	2.76	2.00	0.010 ± 0.135
-810	1.85	4.00	0.123 ± 0.175
-770	1.41	4.00	0.148 ± 0.119
-670	0.67	10.00	-0.047 ± 0.100
-640	0.53	10.00	0.049 ± 0.087

Table A.41: Non-linearities for PMT ZK5363 at 0.15 nA light level.

Appendix B

Possible Background Corrections

B.1 Strangeness and Neutron Electric Form Factor

The measured A_{PV} at the desired Q^2 is used to extract the weak form factor F_W . We then extract the weak charge distribution, i.e. the weak charge radius R_W of the target nucleus from the inverse Fourier transform of F_W . Extraction of the neutron radius, R_n , from R_W requires proper correction for strange quark contributions and effects of the neutron electric charge distribution (at the quark level). Assuming the strange quark form factor, G_s , is the same for the proton and neutron, the Z^0 coupling for the proton and neutron can be expressed as [23]

$$G_p^Z = \frac{1}{4}(1 - 4 \sin^2 \theta_W)G_p - \frac{1}{4}G_n - \frac{1}{4}G_s, \quad (\text{B.1})$$

$$G_n^Z = \frac{1}{4}(1 - 4 \sin^2 \theta_W)G_n - \frac{1}{4}G_p - \frac{1}{4}G_s, \quad (\text{B.2})$$

B.1. STRANGENESS AND NEUTRON ELECTRIC FORM FACTOR

where G_p (G_n) is the proton (neutron) electric form factor; note the magnetic form factor is irrelevant for the spin-zero target. Incorporating these form factors with the point proton (neutron) density, ρ_p (ρ_n), [23] has obtained the weak charge density ρ_W :

$$\rho_W(r) = 4 \int d^3 r' [G_n^Z(r') N \rho_n(|\mathbf{r} - \mathbf{r}'|) + G_p^Z(r') Z \rho_p(|\mathbf{r} - \mathbf{r}'|)], \quad (\text{B.3})$$

where $\rho_p(r)$ and $\rho_n(r)$ normalize to unity, while $\rho_W(r)$ normalizes to Q_W . The weak charge of the nucleus, Q_W , is given by

$$Q_W = -N + (1 - 4 \sin^2 \theta_W) Z. \quad (\text{B.4})$$

From ρ_p , ρ_n , and ρ_W , their respective radii can be extracted as

$$R_i^2 = \frac{1}{N_C} \int d^3 r r^2 \rho_i(r), \quad (\text{B.5})$$

where $i = p, n$ or W and N_C is the normalization constant defined by

$$N_C = \begin{cases} 1 & \text{for proton and neutron} \\ Q_W & \text{for weak charge} \end{cases} \quad (\text{B.6})$$

For R_n much larger than $R_n - R_p$ one can obtain the following relation for R_W : [23]

$$\begin{aligned} R_W \approx R_n + \frac{Z(1 - 4 \sin^2 \theta_W)}{N - (1 - 4 \sin^2 \theta_W) Z} (R_n - R_p) + \frac{1}{2R_n} \{ r_p^2 \\ + \frac{Z - (1 - 4 \sin^2 \theta_W) N}{N - (1 - 4 \sin^2 \theta_W) Z} r_n^2 + \frac{N + Z}{N - (1 - 4 \sin^2 \theta_W) Z} r_s^2 \}, \end{aligned} \quad (\text{B.7})$$

where r_p^2 (r_n^2) is the mean square charge radius of the proton (neutron), and r_s^2 is the mean square strangeness radius. For ^{208}Pb , plugging in $R_n = 5.50$ fm and $\sin^2 \theta_W =$

0.23, [23] has shown that

$$R_W \approx R_n + 0.055(R_n - R_p) + 0.061(\pm 0.002) - 0.0089(\pm 0.0003) - 0.011\rho_s, \quad (\text{B.8})$$

where the second term comes from the neutron skin and is very small for the now-known range of $R_n - R_p$, the third term comes from proton charge radius, the fourth term comes from neutron charge radius [82] and is also very small, while the last term comes from the strangeness radius, which is also shown to be very small by [23]. With that, the neutron radius can easily be inferred from a weak radius with a small correction coming from the proton charge radius [23]:

$$R_n \approx R_W - 0.06 \text{ fm}. \quad (\text{B.9})$$

B.2 Parity Admixtures and Meson Exchange Currents

What if the ground state of the target nucleus is not a parity eigenstate but has some contribution of 0^- ? It has been shown in [83] that in the Born approximation, the parity-violating asymmetry does not come from the parity admixture when there are spin-zero initial and final states. It has also been shown that as long as the exchanged virtual photon carries no spin, there is no parity-violating contribution from this, no matter what the parity of the initial or the final states might be. This is true even if the photon coupling involves a parity-violating meson exchange current [23]. Moreover, meson exchange currents may contribute to altering the weak charge distribution in a nucleus, but mesons can carry weak charge only up to a range much shorter than the

B.3. DISPERSION CORRECTIONS

neutron radius. So we can rule out this effect to cause any considerable complication in the neutron radius size.

B.3 Dispersion Corrections

Dispersion corrections come from multiple EM or weak interactions which excite the target nucleus to at least one intermediate state, as shown in Fig. B.1(b). At the PREX-2/CREX Q^2 range, the elastic flux is of order Z^2 while the inelastic rate is of the order Z . This gives a correction of order α/Z , which is very small.

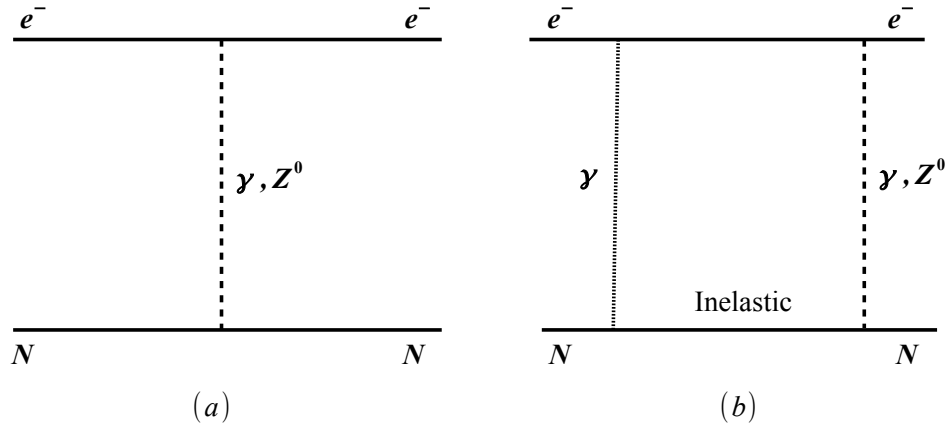


Figure B.1: (a) Electroweak interaction in the Born approximation. (b) Dispersion Corrections.

B.4 Shape Dependence and Surface Thickness

Let us consider, for instance, the weak charge density of a target nucleus in the Wood Saxon form:

$$\rho_W(r) = \frac{\rho_W^0}{e^{\frac{r-c}{a}} + 1}, \quad (\text{B.10})$$

where c is radius parameter and a is the surface thickness. Ideally, one can perform

B.4. SHAPE DEPENDENCE AND SURFACE THICKNESS

a first order derivative of the weak form factor at $Q^2 = 0$ to get the weak radius as given by

$$\langle R_W^2 \rangle \propto \left. \frac{dF_W(Q^2)}{dQ^2} \right|_{Q^2=0}. \quad (\text{B.11})$$

We measure the form factor at a single and small but nonzero Q^2 , where R_n is highly correlated to $F_W(Q^2)$ (see Fig. 2.7). The weak charge radius evaluated from this form factor is sensitive to the surface thickness. It has been shown in [23] that at the PREX kinematics, it is feasible to extract R_n to 1 % from a measured asymmetry, if one knows the surface thickness (a) in Eq. B.10 to only 25 %. And, this is well constrained by existing mean-field models.

Appendix C

CREX Inelastic Contamination

Although the first excited state of ^{48}Ca is relatively large (3.831 MeV), due to high beam energy, and possible natural jitter in beam energy, it lies very close to the elastic spectrum. No published A_{PV} results exist for the inelastic states of ^{48}Ca nuclei. As we mentioned in Sec. 4.1, the downstream main detectors are connected in counting mode DAQ for the entire CREX experiment. This allows us to perform frequent detector alignment checks without requiring invasive hall access. An analysis of the CREX inelastic contamination fraction is given in this section. Note that the information in this appendix is preliminary as the CREX analysis is still not finalized.

Figure C.1 shows the momentum distribution of the ^{48}Ca target in the right-HRS for a typical counting mode run. The peak at ~ 2180.5 MeV/c corresponds to the elastically scattered electrons, and the broad bump expanding between ~ 2174 MeV/c and ~ 2177.5 MeV/c represents many low-lying excited states. It is not easy to estimate the relative strength (cross-section) of each of these excited states. The three excited states shown in Fig. C.1 are chosen based on a trial and error method. The entire spectrum is fitted using a 22 parameter function (a sum of four Crystal Ball¹ functions and a first-order polynomial), where the parameters are initialized

¹This is a Gaussian function with a power-law tail.

such that the total fit function converges with the least χ^2 . The width (or resolution) of each excited state is fixed to the width of the elastic peak. These three excited states (among other excited states contributing to this bump) are found to be the strongest excited states in [84, 85]. The relative strength of each excited state is obtained from the ratio of integrals under the Crystal Ball function corresponding to the excited state and the area under the Crystal Ball function that fits the elastic events.

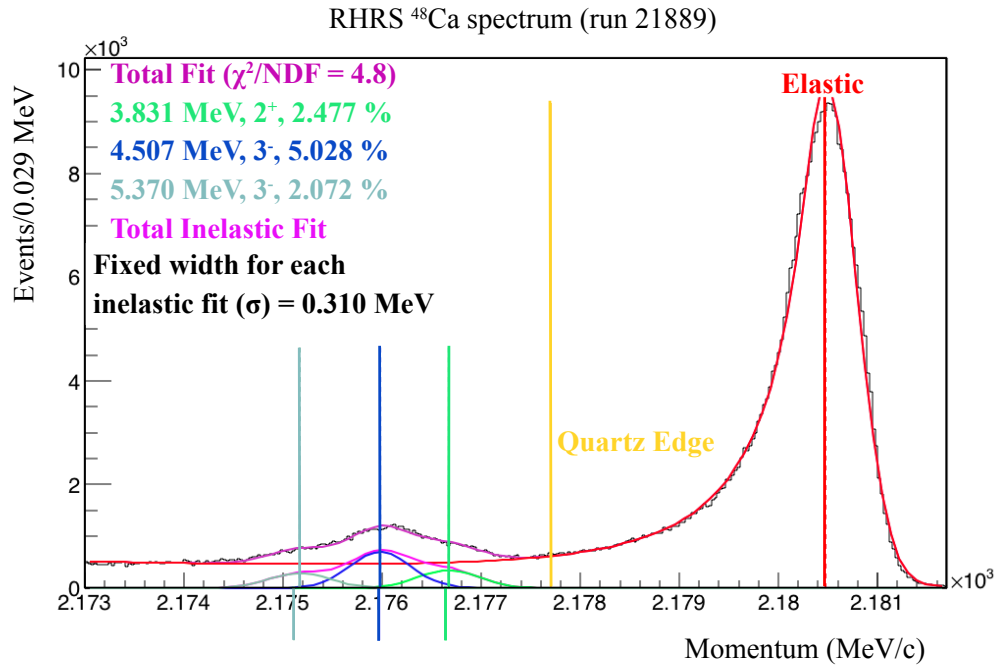


Figure C.1: The momentum (or energy) spectrum of ^{48}Ca . The theoretical locations of three strong excited states relative to the elastic peak are shown by different colored lines below the \hat{x} -axis. The preferred locations by the fit function are shown by the colored lines above the \hat{x} -axis. (Based on preliminary analysis.)

Figure C.2 shows momentum distributions: total flux (top plot), accepted and missed by quartz (middle plot), and acceptance fraction (bottom plot). The acceptance fraction is essentially the probability for each momentum bin to be accepted in the main quartz detector. This probability is obtained by dividing the red histogram in the middle plot by the black histogram in the top plot. The acceptance

probability for each excited state is obtained as the convolution integral of the corresponding Crystal Ball function from Fig. C.1 and probability function from Fig. C.2, normalized to the area under the Crystal Ball function.

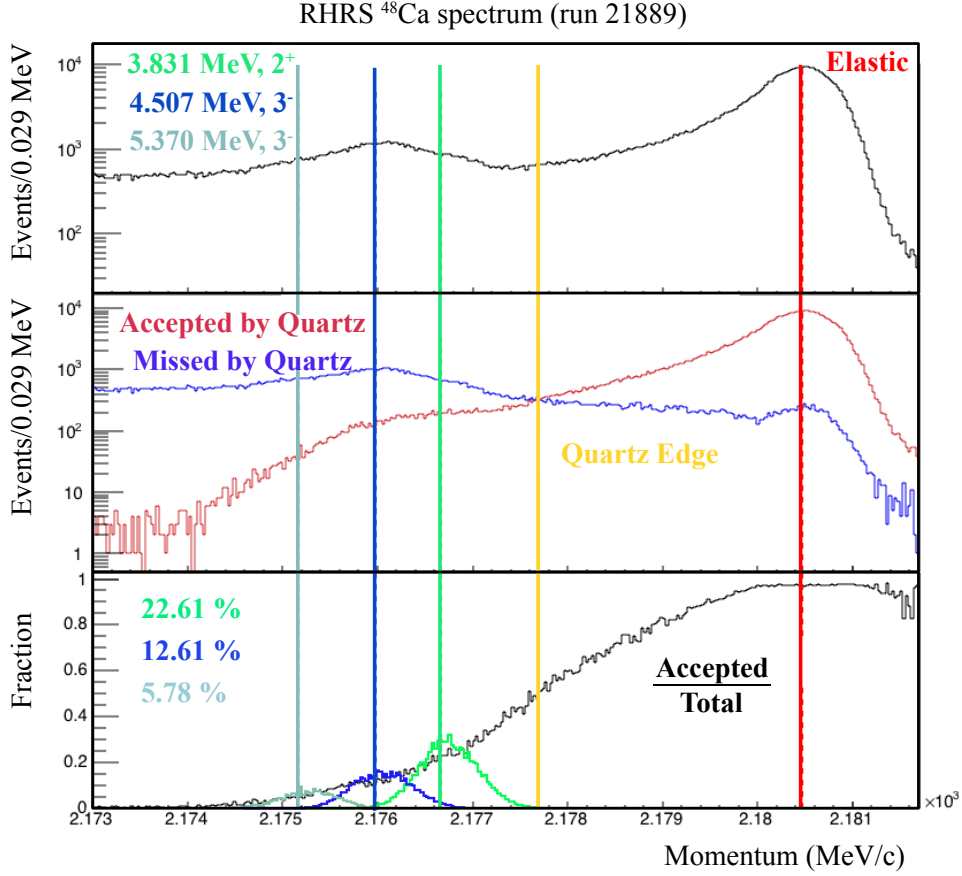


Figure C.2: Quartz acceptance function for CREX. The black histogram in the top plot shows the total flux. In the middle plot, the red histogram shows the flux accepted by the quartz, and the blue histogram shows the events missed by the quartz. The bottom histogram shows the accepted events divided by total events. The relative positions of the elastic peak, quartz edge, and the three excited states are shown in different colored vertical lines. (Based on preliminary analysis.)

As mentioned in Sec. 4.3.5, the background contamination fraction, f_i , for each excited state is obtained as the product of the relative strength, σ_{rel} , (from Fig. C.1) and acceptance probability, $Prob.$, (from Fig. C.2). The contamination fractions for the three excited states of ^{48}Ca are given in Table C.1. We also calculate the relative cross-sections of the three excited states using the inelastic form factors from [84] at

CREX kinematics. It is found that the relative cross-sections from our data (Table C.1) agree fairly well with this calculation.

Ex. State J^π (MeV)	Prob. %	$\sigma_{rel}(\%)$	$f_i(\%)$
2^+ (3.831)	22.61	2.48	0.56
3^- (4.507)	12.61	5.03	0.63
3^- (5.370)	5.78	2.07	0.12

Table C.1: Inelastic background fraction for CREX. (Based on preliminary analysis.)

Appendix D

PREX-2 Transverse Asymmetries

The beam corrected asymmetries during the PREX-2 vertical polarization settings for ^{208}Pb , ^{40}Ca , and ^{12}C are shown in Figures D.1, D.2, and D.3, respectively. As mentioned in Sec. 4.8.1, we use two different approaches: regression and dithering, for correcting the natural beam fluctuations. Because the results from the two techniques are very similar, we report the dither corrected asymmetries here. Note that we take data with the IHWP “IN” and “OUT” (same as for the A_{PV} data set), which helps cancel most of the helicity correlated false systematics. By changing the state of the IHWP setting, we essentially change the sign of the physics asymmetry as compared to the opposite IHWP setting. Therefore, while plotting these data points a proper sign correction has been applied to account for this sign change.

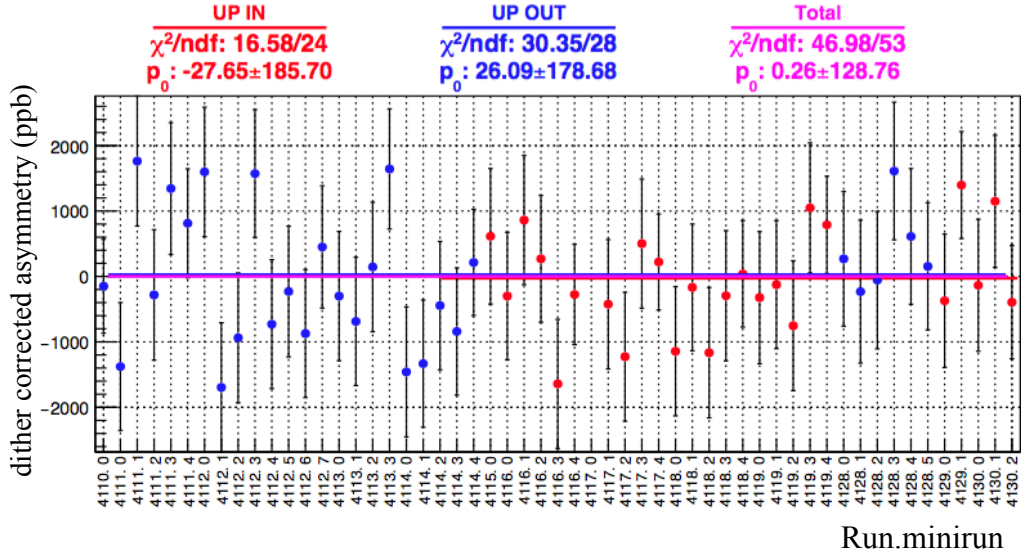


Figure D.1: Dither corrected transverse asymmetries for ^{208}Pb , (red) IHWP IN, (blue) IHWP OUT, and (magenta) total.

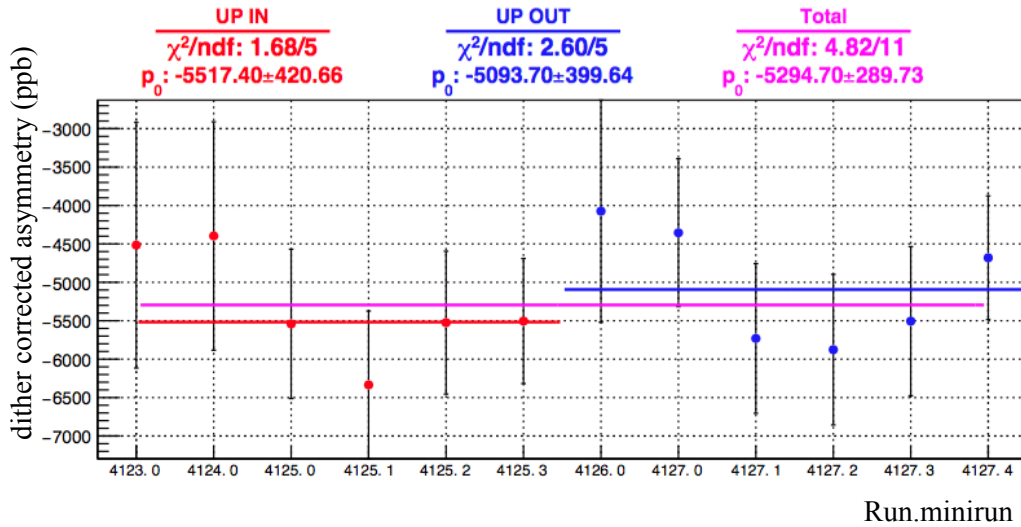


Figure D.2: Dither corrected transverse asymmetries for ^{40}Ca , (red) IHWP IN, (blue) IHWP OUT, and (magenta) total.

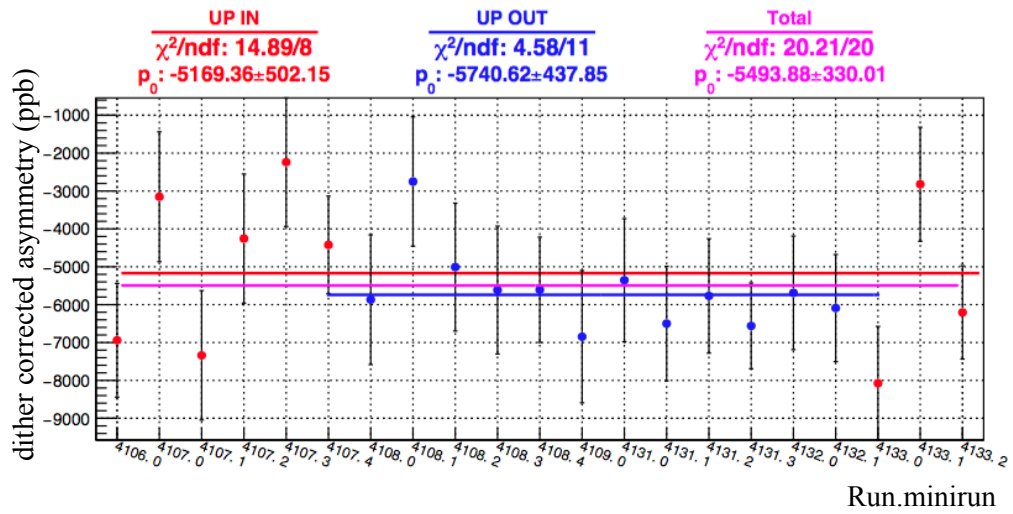


Figure D.3: Dither corrected transverse asymmetries for ^{12}C , (red) IHWP IN, (blue) IHWP OUT, and (magenta) total.

Bibliography

- [1] S. S. M. Wong, “Introductory Nuclear Physics (Wiley-VCH, Weinheim, 1998),” p. 9, ISBN-13: 978-0-471-23973-4, ISBN-10: 0-471-23973-9.
- [2] B. G. Todd-Rutel and J. Piekarewicz, “Neutron-Rich Nuclei and Neutron Stars: A New Accurately Calibrated Interaction for the Study of Neutron-Rich Matter,” *Phys. Rev. Lett.* **95**, 122501 (2005), <https://doi.org/10.1103/PhysRevLett.95.122501>.
- [3] M. Thiel et al., “Neutron skins of atomic nuclei: per aspera ad astra,” *J. Phys. G: Nucl. Part. Phys.* **46**, 093003 (2019), <https://doi.org/10.1088/1361-6471/ab2c6d>.
- [4] C. M. Tarbert et al., “Neutron Skin of ^{208}Pb from Coherent Pion Photoproduction,” *Phys. Rev. Lett.* **112**, 242502 (2014), <https://doi.org/10.1103/PhysRevLett.112.242502>.
- [5] C. J. Horowitz and J. Piekarewicz, “Neutron Radii of ^{208}Pb and neutron stars,” *Phys. Rev. C* **64**, 062802 (2001), <https://doi.org/10.1103/PhysRevC.64.062802>.
- [6] T. W. Donnelly, J. Dubach, and I. Sick, “Isospin dependences in parity-violating electron scattering,” *Nucl. Phys. A* **503**, 589-631 (1989), [https://doi.org/10.1016/0375-9474\(89\)90432-6](https://doi.org/10.1016/0375-9474(89)90432-6).

BIBLIOGRAPHY

- [7] B. T. Reed, F. J. Fattoyev, C. J. Horowitz, and J. Piekarewicz, “Implications of PREX-2 on the Equation of State of Neutron-Rich Matter,” *Phys. Rev. Lett.* **126**, 172503 (2021), <https://doi.org/10.1103/PhysRevLett.126.172503>.
- [8] X. Roca-Maza et al., “Neutron skin thickness from the measured electric dipole polarizability in ^{68}Ni , ^{120}Sn , and ^{208}Pb ,” *Phys. Rev. C* **92**, 064304 (2015), <https://doi.org/10.1103/PhysRevC.92.064304>.
- [9] A. Tamii et al., “Complete Electric Dipole Response and the Neutron Skin in ^{208}Pb ,” *Phys. Rev. Lett.* **107**, 062502 (2011), <https://doi.org/10.1103/PhysRevLett.107.062502>.
- [10] G. Hagen et al., “Neutron and weak charge distributions of the ^{48}Ca nucleus,” *Nature Phys.* **12**, 186-190 (2016), <https://doi.org/10.1038/nphys3529>.
- [11] D. Griffiths, “Introduction to Elementary Particles (WILEY-VCH, Weinheim, 2008),” p. 315, ISBN: 978-3-527-40601-2.
- [12] T. D. Lee and C. N. Yang, “Question of Parity Conservation in Weak interactions,” *Phys. Rev.* **104**, 254-258 (1956), <https://doi.org/10.1103/PhysRev.104.254>.
- [13] C. S. Wu et al., “Experimental Test of Parity Conservation in Beta Decay,” *Phys. Rev.* **105**, 1413-1415 (1957), <https://doi.org/10.1103/PhysRev.105.1413>.
- [14] T. W. B. Kibble, “History of electroweak symmetry breaking,” *J. Phys.: Conf. Ser.* **626** 012001 (2015), <https://doi.org/10.1088/1742-6596/626/1/012001>.
- [15] M. Schirber, “Nobel Prize—Why Particles Have Mass,” *Physics* 6, 111, 11 October 2013, accessed 16 May 2021, <https://physics.aps.org/articles/v6/111>.

BIBLIOGRAPHY

- [16] F. Englert and R. Brout, “Broken Symmetry and the Mass of Gauge Vector Mesons,” *Phys. Rev. Lett.* **13**, 321–323 (1964), <https://doi.org/10.1103/PhysRevLett.13.321>.
- [17] P. W. Higgs, “Broken Symmetries and the Masses of Gauge Bosons,” *Phys. Rev. Lett.* **13**, 508–509 (1964), <https://doi.org/10.1103/PhysRevLett.13.508>.
- [18] G. Guralnik, C. R. Hagen, and T. W. B. Kibble, “Global Conservation Laws and Massless Particles,” *Phys. Rev. Lett.* **13**, 585–587 (1964), <https://doi.org/10.1103/PhysRevLett.13.585>.
- [19] G. Aad et al., “Observation of a new particle in the search for the Standard Model Higgs boson with the ATLAS detector at the LHC,” *Phys. Lett. B* **716**, 1–29 (2012), <https://doi.org/10.1016/j.physletb.2012.08.020>.
- [20] “What is Grand Unification Theory?,” accessed 5 July 2020, <http://www.astronomycafe.net/FAQs/q1050x.html>.
- [21] D. Griffiths, “Introduction to Elementary Particles (WILEY-VCH, Weinheim, 2008),” p. 331–332, SBN: 978-3-527-40601-2.
- [22] C. J. Horowitz, “Parity violating elastic electron scattering and Coulomb distortions,” *Phys. Rev. C* **57**, 3430 (1998), <https://doi.org/10.1103/PhysRevC.57.3430>.
- [23] C. J. Horowitz, S. J. Pollock, P. A. Souder, and R. Michaels, “Parity violating measurements of neutron densities,” *Phys. Rev. C* **63**, 025501 (2001), <https://doi.org/10.1103/PhysRevC.63.025501>.

BIBLIOGRAPHY

- [24] C.J. Horowitz, K.S. Kumar, and R. Michaels, “Electroweak measurements of neutron densities in CREX and PREX at JLab, USA,” *Eur. Phys. J. A* **50**, 48 (2014), <https://doi.org/10.1140/epja/i2014-14048-3>.
- [25] R. Silwal, “Probing the Strangeness Content of the Proton and the Neutron Radius of ^{208}Pb using Parity-Violating Electron Scattering,” (2012), Dissertations, <https://doi.org/10.18130/V3WC4P>.
- [26] N. K. Liyanage, K. Saenboonruang, and R. Michlels, “ Q^2 Measurement for PREX,” E06-002 Technical Note, Jefferson Lab (2011), https://hallaweb.jlab.org/parity/prex/qsq/Q2_PREX.pdf.
- [27] C. Y. Prescott et al., “Parity non-conservation in inelastic electron scattering,” *Phys. Lett. B* **77**, 347-352 (1978), [https://doi.org/10.1016/0370-2693\(78\)90722-0](https://doi.org/10.1016/0370-2693(78)90722-0).
- [28] D. McNulty, “Detectors for High Flux Parity Experiments at JLab: PREX-2, CREX and MOLLER,” *Workshop - Weak Elastic Scattering with Nuclei, Seattle Washington*, 5 March 2019, accessed 31 August 2020, https://www.int.washington.edu/talks/WorkShops/int_19_73W/People/McNulty_D/McNulty.pdf.
- [29] A. Yu. Smirnov, V. D. Borisevich, and A. Sulaberidze, “Evaluation of specific cost of obtainment of lead-208 isotope by gas centrifuges using various raw materials,” *Theoretical Foundations of Chemical Engineering* **46**, 373-378 (2012), <https://doi.org/10.1134/S0040579512040161>.
- [30] V. E. Starodubsky and N. M. Hints, “Extraction of neutron densities from elastic proton scattering by $^{206,207,208}\text{Pb}$ at 650 MeV,” *Phys. Rev. C* **49**, 2118 (1994), <https://doi.org/10.1103/PhysRevC.49.2118>.

BIBLIOGRAPHY

- [31] B. C. Clark, L. J. Kerr, and S. Hama, “Neutron densities from a global analysis of medium-energy proton-nucleus elastic scattering,” *Phys. Rev. C* **67**, 054605 (2003), <https://doi.org/10.1103/PhysRevC.67.054605>.
- [32] A. Trzcinska et al., “Neutron Density Distributions Deduced from Antiprotonic Atoms,” *Phys. Rev. Lett.* **87**, 082501 (2001), <https://doi.org/10.1103/PhysRevLett.87.082501>.
- [33] C. Garcia-Recio, J. Nieves, and E. Oset, “Neutron distributions from pionic atoms,” *Nucl. Phys. A* **547**, 473-487 (1992), [https://doi.org/10.1016/0375-9474\(92\)90034-H](https://doi.org/10.1016/0375-9474(92)90034-H).
- [34] C. J. Horowitz et al., “Weak charge form factor and radius of ^{208}Pb through parity violation in electron scattering,” *Phys. Rev. C* **85**, 032501 (2012), <https://doi.org/10.1103/PhysRevC.85.032501>.
- [35] J. Piekarewicz et al., “Electric dipole polarizability and the neutron skin,” *Phys. Rev. C* **85**, 041302 (2012), <https://doi.org/10.1103/PhysRevC.85.041302>.
- [36] J. Piekarewicz, “Nuclear Structure, Neutron Radii, Error Bars, and Correlations,” *Calcium Radius Experiment (CREX) Workshop, JLab*, 17-19 March 2013, accessed 18 May 2021, https://www.jlab.org/conferences/crex/mon_am/JPiekarewiczCREX.pdf.
- [37] X. Roca-Maza et al., “Giant quadrupole resonances in ^{208}Pb , the nuclear symmetry energy and the neutron skin thickness,” *Phys. Rev. C* **87**, 034301 (2013), <https://doi.org/10.1103/PhysRevC.87.034301>.
- [38] J. Zenihiro et al., “Neutron density distributions of $^{204,206,208}\text{Pb}$ deduced via proton elastic scattering at $E_p = 295$ MeV,” *Phys. Rev. C* **82**, 044611 (2010), <https://doi.org/10.1103/PhysRevC.82.044611>.

BIBLIOGRAPHY

- [39] B. A. Brown et al., “Neutron skin deduced from antiprotonic atom data,” *Phys. Rev. C* **76**, 034305 (2007), <https://doi.org/10.1103/PhysRevC.76.034305>.
- [40] A. H. Lippok and H. Muther, “Relativistic effects in three-nucleon forces for nuclear matter and finite nuclei,” *Phys. Rev. C* **92**, 034312 (2015), <https://doi.org/10.1103/PhysRevC.92.034312>.
- [41] M. Toyokawa, K. Minomo, M. Kohno, and M. Yahiro, “Roles of chiral three-nucleon forces in nucleon-nucleus scattering,” *J. Phys. G: Nucl. Part. Phys.* **42**, 025104 (2015), <https://doi.org/10.1088/0954-3899/42/2/025104>.
- [42] B. A. Loiseau and Y. Nogami, “Three-nucleon force,” *Nucl. Phys. B* **2**, 470-478 (1967), [https://doi.org/10.1016/0550-3213\(67\)90184-8](https://doi.org/10.1016/0550-3213(67)90184-8).
- [43] G. Hagen, T. Papenbrock, D. J. Dean, and M. Hjorth-Jensen, “Medium-Mass Nuclei from Chiral Nucleon-Nucleon Interactions,” *Phys. Rev. Lett.* **101**, 092502 (2008), <https://doi.org/10.1103/PhysRevLett.101.092502>.
- [44] J. P. Vary, S. Popescu, S. Stoica, and P. Navratil, “A no-core shell model for ^{48}Ca , ^{48}Sc and ^{48}Ti ,” *J. Phys. G: Nucl. Part. Phys.* **36**, 085103 (2009), <https://doi.org/10.1088/0954-3899/36/8/085103>.
- [45] J. H. Hamilton, and A. V. Ramayya, “Fission and Properties of Neutron-Rich Nuclei,” *World Scientific*, (2013), <https://doi.org/10.1142/8910>.
- [46] “CEBAF at 12 GeV Schematic,” accessed 20 May 2020, <https://www.flickr.com/photos/jeffersonlab/12599705145>.
- [47] K. D. Paschke, “Controlling helicity-correlated beam asymmetries in a polarized electron source,” *Eur. Phys. J. A* **32**, 549–553 (2007), <https://doi.org/10.1140/epja/i2006-10442-8>.

BIBLIOGRAPHY

- [48] Z. Ahmed, “Measurement Of Neutron Radius In Lead By Parity Violating Scattering Flash ADC DAQ,” (2012), Dissertations, https://surface.syr.edu/phy_etd/120.
- [49] https://wiki.jlab.org/ciswiki/images/e/e7/Jlab_source_PV2.pdf.
- [50] C. Palatchi, “Laser and Electron Beam Technology for Parity Violating Electron Scattering Measurements,” (2019), Dissertations, <https://doi.org/10.18130/v3-vvcs-m369>.
- [51] T. B. Humensky et al., “SLAC’s polarized electron source laser system and minimization of electron beam helicity correlations for the E-158 parity violation experiment,” *Nucl. Instrum. Meth. A* **521**, 261-298 (2004), <https://doi.org/10.1016/j.nima.2003.09.065>.
- [52] K. Saenboonruang, “Measurement of the Neutron Radius of ^{208}Pb Through Parity Violation in Electron Scattering,” (2013), Dissertations, <https://hallaweb.jlab.org/parity/prex/theses/KiadtisakThesis.pdf>.
- [53] B. Moffit, “Elastic Scattering Of Longitudinally Polarized Electrons From ^4He A Measurement of G_E^s at $Q^2 = 0.1 \text{ (GeV/c)}^2$,” (2007), Dissertations, <https://dx.doi.org/doi:10.21220/s2-s083-tg75>.
- [54] K. B. Unser, “The parametric current transformer, a beam current monitor developed for LEP,” *AIP Conference Proceedings* **252**, 266 (1992), <https://doi.org/10.1063/1.42124>.
- [55] D. W. Higinbotham and T. Keppel, “2017 Version: Jefferson Lab Hall A Standard Equipment Manual,” June 2019, <https://hallaweb.jlab.org/github/halla-osp/version/Standard-Equipment-Manual.pdf>.

BIBLIOGRAPHY

- [56] J. M. Grames et al., “Unique electron polarimeter analyzing power comparison and precision spin-based energy measurement,” *Phys. Rev. ST Accel. Beams* **7**, Article 042802 (2004), <https://doi.org/10.1103/PhysRevSTAB.7.042802>.
- [57] A. Rakhman, “The Design and Construction of a Green Laser and Fabry-parot Cavity System for Jefferson Lab’s Hall A Compton Polarimeter,” (2011), Dissertations, https://surface.syr.edu/phy_etd/117.
- [58] A. J. Zec, “Compton Polarimetry for the PREX-II Experiment,” *2020 Fall Meeting of the APS Division of Nuclear Physics*, 29 October-1 November 2020, accessed 20 December 2020, <https://drive.google.com/file/d/1JDybhH2dk3uWs0zjq0wBffQ5YIDfptIB/view>.
- [59] S. C. Dusa, “PREX2-CREX Target,” *PREX2/CREX Collaboration Meeting*, 1 October 2017, accessed 2 March 2018, https://prex.jlab.org/DocDB/0000/000025/003/PREX2target_covrig_oct2017.pdf.
- [60] K. Paschke et al., “PREX-II: PRECISION PARITY-VIOLATING MEASUREMENT OF THE NEUTRON SKIN OF LEAD,” Proposal to Jefferson Lab PAC 38, <https://hallaweb.jlab.org/parity/prex/prexII.pdf>.
- [61] J. Alcorn et al., “Basic instrumentation for hall a at jefferson lab,” *Nucl. Instrum. Meth. A* **522**, 294–346 (2004), <https://doi.org/10.1016/j.nima.2003.11.415>.
- [62] K. G. Fissum et al., “Vertical drift chambers for the Hall A high-resolution spectrometers at Jefferson Lab,” *Nucl. Instrum. Meth. A* **474**, 108–131 (2001), [https://doi.org/10.1016/S0168-9002\(01\)00875-0](https://doi.org/10.1016/S0168-9002(01)00875-0).
- [63] J. L. Autran, D. Munteanu, T. Saad Saoud, and S. Moindjie, “Characterization of atmospheric muons at sea level using a cosmic ray telescope,” *Nucl. In-*

BIBLIOGRAPHY

- strum. Meth. A* **903**, 77-84 (2018), <https://doi.org/10.1016/j.nima.2018.06.038>.
- [64] C. B. Villarreal, “Developing Low Noise, Rad-hard Detectors for Parity Violating Experiments,” (2019), Dissertations, <https://etd.iri.isu.edu/ViewSpecimen.aspx?ID=1828>.
- [65] “PHOTOMULTIPLIER TUBES Basics and Applications, Edition 3a,” https://www.hamamatsu.com/resources/pdf/etd/PMT_handbook_v3aE.pdf.
- [66] B. Lowe, “High-Precision PMT Gain Measurement With Subsequent Quartz Cerenkov Detector Characterization,” (2019), Dissertations, <https://etd.iri.isu.edu/ViewSpecimen.aspx?ID=812>.
- [67] C. Gal, “Radiation dose estimate to quartz for PREX run,” <http://ace.phys.virginia.edu/HAPPEX/4064>.
- [68] C. Ghosh, “Experience with the GEM detectors during the PREX-II Physics run,” *2020 Fall Meeting of the APS Division of Nuclear Physics*, 29 October-1 November 2020, accessed 1 June 2021, <https://drive.google.com/file/d/1h362gWw6DJom8m-1tthGmZ7Lp70Xz0jN/view>.
- [69] T. Ye, “Calibrating the Sensitivity of High-rate Asymmetry Measurements to Beam Motion,” *2020 Fall Meeting of the APS Division of Nuclear Physics*, 29 October-1 November 2020, accessed 1 June 2021, <https://drive.google.com/file/d/1JSC5DyuG100QgTMs--gm7qnHudbx0q/view>.
- [70] D. Adhikari et al., “Accurate Determination of the Neutron Skin Thickness of ^{208}Pb through Parity-Violation in Electron Scattering,” *Phys. Rev. Lett.* **126**, 172502 (2021), <https://doi.org/10.1103/PhysRevLett.126.172502>.

BIBLIOGRAPHY

- [71] A. Norman, “Electron Scattering from Lead Nuclei,” (1978), Dissertations, University of Virginia.
- [72] J. W. Wexler, “Measurement of the Parity Violating Asymmetry in Elastic Electron Scattering off ^{208}Pb ,” (2014), Dissertations, <https://doi.org/10.7275/5987597.0>.
- [73] S. Abrahamyan et al., “Measurement of the Neutron Radius of ^{208}Pb through Parity Violation in Electron Scattering,” *Phys. Rev. Lett.* **108**, 112502 (2012), <https://doi.org/10.1103/PhysRevLett.108.112502>.
- [74] M. Gorchtein and C. J. Horowitz, “Analyzing power in elastic scattering of electrons off a spin-0 target,” *Phys. Rev. C* **77**, 044606 (2008), <https://doi.org/10.1103/PhysRevC.77.044606>.
- [75] S. Abrahamyan et al., “New Measurements of the Transverse Beam Asymmetry for Elastic Electron Scattering from Selected Nuclei,” *Phys. Rev. Lett* **109**, 192501 (2012), <https://doi.org/10.1103/PhysRevLett.109.192501>.
- [76] C. J. Horowitz, J. Piekarewicz, and B. Reed, “Insights into nuclear saturation density from parity-violating electron scattering,” *Phys. Rev. C* **102**, 044321 (2020), <https://doi.org/10.1103/PhysRevC.102.044321>.
- [77] J. Piekarewicz, A. R. Linero, P. Giuliani, and E. Chicken, “Power of two: Assessing the impact of a second measurement of the weak-charge form factor of ^{208}Pb ,” *Phys. Rev. C* **94**, 034316 (2016), <https://doi.org/10.1103/PhysRevC.94.034316>.
- [78] B. T. Reed, Z. Jaffe, C. J. Horowitz, and C. Sfienti, “Measuring the surface thickness of the weak charge density of nuclei,” *Phys. Rev. C* **102**, 064308 (2020), <https://doi.org/10.1103/PhysRevC.102.064308>.

BIBLIOGRAPHY

- [79] C. J. Horowitz, “PREX-II Reveal,” *PREX-2/CREX Collaboration Meeting*, 27 October 2020, accessed 2 April 2021, https://prex.jlab.org/DocDB/0004/000467/001/Horowitz_PREXII.pdf.
- [80] J. Piekarewicz, “Electric dipole polarizability of neutron rich nuclei,” *arXiv:2104.11013v1 [nucl-th]* (2021), <https://arxiv.org/abs/2104.11013>.
- [81] D. Becker et al., “The P2 experiment,” *Eur. Phys. J. A* **54**, 208 (2018), <https://doi.org/10.1140/epja/i2018-12611-6>.
- [82] B. Povh, “Hadronic radii,” *Nucl. Phys. A* **532**, 133-140 (1991), [https://doi.org/10.1016/0375-9474\(91\)90690-8](https://doi.org/10.1016/0375-9474(91)90690-8).
- [83] G. Feinberg, “Polarized electron-nucleus scattering and parity-violating neutral-current interactions,” *Phys. Rev. D* **12**, 3575 (1975), <https://doi.org/10.1103/PhysRevD.12.3575>.
- [84] J. E. Wise et al., “Inelastic electron scattering from ^{48}Ca ,” *Phys. Rev. C* **31**, 1699 (1985), <https://doi.org/10.1103/PhysRevC.31.1699>.
- [85] R. A. Eisenstein et al., “Electron-Scattering Studies on Ca^{40} and Ca^{48} ,” *Phys. Rev.* **188**, 1815 (1969), <https://doi.org/10.1103/PhysRev.188.1815>.